CORA Cork Open Research Archive
Cartlann Taighde Oscailte Chorcaí

Title	Plasmonic gold nanostructures: optical properties and application in mercury detection
Authors	Schopf, Carola
Publication date	2015
Original Citation	Schopf, C. 2015. Plasmonic gold nanostructures: optical properties and application in mercury detection. PhD Thesis, University College Cork.
Type of publication	Doctoral thesis
Rights	© 2015, Carola Schopf. - http://creativecommons.org/licenses/by-nc-nd/3.0/
Download date	2026-11-01 08:57:02
Item downloaded from	https://hdl.handle.net/10468/2165



UCC
University College Cork, Ireland
Coláiste na hOllscoile Corcaigh

OLLSCOIL NA HÉIREANN

National University of Ireland



Plasmonic Gold Nanostructures: Optical Properties and Application in Mercury Detection

A Thesis Presented to the National University of Ireland
for the Degree of Doctor of Philosophy

by

Carola Schopf

Supervised by Dr. Daniela Iacopino



Tyndall National Institute

University College Cork

July 2015

Contents

Chapter 1 - Introduction 1
1.1. Environmental Impact of Mercury 3
1.2. Plasmonic Nanostructures 7
1.2.1. Surface Plasmon Resonance 8
1.2.2. Plasmon Coupling 13
1.3. Characterisation of Plasmonic Nanostructures 19
1.4. Plasmonic Nanostructures in Sensing Applications 23
1.4.1. General Sensing Strategies 23
1.4.2. Nanoparticle Based Mercury Detection Methods 30
1.5. Nanoalloys 35
1.6. Scope of this Thesis 39
Chapter 2 - Optical Properties of Plasmonic Nanostructures Based on Gold and Silver Nanoparticles and Gold Nanorods 43
2.1. Introduction 45
2.2. Experimental Methods 47
2.2.1. Nanostructure Fabrication 47
2.2.2. Nanostructure Characterisation 49
2.2.3. Calculation of Nanostructure Scattering Spectra 51
2.3. Results and Discussion 53
2.3.1. Optical Characterisation of Silver and Gold Nanoparticles 53
2.3.2. Optical Characterisation of Small Gold Nanoparticle Clusters 61
2.3.3. Optical Characterisation of Single Gold Nanorods 65
2.3.4. Optical Characterisation and Application of Gold Nanorod Arrays 68
2.4. Summary and Conclusions 77
Chapter 3 - Gold Nanoparticle Based Hybrid Structures for Mercury Detection 79
3.1. Introduction 81
3.2. Experimental Methods 85
3.2.1. Hybrid Nanostructure Fabrication 85
3.2.2. Hybrid Nanostructure Characterisation 87
3.2.3. Hybrid Nanostructure Mercury Ion Sensing Assessment 88
3.3. Results and Discussion 89
3.3.1. Fabrication and Characterisation of Gold Nanoparticle-C5 Hybrid Nanostructures for Mercury Ion Detection 89

3.3.2. Sensing Assessment of Gold Nanoparticles - C5 Hybrid Structures 96
3.3.3. Fabrication and Characterisation of Silver Nanoparticle - Gold Shell - C5 Hybrid Structures 99
3.3.4. Sensing Assessment Pseudo Silver Core - Gold Shell - C5 Hybrid Nanostructures.. 102
3.4. Conclusion 105
Chapter 4 - Mercury Detection via Gold Nanorod Amalgamation 107
4.1. Introduction 109
4.2. Experimental Methods 111
4.2.1. Sample Preparation 111
4.2.2. Sample Characterisation 112
4.2.3. Theoretical Calculation of Amalgamated Nanorod optical signatures 113
4.3. Results and Discussion 115
4.3.1. Amalgamation of Single Gold Nanorods 116
4.3.2. Characterisation of Amalgamated Single Gold Nanorods 118
4.3.3. Assessment of Mercury Detection via Gold Nanorod Amalgamation 123
4.3.4. Investigation of Amalgamation Mechanism 131
4.4. Conclusion 137
Chapter 5 - Investigation of Gold Nanorod Amalgamation with Darkfield Spectroelectrochemistry 139
5.1. Introduction 141
5.2. Experimental Methods 143
5.2.1. Spectroelectrochemical Sample Preparation 143
5.2.2. Sample Characterisation using Dark Field Optical Microscopy and Spectroscopy 145
5.2.3. Spectroelectrochemical Mercury Reduction and Amalgamation Monitoring .. 145
5.3. Results and Discussion 147
5.3.1. Design of Spectroelectrochemical Cell 147
5.3.2. Working Electrode Characterisation 148
5.3.3. Electrochemical Reduction of Mercury (II) on Gold Nanorods 155
5.4. Conclusion 173
Chapter 6 - Conclusions and Future Work 175
6.1. Summary and Conclusions 177
6.2. Future Work 181
Appendices 183

Declaration

The work presented in this thesis is Carola Schopf's own work unless otherwise stated in the relevant sections. Specifically, Dr. Alfonso Martin has synthesised all nanorods used throughout this work and has fabricated the highly ordered nanorod arrays used in section 2.3.4, Ethel Noonan has provided linked nanoparticle clusters used in section 2.3.2, Dan O'Connell has fabricated ITO coatings on glass cover slips and Dr. Michael Schmidt has recorded the EDX spectrum shown in Figure 4.7.

The work presented in this thesis has not been submitted for another degree, either at University College Cork or elsewhere.

The present thesis is submitted for the degree of Doctor of Philosophy at University College Cork.

Head of the UCC Chemistry Department	Prof. Martyn Pemble
External Examiner	Dr. Robert Pollard
Internal Examiner	Dr. Richard Winfield
Supervisor	Dr. Daniela Iacopino

Abstract

This thesis investigates the application of plasmonic gold nanostructures for mercury detection. Various gold and silver single nanostructures and gold nanostructure assemblies were characterised in detail by correlated single nanostructure spectroscopy and electron microscopy. Several routes for mercury detection were explored: plasmon resonance energy transfer (PRET) upon Hg^{2+} binding to immobilised gold nanoparticle-organic ligand hybrid structures and amalgamation of single immobilised gold nanorods upon chemical and upon electrochemical reduction of Hg^{2+} ions. The amalgamation approach showed large potential with extraordinary shifts of the nanorods' scattering spectra upon exposure to reduced mercury; a result of compositional and morphological change induced in the nanorod by amalgamation with mercury. A shift of 5 nm could be recorded for a concentration as low 10 nM Hg^{2+}. Through detailed time-dependent experiments insights into the amalgamation mechanism were gained and a model comprising 5 steps was developed. Finally, spectroelectrochemistry proved to be an excellent way to study in real time in-situ the amalgamation of mercury with gold nanorods paving the way for future work in this field.

Acknowledgements

I would like to thank my supervisor Daniela Iacopino for giving me the opportunity to work in this interesting field of plasmonic nanomaterials. I am grateful for her advice and guidance throughout the course of my PhD and also for allowing me to broaden my field of view by giving me the opportunity to attend and present my work at international conferences.

I want to thank staff members of the nanotechnology group Aidan Quinn, Alan O'Riordan, Hugh Doyle, Pierre Lovera, Mícheál Burke, Armelle Montrose and past member Brendan Kennedy for their valuable input in group meetings and open office doors for technical questions and advice; in particular Pierre for his help with optimising the spectroscopy setup and Alan, Armelle and Brendan for their electrochemical expertise.

Thanks to Alfonso Martín Ruano and Andrea Pescaglini, the other two angles of "team nanorod", whom I shared many hours in the lab and office with. It was a pleasure working with you exploring the nano-world. I am also grateful to Seán Barry and especially Amélie Wahl for not giving up on me when I had yet another electrochemistry question, and if it was in the pub…
Thanks to the four of you and all other friends I made at the institute for unforgettable times in and out of Tyndall in the past four years in Cork.

I am grateful to Christine Burke for taking on the big task of reading this thesis trying to minimise my German-English constructions.

Thanks also to everyone at Cork Baptist Church, your prayers and support have been invaluable to me.

I want to thank Mícheál for being there when I needed him, his continuous encouragement and support that made me pass through even the most stressful times.

Finally, I would like to thank my family, without them I would not have been able to go the journey to where I am now. Thank you for your continuous support in everything.

I would like to dedicate this dissertation to my parents Karin and Klaus Schopf who always encouraged me to follow my curiosity and interest in science.

Chapter 1 - Introduction

This chapter will give an introduction to the context in which this work is set. Firstly, a necessity for fast, simple, sensitive and selective methods for monitoring mercury levels in the environment is identified. Then, an introduction to plasmonic nanoparticles, their properties and characterisation is given and how these structures are promising candidates for mercury detection. The chapter concludes with presenting the scope of this thesis.

1.1. Environmental Impact of Mercury

Though mercury is a naturally occurring element, for example from volcanic eruptions, mercury as an environmental toxin is primarily a man-made problem since the beginning of industrialisation. Mercury released into the environment results for example from burning fossil fuels, waste incineration, cement production and artisanal gold and silver mining.[1, 2] According to the latest UNEP report, recent estimations of mercury release from human activities are 1010-4070 tonnes annually into the atmosphere and an additional minimum of 1000 tonnes annually directly into water.[3]

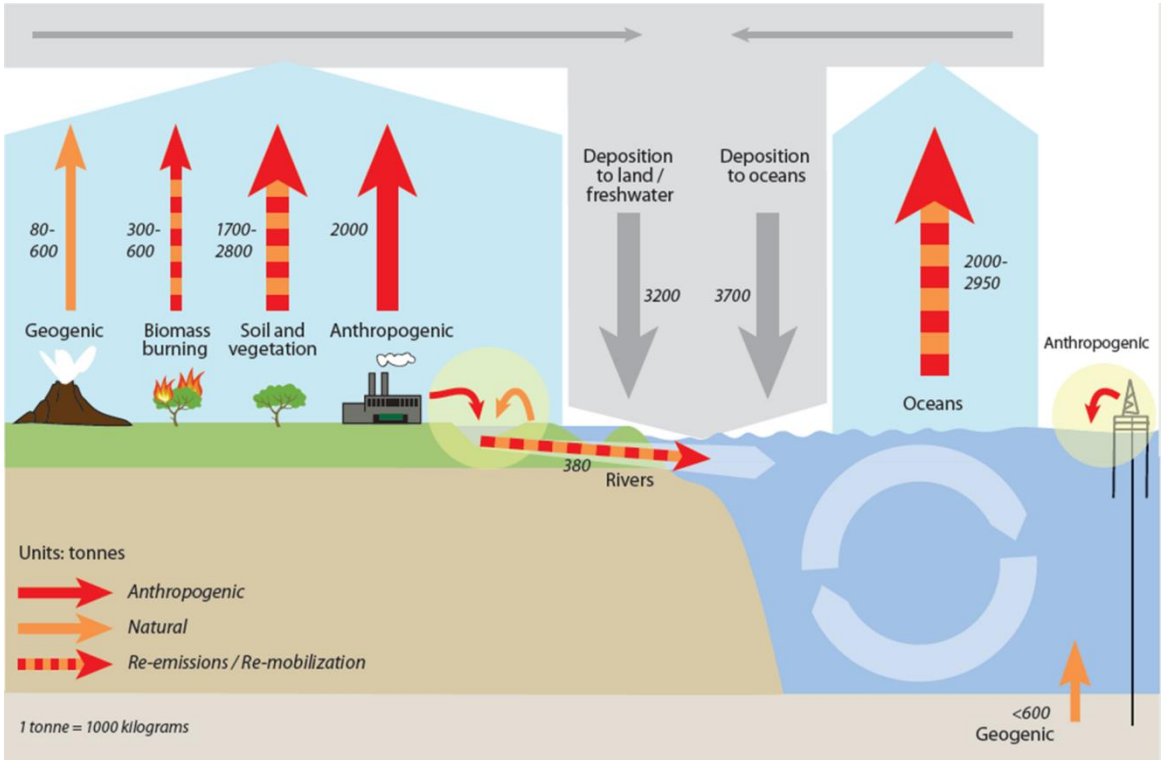


Figure 1.1: Global mercury budgets, based on models, illustrate the main environmental compartments and pathways that are of importance in the global mercury cycle, and the ways in which natural and anthropogenic releases to air land and water move between these compartments. Emissions to air arise from natural sources and anthropogenic sources, as well as re-emissions of mercury previously deposited from air onto soils, surface waters, and vegetation.[3]

East and Southeast Asia have been identified as the main contributors to mercury release, accounting for ~40% of the total global amount. However, once mercury is released into the environment it begins to cycle globally between air water and soil for decades or even centuries, thus diverging rapidly from a regional concern to one of

worldwide significance. Several models exist which highlight the primary pathways of mercury transport, considering both natural and anthropogenic influences on the cycle. Figure 1.1 shows a schematic of a model based mercury cycle. Mercury has been shown to accumulate in water and soil, and it is crucial to monitor and if possible reduce these values.[1, 3] Accumulation of mercury in water is especially of concern, as bacteria can convert inorganic mercury to methylmercury which then can further accumulate in fish and marine mammals. Methylmercury has increased toxicity and increased exposure potential for humans through consumption. Extended exposure to mercury contaminated natural waters or consumption of methylmercury contaminated food can cause accumulation of mercury in the body and can harm the central nervous system, kidneys, immune system, and gastrointestinal tract. The most serious consequences arise for the unborn child exposed to methylmercury caused by mercury intake by the mother.[4, 5]

Standard Mercury Detection Methods

Due to its high toxicity, the world health organisation (WHO) guideline for drinking water quality considers only inorganic mercury concentrations below 6 μg/l (equivalent to 30 nM) safe for human consumption.[6] Monitoring and detecting such low concentrations of mercury in natural waters demand very sensitive detection methods. Indeed, according to the WHO drinking water guidelines methods with a limit of detection (LOD) lower than 1 μg/l (5 nM) should be employed for the detection of inorganic mercury in water. Established methods that can achieve LOD's well below that value include cold vapour atomic absorption spectrometry (CV-AAS) with a LOD down to 6 ng/l (30 pM),[7-9] cold vapour inductively coupled plasma mass spectroscopy (CV-ICP-MS) with a LOD of 6 ng/l (30 pM),[10] atomic fluorescence spectrometry (AFS) with a LOD down to 4.4 ng/l (22 pM),[11-13], cold vapour inductively coupled plasma optical emission spectroscopy (CV-ICP-OES) with a LOD of 4 ng/l (20 pM)[14] and Inductively Coupled Plasma-Atomic Emission Spectroscopy (ICP-AES) with a LOD down to 10 ng/l (50 pM)[15-17]. While these methods can be very sensitive, most require elaborate and time consuming sample preparation and pre-concentration procedures as well as large sample volumes. Additionally, due to the significant cost and size of the aforementioned equipment, there is an ever-present

demand for alternative, simple to use, low cost and fast sensing methods for mercury detection.

Extensive research has, and continues to be undertaken with the aim of satisfying this need using a multitude of sensing methods, from colorimetric, fluorescence, and surface enhanced Raman spectroscopy (SERS) to biochemical, electrochemical, and electrical methods, as well as various sensing platforms like plasmonic nanoparticles, DNA, chelates, electrodes, carbonanotubes and quantum dots.[18-25] Among these, plasmonic nanostructures based detection methods have shown great promise, owing to their plasmonic properties that are finely tuneable, highly sensitive to environmental changes and easy to read out via nanostructure scattering or absorption. Before going into detail about plasmonic nanostructures based sensing strategies, the following sections of this chapter will give an introduction to plasmonic nanostructures and their associated optical properties.

1.2. Plasmonic Nanostructures

Noble metal nanostructures have been in use by artists since Roman times for the intense, non-bleaching colours they produce. A famous example is the Lycurgus Cup, whose colour varies from green in reflection to red in transmission originating from gold nanoparticles embedded in the glass (see Figure 1.2).



Figure 1.2: Picture of the Lycurgus cup (4th century AD), today in the exhibition of the British museum.

The first person to scientifically synthesise and study noble metal nanoparticle colloidal solutions was Michael Faraday in the nineteenth century, who already gained remarkable insights.[26] He described the colloids as having the appearance of solutions but really containing “no dissolved but diffused gold” and further: “the state of division of these particles must be extreme; they have not as yet been seen by any power of the microscope” proving the fact with an experiment similar to the ones by John Tyndall discovering the Tyndall effect.[27] After Faraday’s experimental work, a critical breakthrough in the understanding of the origin of the properties of noble metal nanostructures can be found in Gustav Mie’s work in the early twentieth century. Mie presented a theoretical description of the interaction of light with spherical metal nanoparticles solving Maxwell’s equations for this particular case.[28]

Ever since, plasmonic nanostructures have been an area of intense research.[29] Advances in methods of synthesis [30-37] and characterisation [38-42] of the structures on the one side and a wide range of potential applications in photonics [43-47], sensing [48-51] and catalytic chemistry [52-55] on the other side have incentivised one another.

1.2.1. Surface Plasmon Resonance

The extraordinary properties of noble metal nanostructures result from the fact that they support localised surface plasmon resonance (LSPR). Plasmons are coherent oscillations of the conduction band electrons in a material. These oscillations can be excited by the alternating electric field of incident electromagnetic radiation. Excitation of the conduction electrons causes their displacement with regard to the ionic core and the displacement is creating a restoring Coulomb force leading to an oscillation of the electrons. In a bulk material, surface plasmons are created in the form of standing or propagating waves (shown schematically in Figure 1.3a). However, when the dimensions of a particle are small compared to the wavelength of light, the plasmons are unable to travel, and become localised, forming LSPRs as depicted in Figure 1.3b.[51]

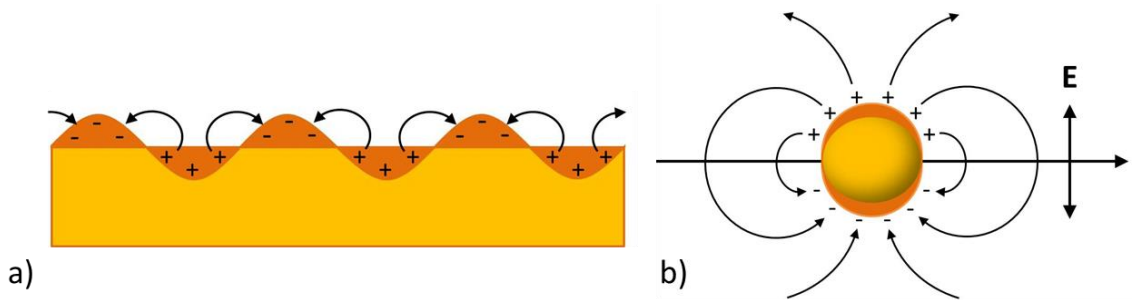


Figure 1.3: Schematic drawings of a) surface plasmon and b) localised surface plasmon.

The interaction of light with a nanoparticle and its response can be calculated by solving Maxwell's equations. Assuming particles much smaller than the wavelength of light allows the application of the dipole approximation that excludes higher polar plasmon modes that appear in larger particles. This approximation leads to simplified expressions for the extinction and scattering cross section (C_{ext}, C_{sca}) for small spherical nanoparticles of volume V with a complex dielectric function $\varepsilon(\lambda) = \varepsilon_1(\lambda) + i\varepsilon_2(\lambda)$,

surrounded by a medium with dielectric constant ε_m and irradiated with light of wavelength λ:[51, 56]

$$C_{ext} = \frac{18\pi\varepsilon_m^{3/2}V}{\lambda}\frac{\varepsilon_2(\lambda)}{[\varepsilon_1(\lambda)+2\varepsilon_m]^2+\varepsilon_2(\lambda)^2} \quad (1.1)$$

$$C_{sca} = \frac{24\pi^3\varepsilon_m^2V^2}{\lambda^4}\frac{(\varepsilon_1(\lambda)-\varepsilon_m)^2+\varepsilon_2(\lambda)^2}{[\varepsilon_1(\lambda)+2\varepsilon_m]^2+\varepsilon_2(\lambda)^2} \quad (1.2)$$

The absorption cross section C_{abs} can be calculated subtracting the scattering cross section from the extinction cross section:

$$C_{abs} = C_{ext} - C_{sca} \quad (1.3)$$

These equations show which parameters influence the absorption and scattering behaviour of a nanoparticle. Both are dependent on the particle properties such as its volume V and its material represented by its dielectric fucntions ε_1 and ε_2. Hence, varying these parameters allows the tuning of the optical properties of a nanoparticle. It has to be noted that C_{sca} is proportional to V^2, while C_{ext} is proportional to V. As a result, small particles will mainly absorb light, while larger particles will mainly scatter light. The variance of absorption and scattering spectra with size for, amongst others, gold nanoparticles was calculated by El-Sayed et al.[57]

Additionally, the plasmon resonance is dependent on the medium which the particle is embedded in, represented by ε_m. The extinction is maximised at the resonance wavelength, when the denominator in equation (1.1) is minimised, i.e. when the equation

$$\varepsilon_1 = -2\varepsilon_m \quad (1.4)$$

is fulfilled. In conclusion, ε_1 determines the wavelength at resonance condition due to its wavelength dependence while ε_2, the damping coefficient, determines the width of the plasmon band. This is often exploited when nanoparticles are employed in sensing applications as platforms to detect changes in the refractive index.

Further, according to the Drude model the real part of a metal's dielectric constant can be described by:[58]

$$\varepsilon_1(\omega) = \varepsilon_\infty - \frac{\omega_p^2}{\omega^2 + \gamma^2} \tag{1.5}$$

With ε_∞ being the high frequency contributions from interband transitions, γ being the collision frequency of the electrons and ω_p the bulk plasma frequency given by

$$\omega_p^2 = \frac{Ne^2}{m\varepsilon_0} \tag{1.6}$$

with e and m the electron charge and effective mass, ε_0 the permittivity of vacuum and, N the conduction electron concentration.[59] Taking equations (1.4)-(1.6) together, it can be shown how a change in the conduction electron concentration, that can be achieved for example by molecules on the nanoparticle surface, redox reactions or electrical charging of a nanoparticle, can modify the dielectric function of the nanoparticle and thus the position of the plasmon resonance wavelength.

A factor that has a tremendous effect on the plasmon resonance of a nanoparticle is its shape. The classical Mie theory is only applicable for spherical particles. By introducing three depolarisation factors, one for each dimension, Gans was able to extend the Mie theory to small spheroidal particles.[60] This Gans theory is often used to describe the LSPR of nanorods of approximately ellipsoid shape. Again, applying the dipole approximation for particles much smaller than the wavelength of light the equivalent equations to (1.1) and (1.2) for ellipsoids are:[56, 61]

$$C_{ext} = \frac{2\pi\varepsilon_m^{3/2}V}{3\lambda}\sum_{j=A}^{C}\frac{\left(\frac{1}{L_j^2}\right)\varepsilon_2(\lambda)}{\left[\varepsilon_1(\lambda) + \left(\frac{1}{L_j} - 1\right)\varepsilon_m\right]^2 + \varepsilon_2(\lambda)^2} \tag{1.7}$$

$$C_{sca} = \frac{8\pi^3\varepsilon_m^2V^2}{9\lambda^4}\sum_{j=A}^{C}\frac{\left(\frac{1}{L_j^2}\right)(\varepsilon_1(\lambda) - \varepsilon_m)^2 + \varepsilon_2(\lambda)^2}{\left[\varepsilon_1(\lambda) + \left(\frac{1}{L_j} - 1\right)\varepsilon_m\right]^2 + \varepsilon_2(\lambda)^2} \tag{1.8}$$

The depolarisation factors L_j along the main axes of the ellipsoid are defined by:

$$L_A = \frac{1-E^2}{E^2}\left[\frac{1}{2e}\ln\left(\frac{1+E}{1-E}\right)-1\right] \tag{1.9}$$

and

$$L_B = L_C = \frac{1-L_A}{2} \tag{1.10}$$

with the eccentricity E calculated from the length l and diameter d of the ellipsoids:

$$E = \left(\frac{l^2-d^2}{l}\right)^{\frac{1}{2}} \tag{1.11}$$

In case of a spherical particle the polarisation factors for all axes become 1/3, which leads back from equations (1.7) and (1.8) to (1.1) and (1.2).

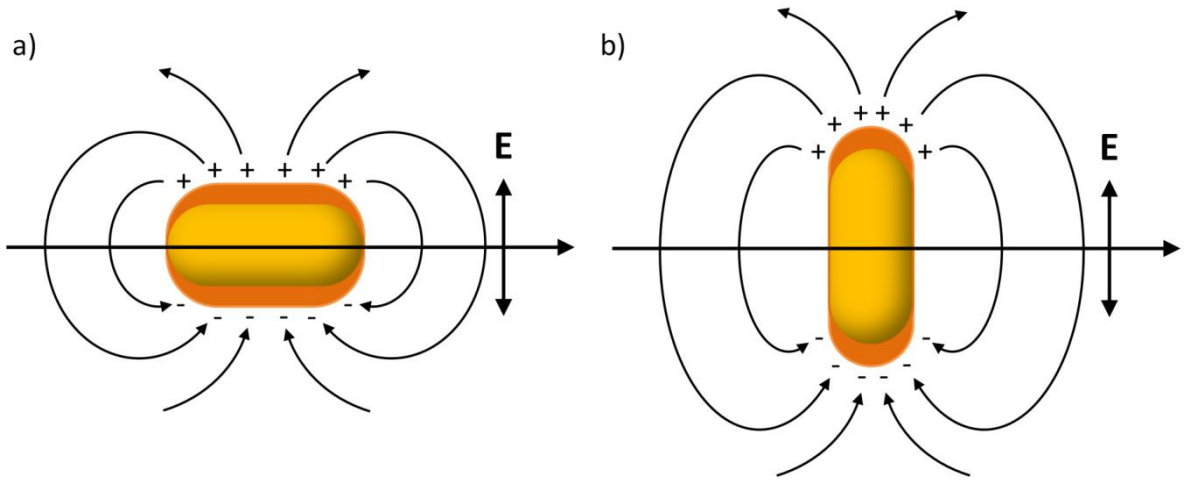


Figure 1.4: Schematic drawings of localised surface plasmon resonances on nanorods a) transversal mode b) longitudinal mode

For other shapes an analytical solution of the Maxwell equations is not possible but numerical methods have to be employed like the discrete dipole approximation (DDA) and finite difference time domain (FDTD).[62] Experimentally, it was shown that the shape of a nanoparticle has a major influence on its plasmon resonance.[63-66] This can be explained with the symmetry of the particles. A spherical nanoparticle is fully symmetrical and can only support one dipolar plasmon mode that is independent of direction. Nanorods with one elongated dimension can support a high energy

transversal and a low energy longitudinal plasmon mode. An illustration of LSPR modes supported by nanorods is shown in Figure 1.4. In general, the more complex the shape of a nanoparticle, the more dipolar modes and also high energy multipolar plasmon modes they support.[67, 68]

Additionally there is a cross correlation between the particle shape and the influence of parameters like the medium surrounding the particle or the conduction band electron concentration. It has been found that more complex shapes like nanorods, and nanotriangles are much more sensitive to a refractive index change of the medium than spherical particles.[59, 69-71]

Experimental examples of the above discussed relations between material parameters and a nanostructures plasmon resonance from a publication by Wang et al. are shown in Figure 1.5 and Figure 1.6. Figure 1.5 shows the dependence of the plasmon resonance on the nanoparticle shape comparing nanospheres with nanocubes that show a very similar spectrum and nanorods whose spectra red-shift with increasing aspect ratio. Figure 1.6a,b show how a nanorod's and a nanobipyramide's plasmon resonance red-shifts with increasing refractive index of the nanostructure's environment. Furthermore, the data presented in Figure 1.6c demonstrates that different nanostructures possess different sensitivity towards the refractive index of the environment, with the nanobipyramide being more sensitive.[71]

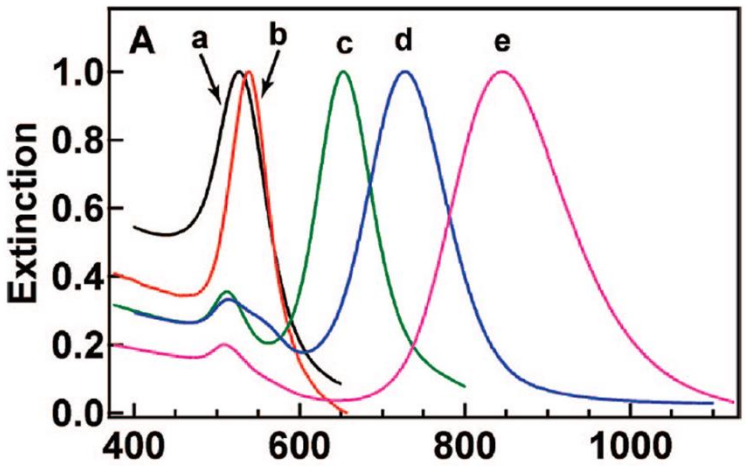


Figure 1.5: Normalised extinction spectra of Au nanoparticles of different shapes and sizes. Spectra a-e correspond to nanospheres, nanocubes and nanorods with aspect ratios of 2.4 ± 0.3, 3.4 ± 0.5, and 4.6 ± 0.8, respectively.[71]

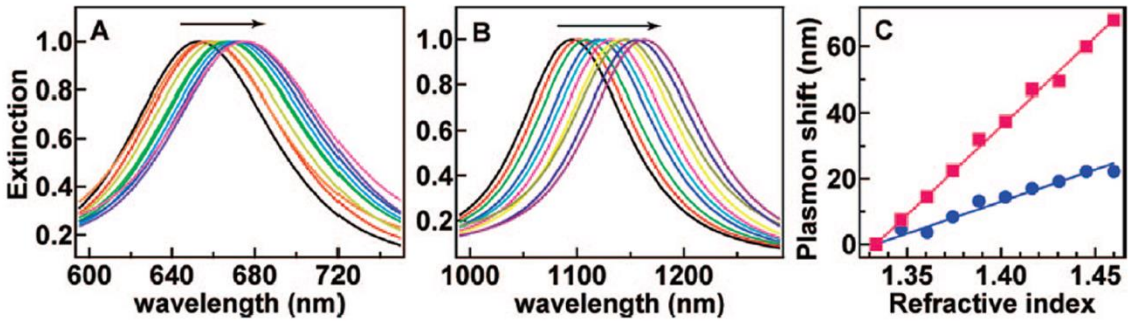


Figure 1.6: (A) Extinction spectra of Au nanorods (aspect ratio 2.4 ± 0.3) in water-glycerol liquid mixtures of varying compositions. (B) Extinction spectra of Au nanobipyramids (aspect ratio 4.7 ± 0.2) in water-glycerol liquid mixtures of varying compositions. Each spectrum is normalized to its maximal extinction intensity. The arrows indicate the direction of increasing volume percentage of glycerol. (C) Dependence of the longitudinal plasmon shift on the refractive index of the liquid mixture for the Au nanorods (blue circles) and nanobipyramids (red squares) shown in (A) and (B), respectively. The lines are linear fits.[71]

1.2.2. Plasmon Coupling

As described earlier, the electron displacement in plasmon resonance leads to the formation of an electric field around a nanoparticle. This field is significantly enhanced compared to the exciting field, decays rapidly with distance from the particle surface and reaches greater values on edges of irregular shaped nanostructures. When two nanoparticles come in close proximity of each other, the electric field of one particle will affect the field of the other. For particles smaller than 100 nm the particles can be treated as interacting dipoles and the restoring force on the displaced electrons of one particle will be affected by the charge distribution of the neighbouring particle(s).[58] Either the restoring force is increased or decreased depending on the polarisation direction of the exciting light. Considering the simplest case, a nanoparticle dimer, the restoring force would decrease for a longitudinal excitation leading to a red-shift of the plasmon resonance and the restoring force would increase for transversal excitation leading to a plasmon resonance blue-shift. Thus, via plasmon coupling new resonance conditions are created.

Nanoparticle Dimers

Nanoparticle dimers have been investigated both theoretically [72-74] and experimentally.[75-77] Nordlander et al., for example, calculated the field distribution for a gold nanoparticle dimer dependent on the interparticle distance, shown in Figure 1.7a demonstrating impressively the enhanced electric field localised in the gap

between the nanoparticles. Peyrade et al. fabricated nanoparticles of varying interparticle spacing and reported the variance of their longitudinal and transversal scattering spectra. (see Figure 1.7b).

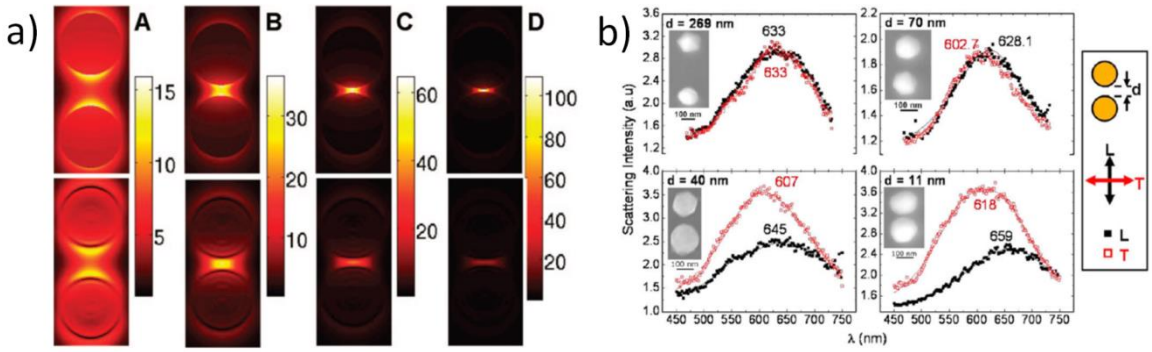


Figure 1.7: a) Calculated field distributions using plasmon hybridisation (top panels) and time dependent local density approximation (bottom panels). The field enhancements were calculated for resonant excitation of the dipolar dimer plasmon using a broadening of δ = 0.27 eV.[73] b) Spectra of longitudinal (L) and transversal (T) scattered light polarisations of gold colloidal dimers with various spacings.[75]

Nanoparticle Chains

Nanoparticle chains have been fabricated and characterised by various methods revealing that the interparticle separation as well as the chain length influence their plasmon resonance.

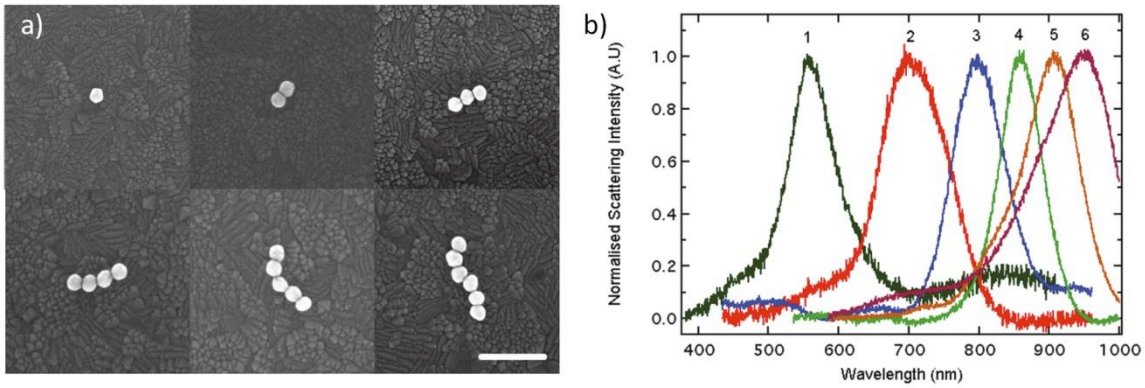


Figure 1.8: a) SEM images of self-assembled nanoparticle chains. Mean diameter of gold particles is 64 nm. Interparticle spacings are estimated at 1 nm. Scale bar = 250 nm. b) Normalised spectra of the nanoparticle chains in (a). Spectra were collected in air on an ITO coated glass substrate. Spectra are numerically labelled according to chain length.[78]

An example is presented in Figure 1.8 from Mulvaney et al. who showed by dark field spectroscopy that the scattering spectra of nanoparticle chains are highly polarised

and red-shift with increasing chain length until they reach an asymptotic maximum at 10-12 nanoparticles.[78] This asymptotic limit exists due to the near-field character of plasmon coupling.[79]

Nanoparticle Clusters

Nanoparticle clusters are another category of structures where plasmon coupling has been studied.[80-83]. The plasmon resonances of trimers, quadrumers and other small nanoparticle clusters do not seem intuitive to grasp anymore. However, a plasmon hybridisation method developed by Nordlander provides a way to understand them.[74, 80, 84] Analogous to molecule orbital hybridisation in molecular orbital theory, the plasmons of complex nanostructures can be understood as the linear combination of the plasmon resonances of the elements that make up the complex nanostructure. While the plasmon hybridisation method is also applicable to single nanostructures, for nanoparticle clusters, group theory and the symmetry of a nanoparticle cluster are of critical importance, as the resulting plasmon resonances have to correspond to a linear combination of irreducible representations of the clusters point group. From the hybridisation method, “bonding” hybridised plasmon modes with lower and “anti-bonding” hybridised plasmon modes with higher energy can then be identified, and from group theory, optically bright modes with a finite dipole moment and dark modes with no dipole moment can be determined. Only the bright modes can be excited by light. Figure 1.9 shows an example where the plasmon hybridisation method was practically applied by Haran et al. to interpret experimental data collected on gold trimers with varying symmetry. In this example it can be seen that in a highly symmetric nanostructure many plasmonic modes are degenerated. When the symmetry is broken, however, new plasmonic modes become visible.[81] Symmetry is also very important in clusters of non-spherical particles, where apart from the position of particles in relation to each other also their orientation affects the plasmon resonance.[85, 86]

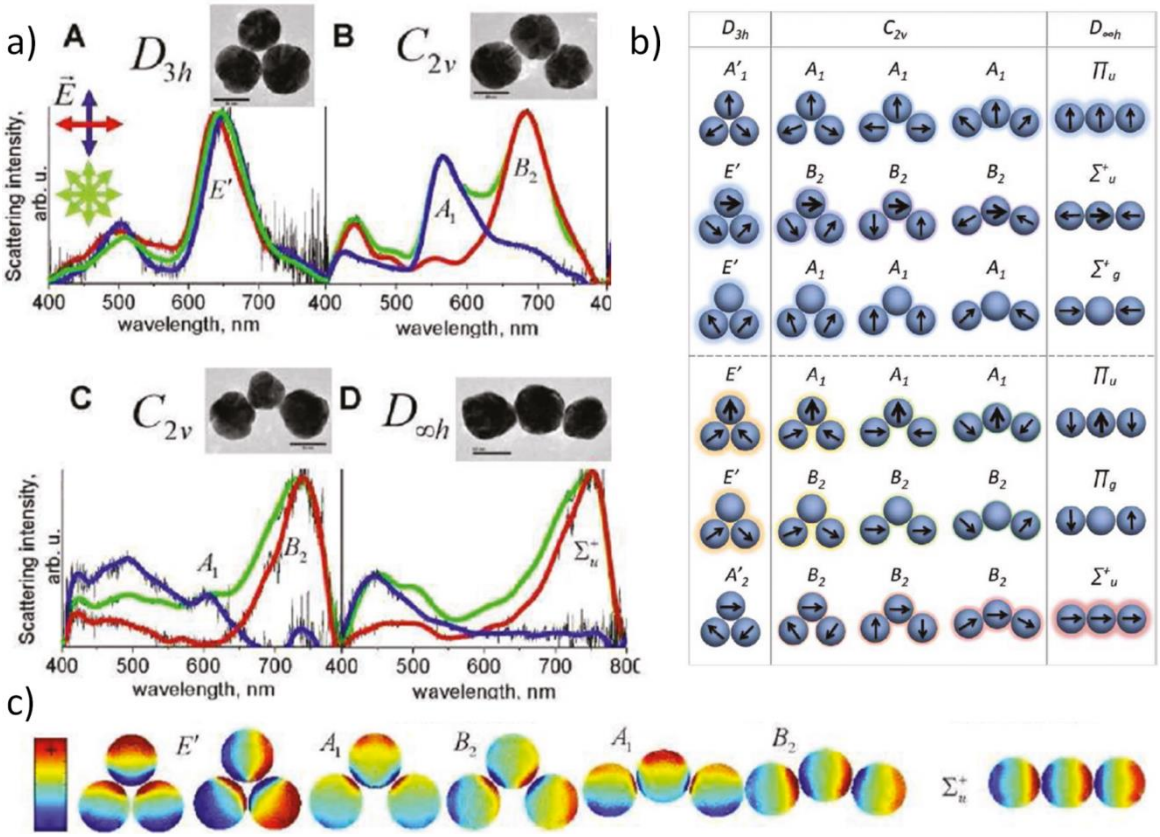


Figure 1.9: a) Scattering spectra of silver nanoparticle trimers showing mode splitting due to gradual opening of the vertex angle. Thin black lines, raw experimental data; colour lines, low pass filter applied. The clusters are excited by either non-polarised light (green) or light linearly polarised along the longitudinal (red) and transverse (blue) directions (which are indicated by arrows of matching colours). The polarised spectra are normalised to the corresponding peaks of the non-polarised spectra. Plasmon mode symmetries of the bonding modes are marked. TEM images of the clusters are shown in the insets (the bars are 50 nm). b) Correlation table of dipolar plasmon eigenmodes of trimers for varying vertex angles, obtained using the plasmon hybridisation theory. Upper part, anti-bonding modes; lower part, bonding modes. The symbols of the corresponding irreps are shown. The thickness of halos surrounding the particles represents the relative "brightness" of plasmon modes, while their colour corresponds approximately to the resonance wavelength. c) Calculated surface charge distributions of the selectively excited bonding modes are shown below the spectra.[81]

Nanoparticle Arrays

The strongly enhanced fields localised in gaps between nanoparticles, so called "hot spots" resulting from plasmon coupling are of great interest for their ability to enhance Raman and fluorescence signals and find applications in the fields of surface enhanced Raman (SERS) [87-90] and fluorescent spectroscopy. [91-93]

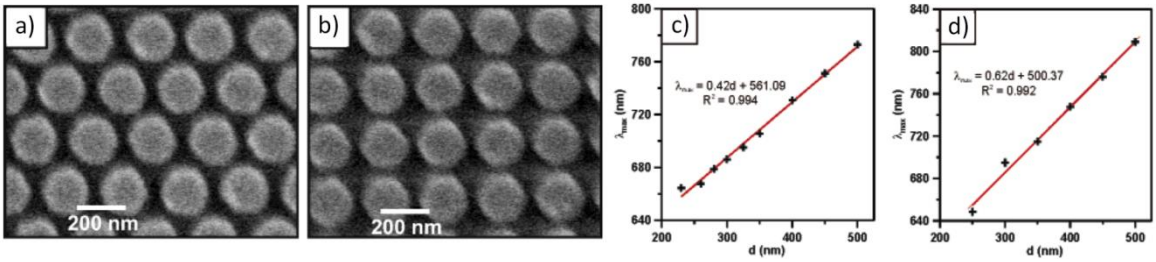


Figure 1.10: Scanning electron micrographs of representative nanoparticle arrays (all 35 nm in height): a) cylindrical nanoparticles with a diameter of 200 nm in hexagonal arrangement, period 260 nm; b) cylindrical nanoparticles with a diameter of 200 nm in square arrangement, period 250 nm. Corresponding plots of lattice spacing (*d*) versus LSPR λ_{max} for measured extinction spectra of Au cylinders in c) hexagonal and d) square arrays (*D*) 200 nm, *h*) 35 nm) with varied nanoparticle spacing.[94]

Consequently, structures that provide a great number of these hot spots are desired for these applications. In this context, two-dimensional arrays of nanoparticles are being investigated. [94-101] Plasmon coupling in these structures was also observed to be inter-particle distance dependent. Schatz et al. studied two-dimensional hexagonal and square periodic arrays of silver and gold nanostructures in experiment and theory. As an example, data for hexagonal and square gold cylinder arrays is reproduced in Figure 1.10, that shows red-shifts of the arrays' plasmon resonances λ_{max} with increasing lattice spacing.[94] For non-spherical nanostructures, again not only the position of the nanostructures but also their orientation with respect to each other is important. In the case of highly ordered nano-rod arrays, this leads to collective, polarised plasmon resonance as was studied theoretically by Nie el al.[98]

1.3. Characterisation of Plasmonic Nanostructures

Optical Characterisation

In the case of noble metals like gold and silver, plasmon resonance can be excited by radiation with a wavelength in the range of visible light. For nanoparticles smaller than 30 nm light extinction is dominated by light absorption, for larger particles light scattering becomes more pronounced [57]. Consequently, measuring the absorbed or scattered light are good methods to observe nanoparticle plasmons and interactions therewith. Methods can be distinguished into ensemble and single-particles methods. A typical ensemble method is UV-Vis absorption spectroscopy which is useful to study bulk solutions of colloidal nanostructures. Through careful comparison of target nanoparticle solutions with UV-Vis spectra of known samples, information about the concentration, average size, shape and agglomeration state of nanoparticle solutions can be obtained.[71, 102-105] A less commonly used method for the characterisation of noble metal nanostructures is dynamic light scattering (DLS).[106, 107]

More detailed characterisation of plasmonic nanostructures can be achieved by single-particle methods, which allow the analysis of individual nanostructures unrestricted by size and shape averaging. This is important especially for chemically synthesised structures, where each synthesis produces a distribution of shapes and sizes.[38, 56, 63] To study single nanoparticles methods where the nanoparticle scattering[108-111], absorption[112-114] or extinction[40, 115-117] is measured were developed. In this context, single particle darkfield spectroscopy where single nanostructure scattering spectra are recorded has proven to be a powerful method. By now it is established as the standard method due to its experimental ease compared to other single particle methods mentioned above. Figure 1.11 shows an illustration of a setup for darkfield spectroscopy. An optical microscope is equipped with a darkfield condenser, inserted between the light source and the sample. The darkfield condenser has a high numerical aperture and, using a central light stop and a mirror system, creates a hollow cone of light, which is focussed on a point on the surface of the sample. An objective with lower numerical aperture than the darkfield condenser is located below the sample. Due to its lower numerical aperture only light that has been scattered by the sample can enter the objective, all light transmitted through the sample passes by

the objective. The scattered light is then directed either towards a camera to form an optical image or towards a spectrograph to obtain the scattering spectrum of individual gold nanostructures or assemblies thereof. To analyse the polarisation of the scattered light a polariser can be inserted either in the illumination path before the condenser or in the collection path before the entrance slit of the spectrometer.

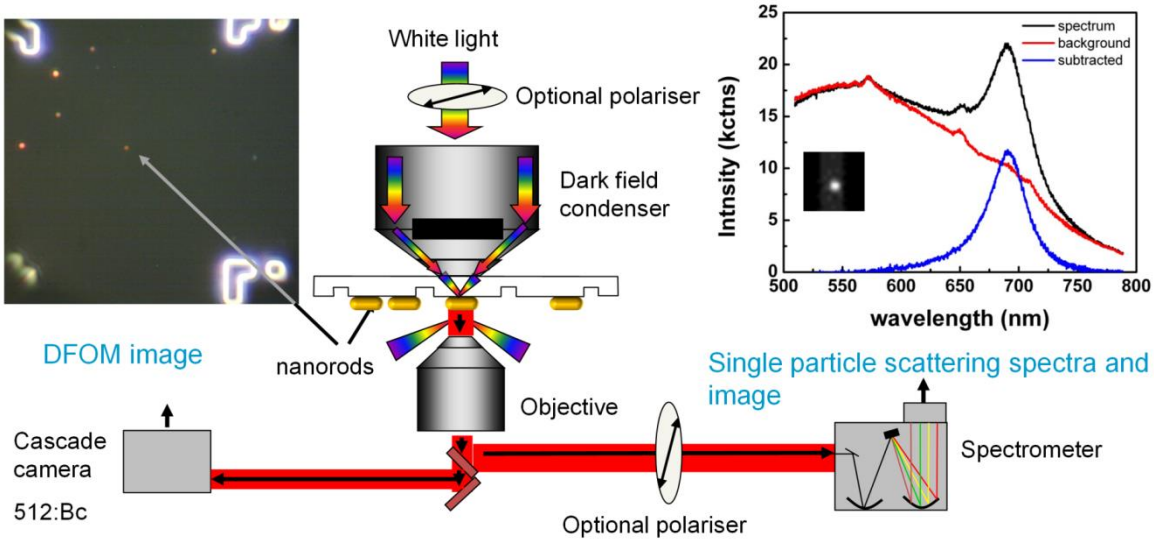


Figure 1.11: Schematic drawing of setup for darkfield imaging and spectra acquisition.

Examples of applied dark field scattering spectroscopy were already shown in the previous section in Figure 1.7, Figure 1.8 and Figure 1.9.

As discussed previously, only larger nanoparticles scatter light efficiently, for smaller nanoparticles (<20 nm) absorption is dominant and other methods have to be employed for optical characterisation. The absorption of single plasmonic nanoparticles can be measured with photothermal imaging techniques,[112-114] extinction by super-continuum white light confocal microscopy[116], spatial modulation spectroscopy[40, 115] or differential interference contrast microscopy.[118] Details about the techniques would be beyond the scope of this thesis but can be found in the indicated references.

Structural Characterisation

As was discussed in Section 1.2.1, a nanoparticles shape, size, composition and, for clusters and arrays, the interparticle distance has a major influence on its plasmon resonance. Therefore, optical characterisation of plasmonic nanostructures is most powerful if it is correlated with structural analysis of the nanostructures as was for

example also applied in the works referenced in Figure 1.7 to Figure 1.10. For this purpose, methods with a spatial resolution in the nm range are required and most commonly used are electron microscopy techniques like scanning electron microscopy (SEM)[66, 119-121] or transmission electron microscopy (TEM)[39, 122-124], but also atomic force microscopy (AFM)[64, 88, 125] are employed. Using transparent conductive substrates like ITO with a type of alignment marks easily allows correlated structural and optical characterisation with SEM and darkfield spectroscopy. This is very important on the one hand to confirm that a nanostructure of interest is optically characterised, and on the other hand to be able to understand the influence of the nanoparticle's structure on its optical signature. TEM is less suited for optical-morphological correlation measurements, however, more detailed structural information like crystal structure, crystal planes of surface facets, and for coupled plasmonic particles interparticle distances can be obtained. Furthermore, with a SEM or TEM equipped with an EDX detector, information about a nanostructure's composition can be acquired.

1.4. Plasmonic Nanostructures in Sensing Applications

1.4.1. General Sensing Strategies

Plasmonic nanostructures have been extensively investigated for sensing applications for species ranging from anions and metal cations to small organic molecules, oligonucleotides and proteins. [51, 126-129]. They provide several advantages compared to fluorophores as they exhibit very strong, and stable optical signatures and don't photobleach or blink. For the example, a 80 nm silver sphere has a scattering cross-section a millionfold larger than the fluorescence cross-section of a fluorescein molecules, and a thousandfold larger than a 80 nm sphere filled with fluorescein molecules.[130] With regards to optical sensing, two approaches can be distinguished. The plasmon resonance of a nanostructure itself can be monitored, where changes occur due to the sensitivity of its plasmon resonance to a nanostructure's environment, shape or composition. Alternatively, the enhanced electromagnetic field originating from plasmon resonance is utilised to enhance signals like Raman and fluorescence. Noble metal nanostructures are also employed in electrical and electrochemical sensing applications but primarily for increasing the electrode surface rather than for their plasmonic properties. Out of the multitude of methods, in the following a selection of sensing strategies that are most commonly pursued is introduced.

Refractive Index Based Sensing

As discussed earlier, the plasmon resonance of a noble metal nanoparticle is dependent on the dielectric function of its environment. A change in the concentration of a molecule in the near field of the nanostructure will lead to a change of the dielectric function of the medium and according to equation (1.4) in turn to a detectable spectral shift of the plasmon resonance. This effect has been made use of in sensing strategies employing plasmonic nanoparticles.[50, 131, 132] Van Duyne et al. for example monitored the attachment of 1-hexadecanethiol on silver nanoparticles by monitoring the particle's red-shift.[50] More selective target analyte detection can be achieved by functionalisation of the nanoparticles' surface with a recognition unit specific to the target analyte.[133-136]

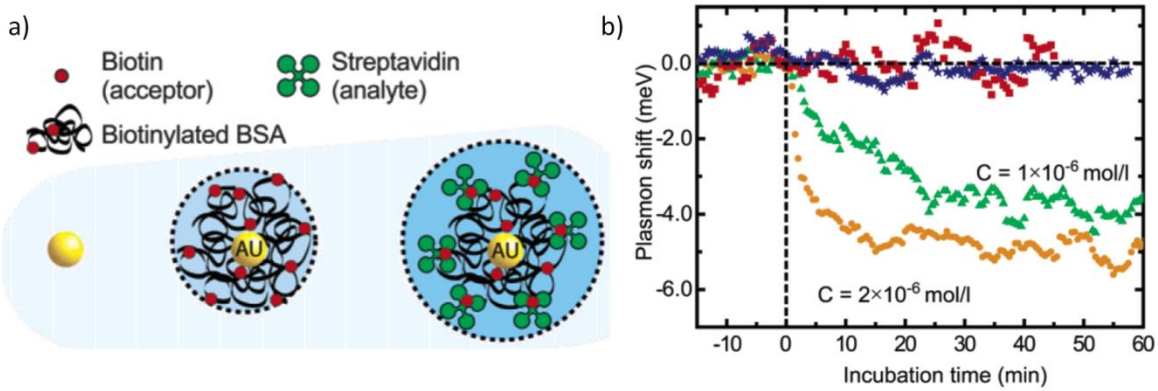


Figure 1.12: a) Principle and schematic representation of a biosensor based on light scattering from a single gold nanoparticle. Single gold nanoparticles are functionalised with biotinylated BSA which subsequently binds streptavidin. b) Resonance shift versus incubation time for different streptavidin concentrations and control experiments. Upon addition of streptavidin at time t = 0 the NPP resonance starts to red shift (green triangles and orange circles), while addition of potassium phosphate storage buffer leaves the resonance position unchanged (red squares). The streptavidin concentration is 1 x 10^{-6} mol/L and 2 x 10^{-6} mol/L for triangles and circles, respectively. Addition of streptavidin to a final concentration of 1 x 10^{-6} mol/L to a nanoparticle coated with nonbiotinylated proteins shows no evidence for unspecific binding events (blue asterisks).[134]

A prominent example is highly selective biotin-streptavidin binding that has been demonstrated for example by Feldmann et al. and is shown in Figure 1.12.[134] When 40 nm gold nanoparticles functionalised with biotinylated BSA were exposed to streptavidin a growing red-shift of the particles plasmon resonance was observed with increasing biotin-streptavidin binding.

Aggregation Based (Colorimetric) Sensing

Another common sensing method with plasmonic nanoparticles is to use the target analyte to trigger aggregation of nanoparticles in solution or the re-dispersion of aggregated nanoparticles. For gold nanoparticle solutions a pronounced colour shift from red to blue induced by plasmon coupling between the aggregated nanoparticles can be observed. Again, usually nanoparticles are functionalised with a recognition unit specific to the target analyte.[137-144] Figure 1.13 shows an example from the work of Thomas et al. for the detection of lead using gallic acid capped gold and silver nanoparticle aggregation. First gold and silver colloidal solutions were synthesised by reduction of the metal salts with gallic acid witch also acts as a capping agent of the nanoparticles.

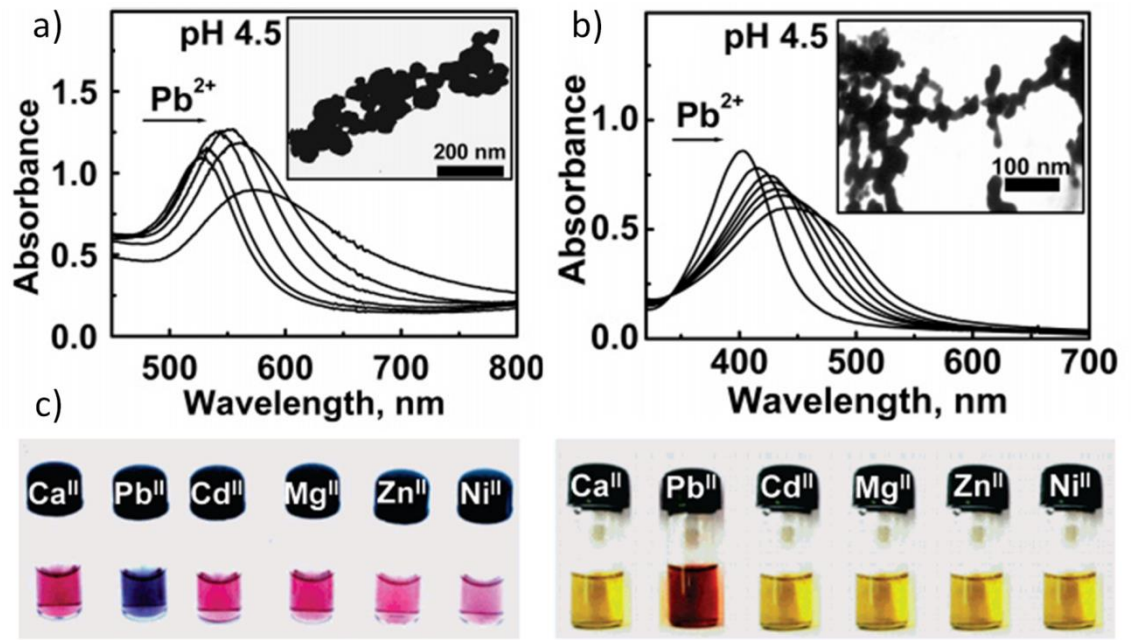


Figure 1.13: Absorption spectral changes of a) Au and b) Ag nanoparticles in water on addition of increasing concentrations of Pb^{2+} ions (0-150 μM). Inset shows corresponding TEM images of Au and Ag nanoparticles in the presence of 100 μM Pb^{2+} ions. c) Au and Ag nanoparticle solutions in the presence of different metal ions ([M^{2+}]) 150 μM).[144]

When Pb^{2+} ions were added to the gold or silver colloids aggregation of the nanoparticles was induced leading to strong optical shifts that could be observed by eye as seen in Figure 1.13c. With this method a limit of detection for Pb^{2+} ions down to the ppm level could be achieved.[144]

Plasmon Resonance Energy Transfer Sensing

If nanoparticles are functionalised with molecules that exhibit one or several absorption bands overlapping with the plasmon band of a nanostructure, they can interact with the structure. The transition of the molecule can couple with the plasmon resonance if the molecule is in the near-field of the nanostructure, an effect called plasmon resonance energy transfer (PRET). This interaction can lead to entirely new features in the absorption and scattering spectra of the nanostructures, plasmon damping or quenching dips in the spectra and has also been used in sensing applications.[145-149]. Figure 1.14 shows an example from Xu et al. where PRET was used to detect TNT.

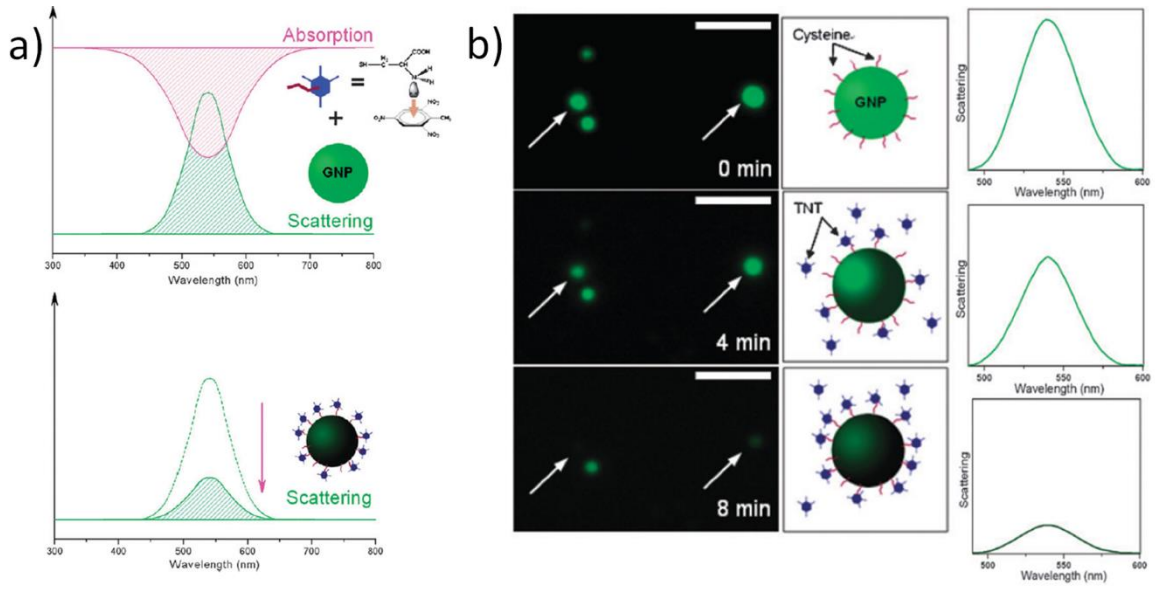


Figure 1.14: a) Schematic representation of TNT detection process based on plasmonic resonance energy transfer (PRET). When the electronic absorption frequency of the donor–acceptor complex overlaps with the Rayleigh scattering frequency of GNP, the selective energy transfer occurs by this spectral overlap. The remarkable resonant quenching on the Rayleigh scattering spectrum is clearly observed. b) Typical time-dependent true colour images of cysteine modified gold nanoparticles after exposure to 1 mM TNT (left), the corresponding schematics (middle) and the corresponding Rayleigh scattering spectra (right). The white arrow points to a single GNP. The scale bars are 2 μm.[147]

As can be seen in Figure 1.14b cysteine functionalised nanoparticles scattered the light strongly. However, due to the broad absorption peak of the cysteine-TNT complex the nanoparticle scattering was quenched when TNT bonded to the cysteine.

Charge Transfer based Sensing

Redox reactions on the surface of plasmonic nanostructures can inject or withdraw electrons from it. This induced charge density modification can be read out as a spectral shift of the nanostructures plasmon resonance and has been first demonstrated by Mulvaney et al. for the catalytic oxidation of ascorbic acid on gold nano-decahedrons. [150] Figure 1.15 shows graphs from this work. The scattering peak of a nano-dodecahedron blue-shifted gradually due to electron injection during ascorbic acid oxidation. The subsequent red-shift of the scattering spectrum is assumed to correspond to an electron withdrawal from the dodecahedron during the reduction of oxygen, which is dissolved in the solution, to water. Furthermore, from the measured blue shift over time and the corresponding charge density values, rates

for both the oxidation and the reduction reactions could be determined. Later this method was also applied to monitor other catalytic redox reactions.[151, 152]

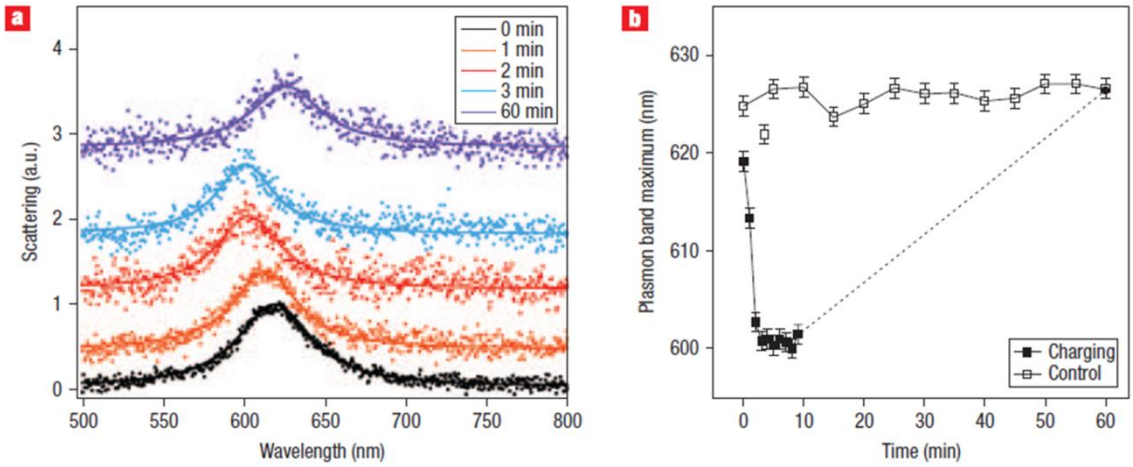


Figure 1.15: a) Scattering spectra of the decahedron before and at 1, 2, 3 and 60 min after electron injection by ascorbate ions. b, Spectral shift as a function of time for the catalysis reaction and for the control experiment. The error bars represent the error in determining the peak position from the Lorentzian fitting procedure.[150]

Fluorescence Based Sensing

In all previous discussed techniques the surface plasmon resonance itself is probed for sensing signal readout. Here the fluorescence of molecules or quantum dots is measured, which can be quenched or enhanced by plasmonic nanostructures. In very close proximity of a plasmonic nanoparticle, non-radiative energy transfer from the fluorophore to the particle leads to fluorescence quenching, however, the enhanced electromagnetic field originating from surface plasmon resonance is able to increase the fluorophores excitation rate and thus enhance the fluorescence signal. As the electromagnetic field is decaying with distance from the plasmonic nanostructure a distance dependent fluorescence quenching or enhancement can be observed.[91] In sensing applications this is taken advantage of in two main ways: Either a fluorophore that has been quenched on the surface of a nanoparticle is released upon binding of the target analyte so that an increase of fluorescence can be detected,[153-158] or the reverse is the case and a fluorophore is brought in proximity of a nanoparticle and its fluorescence is quenched[159-161]. An example where the latter approach was applied by Wu et al. is presented in Figure 1.16.

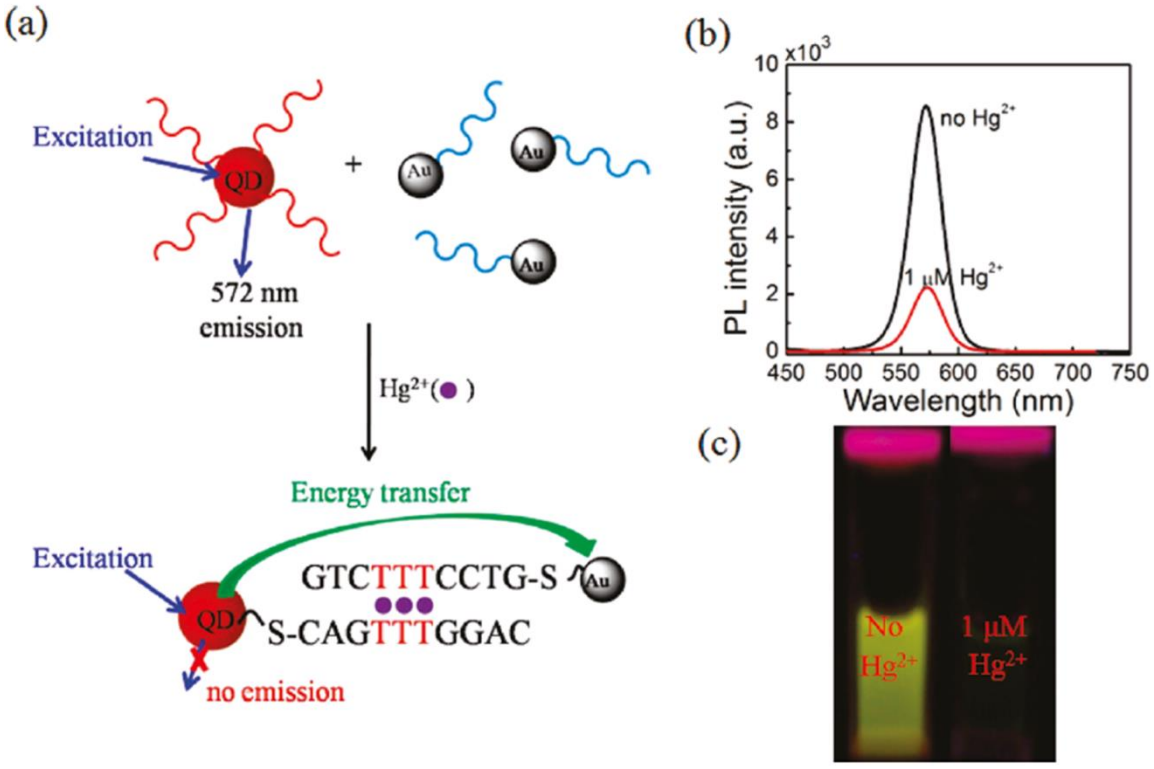


Figure 1.16: a) Schematic illustration of the operating principle of the QD/DNA/Au NP ensemble sensor for Hg^{2+} detection. b) Fluorescence emission spectra and c) photograph under 365 nm laser excitation of the QD/DNA/Au NP solution (96 nM QDs, 104 nM Au NPs, and 0.1 mM ethylenediamine in 0.3 M PBS) before and after addition of 1 μMHg^{2+}.[159]

The sensing solution contains DNA functionalised CdSe/ZnS quantum dots and DNA functionalised gold nanoparticles. The two different DNA strands are complementary ssDNA apart from three intentionally designed thymine-thymine mismatches that can complex Hg^{2+} ions. When no Hg^{2+} is present a strong fluorescence signal can be recorded from the quantum dots. However, if Hg^{2+} is present the DNA strands on the quantum dots and nanoparticles hybridise, thus bringing them in such close proximity that non-radiative energy transfer between the quantum dots and the gold nanoparticles can take place and the fluorescence signal is quenched.[159]

Surface Enhanced Raman Spectroscopy Based Sensing

The Raman signal of a molecule originates from inelastic scattering of photons by the molecule. An incident photon excites an electron of the molecule from a vibrational state to a virtual higher state. If the electron then relaxes to a vibrational state lower or higher than its original state the scattered photon will have either a higher or lower energy than the incident photon. Due to the characteristic vibrational modes of each molecule, the SERS signal contains a spectroscopic fingerprint of the molecule and is

thus very suited for molecule identification. The downside is that inelastic photon scattering is very inefficient and consequently the signal very weak. In surface enhanced Raman spectroscopy (SERS) the strong electromagnetic field localised around plasmonic nanostructures and especially enhanced in the gaps of coupled nanoparticles is used to enhance this otherwise very weak Raman signal of molecules. [162, 163] This mechanism has been used in many creative ways for direct and indirect detection of ions, small organic molecules, oligonucleotides and proteins.[41, 88, 164-170].

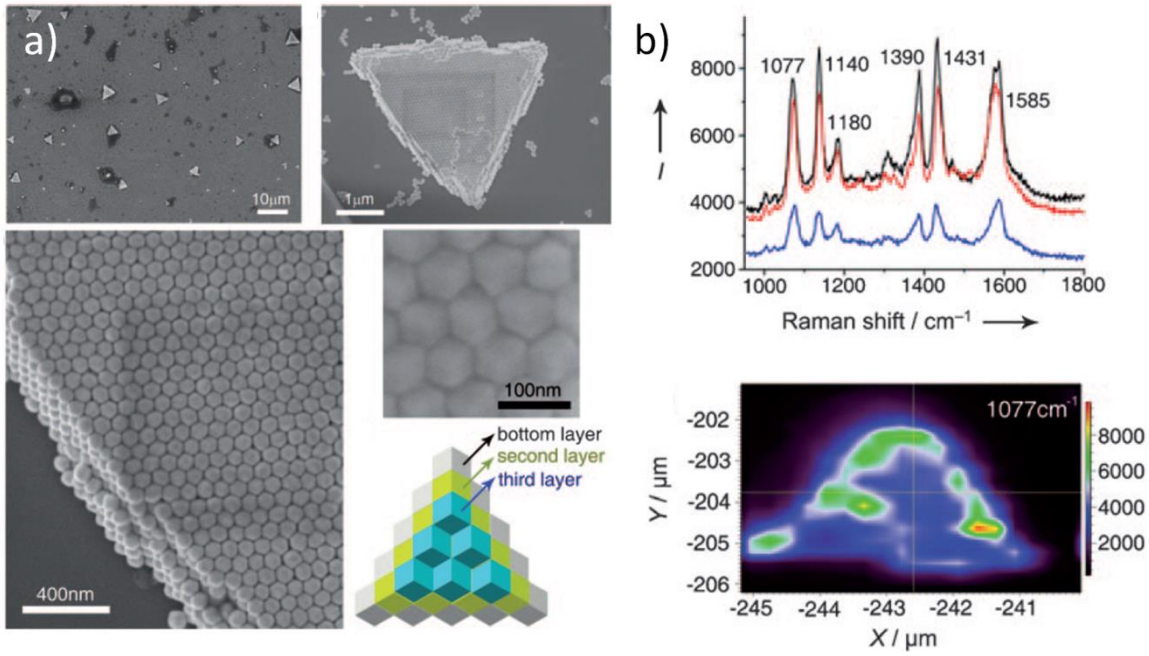


Figure 1.17: a) SEM and schematic images of self-assembled rhombic dodecahedral Au nanocrystals on silicon substrates. b) SERS spectra of *p*-mercaptoaniline at different locations at excitation with 633 nm laser (corner: black, edge: red, centre: blue) and corresponding mapping of superstructures assembled from dodecahedral Au nanocrystals.[165]

Figure 1.17 shows work from Tang et al. as an example. The substrates for Raman signal enhancement were fabricated by self-assembly of rhombic dodecahedral nanocrystals and the application of the assemblies as SERS substrates was demonstrated using p-mercaptoaniline as a model analyte.[165]

1.4.2. Nanoparticle Based Mercury Detection Methods

Aggregation Based Sensor

A very common approach using nanoparticles is to use the mercury ions to trigger the aggregation of nanoparticles in solution. The resulting plasmon coupling between aggregated nanoparticles leads to a pronounced colour shift of the solution from red to blue. This approach has been demonstrated with nanoparticles functionalised with synthetic organic molecules that complex Hg^{2+} ions [171-175] and also biological receptor molecules which approach was pioneered by Mirkin et al.[176-178] Sensitivities down to the μM range could be achieved with this method. To increase the sensitivity of this method secondary effects induced by plasmon coupling in the nanoparticle aggregates like surface enhanced Raman scattering and fluorescence have been combined with nanoparticle aggregation and LODs down to 0.01nM Hg^{2+} have been recorded.[179-182] An example of a method combining nanoparticle aggregation and fluorescence taken from the work of Chen et al. is shown in Figure 1.18.

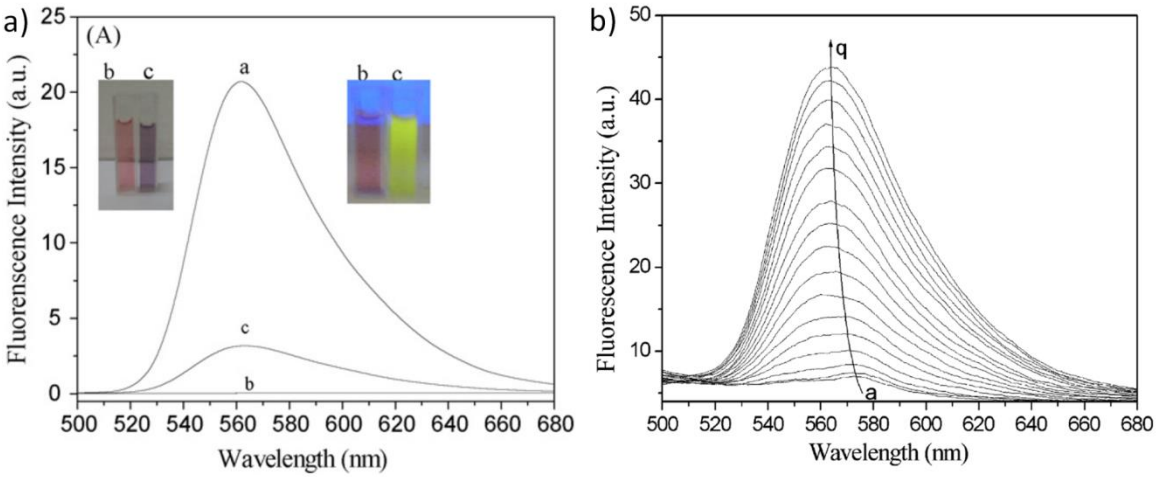


Figure 1.18: a) Fluorescence spectra of solutions of (a) Rh6G and (b and c) Rh6G–Au NPs in the absence (b) and (c) presence of Hg(II) (1.0×10−4 mol L−1). The concentrations of Au NPs and Rh6G were 3.0×10−9 mol L−1 and 1.0×10−7 mol L−1, respectively. Inset light: photograph in sunlight of Rh6G–Au NPs in the absence (b) and presence (c) of Hg(II) (1.0×10−4 mol L−1). Inset left: fluorescence photograph extinction at 365 nm of Rh6G–Au NPs in the absence (b) and presence (c) of Hg(II) (1.0×10−4 mol L−1).b) Fluorescence response of TGA@Au NPs–Rh6G to different concentration of Hg(II) in aqueous solution (×10−9 mol L−1). a: Blank; b: 0.50; c: 1.5; d: 3.0; e: 5.5; f: 8.0; g: 10.5; h: 13.0; i: 15.5; j: 18.0; k: 20.5; l: 23.0; m: 25.5; n: 28.0; o: 30.5; p: 33.0; q: 35.5. TGA@Au NPs: 3.0×10−9 mol L−1, Rh6G: 1.0×10−7 mol L−1, pH, 9.0, 5.0×10−3 mol L−1, tetraborate buffer solution.[179]

Thioglycolic acid functionalised gold nanoparticles were mixed with a Rhodamine B solution, upon which Rhodamine B adsorbs on the surface of the nanoparticles which quenches its fluorescence. When Hg^{2+} ions were added to the solution the nanoparticles aggregated as can be seen in the right image inset in Figure 1.18a. Additionally, Rhodamine B was released from the nanoparticles which recovered its fluorescence as seen in the left image inset in Figure 1.18a. The recovered fluorescence intensity was proportional to the Hg^{2+} ion concentration which was also confirmed in real water samples.[179]

Solid Sensing Platform Based Sensors

A difficulty in methods using nanoparticle aggregation is to maintain colloidal stability and prevent aggregation by other triggers like salts altering the ionic strength of the solution and change of pH.

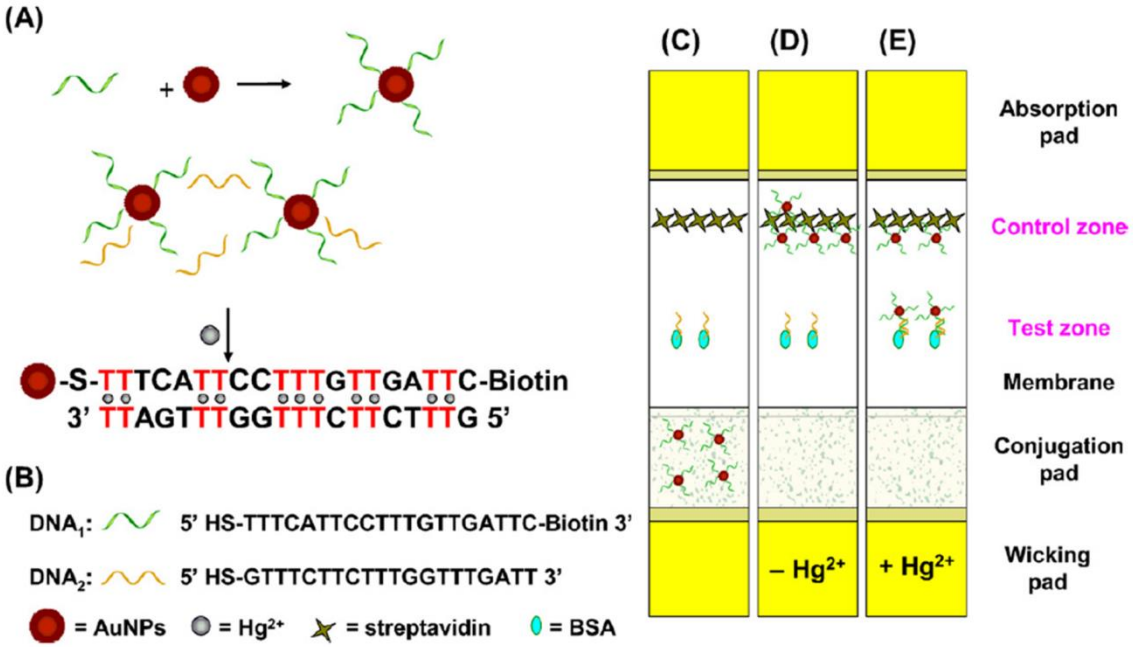


Figure 1.19: Design of the test strip format. (A) Schematic illustration of sensors and theranostic agents for Hg^{2+}. (B) Description of DNA_1 sequence, DNA_2 sequence, AuNPs, Hg^{2+}, streptavidin and BSA. (C) Blank test strip loaded with the DNA-functionalized AuNPs (on the conjugation pad), DNA_2–BSA (test zone) and streptavidin (control zone). (D) Negative test: in the absence of Hg^{2+}, the DNA-functionalized AuNPs were captured at the control zone through streptavidin–biotin interaction, producing a single red line. (E) Positive test: in the presence of Hg^{2+}, the DNA-functionalized AuNPs were captured at the test zone by T-Hg^{2+}-T coordination to complementary DNA in addition to the control zone resulting in two red lines.[183]

Additionally, a liquid sensing platform is less practical to handle in an application, which makes sensing platforms on substrates desirable. Examples thereof are lateral flow test strips [183-185] and other paper based devices [186, 187]. A schematic drawing of the test strip based sensor developed by Guo et al. is shown in Figure 1.19. The strip contains biotin-labelled DNA-functionalised gold nanoparticles loaded into a conjugation pad, a test zone where complementary DNA strands with thymine-thymine mismatches to the strands on the nanoparticles are located, and a control zone where streptavidin is situated. When an analyte solution was placed on the wicking pad, the solution travelled via capillary forces towards the absorption pad. On its way, the solution picked up the gold nanoparticles which then bonded either only via biotin to the streptavidin in the control zone if no mercury was present, or also to the complementary DNA strands via thymine-Hg^{2+}-thymine complexes in the test zone.[183]

Amalgam Based Sensors

All sensing methods discussed so far relied on organic molecules which specifically complex Hg^{2+} ions and induce a change in the nanostructures environment that can be read out. There is, however, a more basic interaction that can be utilised for mercury detection. The elements gold and mercury have a very high affinity for each other and readily amalgamate. The origin of this affinity has been proven to be relativistic[188, 189] but has been known already to the alchemists. Mercury was and is still used in artisan gold mining to extract the smallest crumbs of gold from the soil (still one of the major contributors to mercury pollution).[190, 191] Now the reverse process of removing or detecting mercury from the gas or liquid phase by amalgamation with gold has gained in interest.[192, 193]

The ability of gold surfaces to absorb mercury has been applied in mercury vapour sensors using thin gold layers on piezoelectric substrates where upon mercury deposition the resonance frequency of the vibrating substrate would change [194, 195]. In other methods a change in resistivity, reflectivity or surface plasmon resonance of the gold layer is measured.[196-198] Additionally, gold-mercury amalgamation has been utilised for pre-concentration steps for example for mass spectroscopy or atomic fluorescence and absorption spectroscopy.[199-203]

For amalgamation with gold structures to occur, mercury has to be in its elemental state. This is usually achieved with strong reducing agents like sodium borohydride or stannous chloride.[203-207] Several studies have been reported on nanoparticle based sensing methods, where the compositional change upon amalgamation resulted in a blue shift of the nanoparticles' LSPR. [208-211] The shift for nanoparticles was, however, relatively small to what was found in experiments with nanorods and other non-spherical structures. For non-spherical nanostructures the amalgamation was found to additionally cause a shape change towards a sphere which increases the LSPR shift [187, 206, 212, 213]. An example from the work of Campiglia et al. reporting an extraordinary sensitivity of gold nanorords towards elemental mercury is shown in Figure 1.20.

a)

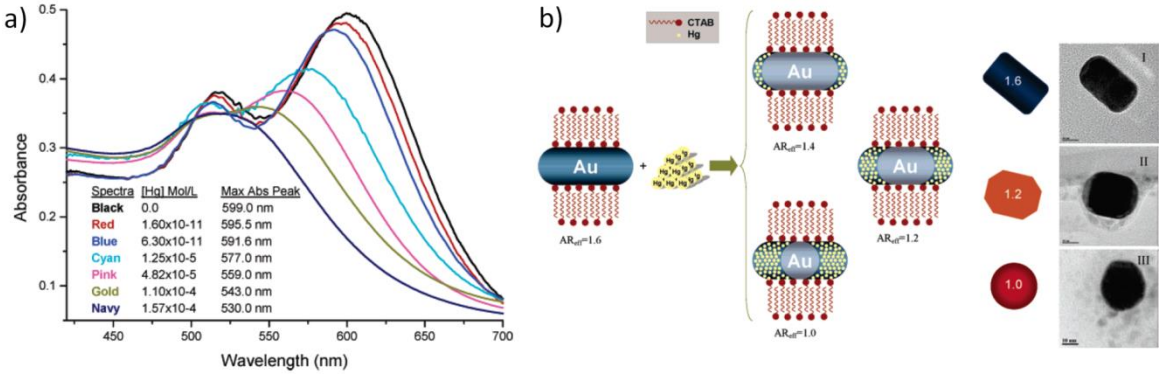


Figure 1.20: a) UV-visible absorption spectra showing the spectral shift at several Hg(II) concentrations. The concentration range between 1.6 x 10-11 and 6.3 x 10-11 M shows the spectra within the linear dynamic range of the calibration curve. The remaining spectra show the overlapping between the longitudinal and transversal absorption bands at higher Hg(II) concentrations. b) Schematic diagram showing the amalgamation of Hg with Au nanorods and TEM analysis of Au nanorods in the absence and the presence of Hg. I) no Hg; II) 1.25 x 10-5 M and III) 1.57 x 10-4 M Hg(II). All solutions were prepared in 1.67 x 10-3 mol/L $NaBH_4$.[206]

Gold nanorods were synthesised with an average aspect ratio of 1.6. Upon addition of Hg^{2+} ions and sodium borohydride reducing agent the UV-Vis spectrum of the nanorod solution notably blue shifted. The authors reported a linear relationship of the spectral shift and mercury concentration in the range between 16 pM and 63 pM and a lower LOD at 0.77 pM. This observation was explained with a shape transition of the nanorods towards nanospheres, evidence of which was delivered in TEM images.[206]

1.5. Nanoalloys

As discussed in the previous section, a compositional change of a plasmonic nanostructure can be utilised for sensing purposes. However, the interest in mixed composition plasmonic nanostructures goes beyond sensing as exciting new properties can arise from introducing a second element or a second phase to a nanostructure. A multitude of bimetallic and trimetallic systems have been investigated [214, 215] but the most studied system is most likely the gold-silver system. Various methods exist to fabricate mixed composition nanostructures.[214] Core-shell particles are commonly synthesised by chemical reduction where first nanoparticles of the core material are synthesised and then the second metal is reduced onto the surface of the first.[124, 216-218] In other methods metal salts are reduced electrochemically [219, 220] or radiolytically.[210, 221, 222] Alloyed structures can be synthesised for example by simultaneous reduction of metal salts under appropriate conditions.[217, 223, 224] Alternatively, core-shell or alloyed nanoparticles have been fabricated physically by evaporation and condensation of the relevant metals.[225, 226] The plasmonic properties of the resulting nanostructures were found to be strongly dependent on the degree of mixing or segregation of the elements in the nanostructure (core-shell vs alloy).

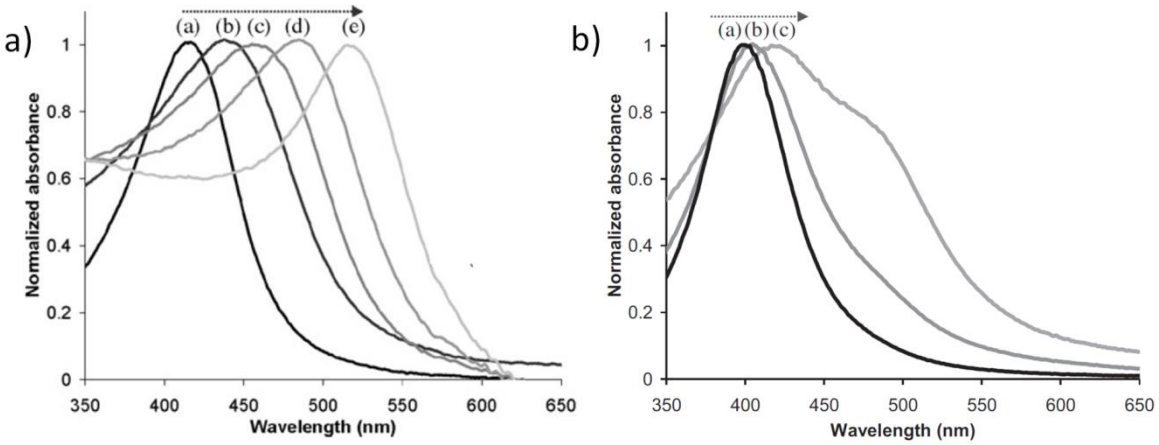


Figure 1.21: a) Plasmon bands of different silver–gold alloy nanodispersions at different Au mole fractions: (a) 0.1, (b) 0.3, (c) 0.5, (d) 0.7, and (e) 0.9. b) Representative plasmon bands of core–shell type nanoparticles-containing aqueous dispersion at different Au mole fractions: (a) 0.1, (b) 0.2, and (c) 0.3.[217]

For example Dékány et al. showed that while the UV-Vis spectra of alloyed nanoparticles with varying gold-silver ratio shift between the plasmon peaks of the single elements according to their composition, core-shell nanoparticles have a complex absorption spectrum with multiple peaks (see Figure 1.21).[217] The core-shell nanostructures can be converted to alloy nanostructures by various methods. Hodak et al. demonstrated that via laser irradiation interdiffusion of the elements in gold-silver core-shell nanoparticles could be induced.[227] Tracy et al. achieved the same by annealing core-shell nanoparticles at 250°C.[228] For other systems the contrary behaviour of transition from an alloyed to a core-shell particle could be observed.[229, 230]

With nanoalloys, a nanostructure's plasmon resonance can be tuned to a specific wavelength,[124, 217, 231] its catalytic behaviour can be modified [232-234] and additionally, core-shell nanoparticles were found to possess enhanced performance as SERS platforms.[235-238] Furthermore these structures offer the possibility to study alloying mechanisms and diffusion at the nanoscale that differs from the bulk material behaviour due to the large surface to volume ratio and the additional surface curvature.[208, 213, 216, 239, 240] For example Figure 1.22 shows work form Mertens et al. who studied nanoalloys formation and diffusion of mercury into gold nanoparticles.

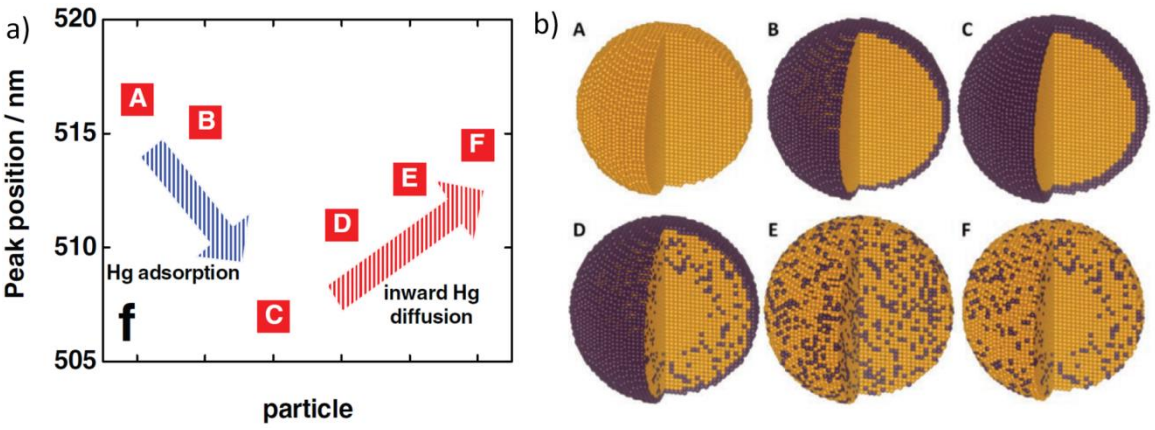


Figure 1.22: a) Calculated maxima in UV–Vis absorption spectra for Au@Hg particle models A–F. b) Representation of the dipole arrangement within 6 Au@Hg particle models for DDA calculations.[208]

Mertens et al. report that comparison of experimental data with DDA and DFT calculations suggest that mercury slowly diffuses towards the centre of a gold nanoparticle, but not completely intermixes due to a large separation energy.[208]

1.6. Scope of this Thesis

Due to its persistence, its ability to circle globally, and the fact that it continues to be widely used despite serious adverse health effects, mercury poses a significant risk to human health and ecological systems. Novel, fast, sensitive and selective mercury detection methods are sought after. In this context noble metal nanostructures with highly sensitive plasmonic properties are promising platforms for sensing applications. The goal of this thesis was to investigate the properties of various plasmonic gold nanostructures and explore their application in mercury detection.

Chapter 2 is dedicated to the analysis and assessment of the optical properties of plasmonic nanostructures as potential building blocks or platforms for sensing applications. In particular, single gold and silver nanoparticles, gold nanorods, gold nanoparticle clusters and highly ordered gold nanorod arrays were characterised with correlated spectroscopic and structural analysis. Silver nanoparticles were found more efficient scatterers than gold nanoparticles of the same size but with less monodisperse size and shape distribution and inferior stability in ambient conditions. Gold nanorods showed widely tuneable and polarised plasmon resonance corresponding to longitudinal and transversal plasmon modes. Polarisation dependent plasmon coupling was observed for nanoparticle clusters and nanorod arrays. Additionally, the application of highly ordered nanorod arrays as anti-clonal tags was demonstrated.

In chapter 3 a plasmon resonance energy transfer (PRET) based detection strategy was explored using immobilised 60 nm gold nanoparticles functionalised with organic molecules that can complex Hg^{2+} ions and exhibit an absorption band close to the plasmon resonance band of the nanoparticles. The initial hybrid sensing structure could be fabricated successfully, but showed no response to Hg^{2+} ions. To improve the spectral overlap between nanoparticle and molecule pseudo-silver core – gold shell nanoparticles were fabricated. Additionally, the Hg^{2+} detection was performed in organic medium where the molecule-Hg^{2+} complex had shown improved stability compared to water. Following these changes a scattering intensity quenching was observed for 100 μM Hg^{2+} concentration.

As various material incompatibilities were encountered for the mercury detection method pursued in chapter 3 hampering the pursuit of this sensing strategy, a decision was made to investigate an alternative route. Therefore, in chapter 4 a fresh start was made taking advantage of the affinity of mercury towards gold directly. Immobilised gold nanorods were exposed to Hg^{2+} ion solutions in presence of reducing agent $NaBH_4$. Single particle dark field spectroscopy showed a remarkable optical response of the gold nanorods. Their plasmon resonance decreased in intensity and blue-shifted strongly. Blue shifts of 5 nm could be recorded for Hg^{2+} concentrations as low as 10 nM. The selectivity of the method was demonstrated versus common interfering metal ions and in local river and tap water. Further time-dependent studies were carried out to gain insights into the mercury deposition and alloying mechanism leading to the observed changes in the nanorods plasmonic signatures. Based on these experiments a 5 step model was proposed.

In chapter 5 a variation of the mercury detection method investigated in chapter 4 was explored replacing the chemical reduction of Hg^{2+} ions to elemental mercury with an electrochemical reduction. The motivation behind this step was twofold. Firstly, an electrochemical reduction of Hg^{2+} in an appropriate electrochemical cell would allow a simultaneous optical observation of the processes involved allowing a deeper insight into the interaction of elemental mercury with gold nanorods. Secondly, in an optimised setup, simultaneous electrochemical and optical signal acquisition might lead to a more sensitive mercury detection method. At the beginning a suitable spectroelectrochemical cell for the intended experiments was designed. The ITO/gold nanorod working electrode was analysed by capacitive charging experiments in KCl before Hg^{2+} was reduced by linear sweep voltammetry (LSV). Without further electrode modification reduction of Hg^{2+} ions was shown to be confined to the nanorod surfaces with negligible contribution from the ITO surface. The method has shown strong optical and electrochemical responses for 5 μM Hg^{2+} concentrations, a lower LOD is yet to be determined. In-situ LSV with dark field spectroscopy in 1-4 μM mercury solutions was performed and additionally, LSV and chronoamperometry (CA) as Hg^{2+} reduction techniques were compared.

Finally, chapter 6 gives a summary of the key results achieved, the conclusions drawn from the presented work and thoughts on future work

Chapter 2 - Optical Properties of Plasmonic Nanostructures Based on Gold and Silver Nanoparticles and Gold Nanorods

In this chapter, single gold and silver nanoparticles, gold nanoparticle clusters, single gold nanorods and highly ordered gold arrays were characterised in detail by correlated single nanostructure spectroscopy and electron microscopy. Based on their respective optical properties, their suitability for application in different sensing methods is highlighted.

Parts of this chapter have been published in:

Au nanorod plasmonic superstructures obtained by a combined droplet evaporation and stamping method *Carola Schopf, Alfonso Martín Ruano, Mícheál Burke, Daniel Jones, Andrea Pescaglini, Alan O'Riordan, Aidan J. Quinn, Daniela Iacopino*, Journal of Materials Chemistry C, **2014**. 2(18): p. 3536-3541

Surface-Enhanced Raman Scattering of 4-Aminobenzenethiol on Au Nanorod Ordered Arrays *Alfonso Martín, Andrea Pescaglini, Carola Schopf, Vittorio Scardaci, Richard Coull, Lorraine Byrne, and Daniela Iacopino*, Journal of Physical Chemistry C, **2014**, 118(22): p. 13260-13267

Facile Formation of Ordered Vertical Arrays by Droplet Evaporation of Au Nanorod Organic Solutions, *Alfonso Martín, Carola Schopf, Andrea Pescaglini, Jing Jing Wang, Daniela Iacopino*, Langmuir, **2014**, 30(34), p.10206-10212

Synthesis, Optical Properties and Self-Assembly of Gold Nanorods *Alfonso Martin, Carola Schopf, Andrea Pescaglini, Alan O'Riordan, Daniela Iacopino*, Journal of Experimental Nanoscience, **2012**, 7, (6), p. 688-702

2.1. Introduction

Plasmonic noble metal nanostructures have received a tremendous attention over the last decades with widespread application in many fields ranging from photonics [43-45, 47] over sensing [48-50] to catalytic chemistry.[54, 55, 241] This continued research effort has spurred great advances in methods relating to both fabrication [30, 123, 242, 243] as well as characterisation [38, 40, 244] of said nanostructures.

An essential tool for furthering the understanding of nanoparticle plasmonic properties and their exploitable applications is the correlation of nanoparticle optical signatures with their size and shape. This is especially relevant for chemically synthesised metal nanostructures where each synthesis invariably produces a range of nanostructure shapes and sizes. Collective measurements of nanostructures dispersed in solution do not reflect the properties of individual nanostructures.[56] Darkfield spectroscopy has emerged in the last 15 years as a powerful tool for the investigation of the spectroscopic signatures of individual metal nanoparticles, where optical properties are highly shape and size dependent. The first spectroscopic studies of single metal nanoparticles were reported by the Schultz and Feldmann groups.[63, 69, 245] Schultz et al. performed correlated transmission electron microscopy/single particle Rayleigh scattering measurements for silver nanoparticles to determine how the frequency of the local surface plasmon resonance depends on the size, shape [63] and local refractive index.[69] Feldmann et al. examined silver and gold spheres and gold nanorods. Their measurements showed a significant reduction in the linewidth of the localised surface plasmon resonance (LSPR) at a given resonance compared to spheres.[245] This was attributed to reduced radiation damping in nanorods.

Bringing plasmonic nanoparticles in close proximity to each other leads to the appearance of new, more complex plasmon resonances caused by coupling of the plasmon resonance modes of the individual particles. Plasmon coupling of nanoparticles has been studied on nanoparticle chains[78, 246] and clusters,[81, 82] also identifying the important role of symmetry of nanoparticle assemblies on the resulting plasmonic states.[81] A consequence of the coupling of the plasmon modes is the occurrence of very high electric fields in the space between the particles, so called

"hot-spots".[247, 248] These highly localised strong electric fields make nanoparticle assemblies interesting as signal amplifiers in applications like surface enhanced fluorescence and Raman spectroscopy. In this context, also large area ordered nanoparticle [94, 97] and nanorod [99, 100] arrays have been studied. High densities of hot-spots, as well as low fabrication costs, make large area nanostructure assemblies interesting for these techniques.

Addressing the need to understand the properties of noble metal nanostructures for their further application, this chapter covers the characterisation of various noble metal nanostructures and assemblies thereof: In the first part, single gold and silver nanoparticles were characterised by correlated electron and optical microscopy where the dependence of a nanoparticle's surface plasmon resonance on its size, shape, material and dielectric environment becomes evident (Section 2.3.1). Furthermore, plasmon coupling between gold nanoparticles in chemically linked, small clusters was studied (Section 2.3.2). The second part of the chapter concerns gold nanorods, covering the characterisation of single gold nanorods and highlighting their anisotropic and tunable optical properties (Section 2.3.3). Additionally, the characterisation and application of highly ordered nanorod arrays is covered showing unique anisotropic properties (Section 2.3.4).

2.2. Experimental Methods

2.2.1. Nanostructure Fabrication

Nanoparticle Linking into Small Clusters

Linking experiments of 60 nm gold nanoparticles (purchased from BBInternational) were performed by Ethel Noonan. The bi-functional linker molecule, $Re_2(DMAA)_4(NCS)_2$ was dissolved in acetone. A 3 ml aliquot of diluted nanocrystal solution (1:1 with tri-sodium citrate to improve the stability of the nanocrystals) was decanted into a clean cuvette. 2 µL aliquots of 10 µM $Re_2(DMAA)_4(NCS)_2$ linker solution were added to the nanocrystal solution at 2 minute intervals and mixed. Before the initial addition of the linker solution and after every subsequent addition the cuvette was inserted into a UV-Vis spectrometer and the UV-Visible extinction spectra were recorded. Additionally, small aliquots of solution were removed and deposited for darkfield and SEM analysis.

Nanorod Synthesis

All gold nanorods used throughout this work were synthesised by Dr. Alfonso Martín after a seed-mediated method pioneered by El Sayed.[32] Briefly, via fast reduction of $HAuCl_4$ with $NaBH_4$ small gold crystals are synthesised which in turn are used as seeds for nanorod growth in a slow reduction of $HAuCl_4$ with ascorbic acid. The typical dimensions of the resulting nanorods are 11 x 41 nm. This type of nanorod has been used for the fabrication of highly ordered nanorod arrays with nanorods aligned parallel to the substrate. For single particle spectroscopy and for the fabrication of nanorod arrays with nanorods perpendicular to the substrate larger nanorods were synthesised by overgrowth of the nanorods obtained from the seed-mediated method after a method developed by Marzán.[90] Ascorbic acid is added to the solution of seed-mediated synthesised nanorods, which reduces remaining Au(I) in the solution. As a result the nanorods grow isotropically up to a size of 23 x 63 nm.

Fabrication of Gold nanorod Arrays Parallel to the Substrate

Parallel and perpendicular nanorod arrays have been fabricated by Dr. Alfonso Martín. As-synthesised gold nanorods were transferred to chlorobenzene according to a method reported by Chen.[249] Subsequently, a 10 µl droplet of the seed-mediated synthesised nanorod solution in chlorobenzene was left to evaporate on a Si/SiO_2

substrate over 3 hours at room temperature covered by a petri dish. This led to the formation of parallel nanorod arrays. In order to fabricate arrays where the nanorods are aligned perpendicular to the substrate a 10 μl droplet of the overgrown nanorod solution in chlorobenzene was left to evaporate on a Si/SiO_2 substrate, uncovered, at room temperature for 20 min. The parallel and perpendicular arrays were then transferred to transparent glass substrates by pressing the glass substrate for 30 s onto the original substrate with the dried droplet. Residual organic surfactant was removed by immersing the substrates for 1 h in isopropanol followed by thorough rinsing of the substrates with fresh isopropanol.

Substrates for Single Nanoparticle Microscopy

Glass substrates for correlated single nanoparticle spectroscopy were coated with a 20 nm indium tin oxide (ITO) film (fabricated by Dan O'Connel). ITO was evaporated in a Leybold SyrusPro 710 e-beam evaporation system in a vacuum chamber evacuated to $< 5 \times 10^{-6}$ Torr and with a background flow of 5 sccm O_2. The system also uses an APS500 plasma source during the evaporation to increase the density of the film and to improve transparency of the film. The evaporation rate of ITO is 0.2 nm/sec. A 20 nm thick ITO coating is conductive, yet transparent and enables correlated imaging of the particles with optical transmission microscopy and scanning electron microscopy (SEM). Additionally, a unique pattern of 10 nm deep lithographically etched binary alignment marks in the ITO layer allows an exact localisation of each particle. The samples were patterned by a standard UV lithography process: hexamethyldisilazane (HMDS) was spun onto the samples at 3000 rpm for 50 s, then S1805 photoresist was spun on at 3000 rpm for 50 s. Subsequently, the samples were hot-plate baked at 115°C for 2 min, before the samples were exposed to UV light beneath the patterned quartz mask in a Karl Suss MA1006 mask aligner. The UV exposure dose was 40 mJ/cm^2. The samples were then developed in Microposit MF319 developer for 25 s, rinsed well in DI water and blow-dried under a stream of nitrogen. After the patterning, the ITO was etched in an STS ICP (Inductively Coupled Plasma) etching system. The etch took place at 10°C and at 8.0 mT using CH_4 (5 sccm) and Ar (45 sccm). The ICP Rf power was 450 W, the platen power was 50 W giving a peak-to-peak voltage V_{pp} of about 435 V. The resulting ITO etch rate was 0.75 nm/sec. After etching the

remaining photoresist was removed by immersing the samples in R1165 resist remover at 90°C for 20 min and rinsing well in DI water followed by blow-drying in N_2.

Sample Preparation for single Nanoparticle Microscopy

To obtain sufficiently spaced nanoparticles and nanorods for single particle darkfield spectroscopy, nanoparticles from a 4.3 pM gold or silver colloid purchased from BBI (60 nm), linked gold nanoparticles or gold nanorods (21 x 61 nm and 39 x 76 nm) from solution with ca. 33 pM, were deposited by flow deposition on ITO coated glass cover slips. Subsequently, the substrates were rinsed with 50°C deionised water to remove surfactants remaining from the nanoparticle/nanorod synthesis and blown dry under a stream of nitrogen.

2.2.2. Nanostructure Characterisation

UV-Vis Spectroscopy

UV-Vis spectra of nanoparticle and nanorod solutions were acquired with an Agilent/HP 8453 UV-Vis Spectrophotometer (200nm < λ < 1100nm). All presented extinction spectra are background subtracted by the extinction spectrum of pure deionised water.

Darkfield Optical Microscopy and Spectroscopy

Scattering spectra of individual nanoparticles, nanoparticle clusters and nanorods were acquired with an inverted IX-71 Olympus microscope with an oil immersion darkfield condenser (Olympus U-DCW, 1.4 NA) and 100x objective (Olympus MPlanApo 100x/0.95 NA). The sample was illuminated with a 100 W halogen lamp. The light collected by the objective was directed either onto a colour CMOS camera (DCC1645C, ThorLabs) for image acquisition or onto the entrance slit of a monochromator (SP-2356, Acton Research). The light was dispersed by an optical grating (300 grooves/mm, blazed at 500 nm, 350nm < λ < 850nm) and directed onto a thermoelectrically cooled, back illuminated CCD (Spec10:100B, Princeton Instruments) for spectra acquisition. The sample polarisation rate was determined by a polariser placed in collection between the sample and the monochromator. The experiments were performed by first recording an image of the sample with a mirror in the light path of the spectrometer. Once a suitable nanostructure was selected, the mirror was switched to the grating to disperse the scattered light and a spectrum was recorded using an

acquisition time of 60 s. Normalised scattering spectra from individual nanostructures were obtained by subtracting and dividing by a background scattering spectrum taken from a nearby clean area on the sample. To determine the peak scattering wavelength, the spectra were fitted with a Lorentzian function

$$y = y_0 + \frac{2B}{\pi}\frac{w}{4(x - x_c)^2 + w^2} \qquad (2.1)$$

with y_0 the intensity offset, x_c the centre wavelength of the peak, w the full with at half maximum and B the area underneath the curve.

Transmission Optical Microscopy and Spectroscopy

Polarisation resolved optical images and transmission spectra of gold nanorod superstructures were equally acquired with the above mentioned inverted IX-71 Olympus microscope with a 100X objective operated in transmission. The sample was illuminated with a 100 W halogen lamp. The light collected by the objective was directed either onto a colour CMOS camera (DCC1645C, ThorLabs) for image acquisition or onto the entrance of slit of a monochromator (SP-300i, Acton Research) equipped with a thermoelectrically cooled, back illuminated CCD (Spec10:100B, Princeton Instruments) for spectra acquisition. The sample polarisation rate was determined by a polariser placed either in excitation or collection as indicated in the relevant sections. Spectra were typically recorded using an integration time of 1-10 s. The extinction was determined according to Lambert-Beer's law: A = -log10(I/I_0) with I being the intensity of the sample spectrum and I_0 being the intensity of the blank spectrum taken from a nearby clean area on the substrate.

Electron Microscopy

Scanning electron microscopy (SEM) images of single nanostructures and nanorod arrays were acquired using a field emission SEM (JSM-6700F, JEOL UK Ltd.) operating at beam voltages of 10 kV. For navigation on the substrate, lithographically etched alignment marks in the ITO coating of glass cover slips were used for single nanostructures and FIB milled alignment marks were used for nanorod arrays. FIB milled alignment marks were made using a Quanta 3D 200i dual-beam Focused Ion Beam (FIB). Individual 4 µm × 1 µm rectangles were fabricated on the sample by

focused ion beam milling; 30 kV beam voltage, 100 pA beam current, a depth of 100 nm. These individual rectangles were arranged in pairs to form “L” shaped marks.

2.2.3. Calculation of Nanostructure Scattering Spectra

To calculate the scattering spectra of gold nanoparticle monomers, dimers and trimers a boundary element method based toolbox for MATLAB was utilised, which was developed and made available by Hohenester et al.[250] The nanoparticles were discretised by spheres with 1444 vertices and a diameter of 60 nm. The dielectric function for the gold nanoparticles was taken from Johnson and Christy,[251] the average dielectric constant of the environment was assumed as 1.33. The distance between coupled spheres in dimers and trimers was estimated to 1 nm based on the length of the used rhenium linker molecules. Dependent on the symmetry of the nanostructure various light polarisation and propagation direction combinations (notation: (pol/dir)) were considered. For a perfectly symmetrical monomer all polarisation and propagation direction combinations of incident light result in the same response and the calculation of the response for one case suffices. For a dimer with $D_{\infty h}$ symmetry three combinations of polarisations and propagation directions of incident light have to be considered: light propagation direction perpendicular with polarisation direction perpendicular (I) and parallel (II) to the long axis of the dimer and light propagation direction parallel and light polarisation perpendicular (III) to the long axis of the dimer. For a trimer with D_{3h} symmetry all 6 light polarisation and propagation direction combinations were considered.

2.3. Results and Discussion

With the aim to understand the properties of noble metal nanostructures for their further application, various nanoparticles, nanorods and nanostructures made thereof were examined regarding their optical properties and assessed towards their suitability as building blocks for enhanced metal ion detection.

2.3.1. Optical Characterisation of Silver and Gold Nanoparticles

To begin with, the simplest type nanostructure, single nanoparticles, were studied to establish the basic properties of plasmonic nanostructures and correlations between various parameters like shape, size, composition and surrounding medium and the nanoparticle's optical properties.

Characterisation of Gold Nanoparticles

Gold nanoparticles with 60 nm diameter were characterised collectively in solution as well as by single particle spectroscopy. The gold nanoparticle colloidal solution showed a typical pink colour in transmission as can be seen in Figure 2.a. However, when a vial of the solution was held against a black background, no light could travel straight through the vial to the observer's eye. The solution appeared in a yellow/green colour, the colour of the light scattered by the colloidal solution. A UV-Vis spectrum of the solution in Figure 2.b shows a peak extinction wavelength at 525 nm. This extinction band lies in the green region of the visible spectrum, matching the colours observed in the solution.

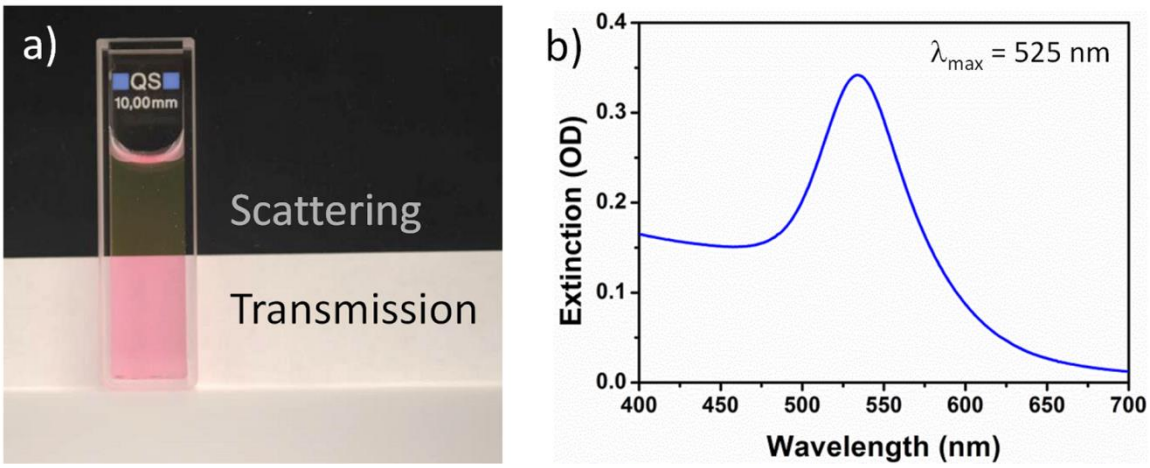


Figure 2.1: a) 60 nm gold nanoparticle colloidal solution in front of a mixed background showing the difference between light scattered by and transmitted through the solution. b) UV-Vis extinction spectrum of 60 nm gold nanoparticle colloidal solution.

To study single nanoparticles, they were deposited on glass substrates and observed under darkfield illumination conditions with an optical microscope. Care was taken to deposit the nanoparticles sufficiently spaced (ideally ~5 μm) to ensure a recorded spectrum would only show contribution from a selected single nanoparticle. The experimental setup for darkfield microscopy is schematically shown in Figure 2.2. An optical microscope was equipped with a darkfield condenser, inserted between the light source and the sample. The darkfield condenser has a high numerical aperture and, using a central light stop and a mirror system, created a hollow cone of light which was focussed onto a point on the surface of the sample. An objective with lower numerical aperture than the darkfield condenser was located below the sample. Due to its lower numerical aperture only light that was scattered by the sample entered the objective and all light transmitted through the sample passed by the objective. The scattered light was then directed either towards a camera to form an optical image or towards a spectrograph to obtain the scattering spectrum of individual gold nanoparticles.

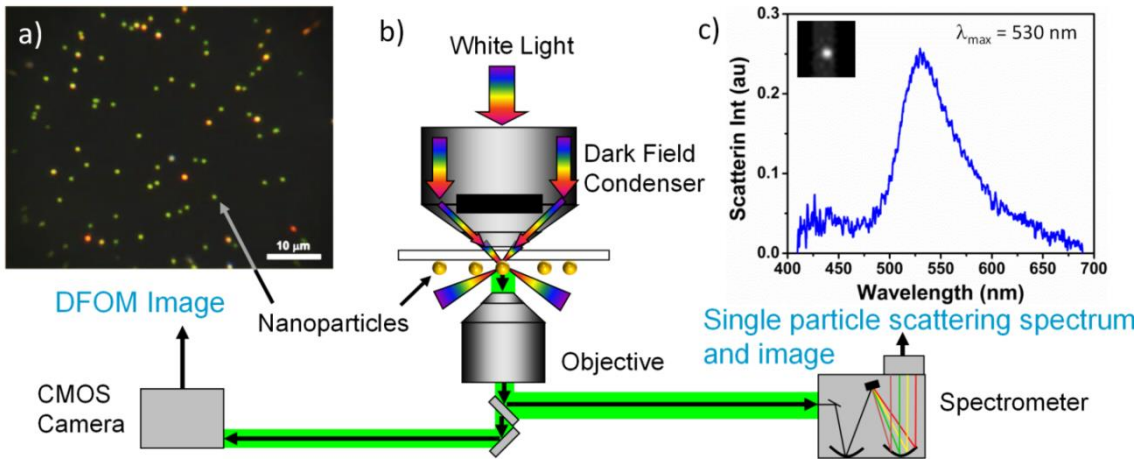


Figure 2.2: Schematic setup for darkfield imaging and spectra acquisition. White light is focussed in a hollow cone onto the sample. Scattered light is collected and directed either to a camera for imaging (typical scattering image of an ensemble of gold nanoparticles shown in the left) or to a spectrometer for spectral analysis (typical spectra of a single gold nanoparticle shown on the right).

A typical darkfield image of deposited gold colloid is shown in Figure 2.2a. Only light scattered by the particles was observed, which was of green colour for most particles. The single particle spectrum shown in Figure 2.2c shows a scattering peak at 530 nm in the green region of the visible spectrum, matching the extinction spectrum of the bulk

solution shown in Figure 2.1b. Looking at individual nanoparticles with darkfield microscopy also revealed that the particles from one batch of solution were, as expected from chemically synthesised nanoparticles, not entirely monodisperse and several different scattering colours were observed.

To investigate the origin of the various colours, correlated darkfield spectroscopy and SEM analysis was performed, which allowed a reliable association of a particle's properties such as size and shape to its scattering properties. For this purpose ITO coated glass substrates were employed, which ensured sufficient conductivity for SEM imaging and sufficient transparency for darkfield microscopy. Additionally, the substrates were covered in etched alignment marks to allow unambiguous identification of single nanostructures in optical and electron microscopy. Figure 2.3 shows a set of typical gold nanostructures found in a gold nanoparticle solution (60 nm diameter) with associated optical signatures that they produced. The majority of the particles (88% occurrence) were like s01 spherical or near-spherical with a measured peak plasmon resonance wavelength between 526 nm and 536 nm. A tetrahedron (s02) was found to exhibit the same resonance wavelength (534 nm) with, however, a slightly broader full width half maximum (FWHM). Apart from the tetrahedron, a general trend could be observed: the greater the deviations of a nanostructure's shape from a perfect spherical shape the stronger the red shift of the peak plasmon resonance wavelength compared to the resonance wavelength of a spherical particle. Hexagons like s03 (9% occurrence) were found to scatter in the range from 554-572 nm and triangles like s04 (2% occurrence) from 583 nm to 606 nm. Compared to the shape dependence, a variance in size has a marginal effect on the peak plasmon resonance wavelength of the particles. However, with decreasing nanoparticle size the scattering intensity of the particles decreases dramatically. This becomes clear from the extinction and scattering cross section equations (1.1) and (1.2). While the extinction cross section scales with V, the scattering cross section scales with V^2. Consequently, the smaller the gold nanoparticles the less they are visible by single particle darkfield microscopy. This makes them less suitable for single particle experiments, and nanoparticles with a diameter below 40 nm are rarely used for that purpose. Calculations of extinction and scattering behaviour of gold nanoparticles of

varying size can also be found in literature by El Sayed [57] and match the experimental findings.

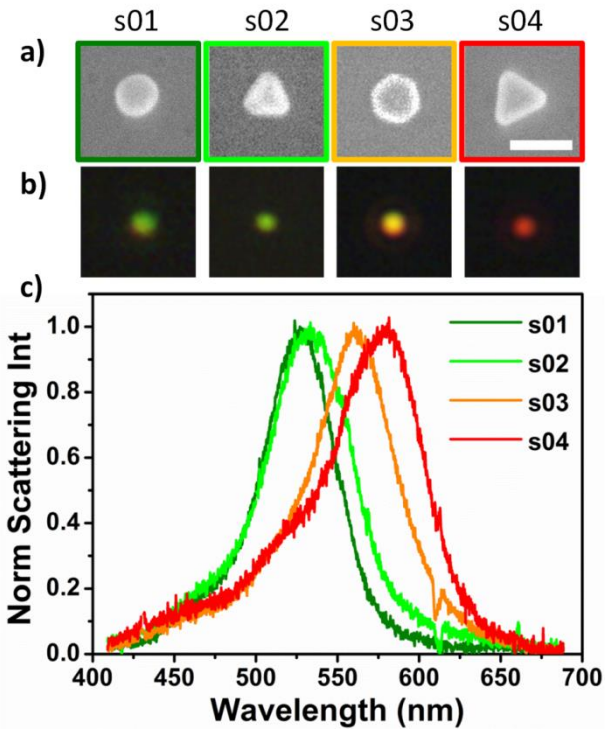


Figure 2.3: Correlated darkfield scattering images and spectra with SEM images of various nanoparticle shapes found in a batch of 60 nm gold nanoparticle colloidal solution (scale bar 100 nm).

Characterisation of Silver Nanoparticles

Silver 60 nm nanoparticle colloidal solution was analysed in the same way as the gold nanoparticle solution. Compared to gold nanoparticles of the same size, silver nanoparticles scattered the light more efficiently which already became evident when looking at the colloidal solution in different lighting conditions as seen in Figure 2.4a.

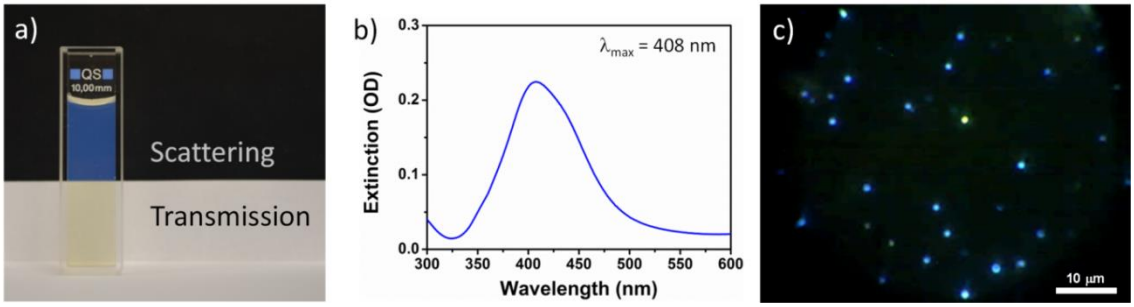


Figure 2.4: a) 60 nm silver nanoparticle colloidal solution in front of a mixed background showing the difference between light scattered by and transmitted through the solution. b) UV-Vis extinction spectrum of 60 nm silver nanoparticle colloidal solution. c) Darkfield scattering image of 60 nm silver nanoparticles deposited from solution on glass substrate.

While the solution looked pale yellow in transmission, it strongly scattered bright blue light. Respectively, the UV-Vis spectrum in Figure 2.4b shows an extinction peak at the edge of the visible spectrum at 408 nm and the darkfield micrograph in Figure 2.4c shows the silver nanoparticles as blue scattering dots. Already from the broader UV-Vis extinction spectrum it became evident that the silver nanoparticle colloidal solution was more polydisperse than the gold nanoparticle solution. To investigate the size and shape variability of particles found in one batch of silver nanoparticle solution and their associated scattering spectra, correlated darkfield spectroscopy and SEM imaging was performed.

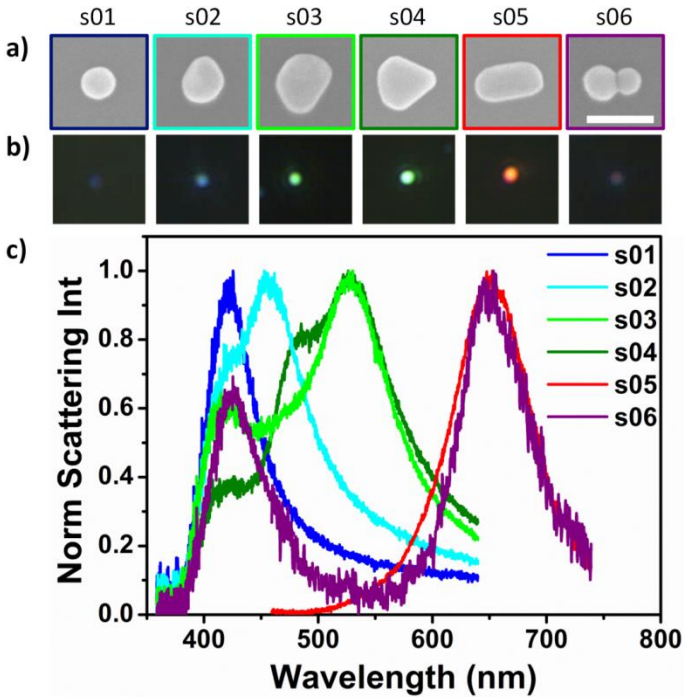


Figure 2.5: Correlated darkfield scattering images and spectra with SEM images of various nanoparticle shapes found in a batch of 60 nm silver nanoparticle colloidal solution (scalebar 100 nm).

Figure 2.5 shows representative types of nanoparticles found in a chemically synthesised batch of 60 nm silver nanoparticles with associated scattering images and spectra. Most particles were indeed spherical like s01 (65% occurrence) with a peak plasmon resonance at 420 nm. In addition, several irregular shaped particles like s02 to s04 were found with complex and red shifted scattering signatures compared to that of spherical particles (33% occurrence). The least common structures found were

nanorods like s05 (1% occurrence) with a peak plasmon resonance around 650 nm and dimers like s06 (1% occurrence) with two scattering bands at 420 and 650 nm.

Advantages of silver nanoparticles are that they scatter the light more efficiently than gold nanoparticles of the same size and their plasmon resonance is tunable throughout a wider range of the visible spectrum. A weakness, however, is their tendency to oxidise in ambient condition once deposited from solution. This causes attenuation to quenching of the particles' scattering and makes nanoparticle surface chemistry more challenging.

Refractive Index Dependence of Plasmon Resonance

Many applications of plasmonic nanoparticles as sensors are based on the sensitivity of a nanoparticle's plasmon resonance band on their dielectric environment. In this section, this dependence is studied for the nanoparticles used in this work. Using glass cover slips, a small cell was built that is thin enough to match the working distance of the condenser and the objective but allows injection of various solvents to measure the influence of the environment on the scattering properties of gold nanoparticles. Representative spectra of a single particle in various media are shown in Figure 2.6.

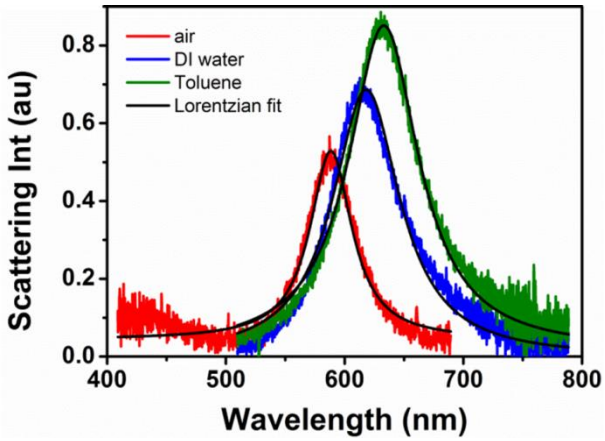


Figure 2.6: Shift of the scattering spectrum of a single gold nanoparticle with the change of the refractive index *n* of the medium (air: *n* = 1, water: *n* = 1.33, toluene: *n* = 1.49).

In air with a refractive index of $n = 1$ the observed nanoparticle exhibited a plasmon resonance peak centred at 586 nm. Increasing the refractive index of the nanoparticle to $n = 1.33$ by injecting the cell with deionised water the nanoparticle's plasmon shifted to 618 nm accompanied by an increase in scattering intensity. Finally, increasing the refractive index of the environment to $n = 1.49$ by injection of toluene

the nanoparticle's plasmon resonance experiences a further red shift to 633 nm and further increase in scattering intensity. In Figure 2.7a the peak plasmon wavelengths of 11 particles are plotted versus the refractive index of the medium. The scattering spectrum of a particle was found to be red shifted linearly with increasing refractive index of the medium. However, particles with a longer initial plasmon wavelength experienced a stronger red shift. The plasmon shift per refractive index plotted in Figure 2.7b was found to be dependent on the nanoparticle's shape. The closer the shape of a particle to a triangle, the stronger was the shift. The scattering of data in Figure 2.7b was attributed to varying influence of the substrate due to the rough surface of the ITO layer.

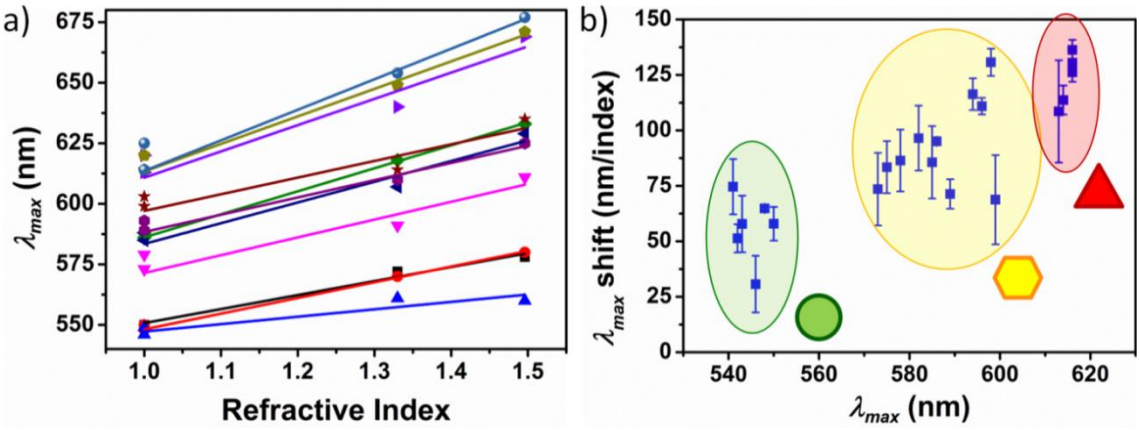


Figure 2.7: a) Shift of the resonance wavelength with the change of the refractive index of the medium for a batch of particles. b) Dependence of the red shift of the resonance wavelength on the shape of the particle.

The refractive index dependence of the scattering spectra could also be satisfactorily modelled for spherical and hexagonal particles adapting a concept from Mulvaney et al.[252] The resonance condition derived from the Mie theory is:

$$\varepsilon_{1.Au} = -\frac{1-L}{L} n_{eff}^2 \qquad (2.2)$$

In this equation n_{eff} is the effective refractive index of the environment

$$n_{eff} = \alpha n_{med} + (1-\alpha) n_{sub} \qquad (2.3)$$

taking into account the influence of the substrate $(1-\alpha)$ and the shape of the particle with the depolarisation factor *L*.

Creating a homogeneous environment for the nanoparticles by using index matching immersion oil the plasmon resonance shift was measured at $n_{eff} = n_{med}$. With this experimental data, equation (2.2) could be solved for the parameter *L* as plotted in Figure 2.8a. The calculated values for *L* showed a linear dependence on λ_{max} following $L = 1.03 - 0.00148\lambda_{max}$. An average value for α of $\alpha_{mean} = 0.48$ was calculated by fitting the experimentally obtained plasmon resonance wavelengths for nanoparticles in air (values for the dielectric function for gold taken from Johnson and Christy [251]).

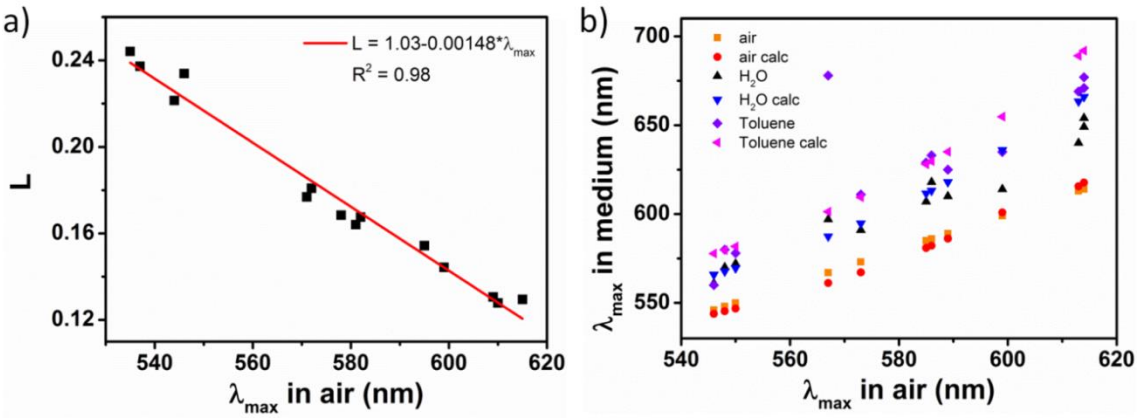


Figure 2.8: a) Correlation of a particle's depolarisation factor with its plasmon resonance wavelength. b) Calculated vs. experimentally determined plasmon peak shifts for gold nanoparticles in various media.

Inserting the thus determined parameters *L* and α in turn into equations (2.2) and (2.3) allowed the calculation of the peak shift for spherical particles in an environment with known refractive index as shown in Figure 2.8b. For particles with a plasmon resonance wavelength below 580 nm in air, the calculated peak positions for water and toluene agreed very well with the experimentally obtained values. For particles with a plasmon resonance wavelength in air above 580 nm the calculated values started to deviate considerably from the experimental ones. This can be explained by the fact, that these particles possess a shape varying strongly from a sphere and the Mie theory cannot be applied here.

2.3.2. Optical Characterisation of Small Gold Nanoparticle Clusters

Self-assembly techniques can be used to form nanoparticle dimers, trimers, n-mers. Bringing nanoparticles in close proximity of each other leads to coupling of their plasmon modes and results in interesting, more complex optical signatures.

In this work, nanoparticles were linked with a rhenium linker molecule of 1 nm length, $Re_2(DMAA)_4(NCS)_2$, resulting in a gap between the particles of approximately this width. Correlated darkfield spectroscopy and SEM imaging on deposited nanostructures was performed to study their optical signatures and the related plasmon coupling. Representative scattering spectra of a monomer, dimer and trimer formed of 60 nm gold nanoparticles are shown in Figure 2.9, the peak positions are noted in Table 2.1.

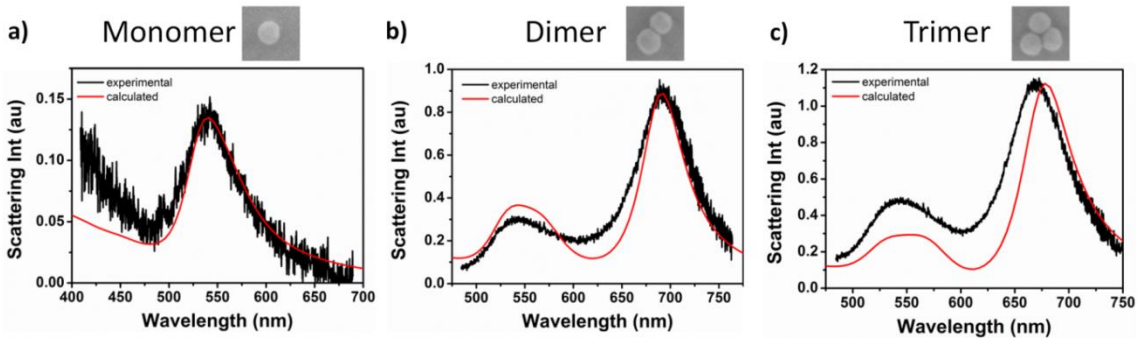


Figure 2.9: Scattering spectra (without polariser) of a) a monomer; b) a dimer; c) a trimer. Experimental data (black), calculated spectra based on a boundary element method solving Maxwell's equations (red).[250]

Table 2.1: experimentally determined and calculated resonance wavelengths for gold nanoparticles (60 nm) monomer, dimer and trimer as shown in Figure 2.9.

	Monomer	Dimer	Trimer
$\lambda_{max,1}$ (exp, calc) (nm)	540, 541	541, 544	542, 551
$\lambda_{max,2}$ (exp, calc) (nm)	-,-	693,691	669, 678

While the spectrum of a monomer shows only a peak at one resonance wavelength, spectra of dimers and trimers show two peaks. One peak lies at a shorter wavelength at approximately the position of a nanoparticle monomer and a second, more intense peak appears at longer wavelengths. The plasmon resonance of all three structures was also calculated using a boundary element method[250] to solve Maxwell's

equations. The nanoparticles were assumed as spherical particles with a diameter of 60 nm and an interparticle separation of 1 nm based on the linker molecule length. It was also taken into consideration that due to the nature of the darkfield condenser, incident light does not hit the particles at 90° but at an angle of 27° to the substrate. The calculated scattering spectra are plotted in red with the experimental data in Figure 2.9 and match the experimental data well.

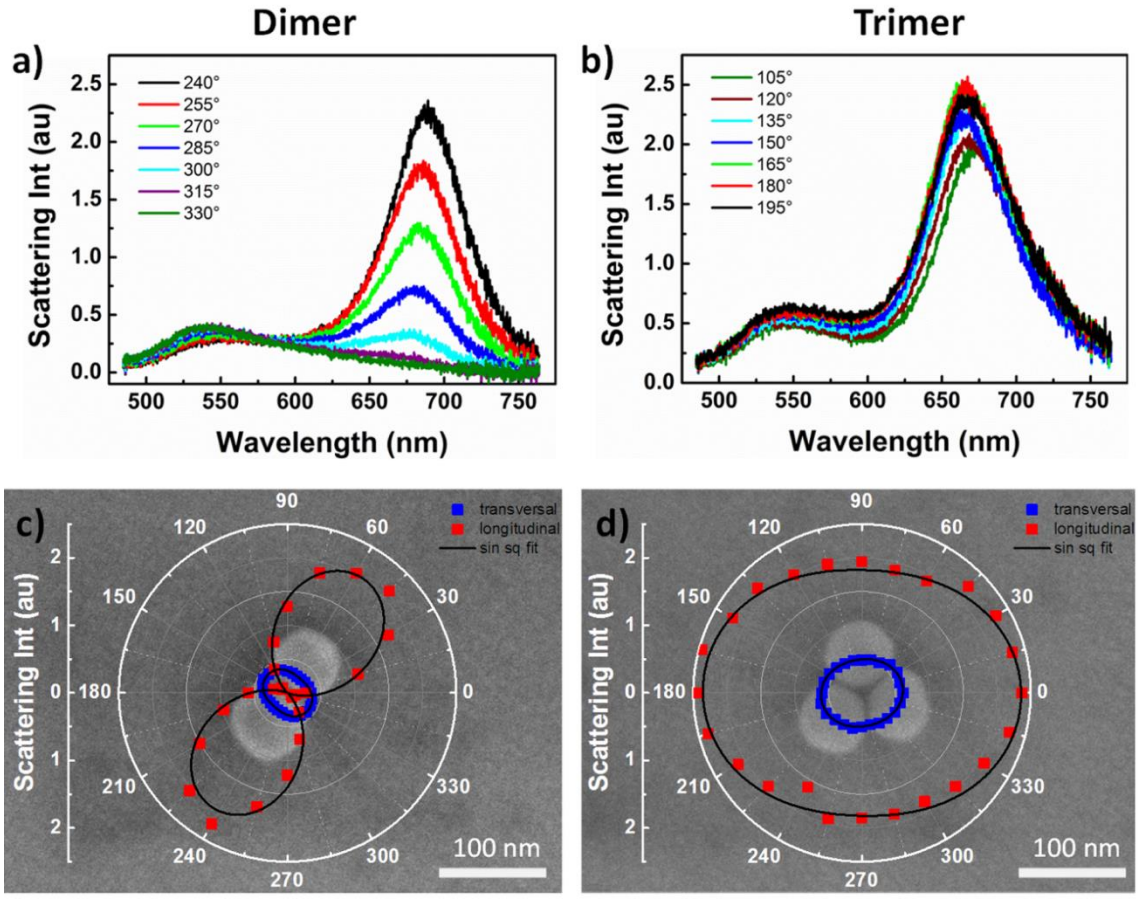


Figure 2.10: a) and b) Polarisation resolved scattering spectra of a 60 nm gold nanoparticle dimer and trimer. c) and d) SEM images of the analysed nanoparticle dimer and trimer overlaid with the transversal and longitudinal peak plasmon intensity in dependence of the polariser angle.

For a polarisation resolved analysis of the scattered light by the nanoparticle clusters a polariser was inserted in the collection path of the microscope setup. Recorded spectra are presented in Figure 2.10a and b. For the dimer the peak at 541 nm shows barely a change in intensity with a change of the polariser angle, while the peak at 693 nm shows a dramatic change in intensity. Comparing the intensity of the scattered light with the orientation of the polariser with respect to the dimer, as shown in Figure

2.10c, this resonance wavelength at 693 nm can be attributed to a plasmon mode along the longitudinal axis of the dimer. The plasmon peak at 541 nm is attributed to a plasmon mode along the transversal axis of the dimer. This behaviour is not observed for the nanoparticle trimers, the peak intensity vs. polariser angle plot shows much less anisotropy. In fact, the spectra of a perfectly symmetrical trimer would not show any anisotropy and the anisotropy recorded here can be attributed to slight imperfections in the symmetry of the studied trimer. This fact is supported by calculated polarisation resolved scattering spectra of the analysed nanoparticle structures shown in Figure 2.11.

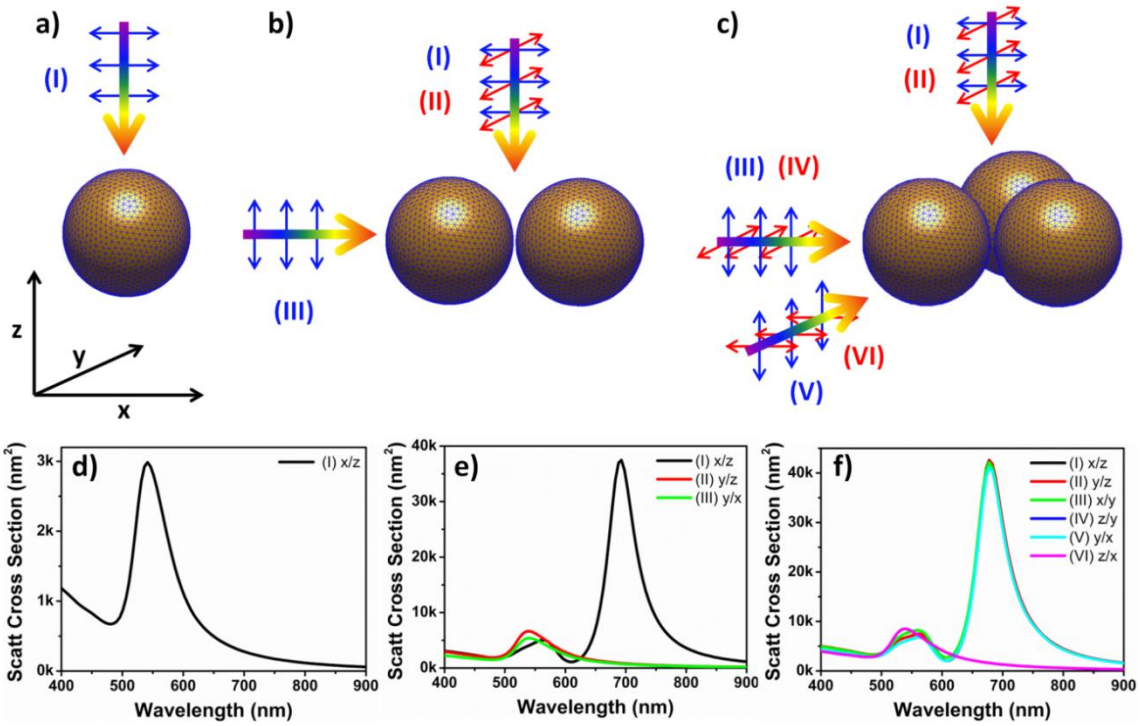


Figure 2.11: Schematic of a discretised 60 nm gold nanoparticle monomer (a), dimer (b) and trimer (c) with the considered incident light propagation directions (rainbow coloured arrow) and polarisation directions (blue and red double arrows) dependent on the nanostructure symmetry. Calculated scattering spectra for 60 nm gold nanoparticle monomers (d), dimers (e) and trimers (f) for the in panel a)-c) indicated incident light conditions (notation : pol/dir).

For perfectly symmetrical monomers only one light propagation and polarisation direction (I) has to be considered and the calculated scattering spectrum shows one plasmon peak at 541 nm. For a dimer the scattering spectrum was calculated for light incident perpendicular to the dimer long axis with polarisations parallel (I) or perpendicular (II) to the dimer long axis. Additionally, due to the illumination geometry

of the darkfield condenser a contribution of out-of-plane plasmon excitation is expected and the scattering spectrum was calculated for light incident parallel to the long dimer axis (III). In condition (I) the spectrum is dominated by a plasmon peak at 691 nm, indicating strong coupling of the dipoles induced in the nanoparticles along the dimer long axis. In contrast, when the plasmon modes are excited perpendicular to the dimer long axis or out-of-plane, the spectra show only one plasmon peak centred at 539 nm. This peak position is only slightly blue shifted from the plasmon peak of a single nanoparticle at 541 nm and indicates very weak, or no coupling of the individual nanoparticle plasmons. Comparing these calculated spectra with the experimentally recorded spectra in Figure 2.10 shows good agreement. The recorded spectra at any angle are linear combinations of the calculated plasmon modes. For the more complex structure of the nanoparticle trimer all possible incident light propagation and polarisation directions were considered and the corresponding scattering spectra were calculated. For perpendicular incident light (I) and (II) identical scattering spectra were calculated with peaks at 678 nm and 562 nm, indicating strong plasmon coupling irrespective of polarisation direction. For incident light conditions (III) and (V) nearly identical scattering spectra to (I) and (II) were calculated, also resulting from plasmon coupling. Only out-of-plane excitation (IV) and (VI) results in single peak scattering spectra (539 nm), showing very weak plasmon coupling. Again, as for the nanoparticle dimer, the calculated scattering spectra agree well with the experimental data obtained for the trimer in Figure 2.10, which can be considered as linear combinations of the calculated plasmon modes.

While for the nanoparticle dimer the two different plasmon modes can be understood as longitudinal and transversal plasmon modes, the case of a trimer is more complex. However, the plasmon hybridisation method developed by Nordlander et al. can provide an explanation for the polarisation independent plasmon resonance.[84] Analogous to molecule orbital hybridisation in molecular orbital theory, the plasmons of complex nanostructures can be described as the interaction of the plasmon resonances of the elements that make up the complex nanostructure. In the case of a nanoparticle trimer with D_{3h} symmetry, group theory analysis reveals that, independent of the polarisation of perpendicular incident light, two pairs of

degenerate bonding and anti-bonding dipolar plasmon modes are excited with each having the same dipole moment in either planar direction. The bonding modes have a lower, the anti-bonding modes a higher energy, thus the corresponding plasmon bands are located at a longer and shorter wavelength respectively, that are both visible at any given polarisation angle.[80]

2.3.3. Optical Characterisation of Single Gold Nanorods

Alongside nanoparticles, nanorods are of great interest as they show a narrow plasmon peak and their resonance wavelength can be tuned by controlling the size and aspect ratio of the nanorod.

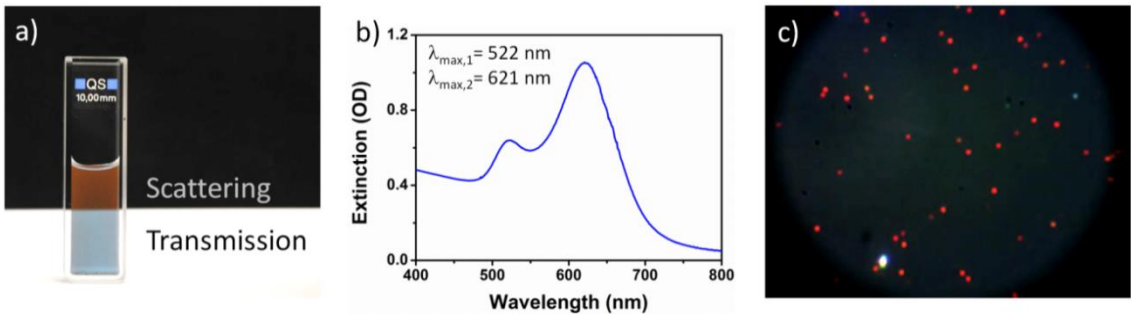


Figure 2.12: a) Gold nanorod colloidal solution in front of mixed background showing the difference between light scattered by and transmitted through the solution. b) UV-Vis extinction spectrum of gold nanorod colloidal solution. c) Darkfield scattering image of gold nanorods deposited from solution on glass substrate.

A vial with a typical colloidal solution of gold nanorods with an average size of 21 x 61 nm is shown in Figure 2.12a, displaying a blue colour in transmission and a red colour in scattering conditions. The corresponding UV-Vis extinction spectrum of the solution is shown in Figure 2.12b. The UV-Vis spectrum of nanorods exhibits two extinction bands that are associated with a longitudinal plasmon mode along the long axis of the nanorods at a longer wavelength (621 nm) and a transversal plasmon mode along the short axis of the nanorods at a shorter wavelength (522 nm). The darkfield micrograph in Figure 2.12c shows gold nanorods as red scattering dots of various shades.

A detailed characterisation of single gold nanorods was performed via correlated darkfield spectroscopy and SEM imaging. Figure 2.13a shows a variety of shapes found in a chemically synthesised batch of gold nanorods with corresponding darkfield images and spectra in Figure 2.13b. Encountered shapes range from small cubes scattering green light from 556 nm to 566 nm, over a square bipyramid scattering at

580 nm and irregular shapes scattering from 582 nm to 589 nm to nanorods of various aspect ratios scattering from 598 nm (AR 1.6) to 665 nm (AR 2.5).

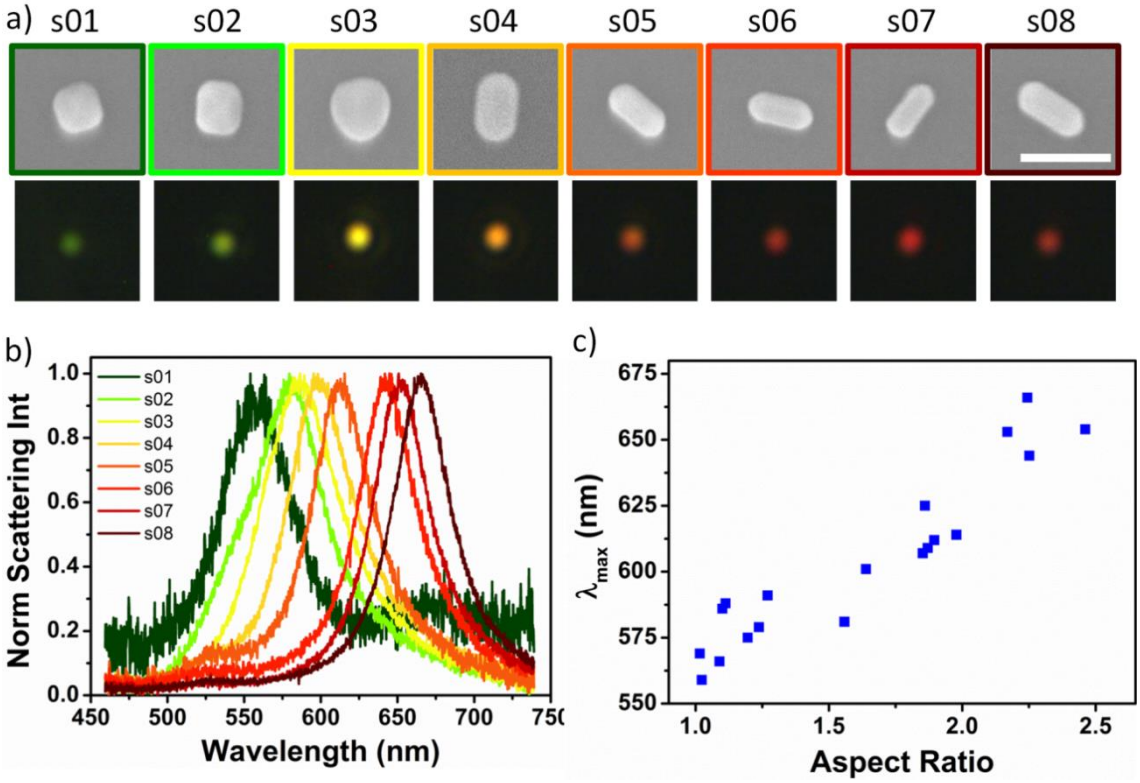


Figure 2.13: a) and b) Correlated dark field scattering images and spectra with SEM images of various shapes found in a batch of gold nanorod colloidal solution (scale bar SEM images: 100 nm). c) Relation between nanorod aspect ratio and its peak plasmon resonance wavelength

Compared to the UV-Vis spectrum, where two extinction peaks are visible, the darkfield scattering spectra show only one peak at longer wavelengths. This is caused by the fact that the scattering intensity of a plasmonic nanostructure is dependent on its dimensions. The scattering cross section of a nanorod approximated by an ellipsoid, as described by equation (1.8), is a sum over the scattering cross sections for the three main axes of the ellipsoid. For the nanorods investigated here, the long axis of the nanorods is of sufficient length for scattered light to be measured. The short axes of the nanorods are too short for efficient light scattering. Consequently the scattering spectrum recorded is dominated by only one, the longitudinal, plasmon peak. Scattering spectra of single nanorods were acquired with peak positions (λ_{max}) ranging from 630 nm to 738 nm. Figure 2.13b and c show how the peak position is shifting linearly with the aspect ratio of the nanorods.

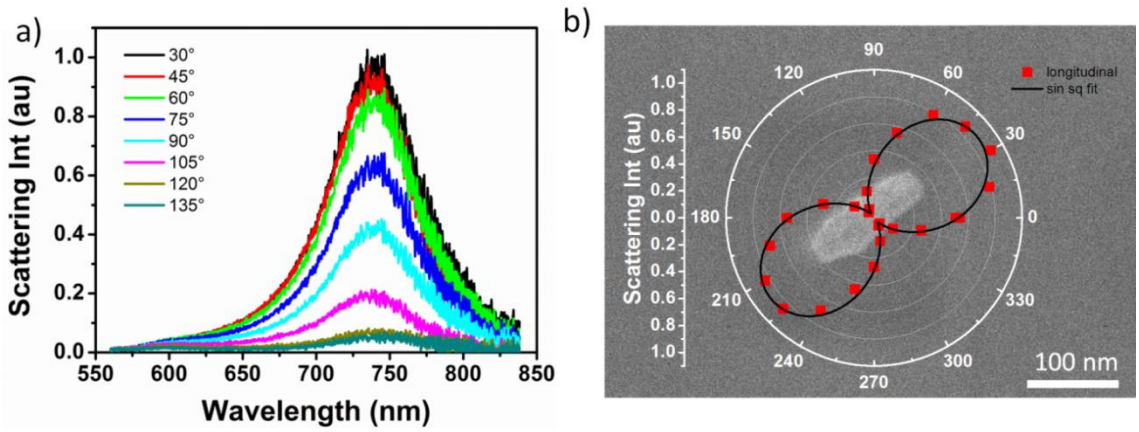


Figure 2.14: a) Polarisation resolved scattering spectra of a gold nanorod. b) SEM image of the analysed nanorod overlaid with the longitudinal peak plasmon intensity in dependence of the polariser angle.

The scattering spectrum of a single nanorod was further characterised by inserting a polariser in the collection path of the microscope setup. The obtained spectra are shown in Figure 2.14a. The scattering intensity reached a maximum value when the polariser was aligned along the longitudinal axis of the nanorod and dropped to zero when the polariser was aligned perpendicular to the longitudinal axis of the nanorod. It is possible to fit the light intensity at 739 nm in dependence of the polariser angle with a $\cos^2$ function (see Figure 2.14b). This demonstrates that all light scattered at 739 nm was polarised along the longitudinal axis of the nanorod as a result of a plasmon resonance mode that was excited in that direction.

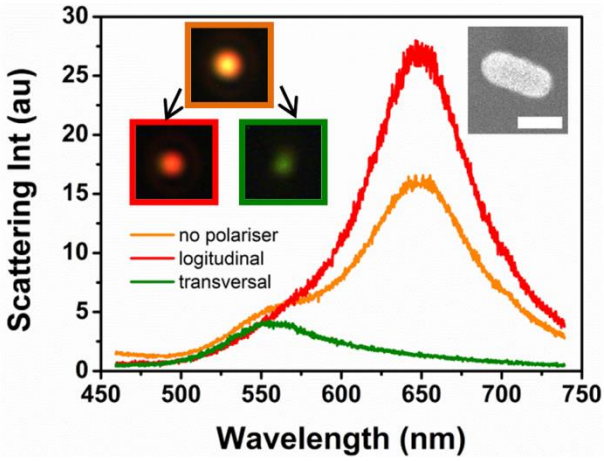


Figure 2.15: Darkfield images and spectra of a 39 x 78 nm nanorod without polariser (orange spectrum and image) and with polariser aligned with the long (red spectrum and image) and short (green spectrum and image) axis of the nanorod. Inset: SEM image of analysed nanorod, scale bar: 50 nm.

Likewise, a plasmon resonance mode is excited along the transversal axis of the nanorod. For this particular nanorod, however, this mode is not visible in light scattering. As previously discussed, the transversal cross section is too small to efficiently scatter the light and the plasmon mode is only visible in absorbance. For nanorods with larger diameters, however, the transversal plasmon mode can also be visible in light scattering. In both, the darkfield images and spectra of a large nanorod in Figure 2.15 the longitudinal and the transversal plasmon mode can be clearly seen and distinguished when light is selectively collected using a polariser aligned with the long or short axis of the nanorod respectively.

2.3.4. Optical Characterisation and Application of Gold Nanorod Arrays

The optical anisotropy of single gold nanorods observed in the previous section also becomes noticeable when nanorods are assembled close to each other and their plasmon modes couple. In particular, this section concerns the study of the plasmon resonance of large area ordered gold nanorod arrays. This is important for possible application of these arrays in techniques like surface enhanced Raman and fluorescence spectroscopy, where the signal amplification is related to the extent of plasmon coupling in the array.

Arrays with Nanorods Aligned Parallel to the Substrate

Highly ordered gold nanorod arrays were fabricated by a method combining droplet evaporation and stamping. The nanorods used to fabricate these arrays were seed-mediated synthesised resulting in nanorod dimensions of 13 x 44 nm (aspect ratio 3.4). UV-Vis spectroscopy of the solution in water showed a transversal extinction peaks at 517 and a longitudinal extinction peak at 737 nm.

The optical properties of these gold nanorod arrays were studied with correlated optical transmission microscopy and spectroscopy and SEM imaging. While areas covered with nanorods look uniformly light green without polariser (Figure 2.16a), after inserting a polariser in excitation different domains can be distinguished that gradually change their colour from light to dark green dependent on the polariser angle (Figure 2.16b, c). The optical images were taken with a polariser in excitation at 30° and 120° where the maximum contrast for the two indicated areas occurred. SEM

imaging (insets Figure 2.16a) reveals that the domains showing opposite colours in the images recorded with polariser consist of highly ordered parallel aligned nanorods with 90° rotated orientation and that the domains appear dark green under polarised excitation perpendicular to the long axis of the nanorods and light green under polarised excitation parallel to the nanorod long axis.

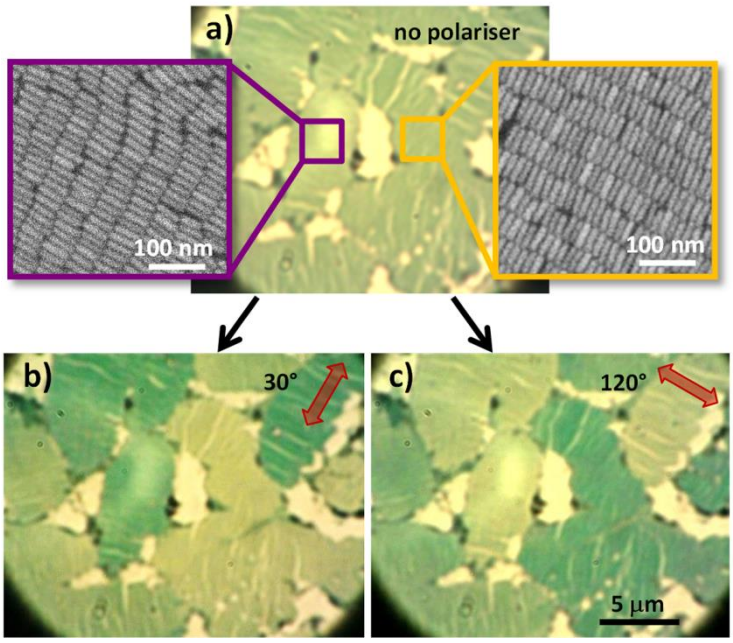


Figure 2.16: a) Transmission image of gold nanorod domains recorded without polariser. Insets: correlated SEM images of the nanorod arrays in the indicated areas showing highly ordered gold nanorod arrays with a difference in orientation of 90°. b),c) Transmission images of the same nanorod arrays recorded with a polariser in excitation at 30° and 120° showing light green to dark green colour shades of nanorod domains dependent on nanorod orientation with respect to the polarisation axis of the polariser.

Extinction spectra from the areas marked purple and yellow in Figure 2.16 were acquired to study this polarisation dependence further. Figure 2.17a shows the extinction spectra taken of the yellow marked area with a polariser inserted in excitation with the polarisation axis aligned parallel and perpendicular to the long axis of the nanorods as well as a spectrum of the same area when no polariser is inserted. The spectrum recorded with un-polarised light is characterised by a broad resonance peak with a maximum at 650 nm and a shoulder at higher wavelengths. The spectrum acquired with polarised light parallel to the direction of the nanorods' long axes (30°, green curve) shows a broad peak at 720 nm. The spectrum acquired with polarised light perpendicular to the direction of the nanorod long axes (120°, blue curve) shows a peak centred at 641 nm. Both peak positions are shifted compared to peaks

observed in UV-Vis. While the longitudinal peak is slightly blue shifted, the transversal peak is strongly red shifted indicating strong plasmon coupling in this direction between the nanorods in the array. Both spectra could be fitted with a single Lorentzian function, showing only contribution of one plasmon mode that was selectively collected: for the 30° spectrum the longitudinal and for the 120° spectrum the transversal plasmon mode of the nanorod array respectively.

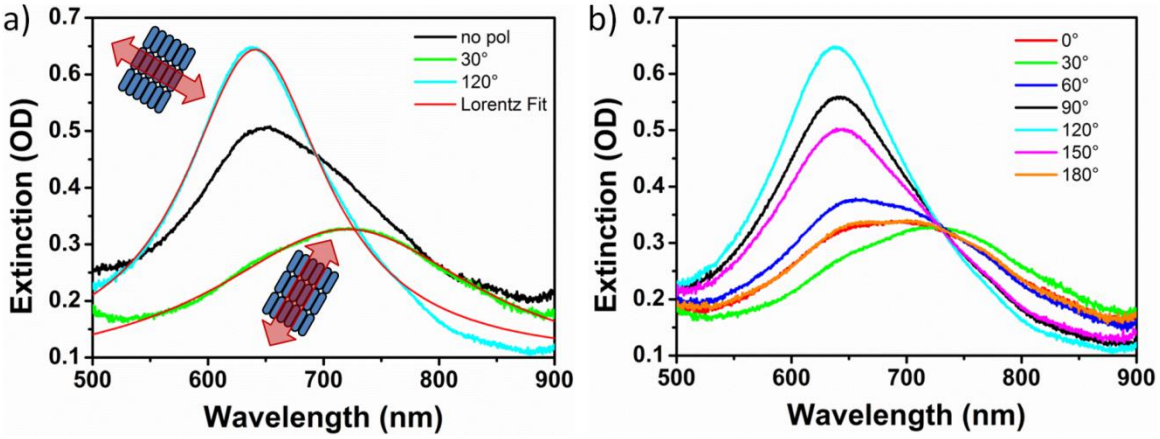


Figure 2.17: a) Extinction spectra of the yellow marked area in Figure 2.16 without polariser and with polariser in excitation aligned with the long (30°) or short (120°) axis of the nanorods. Red lines are Lorentzian fits to the data. b) Polarisation resolved extinction spectra obtained from the yellow marked area in Figure 2.16 for various polariser angles between 0° and 180°.

Complementary to Figure 2.17a, Figure 2.17b shows a set of extinction spectra at polariser angles from 0° to 180° in 30° steps. While the spectra at 30° and 120° show only contribution from a single plasmon mode, the spectra measured between 30° and 120° show contributions from both transversal and longitudinal modes. As the angle increases from 30° to 120°, the contribution from the longitudinal plasmon mode decreases as the contribution from the transversal plasmon mode increases, creating a single isosbestic point at 726 nm.

Describing the spectra mathematically, the extreme spectra obtained at 30° and 120° polariser angle can be fitted with a single Lorentzian function each, $Lorentz_{30}$ and $Lorentz_{120}$ (shown in Figure 2.17a). The extinction spectra taken at any polariser angle can be described as a function of those two fitting functions with the weighing parameters *a* and *b* as described in equation 2.4.

$$y = a \cdot Lorentz_{30} + b \cdot Lorentz_{120} \qquad (2.4)$$

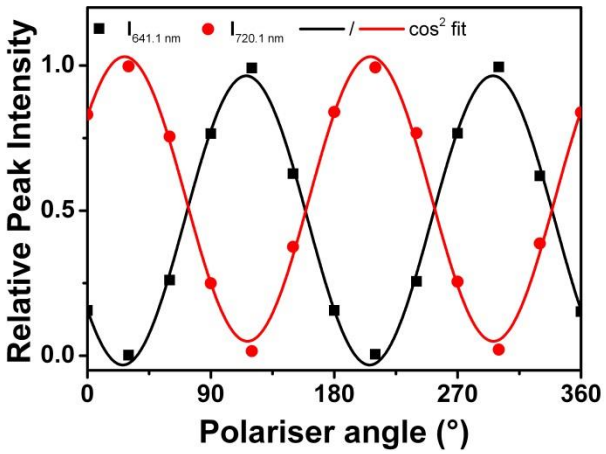


Figure 2.18: Relative contributions of the transversal (black) and longitudinal (red) plasmon modes to the extincion spectra at any given polariser angle with least-squares $\cos^2 \theta$ fit.

With equation 2.4 it is possible to calculate how much each of the functions $Lorentz_{30}$ and $Lorentz_{120}$ are contributing to each spectrum, represented by parameters *a* and *b*. Figure 2.18 shows the plot of these parameter in dependence of the polariser angle. The obtained values for *a* and *b* can be fitted in turn with $\cos^2$ functions. This confirms what was observed visually from the extinction spectra: the plasmon resonance of a highly ordered gold nanorod array consists of two independent plasmon modes of 90° rotated orientation. These can be selectively excited and are assigned to coupled plasmon resonances along the longitudinal and transversal axes of the nanorods forming the array.

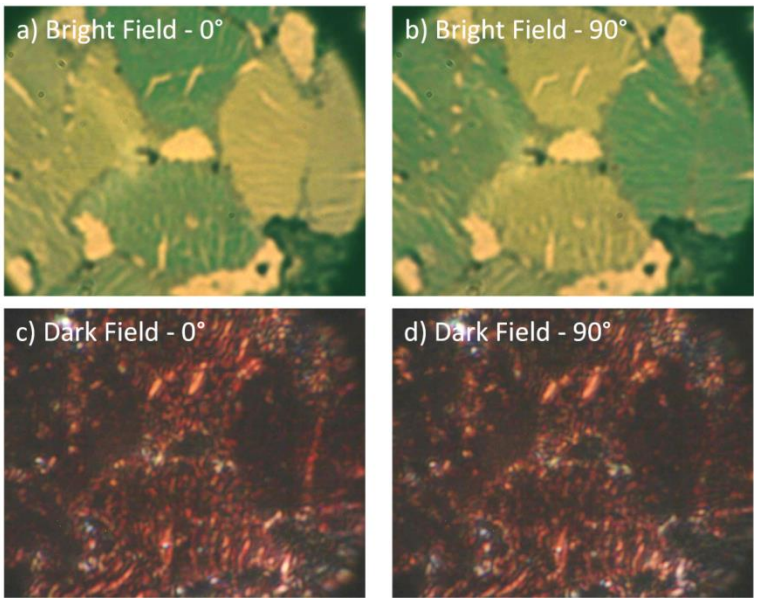


Figure 2.19: Bright field (a, b) and darkfield (c, d) images of the same highly ordered gold nanorod domains recorded with a polariser in excitation at 0° (a, c) and 90° (b, d).

In addition to the previous brightfield transmission microscopy, darkfield microscopy was performed on the nanorod arrays. For direct comparison of the techniques Figure 2.19 shows images of the same area recorded under different conditions. Figure 2.19a and b show ordered nanorod domains at 90° rotated polarised bright field excitation, displaying the same behaviour as was discussed for Figure 2.16. Figure 2.19c and d show the same area at 90° rotated polarised darkfield excitation. The selective excitation of the longitudinal and transversal plasmon mode is clearer in the bright field than in the darkfield images, as the variance in scattered light wavelength with incident light polarisation is difficult to distinguish by eye at these long wavelengths. What is remarkable, however, is, that in darkfield illumination the plasmon coupling and the delocalisation of the plasmon over a nanorod domain becomes clearly visible. Areas where the nanorods are very densely packed appear almost black in darkfield. Here the incident light is absorbed, but not scattered. Contrary, cracks within the domains are the most visible features where the light is scattered. This is due to the fact that in very densely packed nanostructures scattering is supressed while the fields are highly localised in the gaps between the particles and is an indication of ability of these structures to support travelling polarisation waves acting as waveguides with high field-confinement.[58]

Further investigations by correlated polarised optical microscopy and electron microscopy revealed the dependence of the nanorod arrays' plasmon resonance modes on the nanorod packing density. Small changes in the arrangement of nanorods within a domain resulted in large changes of the domain's optical features. A colour transition from red to pale green was observed in domains where nanorods were only loosely packed into side-by-side configuration, see Figure 2.20. A corresponding transition from 735 nm to 580 nm was observed in the spectra recorded under polarised light oriented parallel and perpendicular to the nanorod long axes, respectively. The packing density is expected to have a large effect on the collective plasmon resonance of a nanorod array. It was previously shown on simpler structures that the extent of coupling between plasmonic structures is extremely sensitive to interparticle separation.[77] It is an interesting feature of the nanorod arrays,

however, it has to be added that for the moment control over the packing density of nanorods in the 2-dimensional ordered arrays is limited.

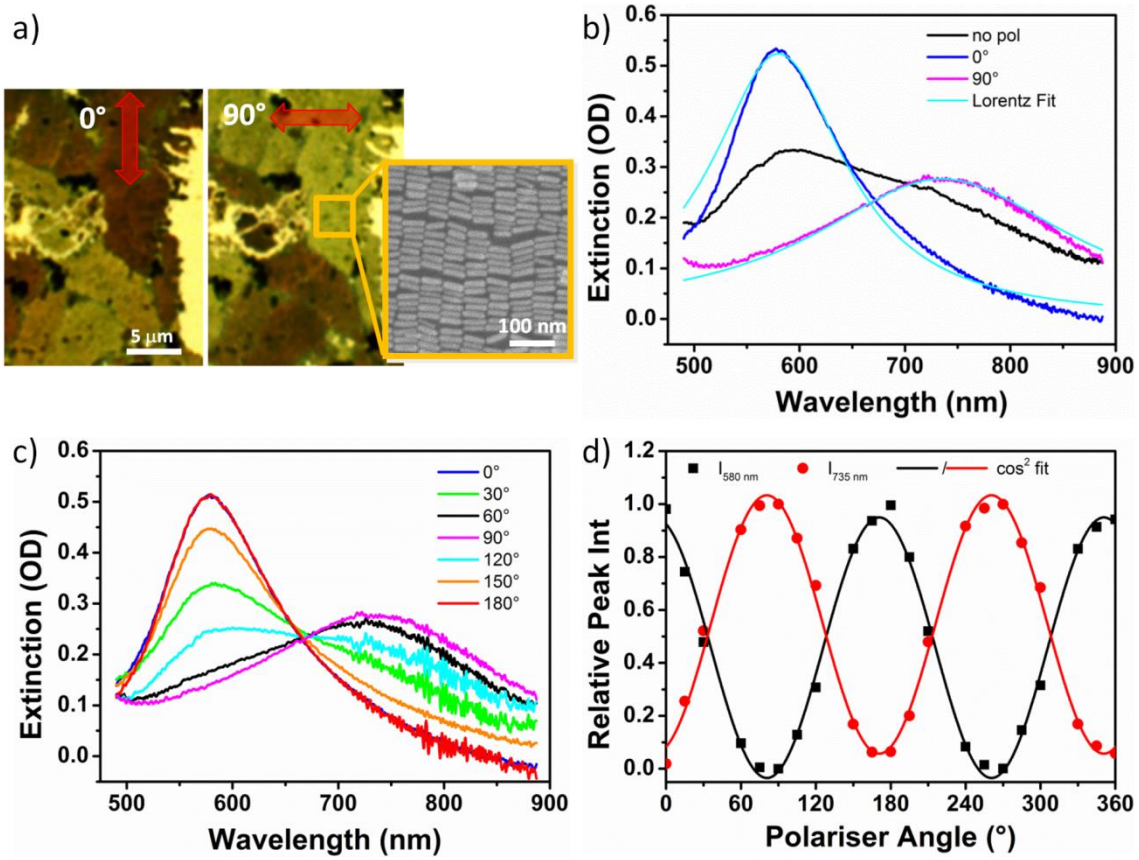


Figure 2.20: a) Polarised transmission images of gold nanorod domains with a polariser in excitation at two different angles with 90° difference showing green to red colour transition associated to the relative orientation of polarised light with the long axes of nanorods that form the domains. Yellow box: close up SEM images of the indicated area showing highly ordered gold nanorod arrays loosely packed. b) Extinction spectra of the yellow marked area without polariser and with polariser in excitation aligned with the short (0°) or long (90°) axis of the nanorods with Lorentzian fits. c) Polarisation resolved extinction spectra obtained from the yellow marked area for various polariser angles between 0° and 180°. d) Relative contributions of the transversal (black) and longitudinal (red) plasmon modes to the extincion spectra at any given polariser angle, fitted by a $\cos^2$ function.

Parallel Nanorod Arrays for Anti-Counterfeit Tags

The organisation of gold nanorods into domains and the arrangement of domains is determined by the balance of Van der Waals forces, capillary forces, surface tension and others operating during the evaporation process. Consequently, the droplet evaporation and stamping method allows control on domain size and side-to-side alignment of the nanorods but does not allow control on the final orientation of domains, or nanorod packing density. This feature was applied to the development of

a novel class of unique plasmonic identifiers. Figure 2.21a-c show polarised optical images of domains stamped on glass coverslips in areas of 900 μm^2, defined by focused ion beam (FIB) milled marks. Due to the high degree of internal order each domain was characterised by a distinct colour. In addition, due to the random orientation of domains, each image displayed a unique distribution of colour intensity patterns. To express this uniqueness numerically, optical images a-c were analysed with common image analysis software (Image J). Each image was split into its individual RGB colour channels from which in turn intensity histograms were extracted. The unique domain pattern (and colouring) resulted in distinctive histograms for each image, as shown in Figure 2.21d. The histograms of the green values were chosen since they showed the highest degree of diversity.

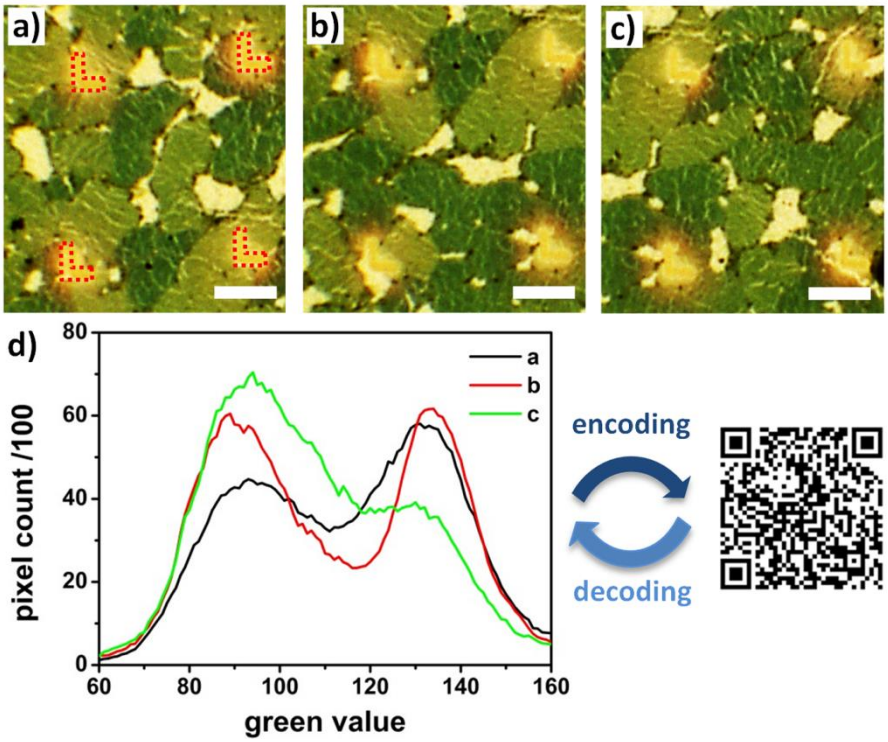


Figure 2.21: a-c) Polarised light transmission images of gold nanorod domains with 30 × 30 μm areas defined by FIB milled alignment marks highlighted in (a) (scale bars 10 μm); d) Green value histograms calculated from images (a)-(c) by image J software. The displayed QR code contains the information of histogram a.

By converting intensity coordinates into text strings unique QR codes were created for each optical image. As an example, the QR code displayed in Figure 2.21d corresponds to the area framed in figure a. As a verification tool, when this QR code was scanned by a QR code reading system, it generated the original text string which in turn could

be converted into the original histogram by a MATLAB code containing the decoding information (for MATLAB code see Appendix B). Based on these findings, the formation of unique patterns that can be incorporated on transparent substrates could constitute the basis for a novel plasmonic encoding system for anti-counterfeit applications.

In our proposed concept FIB milled alignment marks ensured that histograms could be repeatedly taken from precisely the same area on a tag. An additional level of complexity to the encryption could be added by using larger areas containing multiple frames. This way the encoded data could be a mathematical function of the histograms of specific squares. Implementing these substrates as anti-counterfeit tags would require a calibrated reader to ensure a reproducible optical read out of the tags. However, the data shown here serves as prove of concept for this application.

Arrays with Nanorods Aligned Perpendicular to the Substrate

Slightly bigger overgrown nanorods with dimensions 22 x 54 nm were assembled into arrays of nanorods standing perpendicular to the substrate in a hexagonal symmetry. Correlated optical and electron microscopy images of these arrays can be seen in Figure 2.22a.

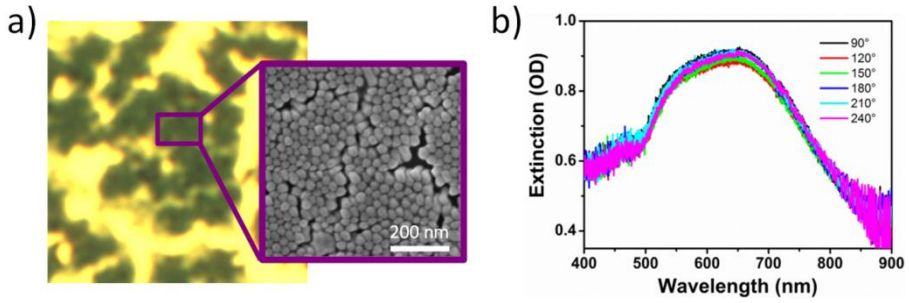


Figure 2.22: a) Transmission image of gold nanorod domains showing dark green colour where the nanorods are aligned perpendicular to the substrate and light green colour where the nanorods are lying parallel to the substrate. b) Polarisation resolved extinction spectra obtained from the purple marked area for various polariser angles between 0° and 360° showing no polarisation dependence of the extinction spectrum.

Figure 2.22b shows the extinction spectra obtained with a polariser in collection. No polarisation dependence of the extinction spectrum can be observed. This can be explained with the isotropic in-plane symmetry of the nanorods themselves and the assembly thereof in the plane of the substrate. In this case only coupling of the transversal plasmon modes of the nanorods is observed, leading to one broad peak in

the extinction spectrum at 646 nm. This large shift from the transversal plasmon peak of the nanorods in solution at 517 nm indicates very strong coupling between the transversal plasmon modes of the assembled nanorods, which is expected from very densely packed nanorods as seen in Figure 2.22a. No coupling in the longitudinal direction is taking place, but a shoulder in the extinction spectrum suggests a contribution of the longitudinal plasmon mode nevertheless.

2.4. Summary and Conclusions

The study of the optical properties of various nanoparticles, nanorods and assemblies thereof as potential platforms or building blocks for enhanced metal ion detection is a crucial step towards their use in sensing applications.

Correlated darkfield spectroscopy and SEM imaging of 60 nm gold and silver nanoparticles showed the dependence of the optical signature of a nanoparticle on its shape and composition. The lower the symmetry of a nanoparticle, the more was the red shift of its plasmon resonance. The tunability of a nanoparticle's plasmon resonance is a useful feature and allows matching of a nanoparticle's properties to requirements depending on an application. Silver nanoparticles showed to be more efficient scatterers than gold nanoparticles of the same size. However, the oxidation of silver nanoparticles in atmosphere makes their application more challenging.

Measurements performed in media with different refractive indices demonstrated that a higher refractive index of the medium leads to a red shift of the plasmon resonance and that nanospheres are less sensitive to these changes than nanohexagons or nanotriangles. The nanoparticles' LSPR sensitivity to the local dielectric environment is in itself useful for sensing applications, however, it can also be used to monitor the attachment of molecules to nanoparticles in the fabrication of more complex structures.

The plasmon resonance of a single gold nanorod was shown to vary with its aspect ratio and the light scattered by a nanorod to be polarised in the orientation of its axes. A narrow FWHM of a nanorod's scattering spectrum, where changes can be easily detected and the tunability of the maximum scattering wavelength over a large range make gold nanorods very promising candidates for sensing applications.

The study of chemically linked dimers and trimers of 60 nm gold nanoparticles showed that plasmon coupling between particles in close proximity leads to new features in the plasmon resonance. Different peaks in the scattering spectra could be attributed to different plasmon modes occurring in the structures. Based on the symmetry of the structures, the scattering spectrum of a dimer has a pronounced polarised character,

while the spectrum of a trimer was shown to be independent of incident light polarisation. The plasmon coupling in nanoparticle clusters and the inherently formed hot spots between nanoparticles make these structures interesting for sensing applications with surface enhanced fluorescence or Raman spectroscopy

Correlated transmission spectroscopy and SEM imaging of large area nanorod arrays showed the influence of large area plasmon coupling on the optical signature of the structure. Due to the symmetry of the arrays, nanorods aligned parallel to the substrate show highly polarised extinction behaviour and nanorods aligned perpendicular don't. Low fabrication costs and a high number of hot spots in large area nanorod arrays make them very suitable platforms for surface enhanced fluorescence or Raman spectroscopy. The enhancement factor is dependent on the strength of the electrical field, which in turn is correlated with the extent of plasmon coupling. Therefore it is desirable to know how to induce the strongest possible plasmon coupling in the arrays. As determined in the experiments described above, the intensity of plasmon coupling is dependent on the polarisation of the excitation beam in relation to the symmetry of the array. This is important in the case of the techniques mentioned above where mostly lasers emitting polarised light are used as excitation sources.

Chapter 3 - Gold Nanoparticle Based Hybrid Structures for Mercury Detection

In this chapter a strategy for mercury detection was explored using plasmon resonance energy transfer (PRET) upon Hg^{2+} binding to immobilised gold nanoparticle-organic ligand hybrid structures. The chapter covers the fabrication and characterisation of an initial hybrid structure, the improvement of the hybrid structure and the mercury sensing assessment of both structures.

3.1. Introduction

Mercury is a highly toxic heavy metal that is widely dispersed in the environment and can be found in water, air and soil. Mercury is not biodegradable and remains in ecological systems and in the food chain indefinitely, exposing top-level predators and humans potentially to very high levels of the toxin.[1, 253, 254] Upon extended exposures to mercury (for example from water or contaminated food) humans can be severely harmed and suffer from brain, heart, kidney, lung and immune system damage.[255, 256] For this reason large efforts have been devoted to the development of strategies for trace detection of mercury in the environment. The WHO guidelines for drinking-water quality state a guideline value for inorganic mercury content in drinking water of 6μg/l, equivalent to a 30 nM solution [6]. Accurate and precise techniques exist for trace mercury analysis (down to nM and pM range) such as Cold Vapour Inductively Coupled Plasma Mass spectrometry (CV-ICP-MS),[10] Atomic Fluorescence Spectrometry (AFS),[12] Inductively Coupled Plasma Atomic Emission Spectroscopy (ICP-AES)][15] and reversed-phase High Performance Liquid Chromatography (HPLC).[257] In spite of their excellent sensitivity these techniques are costly, time consuming (requiring pre-concentration steps), non-portable and solution-based. Therefore, there is a growing interest for development of alternative simpler and lower cost approaches for on-site analysis extending current applicability and leading to novel miniaturised sensing solutions.

Noble metal nanoparticles have been proven particularly suitable for detection of mercury due to their sensitive optical response arising from localised surface plasmon resonance (LSPR). Plasmonic nanoparticles have been successfully used for label-free detection of mercury based on colourimetric (mercury-induced aggregation) response in solution.[174, 258] Sensitivities down to the μM range could be achieved with this method. Additionally, the versatile surface chemistry of plasmonic nanoparticles allows chemical modification with a large range of organic and bio molecules leading to specific interactions with mercury that can enhance the selectivity and sensitivity of nanoparticle based detection methods.[19, 22]

A challenge inherent to the use of nanoparticles in solution is to maintain colloidal stability and prevent aggregation by other triggers like salts altering the ionic strength of the solution and change of pH. Additionally, a liquid sensing platform is less practical to handle in an application, which makes sensing platforms on substrates desirable. Examples thereof are lateral flow test strips [184, 185] and other paper based devices [186, 187].

For this PhD project within the scope of the FP7 project Hysens, hybrid assemblies composed of inorganic nanoparticles and organic ligands were designed for the purpose of detecting Hg^{2+} ions in water based on plasmonic resonance energy transfer (PRET). PRET was first reported by Lee et al. who utilised it for the detection of Cu^{2+} ions in water.[145] PRET can take place when the extinction band of an organic ligand overlaps with the plasmon band of the nanoparticles. In this case transfer of the Rayleigh scattering energy from the particle to the ligand can take place, which leads to a decrease of the nanoparticle's scattering intensity. Consequently, a ligand can either be chosen for the extinction band of the ligand or of the metal-ligand complex to overlap with the plasmon band of the nanoparticle, resulting in either an off-on or on-off detection mechanism.

The structure of the assembly envisaged for this project and the sensing principle is displayed schematically in Figure 3.1.

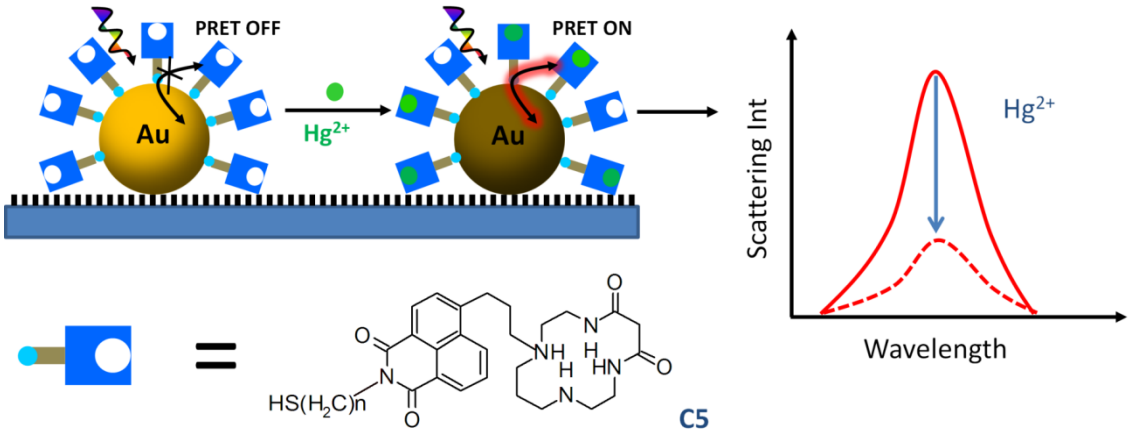


Figure 3.1: Structure of a hybrid assembly consisting of a noble metal nanoparticle functionalised with organic ligands immobilised on a glass substrate. The sensing method is based on detection of a change of scattering intensity of the nanoparticles upon binding of the organic ligand with the target analyte.

Gold nanoparticles are immobilised on a silanised glass substrate and functionalised with an organic ligand C5 capable of forming a complex with the target analyte ions Hg^{2+}. The organic ligand was chosen for the extinction band of the metal-ligand complex and the plasmon band of the nanoparticle to overlap upon binding of the Hg^{2+} ions to the C5 molecules. Thus, in the case of Hg^{2+} binding to the C5 ligands, PRET will lead to a detectable decrease of the scattering intensity of the nanoparticles, which can be observed using darkfield spectroscopy.

This chapter covers fabrication and assessment of the described hybrid structures for Hg^{2+} ion detection. Initial work was dedicated to the fabrication of the designed hybrid assemblies, which consisted of the functionalisation of gold nanoparticles with C5 molecules and the immobilisation of these hybrid structures on glass substrates (Section 3.3.1). These fabricated hybrid structures were characterised with various methods and assessed for their Hg^{2+} detection capabilities (Section 3.3.2). Following on from these results, improved hybrid structures were developed (Section 3.3.3) and assessed (Section 3.3.4).

3.2. Experimental Methods

3.2.1. Hybrid Nanostructure Fabrication

Dicing of Glass Substrates

Glass cover slips were diced into 5 x 5 mm squares with a Disco DAD 3500 dicing saw. During dicing the glass cover slips (gcs) were protected with 1 μm thick soft baked photoresist HiPR6512 to avoid debris deposition on the substrates. Immediately after dicing the photoresist was removed with two 45 minutes baths of resist remover R1165 at 65° C, 10 minutes in deionised water at room temperature and IPA at 60° C before drying the substrates under a flow of nitrogen.

Immobilisation of Nanoparticles on Glass Substrates

Prior to the nanoparticle deposition, the glass substrates were silanised with (3-Aminopropyl)triethoxysilane (APTES) as follows. The diced glass cover slips were cleaned by sonication in acetone followed by deionised water for 10 min, rinsed with deionised water and dried under a stream of nitrogen. For further cleaning and surface activation the substrates were treated with oxygen plasma of 50 W for 5 min immediately before immersion in a 3% APTES:MeOH solution for 30 minutes. To remove excess unbound silane, the substrates were rinsed with methanol and deionised water twice. Finally, the substrates were placed in a fan operated oven at 120 °C for crosslinking of the silane.[259] Nanoparticles from a 4.3 pM gold colloid purchased from BBInternational (60 nm) were deposited by drop deposition. Drops of non-diluted down to 50 x diluted nanoparticle solution were placed for 5-40 minutes on the APTES silanised substrate before wicking the solution, rinsing the substrate with 50 °C deionised water and drying under a flow of nitrogen.

Sample Preparation for Single Nanoparticle Microscopy

To obtain sufficiently spaced nanoparticles for single particle darkfield spectroscopy, nanoparticles from a 4.3 pM gold colloid purchased from BBInternational (60 nm) were deposited by flow deposition on ITO coated glass cover slips with etched alignment marks. Subsequently, the substrates were rinsed with 50 °C deionised water to remove surfactants remaining from the nanoparticle synthesis and blown dry under a stream of nitrogen.

Synthesis of Silver Core - Gold Shell Nanoparticles

To synthesise silver core – gold shell nanoparticles 60 nm silver nanoparticles in solution purchased from BBInternational were used as core material and coated with a thin gold shell by chemical reduction of $HAuCl_4$ with ascorbic acid. 1 ml of silver colloid of 4.32 pM were mixed with 1 ml 34.0 mM sodium citrate tribasic dihydate and 1 ml 0.02M $AuCl_3$ and heated in a reflux system to temperatures between 30 °C and 100 °C. After the reaction mixture had reached the desired temperature 6 µl of 78.8 mM ascorbic acid were injected under vigorous stirring. The reaction mixture was then stirred for further 20 min before cooling down to room temperature for analysis.

Synthesis of Pseudo Silver Core - Gold Shell Nanoparticles

To fabricate pseudo core-shell nanoparticles, first silver nanoparticles were immobilised with APTES on a glass substrate. Substrates with immobilised silver nanoparticles were handled under inert atmosphere at all times to avoid surface oxidation of the nanoparticles. Subsequently a thin film of gold was evaporated by thermal evaporation onto the substrate at $5 \cdot 10^{-5}$ Pa chamber pressure and 2.3 A current through the tungsten boat. At a resulting deposition rate of 0.03 nm/s gold was evaporated until nominal film thicknesses of 4 nm to 10 nm were reached.

Functionalisation of Nanoparticles in Solution

The organic ligand for nanoparticle functionalisation, C5, was synthesised and provided by the Preece Group at University Birmingham (Hysens project partner). To functionalise gold nanoparticles in solution, 1 ml of the as-bought 4.3 pM gold nanoparticle colloid was diluted 3x with a mixture of 0.5 ml deionised water and 1.5 ml ethanol. Then 100 µl 0.25 mM C5:EtOH solution was added to the nanoparticle solution under vigorous stirring. The functionalisation was monitored first every minute then in larger time intervals by UV-Vis spectroscopy.

Functionalisation of Nanoparticles on Substrate

Substrates (ITO or silanised glass) with deposited nanoparticles were functionalised with C5 by immersion of the substrate in 0.25 mM C5:EtOH solution for 24 h; small samples (5 x 5 mm) by immersion, bigger samples (18 x 18 mm) by placing drop on surface and placing substrate in a closed crystallising bath with EtOH soaked tissue to

avoid solvent evaporation. Afterwards the substrates were rinsed with EtOH, sonicated for 5 min in EtOH, and dried under a stream of nitrogen.

3.2.2. Hybrid Nanostructure Characterisation

Darkfield Microscopy and Spectroscopy

Scattering spectra of individual nanoparticles were acquired with an inverted IX-71 Olympus microscope with an oil immersion darkfield condenser (Olympus U-DCW, 1.4 NA) and 100x objective (Olympus MPlanApo 100x/0.95 NA). The sample was illuminated with a 100 W halogen lamp. The light collected by the objective was directed either onto a colour CMOS camera (DCC1645C, ThorLabs) for image acquisition or onto the entrance slit of a monochromator (SP-2356, Acton Research). The light was dispersed by an optical grating (300 grooves/mm, blazed at 500 nm, 350nm < λ < 850nm) and directed onto a thermoelectrically cooled, back illuminated CCD (Spec10:100B, Princeton Instruments) for spectra acquisition. The experiments were performed by first recording an image of the sample with a mirror in the light path of the spectrometer. Once a suitable nanostructure was selected, the mirror was switched to the grating to disperse the scattered light and a spectrum was recorded using an acquisition time of 60 s. Normalised scattering spectra from individual nanoparticles were obtained by subtracting and dividing by a background scattering spectrum taken from a nearby clean area on the sample. To determine the peak scattering wavelength, the spectra were fitted with a Lorentzian function (eq 2.1).

Electron Microscopy

For scanning electron microscopy (SEM) imaging gold nanoparticles were flow deposited (10 x 100 μl) onto n++ doped Si wafer pieces and subsequently rinsed with 40°C deionised water. SEM images of individual gold nanostructures were acquired using a field emission SEM (JSM-6700F, JEOL UK Ltd.), operating at a beam voltage of 10 kV.

SERS

Raman spectra were taken using a Renishaw in Via raman system equipped with a 514 nm, 30 mW Ar ion laser using a 50x, 0.75 NA objective and an integration time of 10 s at 5% laser power.

Fluorescence

Fluorescence imaging and spectroscopy of samples was performed in the same inverted IX-71 Olympus microscope as darkfield analysis. In darkfield mode a suitable location on a sample was selected before switching the illumination to laser excitation in reflection (LDH-P-C-400, PicoQuant). By the fluorophore emitted light was collected with a 100x objective (Olympus MPlanApo 100x/0.95 NA). Using a dichroic mirror (Z405RDC, Chroma Technology) and a 430 nm long pass filter all reflected laser light was removed before the light entered the analysis light path. 80 x 80 μm images were recorded with single photon detectors (SPCM-AQR-14, Perkin Elmer) while the objective was scanned over the sample using a piezo controlled nanopositioning stage (P-733.2CL, Physik Instrumente). Fluorescence spectra were taken by directing the light into the entrance of slit of a monochromator (SP-2356, Acton Research) equipped with a thermoelectrically cooled, back illuminated CCD (Spec10:100B, Princeton Instruments). A grating (300 groves mm^{-1}) dispersed the scattered light and a spectrum was recorded using an acquisition time of 60 s.

3.2.3. Hybrid Nanostructure Mercury Ion Sensing Assessment

Microfluidic Cell

To test the ion detection capability of fabricated samples the substrates were glued into microfluidic cells provided by Hysens partner Mildendo. The borders of the substrate as well as unused ports of the microfluidic cells were additionally sealed with UV-curing optical glue (Type J-91 Lens Bond optical cement (Summers Opticians)). Rubber seals were glued into selected ports for use and tubing was connected to the cell via metal pins into the rubber seals.

Ion Detection

$HgCl_2$ stock solutions with concentrations of 1 mM were prepared using $HgCl_2$ and deionised water. Using a 1 ml syringe, first water or the solvent used for the experiment was injected into the cell and scattering spectra were taken. Subsequently, the analyte solution was injected into the cell and after 10 min of the sample in contact with mercury ions scattering spectra were taken.

3.3. Results and Discussion

3.3.1. Fabrication and Characterisation of Gold Nanoparticle-C5 Hybrid Nanostructures for Mercury Ion Detection

This section covers the fabrication of hybrid nanostructures comprised of gold nanoparticles and C5 organic ligands following two different routes as well as the characterisation of the resulting nanostructures.

Functionalisation of Nanoparticles in Solution

For the functionalisation of the nanoparticles, organic ligand C5 was synthesised and provided by the Preece Group at University Birmingham (Hysens project partner). The molecular structure of C5 is shown in Figure 3.2.

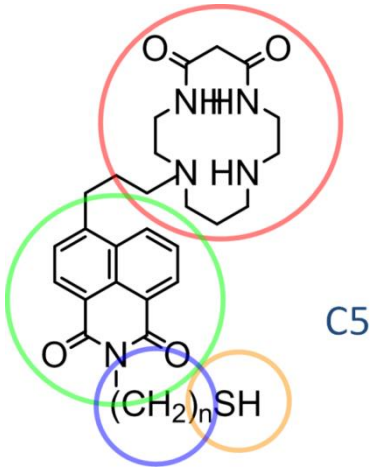


Figure 3.2: Chemical structure of molecules C5 provided by Hysens project partners for the functionalisation of gold nanoparticles. The functional groups of the molecule are highlighted in colour.

The molecule possesses several functional groups designed for the optical detection of mercury via PRET: The thiol group (highlighted in orange) has a known very high affinity for gold and is intended as the anchor group to attach C5 to the gold nanoparticles. On the other end of the molecule, the macroclylic dioxotetraamine croup (highlighted in red) is designed to complex Hg^{2+} ions. The 1,8 naphtalimide group (highlighted in green) defines the optical properties of the molecule and exhibits an absorption band at 440 nm. This absorption band has been shown to be influenced by the dioxotetraamine group and ions chelated by the group.[260] Finally, the alkane chain (highlighted in blue) serves as a spacer between the gold nanoparticle and the

dioxotetraamine group and is intended to improve self-assembly of C5 on the gold surface via van-der-Waals forces.

The first route pursued was the functionalisation of gold particles with C5 in solution. Nanoparticles are typically suspended in aqueous solution and C5 is only soluble in organic solvents, however, a 1:1 mixture of deionised water and ethanol proved to be a suitable medium that preserves a stable gold nanoparticle suspension and C5 solution. To functionalise the nanoparticles, the gold colloid in the water/ethanol mixture and C5 molecules dissolved in ethanol were mixed under vigorous stirring. To monitor the functionalisation, UV-Vis spectra were taken before and at various times after C5 addition and are presented in Figure 3.3.

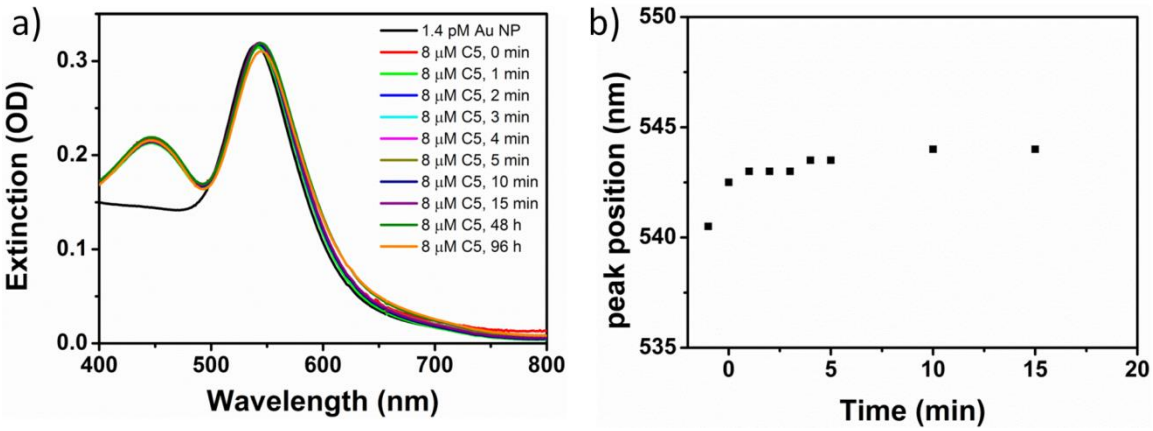


Figure 3.3: a) UV-Vis spectra of gold nanoparticles in a 1:1 deionised water:ethanol mixture before and various times after addition of molecules C5 in ethanol. b) Peak positions of spectra in panel a).

As shown in Figure 3.3a and b, in the water/ethanol mixture the nanoparticles exhibit an absorption peak at 540.5 nm. After addition of C5 in ethanol a red shift of the nanoparticle absorption peak can be observed, and additionally, an absorption peak for the C5 molecules appears at 444 nm. Over time the nanoparticle absorption shifts minimally more to the red but does not decrease in intensity. Also hardly any changes in the molecule absorption are visible. This behaviour clearly indicates that both the nanoparticles and the molecules are stable in at these conditions. The 3.5 nm red shift of the nanoparticle extinction band suggests a successful functionalisation of the nanoparticle with the C5 molecules. As shown previously in chapter 2, an increase of the refractive index of a nanoparticles immediate environment causes a red-shift of

the nanoparticles' plasmon resonance. It is expected that bulky molecules like C5 attached to the nanoparticles cause an increase of the refractive index, thus the extinction peak position shift can be taken as an indicator that C5 molecules are binding to the nanoparticles. This is further supported by the development of the peak shift shown in Figure 3.3a. The initial stronger peak position shift, then levelling off after 5 min further suggests that initially many molecules bind to the nanoparticles and the rate slows down as its surface becomes increasingly covered with molecules.

Immobilisation of Nanoparticles on Glass Substrates

The gold nanoparticle-C5 hybrid structures are aimed to be implemented in a microfluidic based sensing platform. Consequently, the hybrid structures have to be firmly immobilised on substrates that will be mounted in the microfluidic cells. A very well-known method to achieve this is the silanisation of the substrates with amine or thiol terminated silanes,[88, 261-263] to which gold nanoparticles can be attached. In this work (3-Aminopropyl)triethoxysilane (APTES) was used for this purpose.

Prior to silanisation, the substrates were cut to size using a dicing saw. Substrates used in darkfield microscopy need to show a high degree of cleanliness because scattering dirt interferes with darkfield spectra of single particles by overpowering the single particle signal or increasing the background leading to lower signal intensity. Thus, during dicing the glass cover slips (gcs) were protected with photoresist. The photoresist was removed immediately after dicing revealing a pristine surface, which was silanised with APTES. After silanisation, nanoparticles are immobilised on the glass substrates by placing drops of the colloidal solution on the substrates for a certain amount of time. Nanoparticles with a diameter of 60 nm were chosen as these particles proved to be scattering the light sufficiently to be easily monitored with a 50x objective. By adjusting the concentration of the colloidal solution and the deposition time before wicking the remaining solution, the nanoparticle density on the substrate could be controlled. Darkfield images of a selection of different samples are shown in Figure 3.4. A very high controllability of the particle density was achieved, which consequently could be adjusted for the purpose of the substrate. For single particle darkfield spectroscopy the optimum particle density was obtained after immersion of the substrate in 20x diluted gold colloid for 5 minutes.

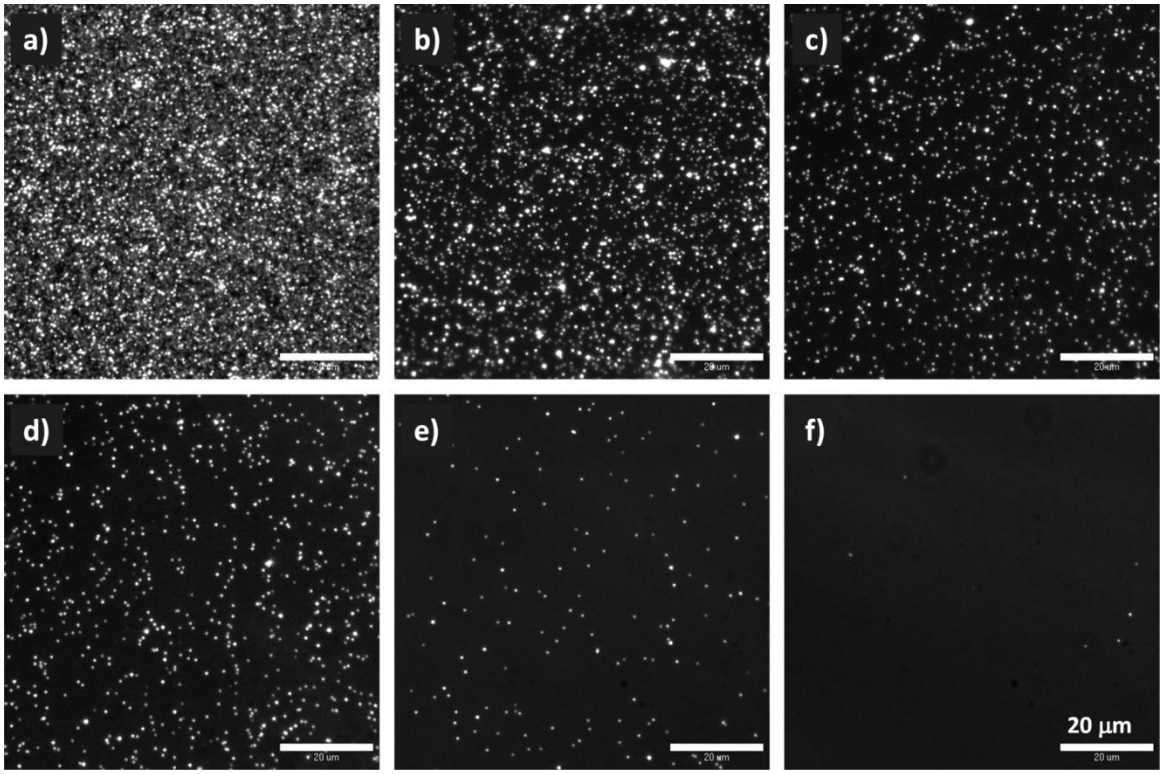


Figure 3.4: Darkfield images of silanised glass cover slips (5x5 mm) with varying density of immobilised 60 nm gold nanoparticles (NP), decreasing from a) to f). deposition conditions: a) 40 min deposition time, non-diluted NP solution, b) 1 min deposition time, non-diluted NP solution, c) 10 min deposition time, 10 x diluted NP solution, d) 5 min deposition time, 10 x diluted NP solution e) 5 min deposition time, 20 x diluted NP solution, f) 5 min deposition time, 50 x diluted NR solution.

This resulted in an average particle distance of 3.9 μm, which ensures darkfield measurements are taken of a single particle only and contribution of neighbouring particles can be ruled out. High density samples are useful where averaging over multiple nanoparticles is desired for an increased spectroscopic signal and were used for techniques like UV-Vis and Raman spectroscopy.

Functionalisation of Nanoparticles on Substrate

To functionalise immobilised nanoparticles with C5 molecules, the glass substrates were immersed for 24 h in 0.25 M ethanolic C5 solution. Several techniques were employed to characterise the nanoparticles before and after the functionalisation steps to confirm the attachment of C5 to the nanoparticles. Figure 3.5 shows UV-Vis extinction spectra of densely deposited gold nanoparticles before and after functionalisation with C5. The same behaviour as for the functionalisation of gold nanoparticles in solution in Figure 3.3 is observed. After immersion of the substrate in

C5 solution a small red shift of 4 nm of the nanoparticle's plasmon resonance peak is observed.

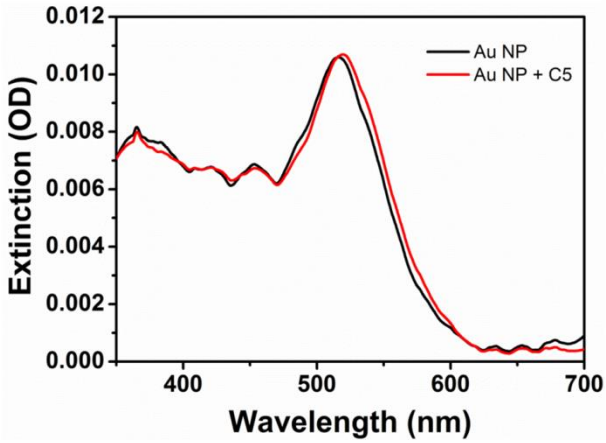


Figure 3.5: UV-Vis spectrum of gold nanoparticles densely immobilised on a glass substrate before and after immersion in C5:EtOH solution.

Substrates with well-spaced nanoparticles (~4 μm separation) were used to monitor the functionalisation of nanoparticles on the single particle level. Darkfield spectra taken of the same particles before and after the functionalisation steps indicate an effective functionalisation of the nanoparticles. Figure 3.6a and c show that immersion in the C5:EtOH solution led to a pronounced plasmon peak shift to the red, again caused by the change of the refractive index of the nanoparticles' environment induced by the C5 molecules. The strong scattering of peak shift values might be due to varying numbers of molecules around the particles. Figure 3.6b shows the results of a control sample immersed in EtOH only, where the peak shift induced by the solvent alone is much smaller than the one induced by the C5:EtOH solution.

To further characterise the C5 attachment SERS was employed. This is a very suitable technique based on the way the SERS signal is generated. Only the signal from molecules in very close proximity of the nanostructure is enhanced. Additionally, the technique provides a fingerprint for the molecule. For these experiments nanostructured silver SERS substrates developed in our group [96] as well as substrates with a very dense layer of silver nanoparticles were treated with the C5:EtOH solution in the same way as the previous substrates. Silver nanostructures were used instead of gold as a laser of the appropriate wavelength for gold structures was not available.

Raman spectra taken of the same locations before and after the immersion are shown in Figure 3.7.

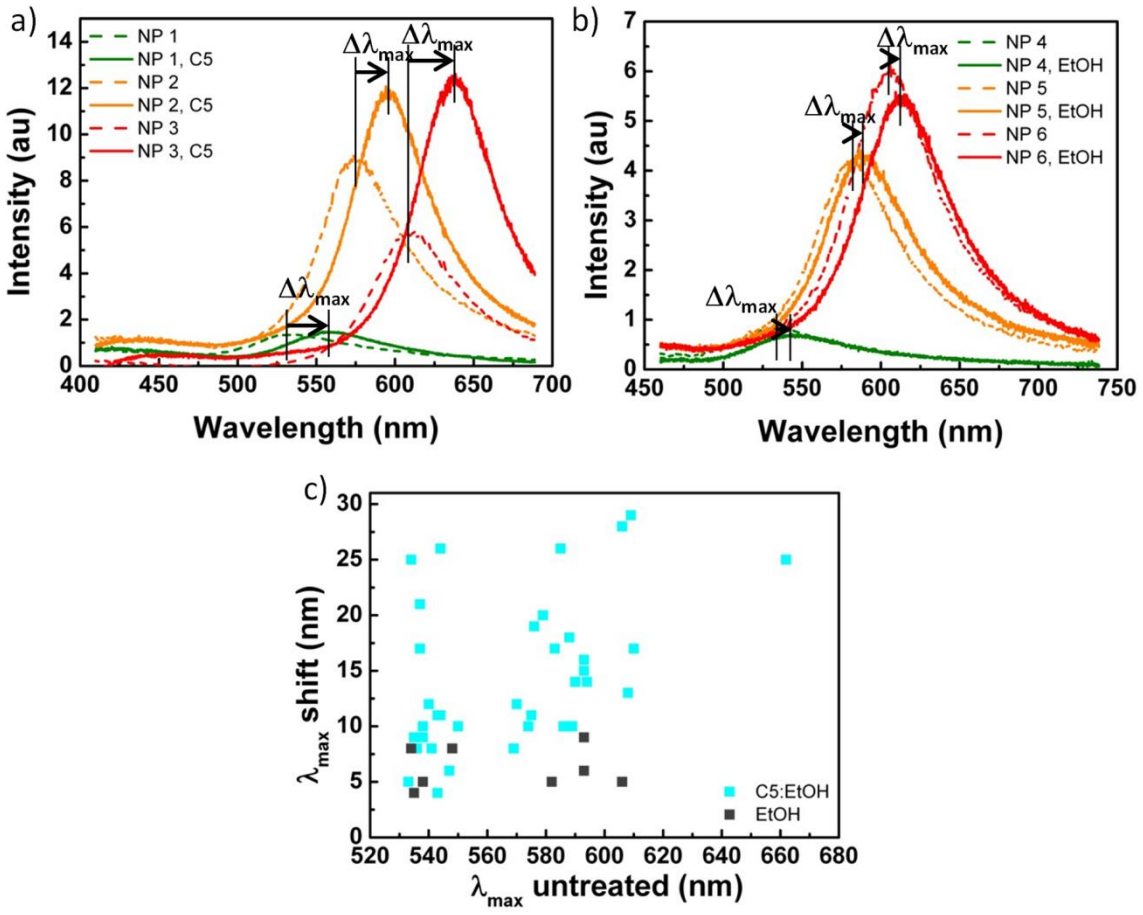


Figure 3.6: a) Darkfield spectra of particles with different shapes/colours before (dashed line) and after (solid line) immersion in C5:EtOH solution. b) Darkfield spectra of particles with different shapes/colours of a control sample before (dashed line) and after (solid line) immersion in the solvent only (EtOH). c) Summary of all analysed particles immersed in C5:EtOH (blue squares) including control sample immersed in EtOH (grey squares).

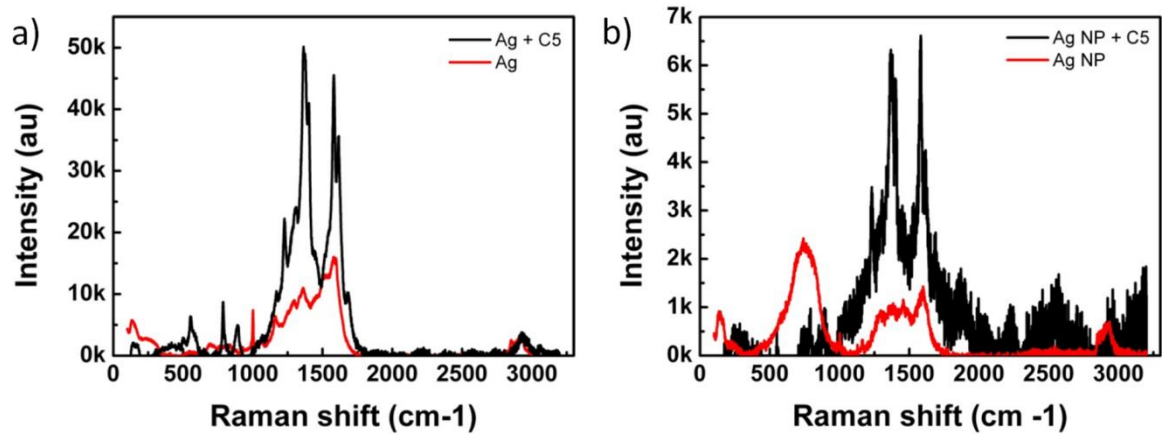


Figure 3.7: Raman spectra of a) a silver SERS substrate and b) a substrate with a high density of silver nanoparticles before (red) And after (black) immersion in C5:EtOH solution.

Before the immersion, both substrates show different Raman baselines based on the different nature of the substrates. After the immersion the same new peaks appear in the spectrum for both substrates, which indicates that C5 is deposited on the silver substrate as well as on the silver nanoparticles.

Finally, the fluorescent properties of the ligand C5 were utilised to further characterise the assembly. Figure 3.8 shows fluorescence lifetime images of a non-functionalised and a substrate with immobilised nanoparticles functionalised with C5. The increase in fluorescence intensity and the average lifetime seen in Figure 3.8b compared to Figure 3.8a, confirmed the presence of C5 on the substrates. Additionally, the fluorescence spectrum taken from a functionalised substrate in Figure 3.8c matched the spectrum reported by Mu et al.[260]

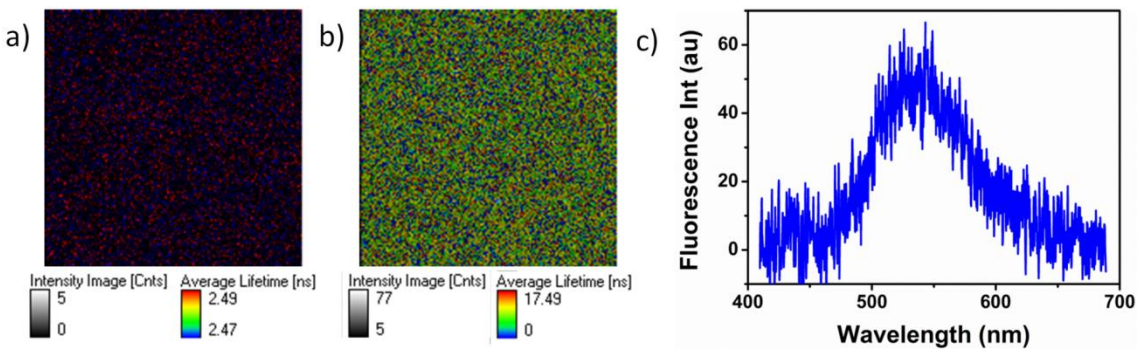


Figure 3.8: Fluorescence lifetime images of an area 80 x 80 μm a) before and b) after deposition of ligand C5. C) Fluorescence spectrum of functionalised sample.

While the previous spectroscopic techniques were only detecting C5 in very close proximity of the nanoparticles, fluorescence spectroscopy reveals information about the entire substrate. Comparing obtained darkfield and lifetime images of the same area in Figure 3.9, it can be seen that also in areas where no nanoparticles are present a fluorescence signal can be recorded.

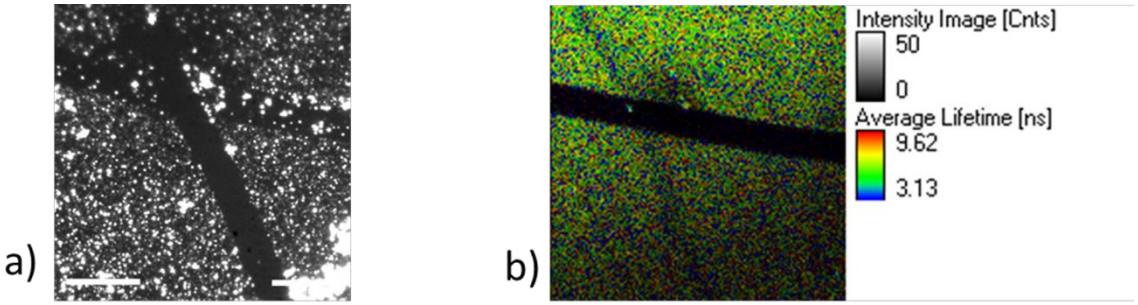


Figure 3.9: a) Darkfield and b) lifetime image of the same area with C5 functionalised gold nanoparticles.

This leads to the conclusion that the C5 molecules do not only attach to the immobilised nanoparticles but also to the substrates. Compared to the low surface coverage of nanoparticles on the substrates required for single particle spectroscopy, a blanket of C5 molecules over the sample may prove problematic for the sensing application. This issue arises from the fact that the thiol-group of the C5 molecule has a very high affinity for mercury based on soft acid-soft base interaction. If C5 molecules are attached in the intended way (with the thiol-group) to the nanoparticle this binding site is not available for mercury ions. If, however, C5 molecules are randomly adsorbed to the glass substrate, exposed thiol-groups create a huge number of competing binding sites for mercury ions, which could severely interfere with mercury detection.

3.3.2. Sensing Assessment of Gold Nanoparticles - C5 Hybrid Structures

To assess the sensing capabilities of the fabricated substrates with nanoparticle-C5 hybrid structures the substrates were integrated into disposable microfluidic chips provided by Hysens project partner Mildendo.

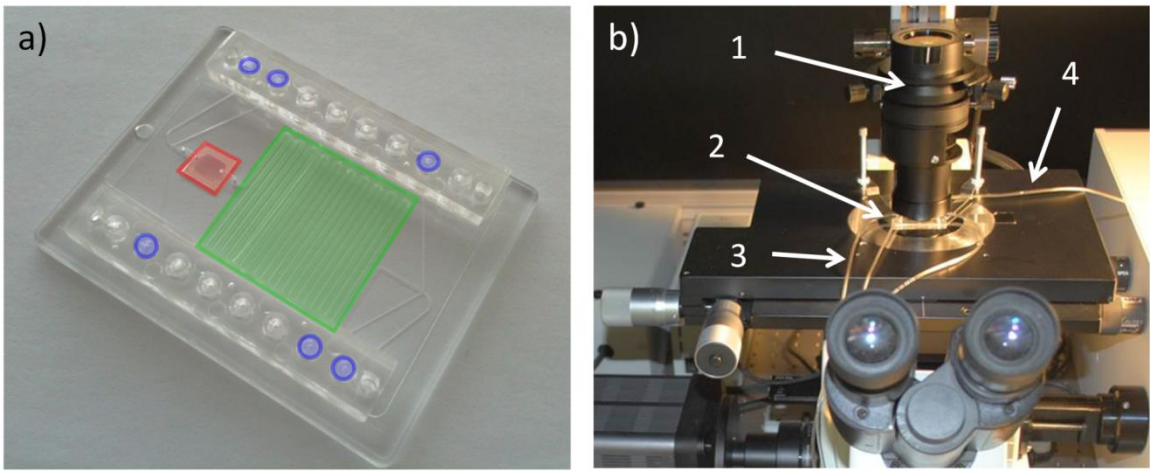


Figure 3.10: a) Microfluidic chip used for ion detection experiments. b) Microfluidic chip in sensing setup in inverted microscope. 1) darkfield condenser, 2) microfluidic cell, 3) inlet tubing for analyte injection 4) outlet tubing to waste container

The chips were used to allow solution exchange without moving any of the optical components. This was necessary as, for experiments where an intensity change is read

out, it is crucial that during the experiment the cell is fixed in the microscope. Small changes in the setup can also produce an intensity change and be mistaken for a sensing signal. An example of a microfluidic chip is shown in Figure 3.10a (for technical drawing see Appendix C). The chip consists of an area in which the functional glass substrate is inserted (red) three inlets and three outlets (blue). Dependent on from which side solutions are injected they can be led through a mixing channel (green) before reaching the active area. Figure 3.10b shows how the microfluidic cell is connected and integrated into the darkfield spectroscopic setup. The microfluidic chip is sandwiched between the darkfield condenser and objective of the microscope, inlet and outlet tubing is connected from the sides.

Figure 3.11 shows the results of mercury ion detection experiments in deionised water on a single nanoparticle. The expected response would be a decrease of scattering intensity induced by the absorption of a complex formed by the organic ligands C5 and mercury ions. Instead a slight increase of the scattering intensity was observed, which might be an effect of the increasing salt content of the solution.

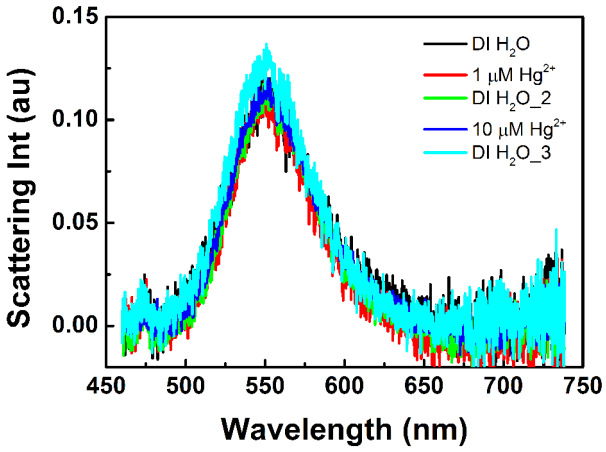


Figure 3.11: Darkfield scattering spectra of PRET hybrid assembly in the Hysens biochip flushed with aqueous solutions of increasing mercury chloride content.

These results indicate that the intended processes are not taking place. Several factors have been identified that might have contributed to that and are discussed in the following section.

In order to enable plasmon resonance energy transfer (PRET) the scattering spectrum of the nanoparticles and the absorption spectrum of the complex formed by the

organic ligands and mercury ions have to overlap.[145, 146] Comparing the scattering spectrum of the used 60 nm gold nanoparticles and absorption spectra of C5 molecules before and after titration with mercury in Figure 3.12a, however, shows this overlap is not ideal with a maximum scattering of the nanoparticles at 550 nm and a molecule extinction of C5 at 440 nm and the C5-Hg^{2+} complex at 483 nm. As an alternative to gold nanoparticles silver nanoparticles were considered. The plasmon resonance wavelength of 60 nm silver nanoparticles shows a good overlap with the extinction band of C5, as can be seen in Figure 3.12a. In this case, PRET would occur without Hg^{2+} present and a scattering increase should occur when the C5-Hg^{2+} complex is formed. However, unfortunately silver nanoparticles are not suitable candidates to substitute the gold nanoparticles as they were shown to oxidise under observation conditions, which quenches their plasmon resonance without any mercury present. An example is shown in Figure 3.12b.

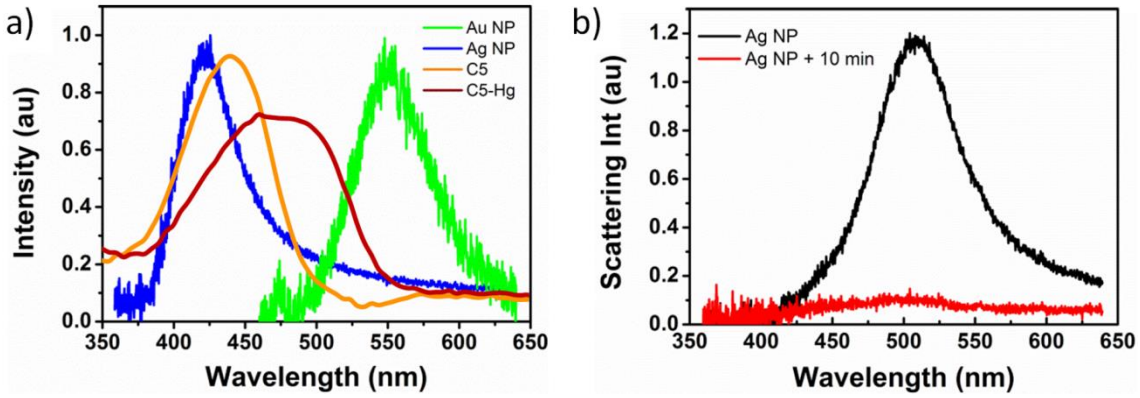


Figure 3.12: a) Comparison of gold and silver scattering spectra with the C5 absorption bands. b) Scattering spectrum of a silver nanoparticle as deposited and after 10 minutes at observation conditions.

Though the spectra in Figure 3.12a show that the overlap between gold nanoparticles and the C5-Hg^{2+} complex is not ideal, there is a certain amount of overlap and a small response from the gold nanoparticles would have been expected. Very likely a second issue caused the lack of response seen in Figure 3.11. Mu et al. have reported the binding of a C5 derivative to Cu^{2+} and Hg^{2+}.[260] In their studies they found that the macrocyclic dioxotetraamine group of the molecule is indeed too small for Hg^{2+} to fit inside the macrocycle, while Cu^{2+} fits in in perfectly. A consequence of this that Cu^{2+} binds very strongly, but Hg^{2+} can only bind very weakly to the dioxotetraamine group

especially in an aqueous environment where Hg^{2+} ions are strongly stabilised by a hydrate shell. However, the authors reported improved stability of the C5 and Hg^{2+} complex in organic media.

Both issues of the absorption-plasmon mismatch and the difficult binding of C5 and Hg^{2+} in aqueous media were addressed by fabricating an improved hybrid structure and testing Hg^{2+} detection in ethanolic solutions which will be covered in the following sections.

3.3.3. Fabrication and Characterisation of Silver Nanoparticle - Gold Shell - C5 Hybrid Structures

As established in the previous section, the originally designed hybrid structure composed of a gold nanoparticle and C5 molecules was not ideal for effective mercury ion detection. In the following, two approaches to increase the overlap of nanoparticle plasmon band and molecule extinction band are described and discussed.

Synthesis of Silver Core - Gold Shell Nanoparticles

A very interesting feature of a nanostructure's LSPR is that it can be finely tuned by controlling the size, shape and composition of the nanostructure. To address the issue of mismatched molecule extinction and nanoparticle scattering bands, the possibilities to tune the plasmon resonance of the nanoparticles with the synthesis of silver-gold core-shell nanoparticles was investigated. Silver core - gold shell was chosen as silver exposed to the analyte/ion solution proved to be unstable and subject to oxidation under the measurement conditions during the sensing experiments.

The initial route pursued consisted in covering commercially available silver nanoparticles (BBInternational) of a diameter of 60 nm with a thin gold shell in a wet-chemical synthesis. $HAuCl_4$ solution was added to silver colloidal solution at elevated temperatures along with ascorbic acid as a mild reducing agent. This caused the gold to reduce on the surface of the silver nanoparticles. Figure 3.13a shows resulting UV-Vis spectra of bare gold and silver nanoparticles for comparison, and of two batches of synthesised core shell nanoparticles. Both of the selected batches shown in Figure 3.13c and d show a plasmon resonance peak between the absorbance peaks of pure gold and silver nanoparticles in the range where the C5-Hg^{2+} complex absorbs.

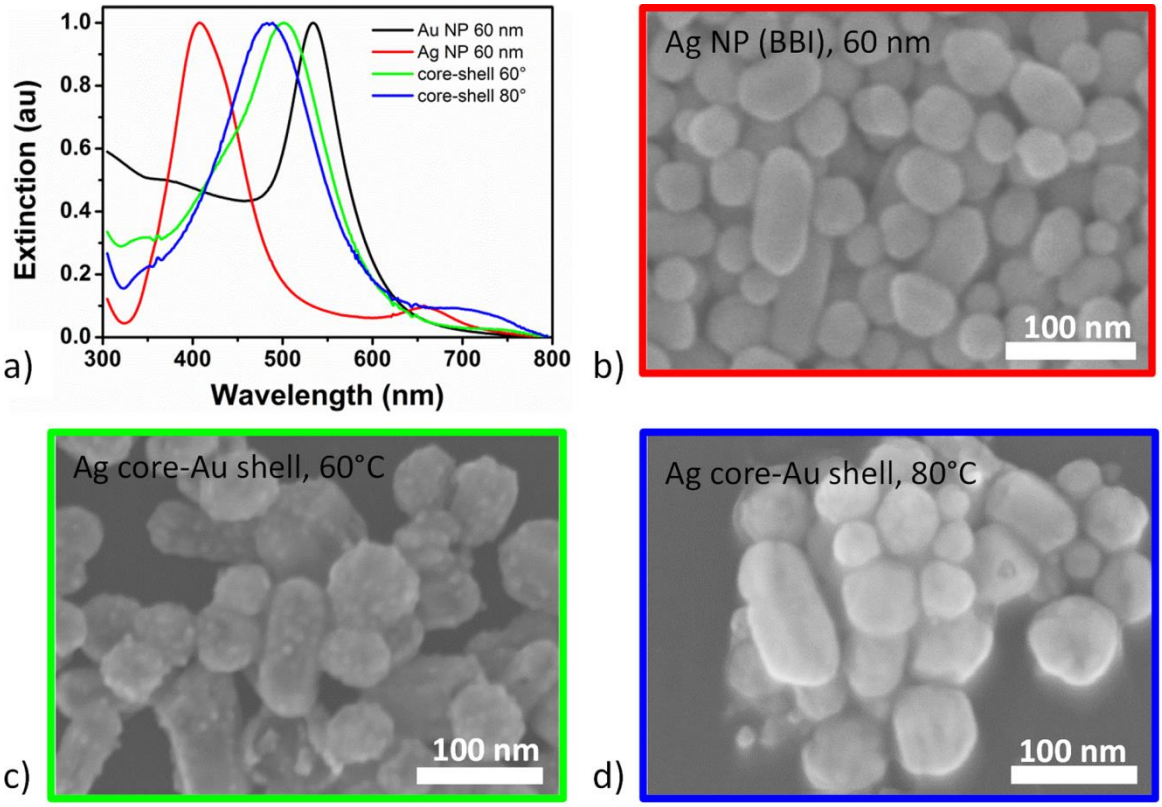


Figure 3.13: a) UV-Vis absorbance spectra of bare gold and silver nanoparticles and the core-shell nanoparticle batches shown in the SEM images c) and d). SEM images of a) bare 60 nm silver nanoparticles and silver core-gold shell nanoparticles synthesised at c) 60° C and d) 80° C.

The SEM images, however, show that the quality of the shell is significantly varying with the core-shell synthesis temperature. In order to prevent oxidation of the silver core the gold shell has to cover it completely. Even pinholes in the gold shell will lead to the oxidation of the silver core of the particles. This process was observable in darkfield scattering mode when the core-shell particles were integrated in the microfluidic cell. Gradually the scattering of the core-shell particles lost its sharp resonance peak and eventually became quenched (data not shown). From the data shown in Figure 3.13, the quality of the gold shell improved from 60° C to 80° C synthesis temperature. However, when increasing the reaction temperature further, the reduction of gold was not limited to the silver nanoparticle “seeds” anymore but occurred also in solution leading to small gold nanoparticles instead of gold shells on the silver nanoparticles. While there are many examples in literature of gold core-silver shell nanoparticles,[124, 218, 228, 264] the reverse structures remain a challenge to synthesise. The cause lies in the higher standard reduction potential of gold (1.8 V)

compared to silver (0.8 V), which was found to be responsible for the pinhole formation in a gold shell on silver cores.[265] While gold chloride is reduced to form a shell layer, silver from the core is being oxidised. Indeed, the process of silver oxidation in a silver-core, gold-shell nanoparticle has been observed before and even been reported to be utilised in the formation of gold nanocages and SERS structures.[265-267]

Synthesis of Pseudo Silver Core - Gold Shell Nanoparticles

Wet chemically synthesised of silver-core/gold-shell nanoparticles showed that a gold shell on silver cores did shift the plasmon resonance of the nanoparticles in the desired wavelength region. However, the resulting core-shell nanoparticles were not defect-free and were found to be unstable under sensing conditions. Alternatively, a new route was developed to fabricate "pseudo" core-shell nanoparticles: Silver nanoparticles were immobilised with a silane on a glass substrate. Care was taken to handle the substrates with immobilised silver nanoparticles under inert atmosphere to avoid surface oxidation of the nanoparticles. Subsequently a thin film of gold was evaporated by thermal evaporation onto the substrate. This gold layer serves three purposes: it causes a red-shift of the silver nanoparticle plasmon mode into the desired region, it protects the underlying silver nanoparticles from oxidation under sensing conditions, and it provides a plain gold surface that should even improve the nanoparticle functionalisation as the surface is free from surfactants.

A gold layer of 5 nm thickness was discovered to result in the desired plasmon shift. Figure 3.14a shows for comparison the plasmon resonance of bare gold and silver nanoparticles and silver nanoparticles with a 5 nm evaporated gold layer. Figure 3.14b shows an SEM image of the silver nanoparticles with gold layer and a darkfield image in the inset. The peak at ~675 nm for the silver nanoparticles with gold layer can be attributed to the plasmon resonance of gold islands between the nanoparticles. They can be seen in the SEM image in Figure 3.14b and as the red areas in the darkfield image in the inset. The peak ~500 nm is the plasmon peak of the particles red shifted from ~450 nm of bare silver nanoparticles by the thin gold layer on the nanoparticles. These can be seen as bright green dots in the scattering image in the inset in Figure 3.14b. To assemble the full hybrid structure the silver nanoparticles and gold layer

were functionalised with C5 as previously reported by immersion for 24 h in C5:EtOH solution.

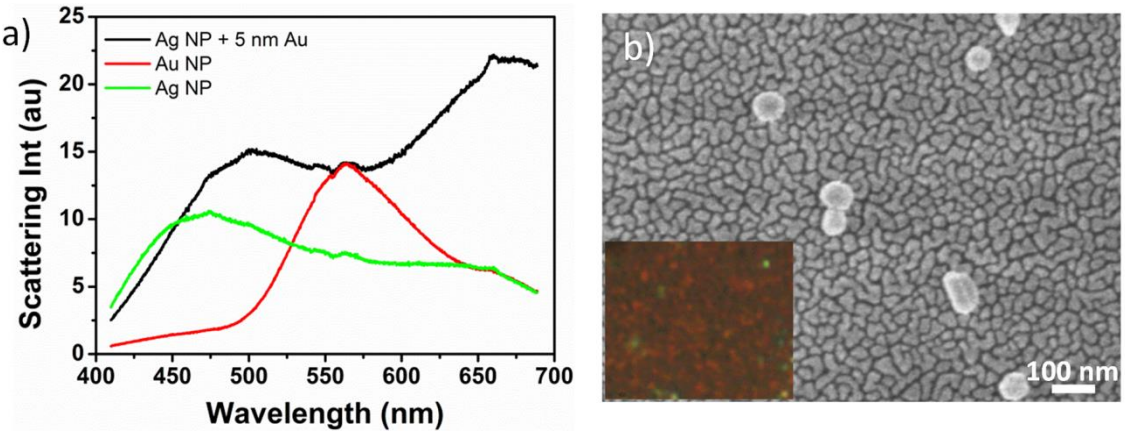


Figure 3.14: a) Darkfield spectra of silver nanoparticles with 5 nm evaporated gold, bare gold and bare silver nanoparticles. b) SEM image of silver nanoparticles with 5 nm evaporated gold. Inset: Darkfield image of the sample.

3.3.4. Sensing Assessment Pseudo Silver Core - Gold Shell - C5 Hybrid Nanostructures

Substrates prepared as described earlier with silver nanoparticles, evaporated gold layer and functionalised with C5 were inserted in the Hysens biochip, for Hg^{2+} detection experiments. After reports in literature according to which C5 does not form a stable complex with Hg^{2+} in water but only in organic solvents like ethanol,[94] the here presented experiments were carried out in ethanol. Figure 3.15 shows a set of results for Hg^{2+} detection on C5 functionalised pseudo silver core - gold shell nanoparticles. The onset of a high intensity peak at ~675 nm can be attributed the plasmon resonance of the gold islands between the nanoparticles, the smaller peak visible as a shoulder at ~500 nm belongs to the gold covered silver nanoparticles. As can be seen in the graphs, repeated flushing with only the solvent EtOH did not alter the scattering intensity of the particles (black and red line). After flushing the cell with 0.1 mM Hg^{2+}:EtOH, the intensity immediately decreased slightly, then further after 10 minutes indicating increased binding of Hg^{2+} to C5 molecules. Flushing the cell with a higher concentration of 1 mM Hg^{2+}:EtOH didn't further decrease the scattering intensity of the particles, which leads to the suggestion that the sensor might have been saturated.

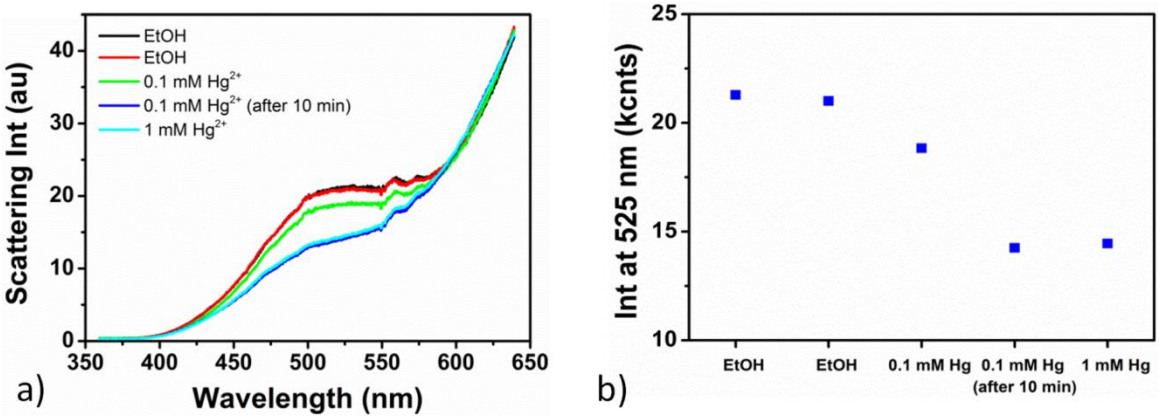


Figure 3.15: a) Darkfield scattering spectra of modified PRET hybrid assembly 2 (silver nanoparticles with 5 nm gold layer) in Hysens biochip flushed with ethanolic solutions of increasing mercury chloride content. b) Particle peak intensities of spectra shown in (a).

Subsequently, a reproduction of the in Figure 3.15 presented data and acquisition of data for lower Hg^{2+} concentrations was attempted. However, the change from aqueous to ethanolic solutions, which was necessary to facilitate C5-Hg^{2+} binding, led to difficult experimental conditions. Ethanol turned out to be extremely challenging for use in the available microfluidic cell as it showed to swell and dissolve components of the tape with which the glass substrate is fixed in the cell as well as reduce the adhesion of the optical glue with which the microfluidic ports are attached to the biochip. This might be even enhanced due to the heat generated from the intense light of the microscope focussed on the sample. The dissolution of the tape had two effects which were floating dirt in the microfluidic cell as well as occurring leakage. Floating dirt and leakages causing dirt on the backside of the chips are problematic as they increase the background scattering and alter the optical signal of the particles. Additionally, leakages caused the introduction of bubbles into the cell after which measurements had to be aborted.

3.4. Conclusion

Two types of PRET hybrid nanostructures were assembled and characterised: C5 functionalised gold nanoparticles and C5 functionalised pseudo silver core - gold shell nanoparticles. The first hybrid is the original proposed hybrid, the second was designed to improve the overlap between nanoparticle scattering and C5 absorption bands. The functionalisation of nanoparticles was confirmed by various methods. In UV-Vis and darkfield spectroscopy a red shift of the nanoparticle plasmon resonance band confirmed the attachment of molecules on the surface of the nanoparticles. Additionally, fluorescence and Raman spectroscopy supported the findings with both methods showing characteristic peaks for the C5 molecule attached to the nanoparticles. It has to be noted, however, that fluorescence spectroscopy also showed that C5 molecules were attaching to the supporting substrate as well as the nanoparticles. This potentially leaves the thiol group of the C5 molecules accessible for the Hg^{2+} ions. As mercury has a high affinity for thiol groups, free thiol groups can severely interfere with mercury detection and decrease the detection sensitivity.

Both types of PRET assemblies were assessed for optical detection of Hg^{2+} ions. The originally designed gold nanoparticle-C5 hybrid structures didn't show a response towards Hg^{2+} ions in water. After improving the original design, improved hybrid structures consisting of pseudo silver core - gold shell nanoparticles functionalised with C5 responded in the form of reduced nanoparticle scattering for a Hg^{2+} concentration of 100 μM in ethanol. While initial Hg^{2+} sensing results with the fabricated hybrid structures can be reported, these were accompanied by various complicating factors. Incompatibility of ethanol with the available microfluidic cells resulted in cell leakage and floating dirt and proved this sensing route to be experimentally extremely challenging. Additionally, other issues for Hg^{2+} detection with the proposed mechanism have to be taken into account. These include a strong affinity of mercury to the thiol groups of the C5 molecules, as well as the affinity of mercury to gold and silver which were used as plasmonic nanostructures. These would result in competing processes to the intended Hg^{2+} attachment to the macrocyclic dioxotetraamine group of the C5 molecules.

Eventually, the decision had to be made not to further investigate this route of Hg^{2+} ion detection via PRET but to instead explore and develop alternative routes for mercury detection, which will be covered in the following chapters.

Chapter 4 - Mercury Detection via Gold Nanorod Amalgamation

This chapter covers the investigation of amalgamation between immobilised single gold nanorods after chemical reduction of Hg^{2+} from solution. The process is investigated in detail and assessed towards its suitability as a method for detecting mercury in aqueous solutions. A limit of detection is established and the method tested in river and tap water. Furthermore, the amalgamation mechanism is studied in time-dependent measurements and a five step model is proposed for the mercury reduction, deposition and amalgamation with gold nanorods.

Parts of this chapter are published in:

Investigation of Au-Hg Amalgam Formation on Substrate-Immobilized Individual Au Nanorods *Carola Schopf, Alfonso Martín, Michael Schmidt, Daniela Iacopino*, Journal of Materials Chemistry C, **2015**, 3(34): p. 8865-8872

4.1. Introduction

Following on from Chapter 3, where efforts were described to employ functionalised nanoparticles for mercury detection, in this chapter an alternative route is being explored based on the amalgamation of gold nanorods. Among nanoparticle shapes, nanorods have been identified as ideal candidates for plasmon sensing due to their large spectral shift for a given change in refractive index, which exhibits much higher sensitivity compared to that of spherical counterparts.[48, 135, 268] For example, sensitive detection of mercury has been reported with gold nanorod solutions spiked with known amounts of Hg^{2+} in presence of reducing agent $NaBH_4$. High selectivity and sensitivity was achieved due to formation of an amalgam between mercury and gold, which shifted the maximum absorbance wavelength of the longitudinal plasmon mode of the nanorod solutions.[206] More recently, the same approach was used to detect mercury with gold nanorods immobilised on glass slides.[212, 269] Also in this case an optical response was observed by measuring collective nanorod absorbance shifts occurring upon amalgam formation. These were accompanied by a visible colour transition of nanorod-coated glass slides from blue to red. Analytical figures of merit showed precise and accurate detection down to nM level.[212] This suggests that sensing, environmental and catalytic performances based on gold nanorod-mercury alloys would display large sensitivity and efficiency due to the high reactivity of nanorods.

However sensitive, a system response based on the collective contribution of many nanorods is inherently broadened by the nanorod size distribution and by the possible presence of small clusters and additionally it is affected by the nanorod spatial distribution.[56, 270] In contrast, the investigation of a response to mercury at a single particle level results in fewer variables than for particle films. Recent work performed by James et al. showed a sensitive response of single nanorods to mercury vapour with attogram resolution.[271] Monitoring single nanorods allowed comparison of shape and size effects with distinct measurements rather than statistical characterisation.

Yet, to date only few studies have been reported on the mercury adsorption and amalgamation mechanism at the nanoscale. The understanding of the mechanism is

mandatory for the design of plasmonic-based mercury sensors with optimised performance as well as miniaturised fluid handling systems. Initial structural and morphological investigation of the mercury deposition process in presence of gold nanoparticles suggested the formation of a core-shell type structure (not an amalgam).[209] However, more recently, experimental investigation supported by theoretical modelling was used by Mertens et al. to demonstrate a mechanism where the initial formation of a core-shell structure was followed by amalgam formation triggered by slow diffusion of mercury into the gold nanoparticle cores.[208] In spite of the enhanced optical responses of non-spherical particles to mercury compared to their spherical counterparts, the mechanisms regulating the formation of gold-mercury alloys for non-spherical particles such as nanorods have been scarcely investigated. To date, studies have largely been focused on silver-mercury amalgam processes,[213] due to the larger reactivity of citrate-stabilized silver nanostructures compared to gold nanostructures. In addition, the close position of mercury and gold on the periodic table makes the monitoring of mercury deposition on gold nanostructures and the characterisation of the resulting alloy structures more difficult.

This chapter covers the use of individual gold nanorods immobilised on solid substrates as plasmonic transducers to detect mercury. The optical response of gold nanorods towards chemically reduced Hg^{2+} was studied. Upon amalgamation of gold nanorods with mercury, a pronounced blue shift of a nanorod's LSPR spectrum could be observed (Section 4.3.1); a result of the combined effects of the change of the nanorod's composition and the change of the nanorod's shape towards a sphere (Section 4.3.2). The sensitivity and selectivity of this method was investigated to assess this method for mercury detection applications, revealing a good selectivity of gold nanorods towards mercury over other heavy metals and sensitivity down to the nanomolar level in real water samples (Section 4.3.3). Additionally, theoretical calculations and time dependent studies were performed giving insights into the multi-step processes involved in the amalgamation (Section 4.3.4).

4.2. Experimental Methods

4.2.1. Sample Preparation

Nanorod Synthesis.

Gold nanorods (AR = 3.0) were synthesised by overgrowth of nanorods fabricated with the seed-mediated method reported by Liz-Marzán et al.[90] As-prepared gold nanorods were centrifuged and redispersed into water, maintaining a CTAB concentration between 0.1 mM and 0.35 mM.

Nanorod Substrate Immobilisation.

Glass microscope slides with etched binary alignment marks to allow the exact localisation of each nanorod were used as substrates. Prior to the nanorod deposition, glass substrates were silanised as follows. Microscope slides were cleaned by sonication in acetone followed by deionised water for 10 min, rinsed with deionised water and dried under a stream of nitrogen. For further cleaning and surface activation the substrates were treated with oxygen plasma of 50 W for 5 min immediately before immersion in a 3% APTES:MeOH solution for 30 minutes. To remove excess unbound silane, the substrates were rinsed with methanol and deionised water twice. Finally the substrates were placed in a fan operated oven at 120° C for crosslinking of the silane.[259]

A 100 μl droplet of gold nanorod aqueous solution was placed on the substrate for 3 min. Immediately afterwards, the substrates were rinsed with 40 °C deionised water to remove excess surfactant and dried under a stream of nitrogen.

Gold Nanorod- Mercury Amalgam Formation

Hg^{2+} stock solutions with concentrations of 10 mM, 1 mM, 100 μM and 10 μM were prepared using $HgCl_2$ and deionised water. $NaBH_4$ in excess (0.01 M) was employed for the chemical reduction of Hg^{2+}. Glass substrates with immobilised nanorods were firstly immersed in 10 ml 0.01 M $NaBH_4$ for 10 min. Subsequently, the nanorod substrates were immersed in fresh $NaBH_4$ solutions (10 ml, 0.01 M, 10 min) to which 2 - 10 μl aliquots from $HgCl_2$ stock solutions were added to produce a desired Hg^{2+} concentration. The substrates were then removed from the solutions, rinsed thoroughly with deionised water and dried under a stream of nitrogen before

acquiring darkfield images and spectra of single nanorods immobilised on the substrate. This procedure was repeated for solutions with increasing Hg^{2+} concentration. Of note, for each step fresh $NaBH_4$ solution was prepared due to the short half-life of the borohydride ions in water.

For the real water analysis, a sample of river water was taken from the river Lee outside the institute and a sample of tap water was taken from a tap in the institute. 100 ml of each sample was externally analysed by ICP-MS on its metal contents by a certified testing service (Fitz Scientific). For mercury detection measurements the river and tap water was filtered (0.45 μm pore diameter) and spiked with $HgCl_2$ to produce concentrations between 5 nM and 100 nM.

4.2.2. Sample Characterisation

Darkfield Microscopy.

Scattering spectra of individual gold nanorods were acquired with an inverted IX-71 Olympus microscope with an oil immersion darkfield condenser (Olympus U-DCW, 1.4 NA) and 100x objective (Olympus MPlanApo 100x/0.95 NA). The sample was illuminated with a 100 W halogen lamp. The light collected by the objective was directed either onto a colour CMOS camera (DCC1645C, ThorLabs) for image acquisition or onto the entrance slit of a monochromator (SP-2356, Acton Research). The light was dispersed by an optical grating (300 grooves/mm, blazed at 500 nm, 350nm < λ < 850nm) and directed onto a thermoelectrically cooled, back illuminated CCD (Spec10:100B, Princeton Instruments) for spectra acquisition. The experiments were performed by first recording an image of the sample with a mirror in the light path of the spectrometer. Once a suitable nanostructure was selected, the mirror was switched to the grating to disperse the scattered light and a spectrum was recorded using an acquisition time of 60 s. Normalised scattering spectra from individual nanostructures were obtained by subtracting and dividing by a background scattering spectrum taken from a nearby clean area on the sample. To determine the peak scattering wavelength, the spectra were fitted with a Lorentzian function (equation 2.1).

Electron Microscopy.
For morphological characterisation, SEM images of individual gold nanostructures were acquired using a field emission SEM (JSM-6700F, JEOL UK Ltd.), operating at a beam voltage of 10 kV. For statistical size and shape analysis of as-deposited and amalgamated nanorods, software ImageJ has been used to measure the length *l* and width *w* of 300 nanorods per sample. Additionally, the nanorod aspect ratio and volume were calculated from each nanorod from these measured *l* and *w* values assuming a cylindrical, hemisphere capped shape of the nanorods. Elemental analysis was performed using an Oxford Instruments Aztec EDX system equipped with X-Max 80 detector attached to an FEI Helios Nanolab 600i (DualBeam field emission SEM/FIB), operating at an SEM beam voltage of 20 kV. In order to reduce the overlap between the gold and mercury signal the L series was manually chosen for quantification.

4.2.3. Theoretical Calculation of Amalgamated Nanorod Optical Signatures

To calculate scattering spectra of gold-mercury core-shell nanorods a model reported for gold-silver core-shell nanorods by Guyot-Sionnest has been used.[124] The core-shell nanorod is described by the semiaxes of the core $a_1 = b_1 < c_1$ and the dielectric function of the core ε_1, the semiaxes of the confocal shell $a_2 = b_2 > c_2$ and the dielectric function of the shell ε_2. The scattering cross section was calculated using

$$C_{sca} = \frac{k^4}{6\pi}\left[\left(\frac{2}{3}\right)|\alpha_1|^2 + \left(\frac{1}{3}\right)|\alpha_3|^2\right] \tag{4.1}$$

with k being the wavenumber of the medium $k = 2\pi/\lambda$, and α_1 and α_3 being the polarisabilities along the short axes (1) and long axis (3) of the nanorod.

$$\alpha_1 = \alpha_2 = \frac{V\left\{(\varepsilon_2 - \varepsilon_m)\left[\varepsilon_2 + (\varepsilon_1 - \varepsilon_2)\left(L_1^{(1)} - fL_1^{(2)}\right)\right] + f\varepsilon_2(\varepsilon_1 - \varepsilon_2)\right\}}{\left[\varepsilon_2 + (\varepsilon_1 - \varepsilon_2)\left(L_1^{(1)} - L_1^{(2)}\right)\right]\left[\varepsilon_m + (\varepsilon_2 - \varepsilon_m)L_1^{(2)}\right] + fL_1^{(2)}\varepsilon_2(\varepsilon_1 - \varepsilon_2)} \tag{4.2}$$

$$\alpha_3 = \frac{V\left\{(\varepsilon_2 - \varepsilon_m)\left[\varepsilon_2 + (\varepsilon_1 - \varepsilon_2)\left(L_3^{(1)} - fL_3^{(2)}\right)\right] + f\varepsilon_2(\varepsilon_1 - \varepsilon_2)\right\}}{\left[\varepsilon_2 + (\varepsilon_1 - \varepsilon_2)\left(L_3^{(1)} - L_3^{(2)}\right)\right]\left[\varepsilon_m + (\varepsilon_2 - \varepsilon_m)L_3^{(2)}\right] + fL_3^{(2)}\varepsilon_2(\varepsilon_1 - \varepsilon_2)} \tag{4.3}$$

with V being the volume of the nanorod $v = 4/3a_2b_2c_2$, f being the volume fraction of the nanorod core $f = a_1b_1c_1/a_2b_2c_2$ and $L_1^{(k)}$ and $L_2^{(k)}$ being the geometrical factors.

$$L_3^{(k)} = \frac{1-E_k^2}{E_k^2}\left(-1+\frac{1}{2E_k}\ln\frac{1+E_k}{1-E_k}\right) \qquad L_1^{(k)} = \frac{1}{2}\left(1-L_3^{(k)}\right) \qquad (4.4, 4.5)$$

$$E_k^2 = 1-\frac{a_k^2}{c_k^2} \qquad (k = 1.2) \qquad (4.6)$$

For the dielectric functions of the core and shell materials values were taken for bulk gold from Johnson and Christy[251] and for bulk mercury from Inagaki.[272] Calculated scattering spectra were obtained by fitting the calculated data points with a Lorentzian function from which the wavelength of maximum scattering intensity λ_{max}, the full width at half maximum (FWHM) and the scattering intensity could be extracted.

4.3. Results and Discussion

Gold nanorods were synthesised according to an overgrowth method reported by Marzán et al.[90] The method produced gold nanorods of average size 21(± 4) × 61(± 6) nm. Figure 4.1 shows for comparison an extinction spectrum of the nanorods dispersed in aqueous solution, a collective extinction spectrum of the nanorods densely deposited on a glass substrate and an example of a scattering spectrum of a single deposited nanorod on a glass substrate. The extinction spectrum of nanorods dispersed in aqueous solution presented characteristic transversal and longitudinal plasmon peaks centred at 520 nm and 660 nm, respectively (Figure 4.1, black curve).

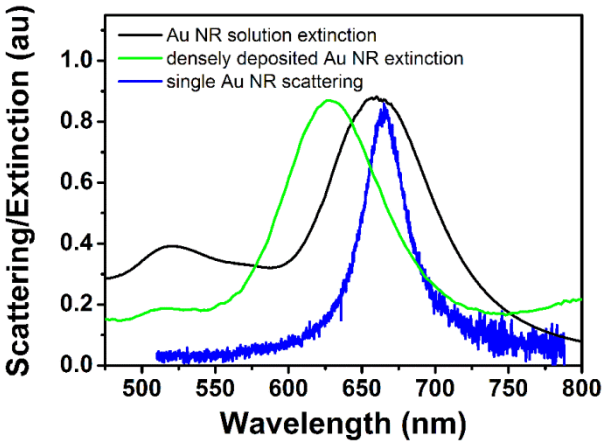


Figure 4.1: Extinction spectra of gold nanorods dispersed in aqueous solution (black curve) and deposited on glass substrate (green curve); scattering spectrum of single gold nanorod deposited on glass substrate (blue curve).

The FWHM of the longitudinal peak was determined to be 78 nm. For densely deposited nanorods on glass substrates the transversal and longitudinal plasmon peak positions shifted to 515 nm and 631 nm, respectively (Figure 4.1, green curve). This can be attributed to the changed dielectric environment upon deposition of the nanorods and contribution of plasmon coupling between nanorods deposited close to each other. The longitudinal peak's FWHD slightly decreased to 72 nm. In comparison, the scattering spectrum of a single nanorod recorded by darkfield spectroscopy showed only the plasmon peak associated with the longitudinal mode. The spectrum was centred at 666 nm with a FWHM of 37 nm (Figure 4.1, blue curve), much narrower compared to the spectra of nanorod ensembles. Ensemble spectra of chemically synthesised nanorods are always broadened by a distribution of nanorod shapes and

sizes. This suggests that the use of single nanorod optical signatures should provide a more accurate detection of optical peak shifts than collective optical signatures. In the following sections, the response of single gold nanorods to the exposure to mercury is studied.

4.3.1. Amalgamation of Single Gold Nanorods

To investigate the optical response of single gold nanorods to chemically reduced mercury, the nanorods are immobilised on glass substrates sufficiently spaced to allow optical signal collection from single nanorods (~ 5 μm spacing).

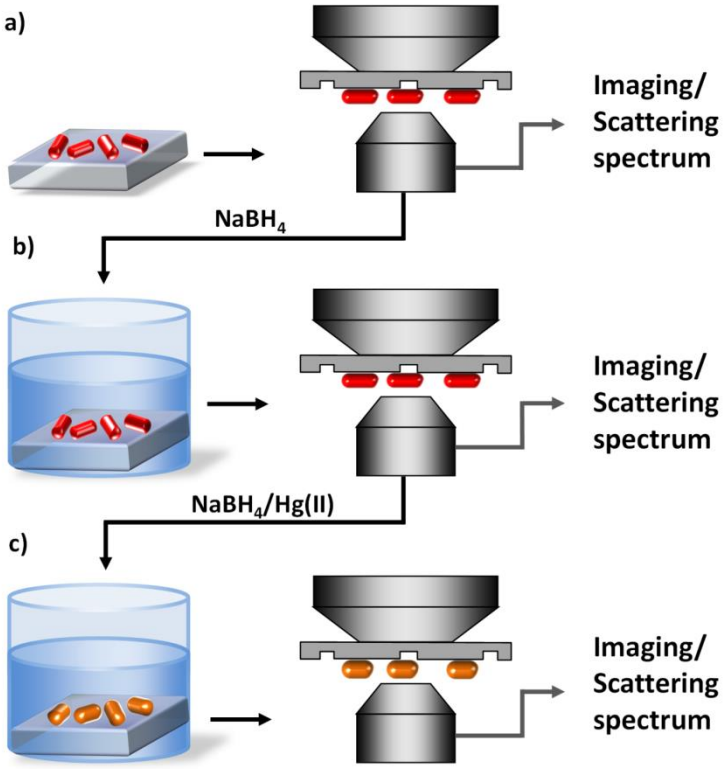


Figure 4.2: Schematic of gold nanorod amalgamation procedure with substrate-immobilised nanorods: Darkfield microscopy is firstly performed on gold nanorod substrates and scattering spectra are recorded of selected nanorods (a); Substrates are immersed in $NaBH_4$ solution and spectra of the same selected nanorods are recorded by darkfield spectroscopy (b); Substrates are immersed in $HgCl_2/NaBH_4$ solution and spectra of the nanorods are recorded again by darkfield spectroscopy (c).

Figure 4.2 shows the procedure used for monitoring the optical signatures of single gold nanorods before and after contact with mercury containing solutions. Specifically, a substrate with immobilised nanorods is placed in an optical microscope and darkfield images and scattering spectra of selected nanorods are collected (a). The glass slide with gold nanorods is subsequently immersed in an aqueous solution of $NaBH_4$ and

placed again in the optical microscope where darkfield images and scattering spectra of the same selected nanorods are collected (b). This step is performed in order to ensure that exposure to the reducing agent $NaBH_4$ does not generate any optical response of the nanorods. Subsequently, the nanorod substrate is immersed in aqueous solutions of $NaBH_4$ containing aliquots of $HgCl_2$ solution. Darkfield images and scattering spectra of the same selected nanorods are recorded after immersion in the mercury containing solution (c) and any spectral shifts recorded. For some nanorods this last step was be repeated with solutions of increasing mercury concentration.

Figure 4.3 shows a representative set of data for a gold nanorod passing through the procedure described above.

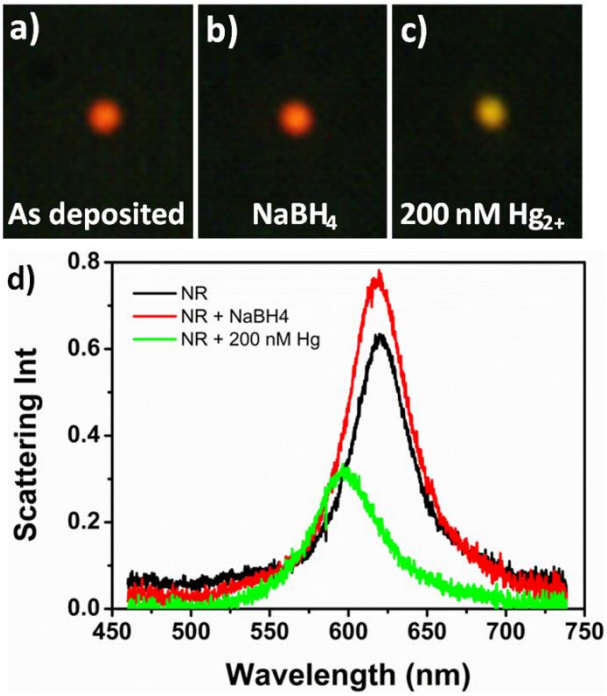


Figure 4.3: a) Scattering images of an individual gold nanorod a) as deposited; b) after immersion in 10 μM $NaBH_4$; c) after immersion in 200 nM $HgCl_2$, $NaHB_4$ solution; d) Gold nanorod scattering spectra corresponding to processes a-c).

Figure 4.3a shows a darkfield image of a gold nanorod displaying typical red scattering colour. After immersion in $NaBH_4$ aqueous solution in absence of $HgCl_2$, no visible changes were observed in the scattering characteristics of the same nanorod (Figure 4.3b). However, a pronounced transition of the scattering colour from red to yellow was observed after addition of 200 nM $HgCl_2$, as shown in Figure 4.3c. The corresponding nanorod scattering spectra are shown in Figure 4.3d. The as-deposited

nanorod spectrum displayed a longitudinal LSPR with a peak scattering intensity at λ_{max} 621 nm and full with half maximum (FWHM) of 43 nm. Upon immersion into $NaBH_4$ solution, the scattering spectrum showed a minimum blue shift of 1 nm. This change might have been caused by the interaction of $NaBH_4$ with the nanorod surfactant shell, which slightly altered the nanorod's local dielectric environment. Alternatively it might have resulted from free electron injection into the gold nanorods by the borohydride ions as was described by Mulvaney.[59, 273] The observed increase in peak intensity compared to the spectrum of the as-deposited nanorod was most likely not caused by $NaBH_4$, but occurred due to slightly different imaging conditions as a consequence of mounting and dismounting of the sample on the microscope between measurements. For some samples the scattering intensity decreased after immersion in $NaBH_4$ solution whereas for other samples it increased. In contrast, after immersion of the substrate in $HgCl_2$ containing solution, pronounced changes were observed. In particular, the green spectrum of Figure 4.3d displayed a decreased scattering intensity, a λ_{max} shifted to 599 nm (equivalent to a 22 nm blue shift compared to the spectrum of the as-deposited nanorod) and a FWHM of 54 nm (equivalent to an 11 nm broadening compared to the spectrum of the as-deposited nanorod). This strong response to 200 nM $HgCl_2$ solution is promising behaviour for sensitive detection of mercury in aqueous solutions. In the following sections, first the nanostructures resulting from the process, then the mercury detection process itself are investigated in more detail.

4.3.2. Characterisation of Amalgamated Single Gold Nanorods

Aspect Ratio Dependence of the Optical Response

When nanorods are employed in sensing applications it has been reported previously that the magnitude of a nanorod's response is related to its aspect ratio.[131, 135] To assess the dependence of the nanorods' optical response towards mercury on their initial aspect ratio, Figure 4.4 shows the plot of the nanorods' response (λ_{max} shifts) after immersion in 200 nM $HgCl_2$ solutions vs. their original scattering wavelength (λ_{max}).

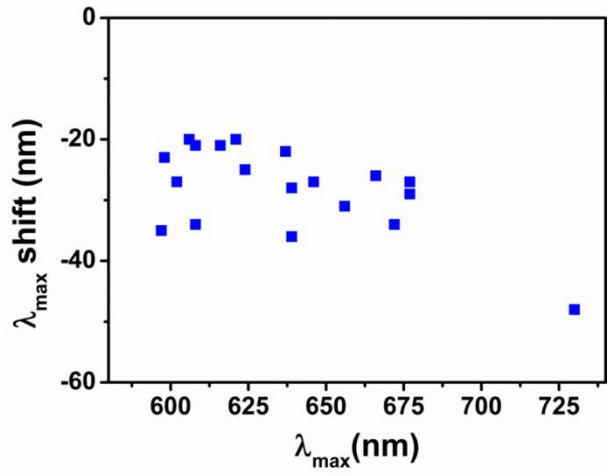


Figure 4.4: Measured λ_{max} shifts for 19 nanorods exposed to 200 nM $HgCl_2$, 0.01 M $NaBH_4$ solution.

All measured structures showed blue shifts and nanorods with longer initial scattering wavelengths, corresponding to higher nanorod aspect ratios, showed slightly more pronounced blue shifts. These finding are in agreement with data reported by Bootharaju et al. on the interaction of Hg^{2+} with gold nanoparticles, where larger shifts were obtained from red scattering particles compared to green and blue.[211] The same behaviour was also reported by James et al., who found larger aspect ratio (AR) nanorods more sensitive to mercury vapours than smaller AR nanorods.[271] The variability of λ_{max} shifts for nanorods with the same original λ_{max} indicates, however, that besides the expected aspect ratio dependence other factors did contribute to the magnitude of the λ_{max} shifts. Factors like surface area to nanorod volume ratio are likely to play a role. However, a detailed SEM correlated amalgamation experiment was not conclusive, as deposited carbon from the electron beam was found to interfere with the nanorods' response.

Morphological Changes in Amalgamated Nanorods

To qualitatively correlate the observed optical transitions to morphological changes, gold nanorods were immobilized on SiO_2 substrates and exposed to $HgCl_2$ solutions of increasing concentration. Figure 4.5a-d show representative SEM images of as-deposited nanorods and nanorods exposed to 500 nM - 10 μM $HgCl_2$ solutions showing morphological transition from elongated to spherical shape.

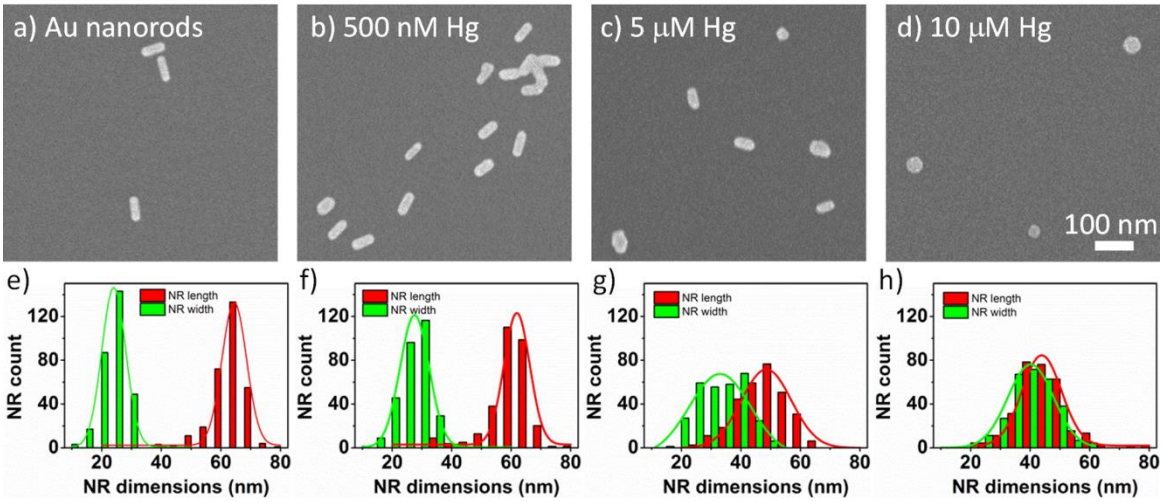


Figure 4.5: SEM images of nanorods a) as-deposited and after immersion in b) 500 nM, c) 5 μM and d) 10 μM Hg(II) containing solutions; e-f) corresponding length (red) and width (green) analysis averaged over 300 nanorods.

SEM image analysis was used to extract shape and size transitions associated with exposure to mercury. Histograms for the nanorod length and width obtained from image analysis of 300 nanorods per sample are shown in Figure 4.5e-g.

Table 4.2: Average dimensions and standard deviations of nanorods after immersion in solutions with $HgCl_2$ concentrations ranging from 50 nM to 10 μM determined from 300 measured nanorods per sample.

Sample	Avg. NR length (nm)	Avg. NR width (nm)	Avg. NR aspect ratio	Avg. NR volume (nm^3)	Avg calc Hg cont. (at-%)
Au nanorod	61 ± 6	21 ± 4	3.0 ± 0.6	20000 ± 2000	0
50 nM Hg	60 ± 6	23 ± 5	2.7 ± 0.6	22000 ± 3000	6
100 nM Hg	60 ± 5	22 ± 4	2.9 ± 0.5	21000 ± 4000	3
500 nM Hg	58 ± 7	25 ± 5	2.4 ± 0.5	24000 ± 2000	12
1 μM Hg	58 ± 5	25 ± 5	2.4 ± 0.5	26000 ± 5000	17
5 μM Hg	45 ± 8	31 ± 8	1.6 ± 0.5	27000 ± 4000	19
10 μM Hg	42 ± 8	39 ± 9	1.1 ± 0.3	38000 ± 5000	38

As-deposited nanorods were well distinguishable from each other and showed average length and width of 61±6 nm × 21±4 nm (AR = 3.0 ± 0.6), respectively (Figure 4.5a, e). For $HgCl_2$ concentrations below 500 nM barely any shape changes were detected. For a $HgCl_2$ concentration of 500 nM small shape changes were observed in areas of well-separated nanorods. The average size was determined to 58 ± 7 nm × 25 ± 5 nm, corresponding to an average AR of 2.4 ± 0.5 (Figure 4.5b, f). In areas of high density,

coalescence of particles was observed, in agreement with coalescence observed by Mertens et al. for citrate stabilized gold nanoparticles exposed to Hg.[208] For 5 μM $HgCl_2$ concentration, marked shape transition was observed with a calculated AR of 1.6 ± 0.5 (Figure 4.5c, g). Finally for 10 μM $HgCl_2$ concentration complete transition of Au nanorods to spherical-shaped particles (AR = 1.1 ± 0.3) was observed (Figure 4.5d, h). The morphological changes recorded for nanorods exposed to mercury are summarised in Table 4.1.

The shape transformation observations coincide with the solubility limit of elemental mercury in water at a concentration of 300 nM.[274] Above 300 nM mercury droplets instead of individual mercury atoms are expected in solution which might aid a nanorod shape transition. However, correlated SEM images (Figure 4.6) show clearly that the shape change of the nanorods does not only consist in precipitation of mercury droplets onto the nanorods, but an actual reshaping of the nanorods.

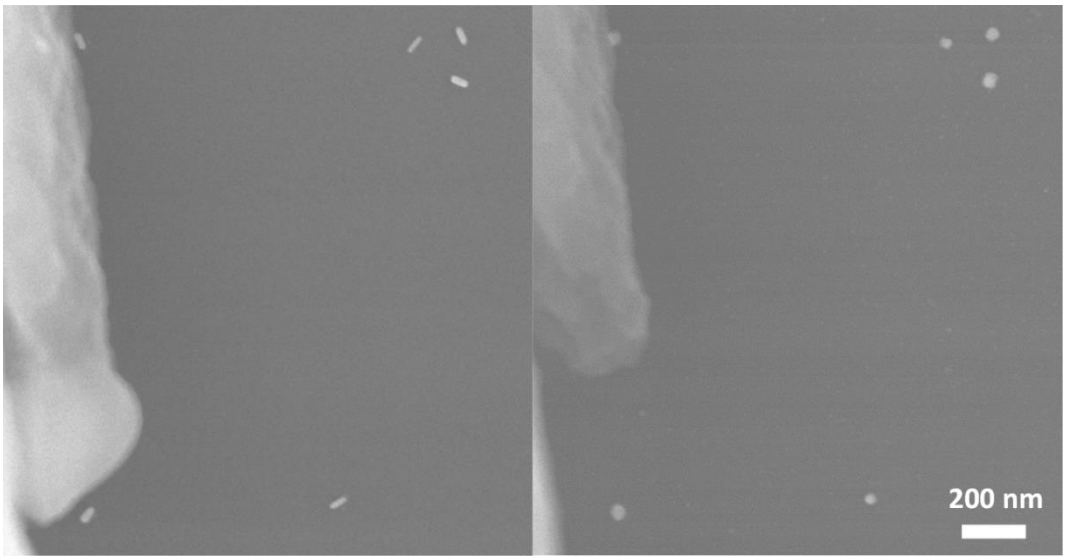


Figure 4.6: Correlated SEM image of gold nanorods on a TEM grid before and after exposure to 5 μM $HgCl_2$, 0.01 M $NaBH_4$ solution.

While no shape transition was observed for Hg concentrations of 100 nM and below by SEM imaging, the strong optical response of the gold nanorods to 200 nM Hg shown in Figure 4.3 suggests that it was a contributing factor. In the work of James et. al where no shape transition was reported, the optical shifts were max 3.8 nm.[271] Most probable, this issue arises from the difference in particle densities of the samples. The density of nanorods deposited on glass substrates (optical analysis) was kept low in

order to ensure minimum aggregation and light collection from isolated particles. In contrast, for SEM analysis the density of nanorods on the SiO_2 substrate was purposely increased in order to perform statistical analysis. Since for mercury solutions of equal concentrations the magnitude of the effects caused by mercury depends on the density of deposited nanorods, only qualitative correlation between results obtained by optical and electron microscopy analysis can be considered accurate.

Additionally, from the measured nanorod length and width figures, the nanorod volumes were calculated assuming a hemisphere capped cylindrical shape of the nanorods. Evidence that amalgamated nanoparticles retain a three-dimensional structure was obtained by tilted SEM imaging (not shown). The volume calculations showed that the volume of as-deposited nanorods was on average 20000 nm^3 and at the end of the reshaping process (10 μM $HgCl_2$) the average nanorod volume increased to 38000 nm^3, corresponding to an increase in volume of 90% and a calculated average mercury content of 38 at%.

Compositional Changes in Amalgamated Nanorods

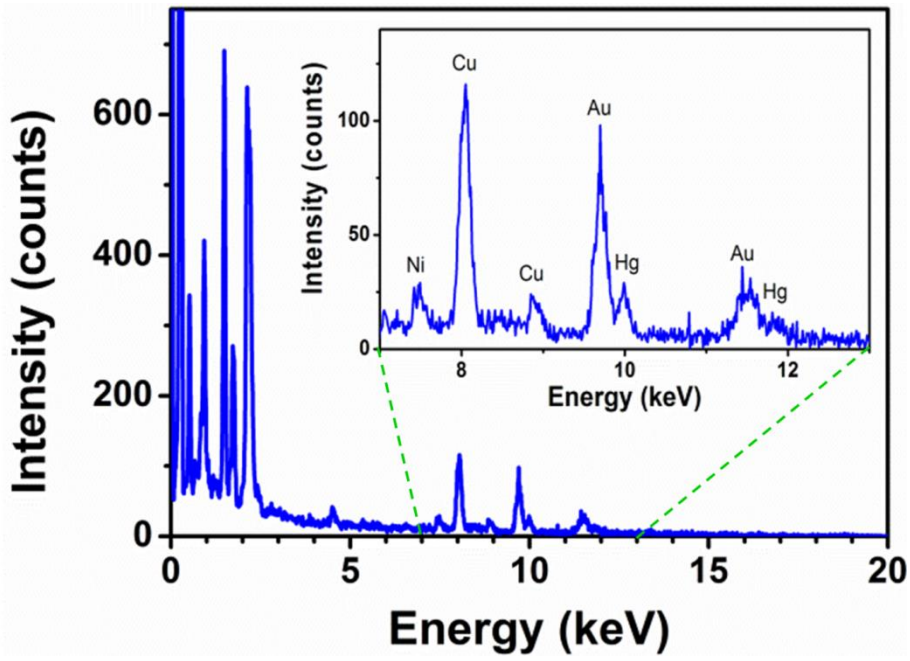


Figure 4.7: EDX spectrum of a single gold nanorod after exposure to 5 μM $HgCl_2$, 0.01 M $NaBH_4$ solution.

In order to demonstrate that the observed volume increase was associated with the incorporation of mercury into the metal structure, EDX analysis were performed on deposited nanorods exposed to 5 μM $HgCl_2$ (see Figure 4.7). Spectra for monomer, dimer and n-mer nanorods deposited on TEM carbon-grids were recorded and showed that all nanorod structures had equivalent compositions. The nanodods contained two elements: gold with an average content of 77.6 ± 4.0 atom % and mercury with an average content of 22.4 ± 1.8 atom %. The signal observed for copper was obtained from the material of TEM grids on which the nanorods were deposited.

4.3.3. Assessment of Mercury Detection via Gold Nanorod Amalgamation

As established in the previous section, single gold nanorods showed repeatedly a strong, quantifiable optical response towards chemically reduced Hg^{2+} which is caused by the combined effects of morphological and compositional changes in the nanorods. In the following section, the suitability of this method for the detection of Hg^{2+} in aqueous solutions is assessed in terms of sensitivity, reproducibility and selectivity.

Sensitivity and Reproducibility

In order to gain a better understanding of the mercury deposition process, more detailed measurements were performed. First of all the effect of exposure to $NaBH_4$ was investigated, in order to exclude any optical contribution from the reducing agent during exposure to mercury.

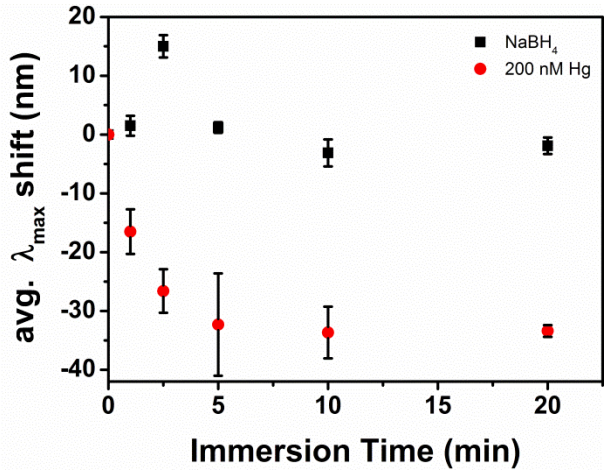


Figure 4.8: λ_{max} shift of nanorod scattering band over time averaged over 10 nanorods immersed in 0.01 M $NaBH_4$ solution (black squares) and immersed in $NaBH_4$ solution after addition of 200 nM $HgCl_2$ (red circles).

The λ_{max} shift was measured against time and averaged over 10 nanorods (see Figure 4.8, black squares). Initially (2 min), a red shift occurred, followed by a blue shift back to the initial wavelength. After 5 min small blue shifts in the λ_{max} were measured, until after 20 min no further spectral changes were detected. As the process appeared complete after 10 min, substrates with immobilised nanorods were immersed for 10 min in reducing agent solution and were spectroscopically analysed prior to immersion in $HgCl_2$ containing $NaBH_4$ solutions. In a similar manner, the effect of immersion time in $HgCl_2$ solutions was tested with a 200 nM $HgCl_2$ solution by monitoring the spectral changes of 10 nanorods over time (see Figure 4.8, red circles).

A strong blue shift occurred within the first 5 min, after which λ_{max} reached a plateau and no further spectral changes were detected after 10 min. Therefore, in all experiments substrates were immersed in $HgCl_2/NaBH_4$ solutions for 10 min before spectral examination.

Subsequently, the nanorods' response to increasing mercury concentrations was studied. Figure 4.9a displays darkfield scattering images of an individual nanorod exposed to mercury solutions of increasing concentrations.

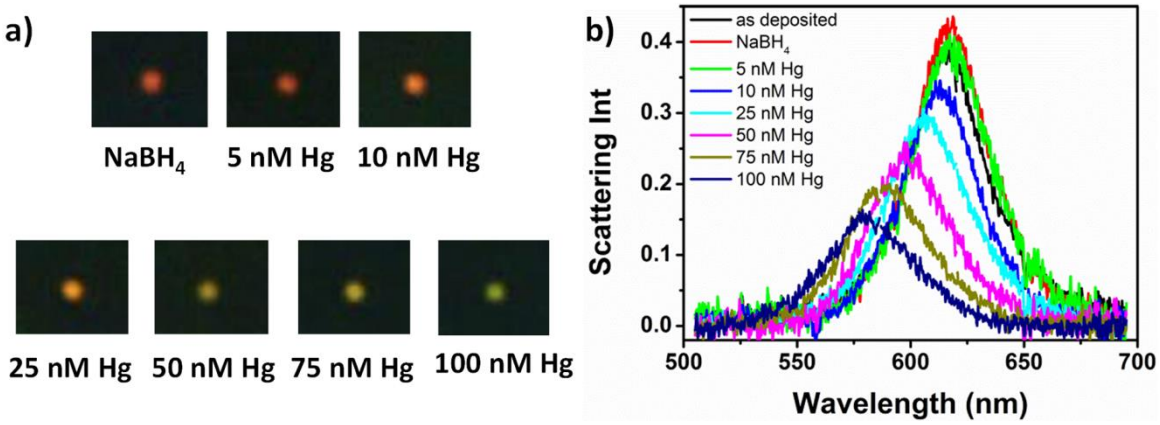


Figure 4.9: a) Scattering images of an individual nanorod (NR) exposed to increasing $HgCl_2$ concentrations of 5 nM - 100 nM; b) Corresponding scattering spectra of nanorod imaged in a); c) LSPR maximum wavelength position for 10 nanorods as-deposited and exposed to 5 - 100 nM $HgCl_2$ concentrations.

A gradual colour change from intense red to green was observed for this particular nanorod following 10 min immersion in $HgCl_2/NaBH_4$ solution between 5 nM and 100 nM $HgCl_2$. The corresponding scattering spectra are shown in Figure 4.9b. In all

measurements, the maximum peak intensity of the Lorentzian fit to the peak was taken as the position of maximum scattering intensity λ_{max} and was used to determine its shift. The as-deposited nanorod was characterised by a peak scattering intensity at λ_{max} 616 nm, which after immersion in $NaBH_4$ shifted slightly to 617 nm. The scattering gradually decreased in intensity with exposure to increasing concentrations of mercury. More importantly, the λ_{max} progressively blue shifted from 617 nm to 579 nm as the $HgCl_2$ concentration increased from 5 nM to 100 nM.

Figure 4.10a shows normalized scattering spectra of the single gold nanorod from Figure 4.9 exposed to increasing amounts of $HgCl_2$ where the λ_{max} shifts become very clear. In particular, λ_{max} moved from 617 nm to 616 nm, 612 nm, 606 nm, 599 nm, 587 nm and 579 nm as the Hg(II) concentration increased from 0 nM to 5 nM to 10 nM, 25 nM, 50 nM, 75 nM and 100 nM, respectively.

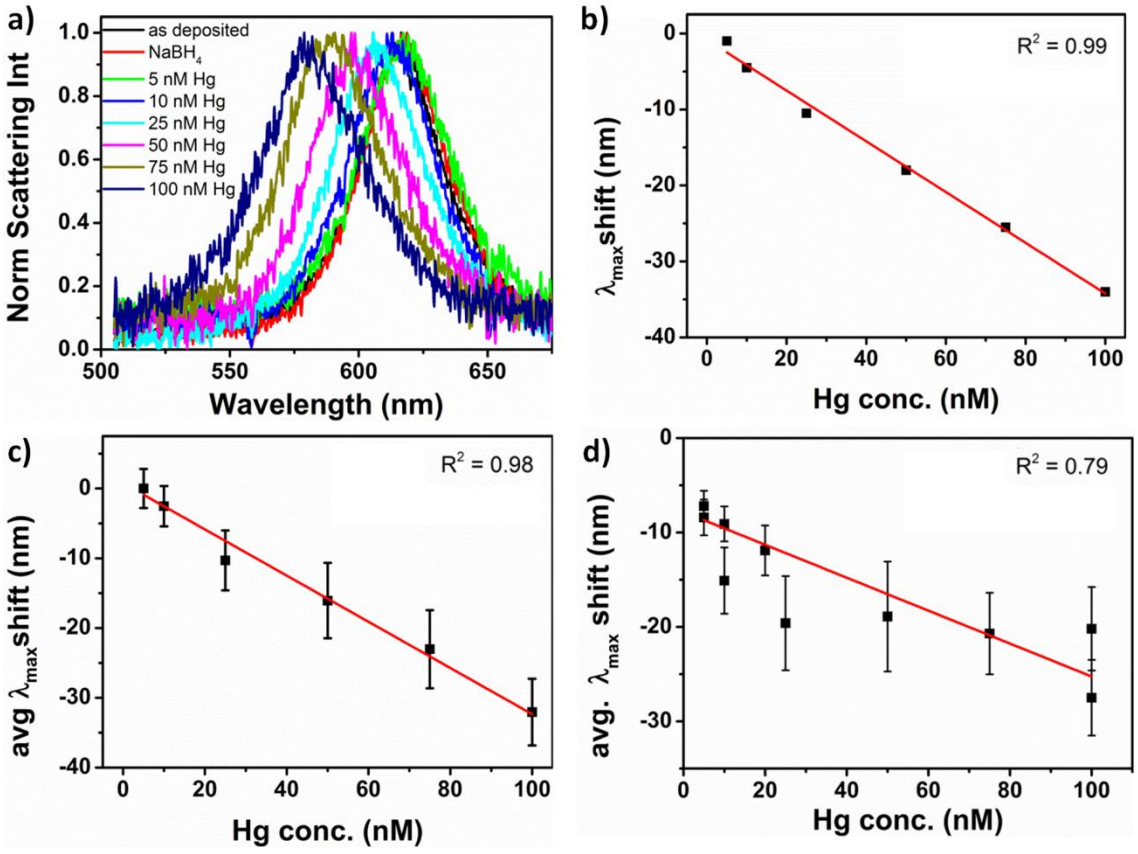


Figure 4.10: a) Normalised scattering spectra of an individual gold nanorod exposed to incremental amounts of $HgCl_2$ in presence of reducing agent $NaBH_4$. Linear fits to nanorod scattering spectrum maximum shifts in dependence of $HgCl_2$ concentration b) for a single nanorod c) averaged over twelve nanorods on one sample, d) averaged over 10 nanorods per sample for one sample per data point.

The observed spectral changes and the colour transition towards the green correlated well with the combined effects of the nanorods' compositional change and the observed decrease in AR.[275, 276]

Closer observation also revealed a slight increase in FWHM of scattering spectra obtained at higher mercury concentrations. This is expected due to increased plasmon damping in mixed composition particles.[124, 210] Figure 4.10b reports the λ_{max} shift of a single gold nanorod in dependence of the $HgCl_2$ concentration. λ_{max} values were extracted from Lorentzian fits to the recorded nanorod scattering spectra. A linear response with an R^2 = 0.99 was obtained for measurements performed in the 5 nM to 100 nM $HgCl_2$ concentration range, demonstrating the potential of this system for sensitive environmental analysis. The exposure of gold nanorods to 5 nM $HgCl_2$ solution resulted in a -1 nm shift, which was below the spectral resolution of 2 nm of the used optical setup. Exposure to 10 nM $HgCl_2$ solution, however, resulted in a -5.0 nm shift, well above the spectral resolution, suggesting that slightly lower concentrations could be detected by the system.

For comparison, Figure 4.10c reports the λ_{max} shift averaged over 12 gold nanorods as a function of the $HgCl_2$ concentration. A linear response with an R^2 = 0.98 was still obtained for measurements performed in the 5 nM to 100 nM $HgCl_2$ concentration range. However, relatively high standard deviation values were associated to the measurements, which reduced the sensitivity down to an estimated 45 nM limit of detection (LOD). The LOD was estimated with LOD = 3 *stdev*/*m* with *stdev* being the maximum standard deviation obtained for the data points in Figure 4.10c and *m* being the slope of the linear fit to the data points. This variability arose from nanorod size and shape variations resulting from the chemical nanorod synthesis; the geometric distribution resulted in a corresponding distribution of nanorod sensitivities.

Further reduced linearity and increased standard deviation was experimentally observed measuring λ_{max} shifts *vs.* $HgCl_2$ concentrations using nanorods deposited over different substrates (see Figure 4.10d). This was ascribed to the inevitable difference in nanorod distribution and density between substrates. The impact of nanorod size and shape distribution on their sensitivity towards mercury vapour was reported by James

et al.[271] The authors observed that larger AR nanorods were more sensitive than shorter AR nanorods. The same authors also reported that the density of nanoparticles in a film affected the mass limit of detection.[275] The shifts in LSPR wavelength depended on the mercury adsorbed per particle and were found to be directly proportional to the surface density of nanoparticles in the film. This issue has to be taken into account as it would affect the sensor response even if only individual nanoparticles were probed. The fabrication of substrates with a known number of deposited nanorods of homogeneous size (achievable by lithography processes) would eliminate potential sensitivity variations due to differences in nanoparticle density and shape distribution on the substrate and increase the reproducibility of mercury detection. Alternatively, normalising the λ_{max} shift as function of [Hg]/number of nanorod could be effective in addressing these issues. The use of dedicated spectroscopic imaging tools (e.g. hyperspectral imaging) for collection of individual spectroscopic responses from a large number of nanorods could also be considered for improving the reproducibility.[276] However, in both cases sensitivity reduction might occur due to the probing of multiple nanorods.

Selectivity

In order to investigate the selectivity of the mercury amalgamation process, gold nanorods were exposed to 100 nM solutions of $HgCl_2$, $Cd(ClO_4)_2$, $PbCl_2$, $NiCl_2$, $MnCl_2$ or $CuCl_2$ in presence of 0.01 M $NaBH_4$.

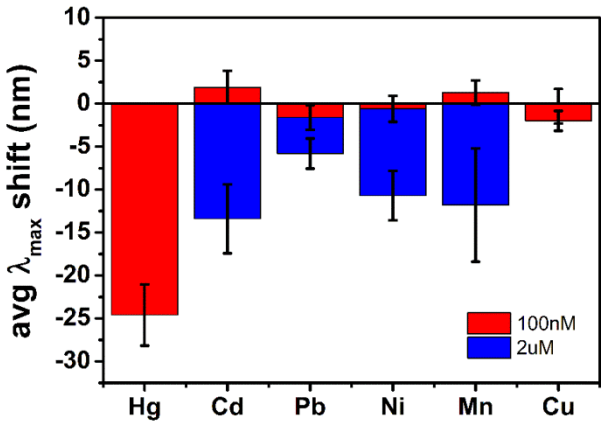


Figure 4.11:Average scattering maxima wavelength shifts of gold nanorods exposed to 100 nM $HgCl_2$ and 100 nM or 2 μM $Cd(ClO_4)_2$, $PbCl_2$, $NiCl_2$, $MnCl_2$ or $CuCl_2$.

Results are shown in Figure 4.11 for a $HgCl_2$ concentration of 100 nM and competitive ion concentrations of 100 nM (red columns) and 2 μM (blue columns), respectively. Each column represents the λ_{max} shift averaged over 10 measured nanorods analysed after 10 min exposure to the investigated ion. At a 100 nM concentration of $PbCl_2$, $NiCl_2$ and $CuCl_2$ the nanorods' LSPR showed a small blue shift below 3 nm. 100 nM $Cd(ClO_4)_2$ and $MnCl_2$ solutions caused a LSPR red shift also below 3 nm. In contrast, a 100 nM $HgCl_2$ solution caused a strong LSPR blue shift of 25 nm. When the competitor ion concentration was increased by 20 times, all ions showed blue shifts between 7 and 12 nm, still reasonably small compared to the lower concentration mercury response. The specificity of mercury detection could be attributed to the high standard reduction potential of Hg^{2+} (+ 0.851 V) compared to the other M^{2+} ions (Cd^{2+} = -0.403V; Pb^{2+} = -0.126 V; Ni^{2+} = -0.257 V; Mn^{2+} = -1.185 V; Cu^{2+} = +0.342 V).[277] In addition, the lower cohesive energy of Hg (0.67 eV) compared to other metals, such as Cd (1.16 eV), Pb (2.03 eV), Ni (4.44 eV), Mn (2.92 eV) and Cu (3.49 eV)[278] would have facilitated adsorption of mercury on gold followed by interdiffusion of the elements compared to the other metals, where no changes associated to nanorod morphology are expected.

Finally the detection of mercury was tested in real water samples to assess its efficacy in a complex matrix. A sample of river water was taken from the river Lee outside the institute and a sample of tap water was taken from a tap in the institute. Parts of the samples were externally analysed by ICP-MS on its metal contents by a certified testing service. The river water contained: 1.52 μM aluminium, <0.09 nM cadmium, 15.53 nM copper, 291.33 nM iron, <0.01 nM lead, 189.49 nM manganese, <0.15 nM mercury and <4.60 nM nickel. The tap water contained: 719.74 nM aluminium, <0.8 nM cadmium, 1.66 nM copper, 167.17 nM iron, <1.83 nM lead, 184.39 nM manganese, <0.20 nM mercury and 11.04 nM nickel. The river and tap water was filtered (0.45 μm pore diameter) and spiked with $HgCl_2$ in a concentration range of 5-100 nM for measurements.

Figure 4.12 shows the response of gold nanorods towards Hg^{2+} ions in river water. The single nanorod spectra in Figure 4.12a show a shift of the peak scattering wavelength λ_{max} from 665 nm to 672 nm after immersion of the sample in 0.01 M $NaBH_4$ river water. Following this red shift, after treating the sample with $HgCl_2$ containing

solutions λ_{max} gradually blue shifted from 672 nm to 671 nm, 666 nm, 661 nm, 654 nm and 644 nm as the concentration increased from 5 nM to 75 nM $HgCl_2$. For 100 nM $HgCl_2$ again a red shift to 649 nm was observed. The initial red shift after immersion in in 0.01 M $NaBH_4$ river water was observed for all 10 analysed single nanorods (see average shift in Figure 4.12b) and also in a repeat experiment (data not shown).

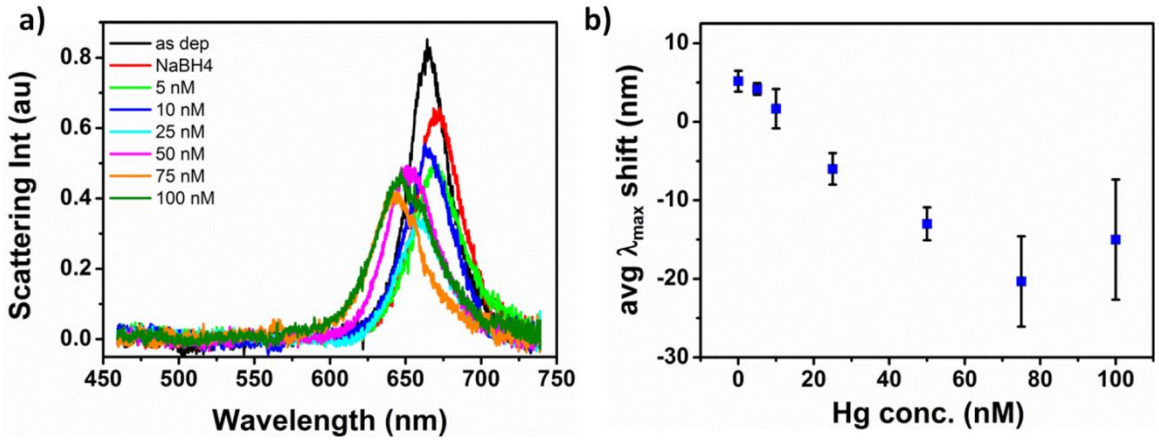


Figure 4.12: a) Typical set of scattering spectra for an individual gold nanorod exposed to incremental amounts of $HgCl_2$ in presence of reducing agent $NaBH_4$ in river water. b) Average scattering maxima wavelength shifts of gold nanorods in dependence of $HgCl_2$ concentration in river water averaged over ten nanorods on one sample.

As this was not observed in the experiments carried out in DI water some component present in the river water must have been deposited on the nanorods to cause the red shift. The red shift could have been caused by the deposition of one of the metals present in higher concentration like aluminium, iron or manganese, but also organic components that might be present in the river water. Whatever the cause of the red shift, the nanorods are evidently still accessible to reduced mercury in solution as the nanorods scattering spectrum is gradually blue shifting with increasing mercury content in the solution. Compared to the peak position in $NaBH_4$ solution, small blue shifts are observed for 5 and 10 nM mercury concentrations, however, only for concentrations above 10 nM a blue shift with respect to the as deposited nanorod can be registered. Consequently, while it is theoretically feasible, further refinements would have to be made to the current method to be able to detect concentrations of 10 nM and below in river water. Pointing to a further challenge for mercury detection in river water is the red shift of the nanorods' scattering spectrum that was observed at 100 nM $HgCl_2$ concentration. The shift was caused by the appearance of a deposit

on the sample. The deposit was not investigated in close detail, however, while it was not possible to remove it with water it could be removed by gentle rinsing with ethanol, indicating possibly organic material. Interferences of this kind are a challenge for any nanoscale sensor and would have to be addressed by development of a suitable pre-treatment of the analyte solution before the analysis.

Furthermore, real water mercury detection in tap water was investigated. Figure 4.13 shows the response of gold nanorods towards $HgCl_2$ in tap water. The as deposited nanorod's peak scattering wavelength λ_{max} of 618 nm remained unchanged after immersion in 0.01 M $NaBH_4$ tap water, then gradually blue shifted to 616 nm, 611 nm, 602 nm, 588 nm and finally 580 nm as the concentration increased from 5 nM to 100 nM $HgCl_2$.

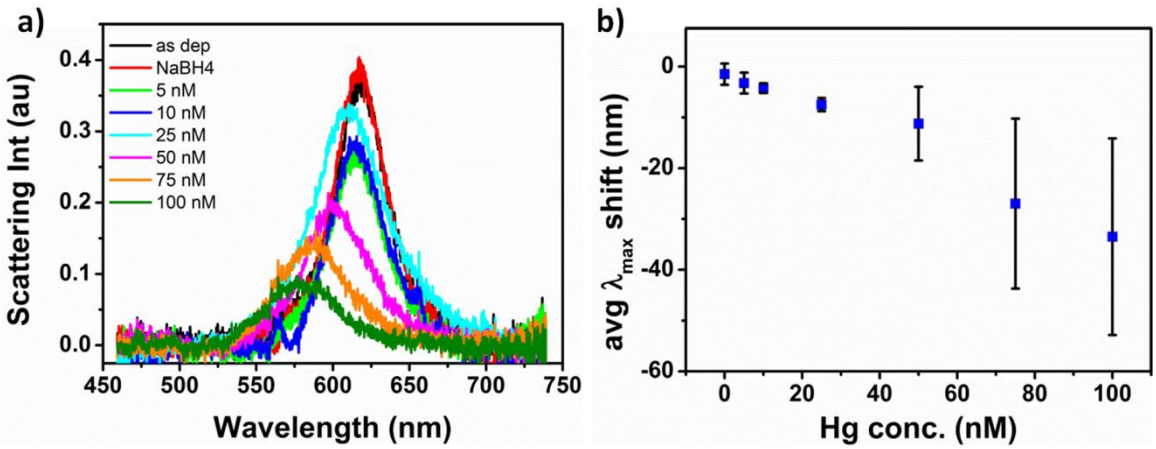


Figure 4.13: a) Typical set of scattering spectra for an individual gold nanorod exposed to incremental amounts of $HgCl_2$ in presence of reducing agent $NaBH_4$ in tap water. b) Average scattering maxima wavelength shifts of gold nanorods in dependence of $HgCl_2$ concentration in tap water averaged over ten nanorods on one sample.

Contrary to the measurements in river water, in tap water no red shift was observed after immersion of the sample in 0.01 M $NaBH_4$ solution without $HgCl_2$. Consequently, any λ_{max} shifts observed were attributed to the effect of mercury with a blue shift of 2 nm for a $HgCl_2$ concentration of only 5 nM. Unfortunately, also for the experiments in tap water after several measurement cycles the same deposit as observed in the river water experiments appeared on the sample. As the deposit did not cover all areas of the sample homogeneously diverging responses of nanorods at different locations on

the sample were obtained leading to the large error bars in the average λ_{max} shifts for 50 nM, 75 nM and 100 nM $HgCl_2$ concentrations in Figure 4.13b.

4.3.4. Investigation of Amalgamation Mechanism

Theoretical Calculations of Amalgamated Nanorod Scattering Spectra

Taken together, from the experimental findings, the shape transition as well as the change in chemical composition of amalgamated nanorods can be considered responsible for the observed scattering spectra of nanorods exposed to mercury, which appeared blue shifted, lowered in intensity and broadened compared to the spectra of as-deposited nanorods. In the following, the two factors are discussed separately. The λ_{max} blue shift associated to the decrease in nanorod aspect ratio is well known and has been extensively investigated.[279] Consequently, the reduction of the nanorods' aspect ratio seen with SEM analysis is expected to contribute to a blue shift of the nanorod scattering spectrum. Additionally, the shortening of the nanorod long axis during the shape transformation contributes to the lower intensity of the longitudinal scattering peak. Theoretical calculations were performed to assess the influence of the nanorod composition resulting from amalgamation on its λ_{max}, whereby the effect of the compositional change was taken in consideration independently from the above mentioned shape transition. For this purpose the nanorods were assumed as core-shell structures: at the centre a gold core with the average dimensions of 61 x 21 nm surrounded by a mercury shell of varying thickness to achieve a series of atomic ratios of mercury to gold. The scattering cross sections C_{scat} of core-shell nanorods with 0 to 50 at% Hg were calculated by adopting a dipole-limited model reported by Guyot-Sionnest for gold-silver core-shell nanorods[124] and James for gold-mercury core-shell nanorods.[271] Dielectric functions without size-dependent corrections were taken for bulk gold from Johnson and Christy[123] and for bulk mercury from Inagaki,[272] the average dielectric constant of the environment was estimated at 1.33. The calculated data points were fitted with Lorentzian functions to determine the maximum peak wavelengths and FWHM. Figure 4.14a shows the effect of change in nanorod composition represented by gold-mercury core-shell nanorods with mercury shells of increasing thickness corresponding to mercury concentrations of 0, 5, 10, 20, 30, 40 and 50 at%. A progressive blue shift of λ_{max} from

619 to 498 nm was calculated as the mercury percentage was increased from 0 to 50 at%, a trend that has been experimentally observed in Figure 4.9b. For these calculations, the volume of the nanorod core was considered constant. However, using this core-shell model one has to also take into consideration that by adding mercury shells of uniform thickness onto the gold core the dimensions of the nanorod alter somewhat: the volume of the nanorod increases and the aspect ratio decreases slightly. The effect of these changes was estimated by calculating the scattering spectra for a gold-gold core-shell nanorod with the same initial dimensions as the previously considered gold-mercury core-shell nanorod. The resulting spectra are presented in Figure 4.14b.

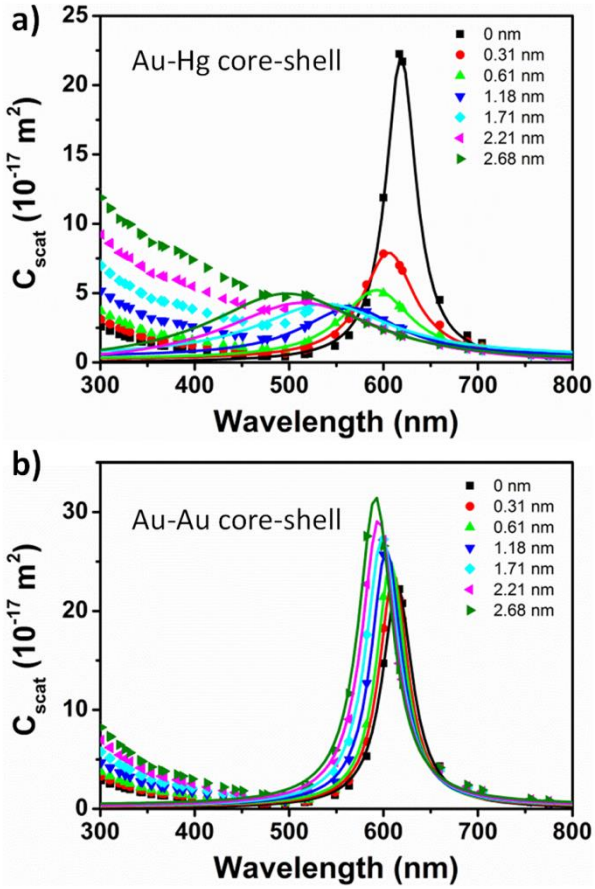


Figure 4.14: a) Calculated scattering cross sections for a gold-mercury core-shell nanorod with fixed gold core dimensions of 61 x 21 nm and increasing mercury shell thickness from 0 to 2.68 nm corresponding to 0, 5, 10, 20, 30, 40 and 50 at% mercury composition of the nanorod. b) Calculated scattering cross sections for a gold-gold core-shell nanorod with gold core dimensions of 61 x 21 nm and increasing gold shell thicknesses from 0 to 2.68 nm corresponding to 0, 5, 10, 20, 30, 40 and 50 at% mercury composition of the nanorod.

As the shell thickness increases and the nanorod AR decreases, the nanorod λ_{max} undergoes a slight blue shift. The intensity of the scattering peak increases due to the elongation of the long axis of the nanorod and the increase of nanorod volume. Comparison with the experimentally observed scattering spectra leads to the conclusion that this effect caused by the slight nanorod size modification can be considered minor in comparison to the changes arising from the dielectric properties of a mercury shell shown in Figure 4.14a.

Time-Dependent Studies of Nanorod Amalgamation

To gain insights into the mechanism of mercury-gold amalgam formation, time dependent darkfield experiments were carried out.

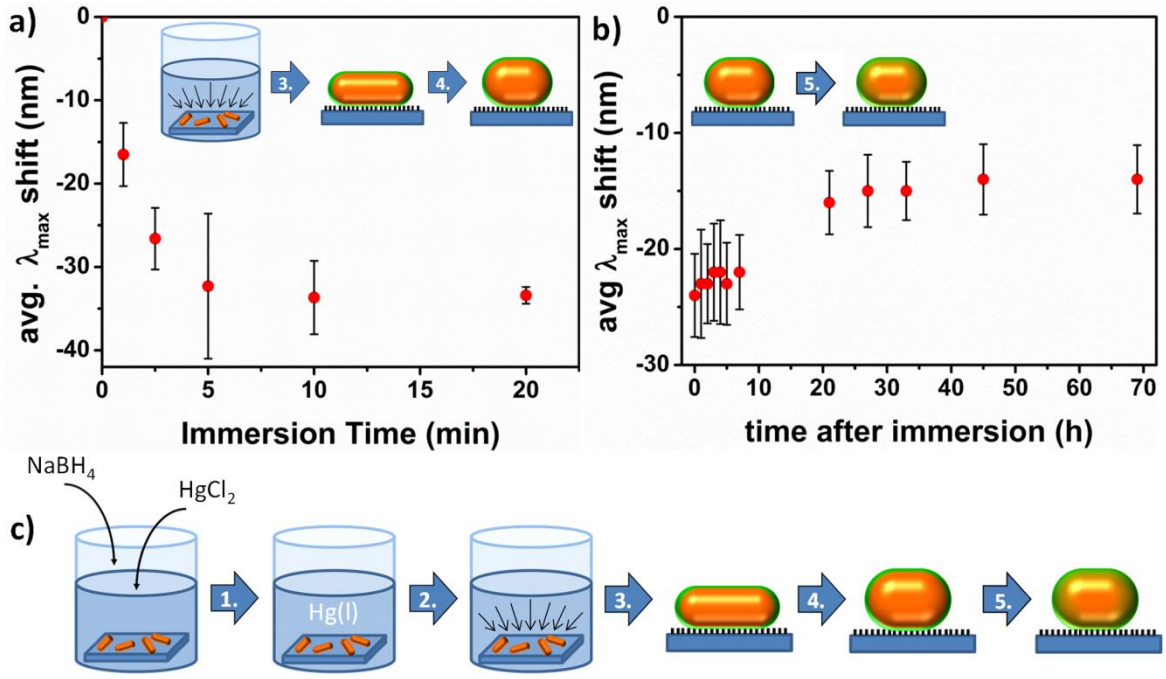


Figure 4.15: a) Averaged λ_{max} shifts in dependence of nanorod immersion in 200 nM $HgCl_2$, 0.01 M $NaBH_4$ solutions; b) Averaged λ_{max} LSPR shifts of nanorods exposed to air after immersion for 10 min in 100 nM $HgCl_2$, 0.01 M $NaBH_4$ solution; c) schematic of proposed amalgamation process.

In a first series of measurements the influence of immersion time of gold nanorods in $HgCl_2$/$NaBH_4$ solutions was investigated. Immobilised nanorods on glass substrates were immersed in 200 nM $HgCl_2$, solutions for 1, 2.5, 5, 10 and 20 min, respectively. Darkfield spectra were taken of 10 nanorods per substrate. The averaged optical responses (λ_{max} shifts) obtained for each immersion time are plotted in Figure 4.15a. Large blue shifts were observed in the first 5 min. Afterwards, progressively smaller

blue shifts were detected until for immersion times longer than 10 min no further optical changes were measured, sign that the deposition of mercury onto the gold nanorods was complete.

Figure 4.15b shows the λ_{max} shift evolution of amalgamated nanorods at various times after the exposure of the immobilised nanorods to mercury. A progressive λ_{max} red shift was observed, as determined by averaging the optical response of the same 10 nanorods analysed at every point in time as indicated in Figure 4.15b. The timescale for this process was slow with relatively large red shifts recorded in the first 10 hours, which relaxed into a plateau over the following 60 hours.

According to these experimental findings a hypothesis is made that the amalgamation process proceeded in 5 distinct steps as schematically illustrated in Figure 4.15c:

Step 1 consisted in reduction of Hg^{2+} by $NaBH_4$ and was driven by the positive redox potential of the reactions, as shown below:[277]

$$Hg^{2+}(aq) + 2\,e^- \rightarrow Hg(aq) \qquad 0.85V$$

$$2H^-(aq) \rightarrow H_2(aq) + 2\,e^- \qquad 2.25V$$

Step 2 was the transport of reduced mercury to the surface of gold nanorods. Step 3 corresponded to the deposition of mercury on the nanorod surfaces, leading to the formation of a gold core-mercury shell structure. This process was favoured by the high affinity between gold and mercury. Step 4 consisted in nanorod reshaping into reduced AR nanorods. We assume that during this step the nanorods maintained their gold core-mercury shell structure to a large extent. However, a certain degree of gold atom dissolution into the mercury shell was likely facilitated by the lower cohesive energy of mercury (0.67 eV/atom) versus gold (3.81 eV/atom).[278] As a consequence, diffusion of gold atoms at the gold/mercury interface or in the mercury shell led to the nanorod shape transformation. Steps 1-4 occurred as the substrate-immobilised nanorods were immersed in mercury solutions in the timeframe shown in Figure 4.15a (see schematic inset) and contributed to the observed large spectral blue shifts of nanorod scattering peaks. SEM images of nanorods taken immediately after immersion in 10 uM $HgCl_2$ solution confirmed that the nanorod shape transition is completed at

this point in time (see Figure 4.16). However, after the mercury-gold nanorods were taken out of the $HgCl_2$ solution, a red shift of the nanorod scattering spectra was observed, in the long timeframe shown in Figure 4.15b. We assume this process consists in diffusion of mercury deeper into nanorod lattices (see schematic inset). The attribution of spectral red shifts to inward diffusion of mercury atoms was also proposed by Mertens for spherical gold nanoparticles based on detailed experimental and theoretical findings.[208]

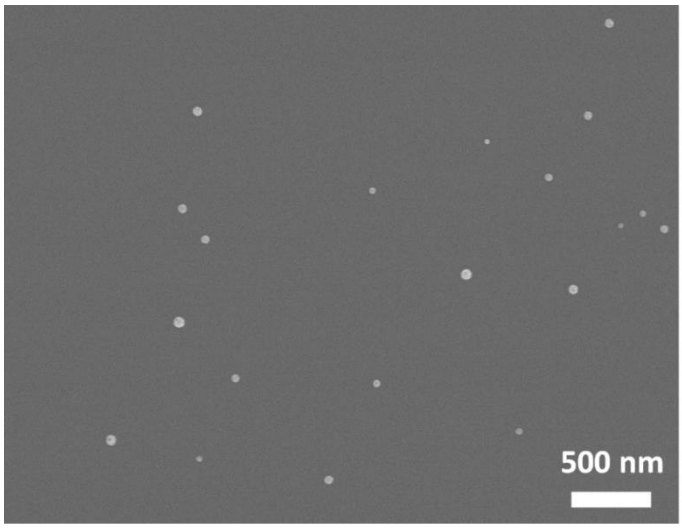


Figure 4.16: SEM image of gold nanorods taken immediately after immersion in 10 μM $HgCl_2$ solution.

4.4. Conclusion

In conclusion, individual gold nanorods immobilised on substrates displayed a strong spectroscopic response when exposed to chemically reduced mercury. The response was ascribed to formation of a mercury-gold amalgam which caused alteration in nanorod shape and composition. This constituted the basis for demonstration of highly sensitive and selective sensing based on single nanorods. In fact, appreciable λ_{max} shifts in single nanorods were obtained for $HgCl_2$ concentrations as low as 5 nM and the λ_{max} shift response was linear within Hg^{2+} concentration range 5 nM - 100 nM. Mercury detection could also be demonstrated in spiked river and tap water samples. However, the carried out experiments showed also that a gap still exists between laboratory use demonstration and applicability to real samples. In particular, for the presented method issues related to nanostructure shape and density distributions as well as minimising interferences in complex real water matrices will have to be addressed before highly sensitive real-world analysis can be performed. Nevertheless, the reported linear correlation and high selectivity make this approach potentially suitable for on-site mercury analysis using a miniaturised portable spectrometer.

Additionally, the mechanism of nanoscale gold-mercury amalgamation formation was investigated. A mechanism for amalgam formation was proposed comprising 5 main steps, including Hg^{2+} reduction, mercury deposition on nanorod surfaces and consequent reshaping and diffusion of mercury into nanorod lattices. The understanding of the mechanism regulating the incorporation of mercury into metal nanorods and the consequent reshaping process are technologically important for a number of applications ranging from sensing to catalysis. The present work also shows that nanoparticle alloys with specific optical features can be synthesized by control of the mercury deposition conditions.

Chapter 5 - Investigation of Gold Nanorod Amalgamation with Darkfield Spectroelectrochemistry

This chapter covers the investigation of electrochemical reduction of Hg^{2+} on immobilised single gold nanorods and subsequent amalgam formation. A suitable spectroelectrochemical cell was designed for in-situ real-time darkfield transmission spectroscopy during electrochemical experimentation. The ITO/gold nanorod working electrode was analysed by capacitive charging experiments in KCl before Hg^{2+} was reduced by linear sweep voltammetry (LSV). In-situ real-time darkfield spectroscopy during LSV in 1-4 μM mercury solutions was performed and additionally, LSV and chronoamperometry (CA) as Hg^{2+} reduction techniques were compared.

5.1. Introduction

In the previous chapter a very sensitive optical response of gold nanorods to chemically reduced mercury was demonstrated. While the use of $NaBH_4$ as a reducing agent comes with many positives like a very fast and complete reduction of all Hg^{2+} ions present in the solution and facile experimental procedure, it comes with negatives as well. Foremost is the hydrogen evolution from the oxidation of the hydride ions which prohibits in-situ experimentation for further study of the processes occurring during Hg^{2+} reduction and nanorod amalgamation. Additionally, due to the strength of $NaBH_4$ as a reducing agent, many interfering metal ions potentially present in the solution may be reduced as well and hence may diminish the selectivity and sensitivity of the method. To overcome these limitations a promising method is single particle dark field spectroelectrochemistry whereby an electrochemical setup is used for a targeted reduction of Hg^{2+} ions while in-situ the spectroscopic response of single nanoparticles can be recorded in real time.

In a general sense, spectroelectrochemistry combines the benefits of various spectroscopic methods like UV-Vis, NIR and IR absorption, Raman spectroscopy, X-Ray or magnetic resonance spectroscopy with the benefits of electrochemistry. It is commonly used for the identification of species by spectroscopy while studying the kinetics of a reaction electrochemically.[280-282] More recently, spectroelectrochemical methods were shown to deliver enhanced characterisation of nanostructured electrodes, nanoelectrodes and charge-transfer at the nano level. For this purpose, the spectroscopic techniques included surface enhanced Raman scattering (SERS)[283-285], electrochemiluminescence (ECL)[286-288] or darkfield scattering.[276, 289, 290] For example, Mulvaney et al. studied the electrochemical charging of single gold nanorods in KCl, detecting a spectral tuning of the nanorods scattering wavelength using dark field spectroelectrochemistry.[289] Very recently the same group reported monitoring of underpotential deposition of silver on gold nanostars by darkfield spectroelectrochemistry.[219] Silver was found to form a layer on the gold nanostars, leading to a blue-shift of the nanostars' scattering spectrum of more than 100 nm. In this context, the gold-mercury system studied in this work is promising to be an interesting subject as the deposition of mercury on gold nanorods

is expected to additionally lead to the amalgamation of mercury with the gold and to a shape transition of the nanorods similar to what was observed in Chapter 4. In-situ measurements facilitated by the spectroelectrochemical setup are expected to bring new insights into the amalgamation process and could potentially lead to an improved mercury detection method.

To the best of my knowledge, this is the first time the reduction of Hg^{2+} ions on gold nanorods and resulting amalgamation was studied by single particle darkfield spectroelectrochemistry. For this purpose, a suitable spectroelectrochemical cell comprised of an ITO/gold nanorod working electrode, platinum counter electrode and platinum pseudo reference electrode was designed compatible with a darkfield transmission optical setup (Section 5.3.1). The ITO/gold nanorod working electrode was analysed by capacitive charging experiments in Potassium Chloride (KCl) solution (Section 5.3.2) before Hg^{2+} from 5 μM solution was reduced by linear sweep voltammetry (LSV). Experiments showed that no passivation of the ITO substrate was required and that the Hg^{2+} reduction was confined to the gold nanorod surfaces leading to a pronounced blue shift of the nanorod scattering spectra of up to 197 nm. SEM imaging showed a corresponding shape transition of the nanorods. In-situ real-time dark field spectroscopy during LSV in 1-4 μM mercury solutions was performed and additionally, chronoamperometry (CA) was assessed as an alternative Hg^{2+} reduction method (Section 5.3.3).

5.2. Experimental Methods

5.2.1. Spectroelectrochemical Sample Preparation

Nanorod Synthesis

Gold nanorods were synthesised after a seed-mediated method pioneered by El Sayed.[32] Briefly, via fast reduction of $HAuCl_4$ with $NaBH_4$ small Au crystals are synthesised, which in turn are used as seeds for nanorod growth in a slow reduction of $HAuCl_4$ with ascorbic acid. The typical dimensions of the resulting nanorods are 11 x 41 nm. Subsequently larger nanorods were synthesised by overgrowth of the nanorods obtained from the seed-mediated method after a method developed by Marzán.[291] Ascorbic acid is added to the solution of seed-mediated synthesised nanorods, which reduces remaining Au(I) in the solution. As a result the nanorods grow isotropically up to a size of 39 x 76 nm.

Working Electrode Fabrication

Transparent electrodes required for spectroelectrochemical experiments consisted of glass substrates coated with a 20 nm ITO film (fabricated by Dan O'Connel) modified with gold nanorods.). ITO was evaporated in a Leybold SyrusPro 710 e-beam evaporation system in a vacuum chamber evacuated to < 5 x 10^{-6} Torr and with a background flow of 5 sccm O_2. The system also uses an APS500 plasma source during the evaporation to increase the density of the film and to improve transparency of the film. The evaporation rate of ITO is 0.2 nm/sec. A 20 nm thick ITO coating is conductive, yet transparent and enables correlated imaging of the particles with optical transmission microscopy and scanning electron microscopy (SEM). Additionally, a unique pattern of 10 nm deep lithographically etched binary alignment marks in the ITO layer allows an exact localisation of each particle. The samples were patterned by a standard UV lithography process: hexamethyldisilazane (HMDS) was spun onto the samples at 3000 rpm for 50 s, then S1805 photoresist was spun on at 3000 rpm for 50 s. Subsequently, the samples were hot-plate baked at 115°C for 2 min, before the samples were exposed to UV light beneath the patterned quartz mask in a Karl Suss MA1006 mask aligner. The UV exposure dose was 40 mJ/cm^2. The samples were then developed in Microposit MF319 developer for 25 s, rinsed well in DI water and blow-dried under a stream of nitrogen. After the patterning, the ITO was etched in an STS

ICP (Inductively Coupled Plasma) etching system. The etch took place at 10°C and at 8.0 mT using CH_4 (5 sccm) and Ar (45 sccm). The ICP Rf power was 450 W, the platen power was 50 W giving a peak-to-peak voltage V_{pp} of about 435 V. The resulting ITO etch rate was 0.75 nm/sec. After etching the remaining photoresist was removed by immersing the samples in R1165 resist remover at 90°C for 20 min and rinsing well in DI water followed by blow-drying in N_2.

Next the transparent ITO substrates were modified with gold nanorods. To obtain sufficiently spaced nanorods for single particle dark field spectroscopy, gold nanorods (39 x 76 nm) from solution with ca. 33 pM, were deposited by flow deposition on ITO coated glass cover slips. Subsequently, the substrates were rinsed with 40 °C deionised water to remove surfactants remaining from the nanoparticle/nanorod synthesis and blown dry under a stream of nitrogen.

Spectroelectrochemical Cell Fabrication

The spectroelectrochemical cell was assembled layer by layer for each working sample. Spacers for electrical insulation and formation of the cell were purchased from Stratech (Secure Seal Imaging Spacers). First copper foil tracks (25 μm thickness) were attached to one side of an optical imaging spacer (9 mm well diameter, 120 μm thickness), in order to electrically contact the transparent, nanorod modified working electrode. This spacer was then attached to the working electrode making sure the copper tracks were completely enclosed by the spacer to prevent any contact of the copper with the solution later. The spacer forms the first layer of a central well and the hole in the spacer defines the area of the exposed working electrode. Next, a Pt wire (50 μm thickness) was placed between this first and a second imaging spacer such that a short piece of Pt wire was exposed to act as a pseudo-reference electrode. On top of the second imaging spacer a coiled Pt wire (50 μm thickness) was placed around the well in the centre of the spacers to act as a counter electrode. Finally, a silicone spacer (13 mm well diameter, 500 μm thickness) was attached concentrically to the imaging spacers to create the final well with a volume of 82 μl. The spectroelectrochemical cell could then be sealed on top with a clean glass cover slip after solution injection.

5.2.2. Sample Characterisation using Dark Field Optical Microscopy and Spectroscopy

Scattering spectra of individual nanorods were acquired with an inverted IX-71 Olympus microscope with an oil immersion darkfield condenser (Olympus U-DCW, 1.4 NA) and 100x objective (Olympus MPlanApo 100x/0.95 NA). The sample was illuminated with a 100 W halogen lamp. The light collected by the objective was directed either onto a colour CMOS camera (DCC1645C, ThorLabs) for image and video acquisition or onto the entrance slit of a monochromator (SP-2356, Acton Research). The light was dispersed by an optical grating (300 grooves/mm, blazed at 500 nm, 350nm < λ < 850nm) and directed onto a thermoelectrically cooled, back illuminated CCD (Spec10:100B, Princeton Instruments) for spectra acquisition. The sample polarisation rate was determined by a polariser placed in collection between the sample and the monochromator. The experiments were performed by first recording an image of the sample with a mirror in the light path of the spectrometer. Once a suitable nanostructure was selected, the mirror was switched to the grating to disperse the scattered light and a spectrum was recorded using an acquisition time of 30 s for an individual spectrum or 1 s with 1 spectrum/s for continuous spectra acquisition in real-time measurements. The scattering spectra were background corrected by subtracting and dividing by a background scattering spectrum taken from a nearby clean area on the sample. To determine the peak scattering wavelength the spectra were fitted with a Lorentzian function (equation 2.1)

5.2.3. Spectroelectrochemical Mercury Reduction and Amalgamation Monitoring

Spectroelectrochemical experiments were performed using an IVIUM PocketSTAT in a three electrode system, whereby gold nanorod modified ITO coated glass cover slips were used as the working electrode and 50 μm Pt wires as counter and pseudo-reference electrodes. A 0.1 M KCl solution at pH 6.5 was used as supporting electrolyte, to which various amounts of $HgCl_2$ were added for the nanorod amalgamation experiments. Initially, for every sample Linear Sweep Voltammetry (LSV) and for some samples Cyclic Voltammetry (CV) and/or Chronoamperometry (CA) were

performed in 0.1 M KCl. For all LSV and CV measurements the potential was scanned at a rate of 50 mV/s with a potential step height of 10 mV. Scattering spectra of selected gold nanorods were recorded before and after the electrochemical step or in real-time during the electrochemical step. The solution was then exchanged for 0.1 M KCl with added $HgCl_2$ for mercury concentrations ranging from 1 μM to 5 μM. Again LSV, CV or CA measurements were performed with scattering spectra taken of the same selected nanorods before and after or in real-time during the electrochemical step. For background subtraction the I-V and I-t curves obtained from the scans in only KCl were subtracted from the respective data obtained in Hg(II) containing electrolyte.

5.3. Results and Discussion

5.3.1. Design of Spectroelectrochemical Cell

Spectroelectrochemical cells for combination of UV-Vis- or Raman-spectroscopy with electrochemical methods are readily commercially available. However, this is not the case for combination of darkfield transmission spectroscopy with electrochemistry, due to limited research in this field to date. Various boundary conditions have to be taken into considerations when designing a cell for this application. For electrochemistry a three electrode system is required that allows easy connection to a potentiostat. For integration of the cell into a darkfield optical system additional constraints apply: transparency of the electrochemical cell for transmission measurements, cell thickness of 1 mm due to the numerical apertures of the dark field condenser and objective between which the cell is placed, and sealing of the cell to allow application of index matching immersion oil.

A schematic of the final spectroelectrochemical cell design is shown in Figure 5.1a.

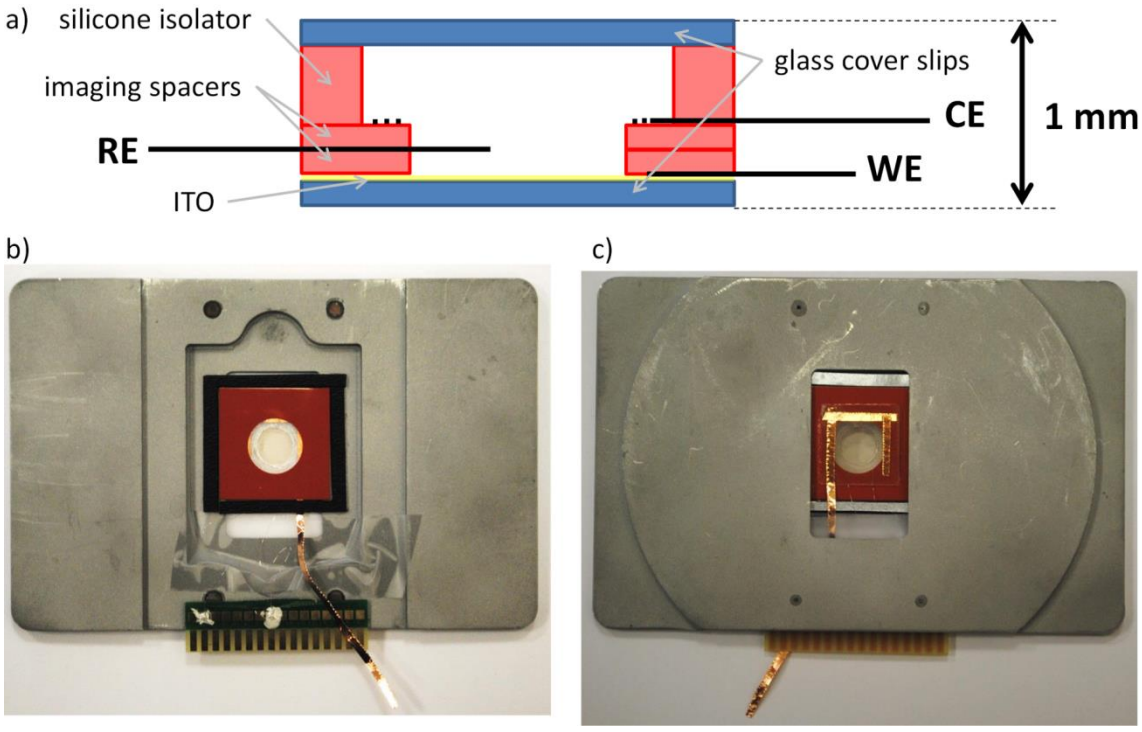


Figure 5.1: a) Schematic cross section of the designed spectroelectrochemical cell indicating positions of the ITO/gold working electrode (WE), platinum pseudo-reference electrode (RE) and counter electrode (CE). Photographs of the spectroelectrochemical cell mounted in the aluminium holder viewed from b) the top and c) from the bottom.

From the bottom to the top the spectroelectrochemical cell is made of a glass cover slip with a 20 nm ITO coating and immobilised gold nanorods forming the working electrode. Copper foil tracks are contacting the gold nanorods via the ITO layer. Two 0.12 mm thick double adhesive imaging spacers electrically insulate all copper tracks and define with a 9 mm inner hole diameter the exposed active area of the working electrode in the centre of the cover slip. A platinum wire is positioned between the two imaging spacers such that a piece is exposed to act as a pseudo reference electrode. Around the perimeter of the central well a coiled platinum wire serves as a counter electrode. A 0.5 mm thick silicone spacer with a 13 mm inner diameter creates the main chamber of the cell which can then be sealed off by a cover slip on top after injection of a solution. The cell is then placed in a custom made aluminium holder compatible with the microscope stage to allow for the spectroelectrochemical investigation of mercury - gold nanorod amalgamation. The cell is held in place in a fixed frame leaving it accessible for contact with the dark field condenser from above and an objective from the bottom. While the working electrode is connected via copper foil strips, the platinum counter and pseudo reference electrodes are connected to contact pads with conductive silver paint as can be seen in Figure 5.1b,c. The electrodes can then be easily connected to a potentiostat via crocodile clips to the contact pads.

5.3.2. Working Electrode Characterisation

Capacitive Charging of Gold Nanorods

Spectroelectrochemistry was chosen as a method with the intention of spectroscopically observing the amalgamation of single gold nanorods with mercury before, during and after a controlled, electrochemical reduction of Hg^{2+} on the nanorods. Therefore, it is of primary importance to verify that gold nanorods are in conductive contact with the ITO. As surface plasmon resonance is an effect based on the oscillations of the conduction band electrons, it is expected to be modified by decreasing or increasing the free electron density in a nanorod induced by charging of a nanorod.[59, 273, 289] Thus, non-faradaic charging experiments while recording the nanorods optical signature have been carried out. For this purpose LSVs and CVs were performed in 0.1 M KCl while recording in-situ in real-time a single gold nanorod's

scattering spectrum every second. Figure 5.2 shows the recorded potential and current during LSV with correlated scattering spectra.

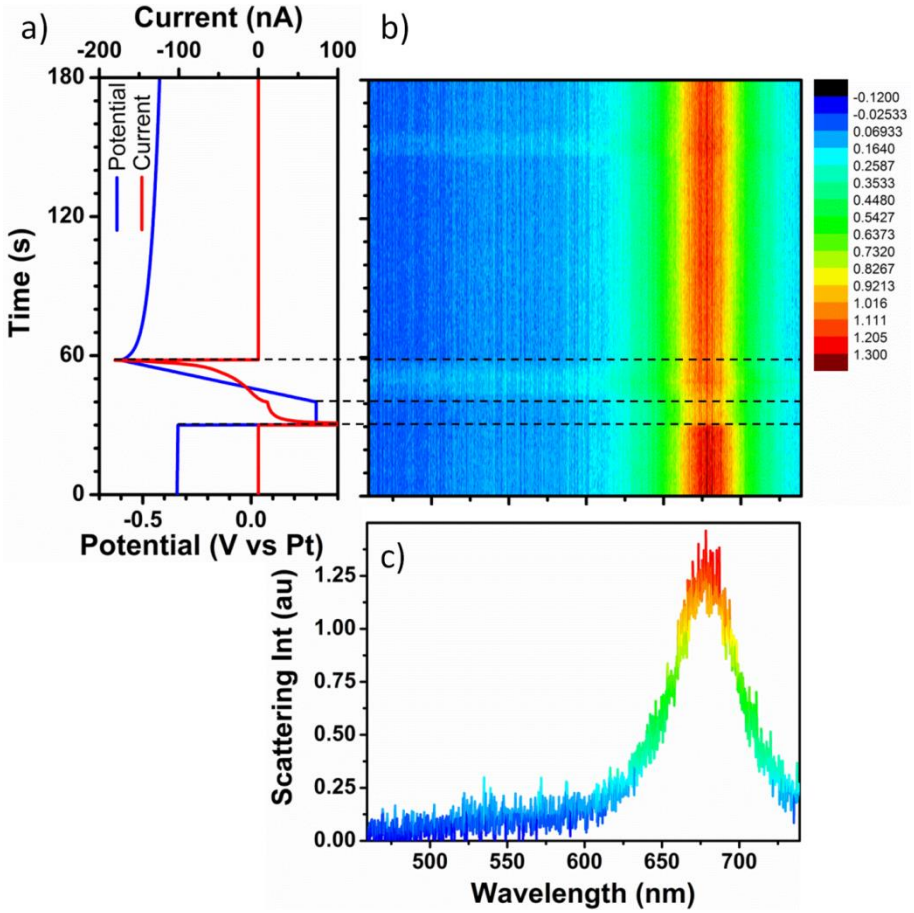


Figure 5.2: a) Potential and Current curves for a 0.3 V to -0.6V LSV in 0.1 M KCl. b) 2D plot of 180 single nanorod scattering spectra recorded during the LSV. c) Spectrum recorded at 0s as typical example for a single nanorod scattering spectrum showing colour assignment to scattering intensity values.

First the open cell potential (ocp) was monitored for 30 s, then the potential was held at 0.3 V for 10 s before it was scanned linearly to -0.6 V at a rate of 50 mV/s in 10 V steps and finally the ocp was recorded for further 240 s. Throughout the experiment scattering spectra of the observed nanorod were recorded every second. As an example the first scattering spectrum recorded is shown in Figure 5.2c. This graph also illustrates the assignment of colours to scattering intensity values of the spectra for the colour mapping. In Figure 5.2b all 180 recorded spectra are displayed in a 2D colour map. By fitting the recorded scattering spectra with a Lorentzian function the peak position λ_{max}, the peak intensity and the full width at half maximum (FWHM) can be extracted. The values for these parameters are plotted in Figure 5.3. During the first

30 s of ocp λ_{max}, the peak intensity and the FWHM remained constant with minor noise fluctuations. During the 10 s at 0.3 V, λ_{max} shifted gradually to shorter wavelengths while the peak intensity dramatically dropped and the FWHM increased significantly. During the linear sweep period, λ_{max} further decreased while the peak intensity increased and the FWHM decreased again. Finally, during the following opc period λ_{max} slowly shifted to higher wavelengths again, the peak intensity further recovered towards its initial value and the FWHM remained constant apart from noise fluctuations.

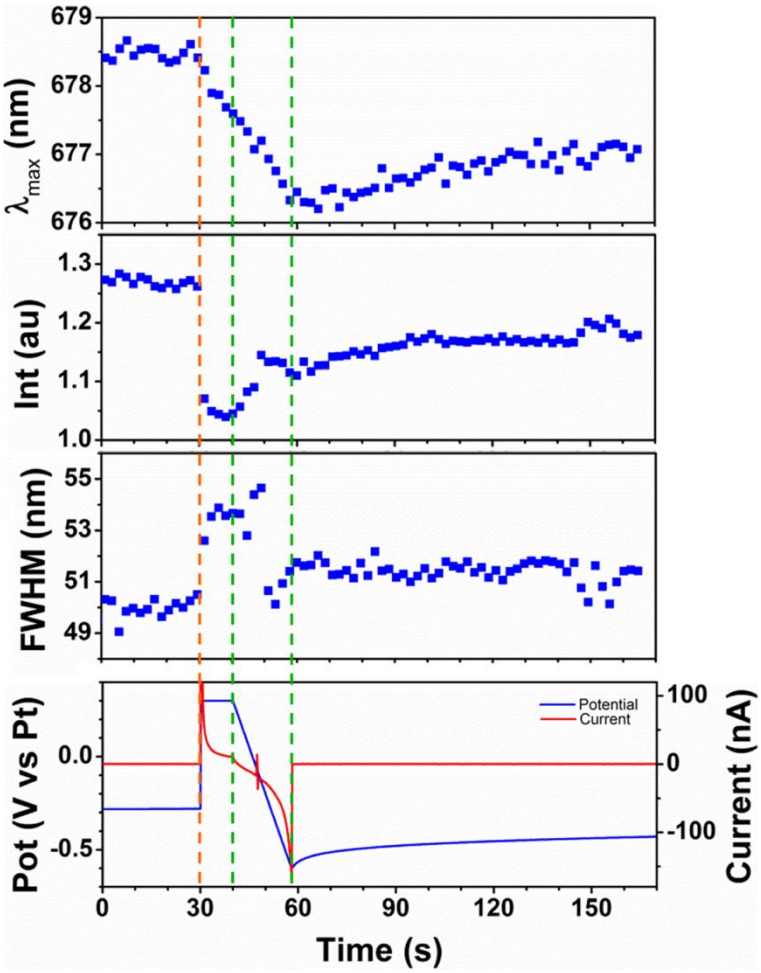


Figure 5.3: λ_{max}, peak intensity and FWHM values extracted from Lorentzian fits to spectral data correlated with potential and current curves recorded during LSV.

The drop of λ_{max} during the 10 s at 0.3 V was not anticipated and lacks an explanation. The linear decrease of λ_{max} during negative charging of the nanorod, however, was expected and is consistent with the electron density tuning model.[59, 289]

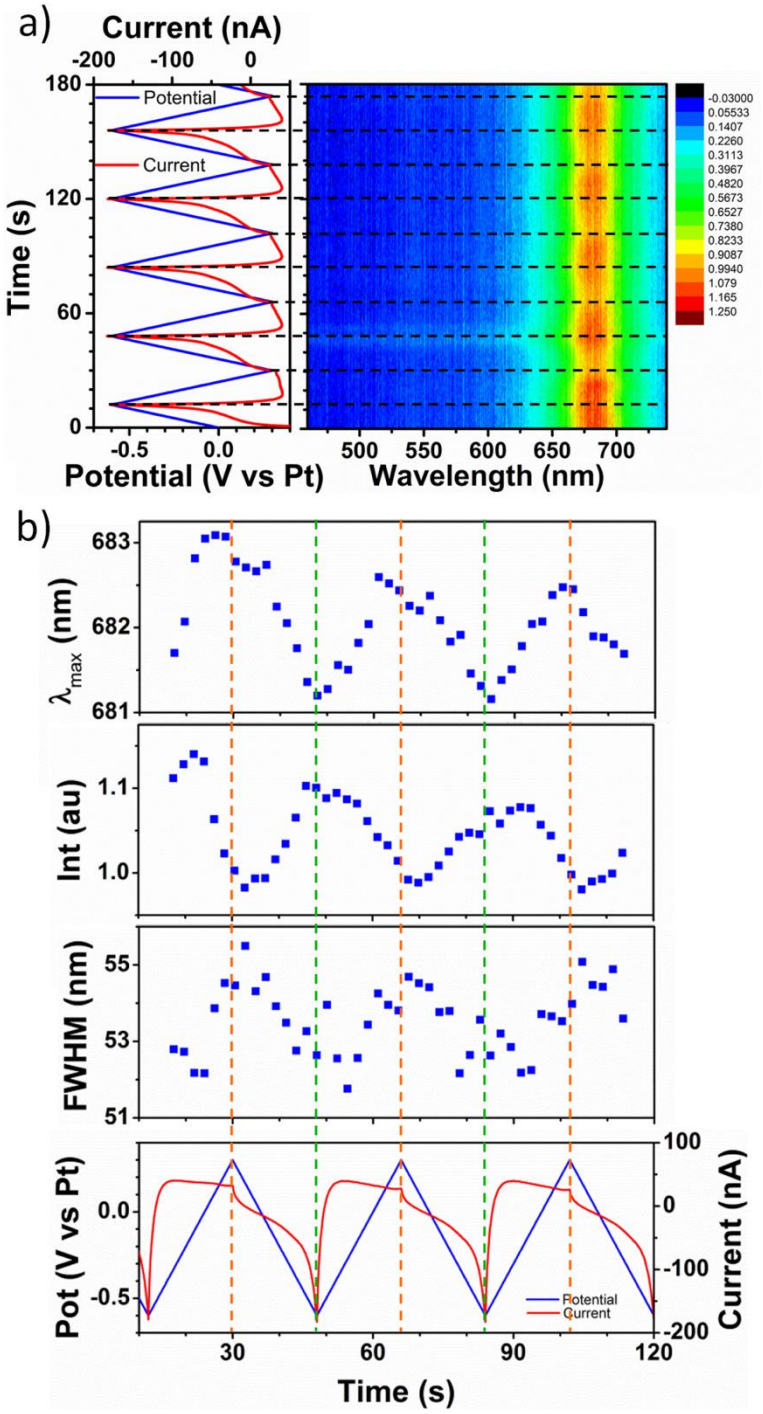


Figure 5.4: a) Potential and Current curves for a 0.3 V to -0.6V (starting at 0 V) CV in 0.1 M KCl correlated with a 2D plot of 180 single nanorod scattering spectra recorded during the LSV. b) λ_{max}, peak intensity and FWHM values extracted from Lorentzian fits to spectral data correlated with potential and current curves recorded during CV.

The changes in peak intensity and FWHM, on the other hand, cannot be explained by the electron density tuning process. Several models have been proposed in literature for the surface plasmon damping at positive potentials. Dahlin et al. suggested the formation of a gold chloride complex forming an optically lossy layer on the gold

surface.[292] Klar et al. suggested adsorbate damping following the hydration of the gold surface.[290] Both approaches deliver possible explanations for the increased FWHM of the nanorods scattering spectra.

Additionally, non-faradaic charging experiments while recording the nanorods optical signature have been carried out using cyclic voltammetry (CV) in 0.1 M KCl. Figure 5.4 shows the recorded potential and current during CV with correlated scattering spectra. When the potential is swept linearly back and forth in cycles it can be seen that the charging and discharging of the nanorod is a reversible process. λ_{max} and the FWHM increase and decrease with the applied potential, while the peak intensity shows the opposite behaviour. While this particular nanorod showed quite a linear behaviour, it has to be mentioned that in similar experiments in NaCl where many nanoparticles were monitored in parallel Landes et al. showed that the optical response of nanoparticles to electrochemical charging can be quite diverse with reversible and irreversible, linear and non-linear behaviour.[276]

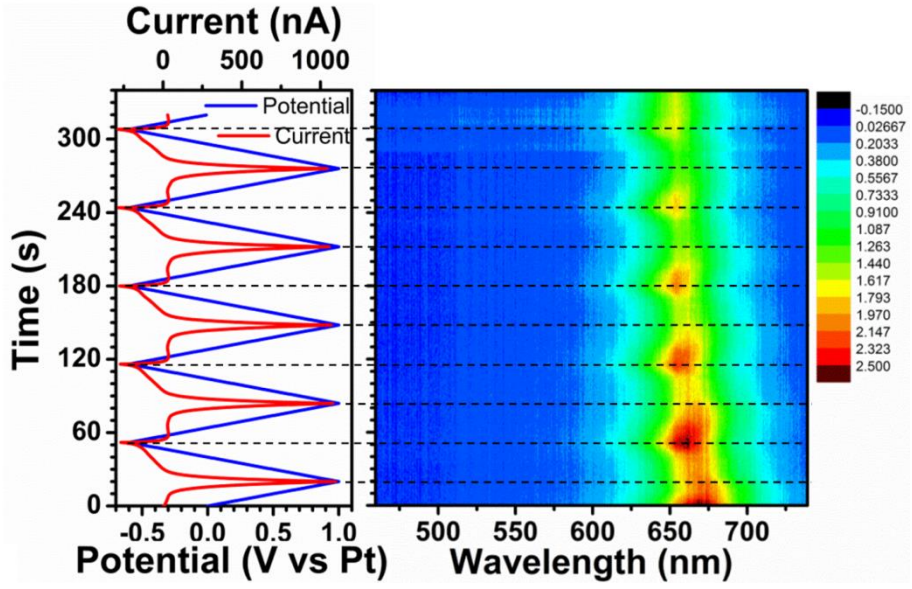


Figure 5.5: a) Potential and current curves of a CV between -0.6 V and 0.3 V in 0.1 M KCl correlated with a 2D plot of 180 single nanorod scattering spectra recorded in-situ during the CV. b) Potential and current curves of a CV between -0.6 V and 1 V in 0.1 M KCl correlated with a 2D plot of 340 single nanorod scattering spectra recorded during the CV.

When a wider potential window for the CV scans was chosen as shown in Figure 5.5, the scattering spectra of the observed nanorod shifted irreversibly to shorter wavelengths and decreased in intensity. As this most likely can be attributed to the

oxidation of gold from the nanorods for future experiments the potential scan window was restricted to 0.3 V to -0.6 V.

In conclusion, the capacitive charging experiments serve to prove that the gold nanorods are in conductive contact with the ITO and applying a potential to the working electrode can increase and decrease the electron density in the nanorods making them active sites for redox reactions.

Influence of light intensity

The intensity of light that the sample is exposed to during measurements was found to be an additional parameter that has influence on the spectroelectrochemical measurements. Changes in the current measured during Chronoamperometry (CA) were observed in the absence of light, in the presence of ambient light and when the halogen lamp of the microscope was switched on and this light intensity varied (see Figure 5.6a). The light intensity was varied between the two black lines in the graph and the measured reduction current increased under high light intensity, and decreased under low light intensity. Secondly, the slope at which the potential recovered after CA towards the equilibrium open cell potential was higher with the lamp of the microscope switched on compared to when it was switched off (see Figure 5.6b and c. These fluctuations dependent on the light intensity the sample was exposed to, can be attributed to the occurrence of a photo current in the ITO layer. The band gap of ITO lies at 3.5 eV, corresponding to a 354 nm wavelength of light. As the halogen lamp used in the optical set up has very low output at these wavelengths the photocurrent is most likely be caused by trap states in the ITO which are commonly found in semiconductors.[293-295] Consequently, it is important for spectroelectrochemical experiments where ITO is used as a transparent electrode to keep the light intensity constant throughout the experiments. This has been adhered to in all future experiments.

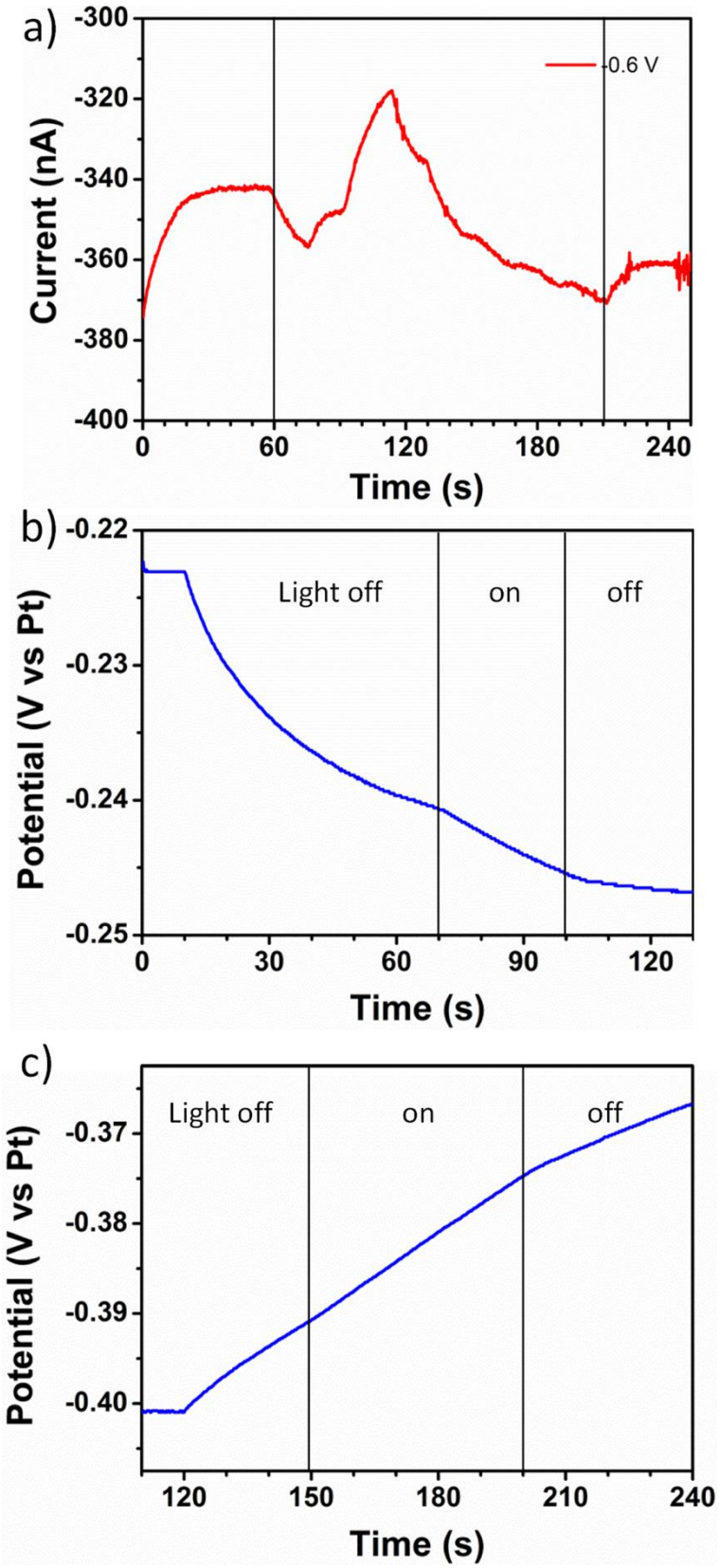


Figure 5.6: a) Current fluctuations with light intensity during chronoamperometry (CA) at -0.6 V in KCl, b) Potential progression during ocp after CA at a potential above the equilibrium potential with light switched off or on. c) Potential evolution during ocp after CA at a potential below the equilibrium potential with light switched off or on.

5.3.3. Electrochemical Reduction of Mercury (II) on Gold Nanorods

After verifying that electrons can be injected into the gold nanorods attached to ITO, experiments were aimed at studying if Hg^{2+} reduction takes place and if it takes place on the gold nanorods or if further modifications of the working electrode are necessary. Figure 5.7 shows linear sweep voltammograms for 0.1 M KCl and 0.1 M KCl containing 5 µM $HgCl_2$ at an ITO working electrode with immobilised gold nanorods and at a bare ITO working electrode. In the case of a gold nanorod modified ITO electrode a strong reduction peak at -0.3 V can be observed for 5 µM $HgCl_2$ in 0.1 M KCl while no peak is observed for KCl alone (Figure 5.7a). Scans over a wider potential window (1 V to -0.6 V, data not shown) displayed no further peaks, thus confirming the observed peak can be associated to the reduction of Hg^{2+}. The shoulder at -0.1 V could not be assigned to any electrochemical process with certainty. It might be related to the formation of a monolayer of Hg prior to its evolution as a multilayer, or the reduction of Hg^{2+} to Hg_2^{2+} species, which according to the electrochemical series takes place at slightly more positive potentials than the reduction of Hg^{2+} to Hg. The increase of current below ~-0.4 V observed in presence and absence of $HgCl_2$ can most likely be attributed to the onset of hydrogen evolution.

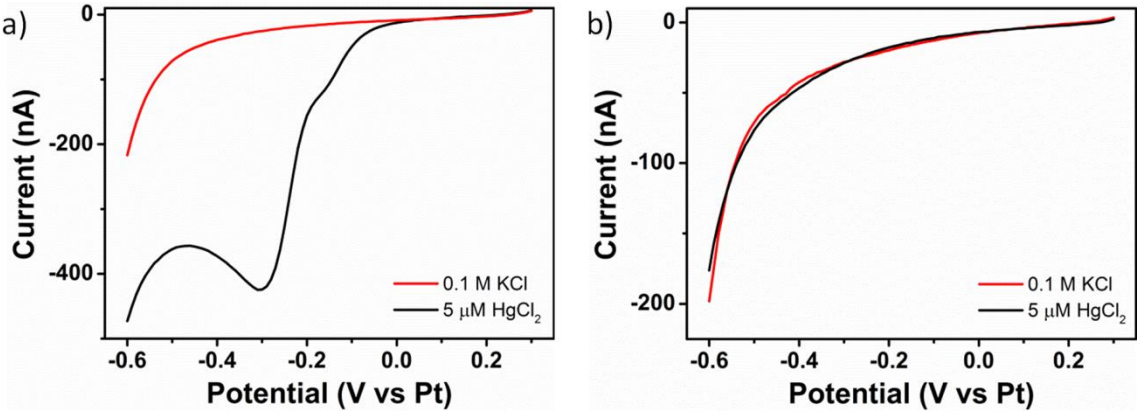


Figure 5.7: a) LSV in 0.1 M KCl and 0.1 M KCl containing 5 µM $HgCl_2$ on a nanorod modified ITO electrode. b) LSV in 0.1 M KCl and 0.1 M KCl containing 5 µM $HgCl_2$ on a bare ITO electrode.

In contrast, the linear sweep voltammograms at the bare ITO substrate show nearly identical curves for the scans in KCl solution with and without 5 µM $HgCl_2$ (Figure 5.7b), leading to conclude that, if at all, only very small amounts of Hg^{2+} were reduced in this

case. Additionally, the linear sweep voltammograms at both electrodes for KCl are very similar in shape and current magnitude, which suggests that the capacitive charging and the onset of hydrogen evolution are mainly taking place at the ITO surface, while the Hg^{2+} reduction is confined to the surface of gold nanorods with negligible contributions from the ITO surface. Thus, no passivation of the ITO surface is necessary.

Influence of Nanorod Density on Spectroelectrochemical Response

Gold nanorods were identified as active sites for electrochemical reduction of Hg^{2+} in the previous section. Consequently, it is expected that the nanorod density has an influence on the measured reduction currents. Analogous data sets for the electrochemical reduction of Hg^{2+} on a substrate with high nanorod density (~8 NR/100 μm^2) and low nanorod density (~1 NR/100 μm^2) were recorded and are shown in Figure 5.8 and Figure 5.9 respectively. The nanorod density for both samples was estimated based on five 48 μm x 60 μm images from random locations per sample. Figure 5.8a-d) show optical dark field images of a working electrode with high density gold nanorods in a) 0.1 M KCl before LSV, b) 0.1 M KCL after LSV, c) 0.1 M KCl, 5 μM $HgCl_2$ before LSV, d) 0.1 M KCl, 5 μM $HgCl_2$ after LSV. Panel e) shows single particle scattering spectra of the circled nanorod in panel a) for the same four conditions as shown in a)-d) and panel f) shows the linear sweep voltammograms in 0.1 M KCl and 0.1 M KCl, 5 μM $HgCl_2$, and the resulting subtracted curve. Figure 5.9 shows analogous results for a working electrode with lower nanorod density.

To begin with, for both samples LSV in 0.1 M KCl does not show any features apart from the onset of hydrogen evolution at the most negative potentials (starting from ~-0.4V). In parallel, darkfield images and scattering spectra of the nanorods before and after LSV in KCl, for both samples show no significant optical changes; λ_{max} and the FWHM remained the same, only a slight decrease in the scattering intensity was observed after the LSV, which might be associated to minor changes in the electron density of the nanorods after the LSV. This would be consistent with what was observed in the capacitive charging experiment discussed in a previous section (see Section 5.3.2.).

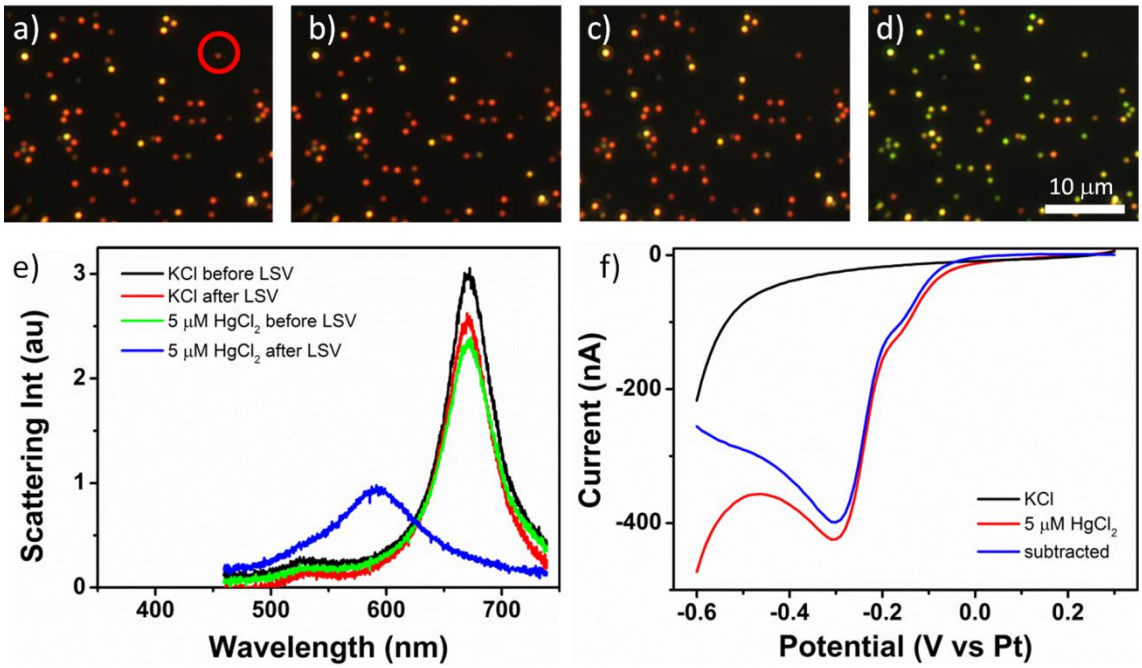


Figure 5.8: Darkfield images of gold nanorods a) in KCl as deposited, b) in KCl after LSV, c) in 0.1 M KCl, 5 µM $HgCl_2$, d) in 0.1 M KCl, 5 µM $HgCl_2$. Nanorod density ~8 NR/100 µm^2. e) Scattering spectra of a single nanorod (marked with a red circle in a)) before and after LSV in 0.1 KCl and 0.1 M KCl, 5 µM $HgCl_2$. f) Voltammograms of LSVs in 0.1 KCl (red curve) and 0.1 M KCl, 5 µM $HgCl_2$ (black curve) and the subtracted curve (blue curve).

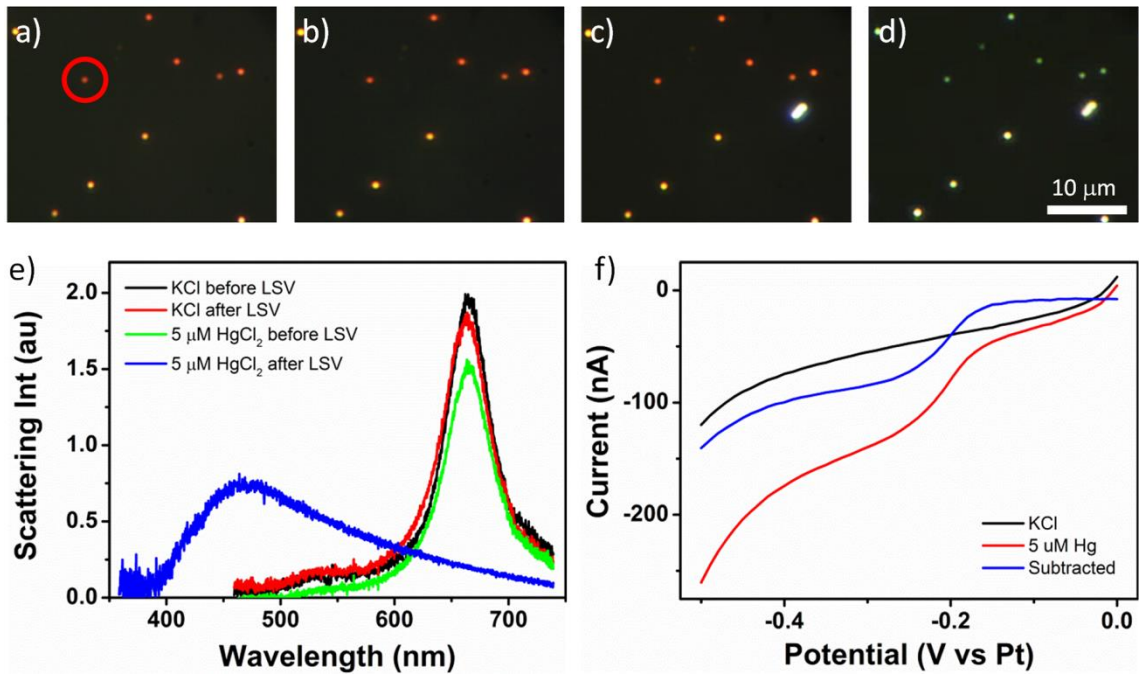


Figure 5.9: Darkfield images of gold nanorods a) in KCl as deposited, b) in KCl after LSV, c) in 0.1 M KCl, 5 µM $HgCl_2$, d) in 0.1 M KCl, 5 µM $HgCl_2$. Nanorod density ~1 NR/100 µm^2. e) Scattering spectra of a single nanorod (marked with a red circle in a)) before and after LSV in 0.1 KCl and 0.1 M KCl, 5 µM $HgCl_2$. f) Voltammograms of LSVs in 0.1 KCl (red curve) and 0.1 M KCl, 5 µM $HgCl_2$ (black curve) and the subtracted curve (blue curve).

Hence, the electrochemical response and the corresponding darkfield images and scattering spectra of the nanorods before and after LSV in 0.1 M KCL are in very good agreement.

After exchanging the solution to 0.1 M KCl containing 5 μM $HgCl_2$, the λ_{max} still remains unchanged. The slight differences in scattering intensity might be again due to changes in the electron density of the rods, as the composition of the electrolyte and thus the ion layer around the nanorods has changed. Subsequently, LSV in the $HgCl_2$ containing solution was carried out. For the sample with high nanorod density (Figure 5.8) the voltammogram shows a large distinct reduction peak at -0.3 V and in parallel the darkfield images show a colour change of the nanorods from mainly red to mainly green. The scattering spectrum of the nanorod circled in Figure 5.8a shows a strong blue shift of the nanorod's λ_{max} from 671 nm to 592 nm, a ~2.5 fold drop in intensity and a broadening of the scattering peak's FWHM from 53 to 97 nm. Consequently, the electrochemical and optical responses seem to correlate well. Additionally, the trends of the changes to the nanorods scattering signature were very consistent with what was observed for the chemical reduction of $HgCl_2$ solutions in Chapter 4 and can be attributed to compositional and morphological changes occurring to the gold nanorods upon amalgamation with reduced mercury. The morphological changes were confirmed by SEM imaging of the sample after spectroelectrochemistry (see Figure 5.10).

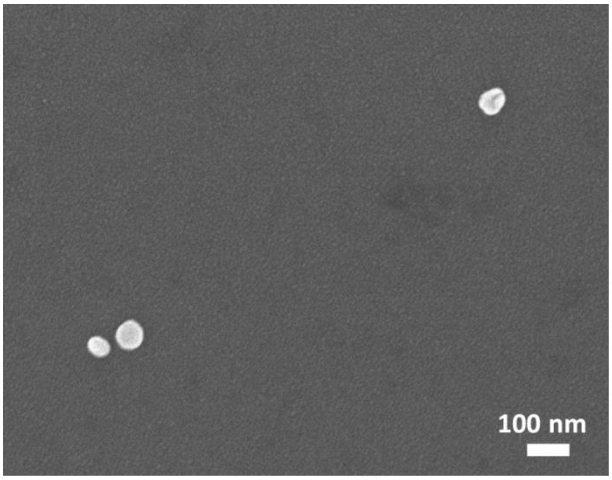


Figure 5.10: SEM image of the low nanorod density working electrode after LSV.

For the sample with lower nanorod density (Figure 5.9) similar results were obtained, i.e., the electrochemical response correlates well with the corresponding optical response of the nanorods before and after LSV in 0.1 M KCl containing 5 μM $HgCl_2$. However, compared to the higher density sample, the voltammogram displays a relatively small, yet evident shoulder at -0.25 V with a much lower current magnitude. In contrast, the blue shift of the nanorods' λ_{max} turned out even stronger than for the sample with higher nanorod density. The single particle scattering spectrum of the NR circled in Figure 5.9a blue shifted very strongly from 664 nm to 467 nm and simultaneously the intensity dropped ~2.5 fold and the scattering peaks FWHM broadened strongly from 53 nm to 176 nm.

Integrating the measured current over time yields the charge flown for each sample to $2.72 \cdot 10^{-6}$ C for the higher density sample and $6.17 \cdot 10^{-7}$ C for the lower density sample. Bringing this in relation with the nanorod density of the sample, this yields $1.52 \cdot 10^{6}$ reduced mercury atoms per nanorod for the higher density sample and $2.46 \cdot 10^{6}$ reduced mercury atoms per nanorod for the lower density sample. With an average nanorod size of 39 x 76 nm, as determined by SEM imaging, mercury:gold atom ratios of 23:77 and 31:69 result for the higher and lower density sample respectively. As expected, a higher mercury:gold atom ratio leads to a stronger blue shift of the nanorods' plasmon resonance. This 1.6-fold increase of mercury atoms reduced at the low density nanorod sample could be explained by differences in the diffusional mass transport behaviour. Migration and convection effects may be considered as negligible since the experiments were undertaken in presence of excess electrolyte, in static un-agitated environments, at constant temperature and over short time periods.

According to literature, using sweep voltammetry techniques, closely separated nanostructures tend to give rise to peak-shaped responses due to diffusion limited behaviour. Only limited supply of fresh analyte is available and competition for that supply between adjacent nanostructures occurs. On the other hand, widely separated nanostructures tend to display steady-state behaviour due to enhanced mass transport arising from individual radial diffusion. Fast and constant supply of fresh analyte is available for each nanostructure independent from adjacent nanostructures.[296, 297]

For example, as was shown theoretically and experimentally by Wahl et al., 50 nm x 100 nm x 45 µm nanowire electrodes parallel within an array behave diffusionally independent with an inter-electrode distance of 13 µm or larger (using sweep voltammetry techniques at scan rates higher than 5 V/s).[298] In this work ITO/nanorod electrodes with the high nanorod density may have been characterised by strongly overlapping diffusion layers of the nanorods as the average distance between each nanorod was relatively small (~5/6 µm). Thereby replenishment of fresh Hg^{2+} during LSV measurements would be limited, leading to the peak-shaped linear sweep voltammogram observed in Figure 5.8. Likewise, the ITO/nanorod electrodes with lower nanorod density may have been characterised by independent radial diffusion layers for each nanostructure, as the average distance between each nanorod was much larger (~10/11 µm), thereby abundant supply of fresh Hg^{2+} during LSV measurements was provided leading to a steady-state linear sweep voltammogram, as observed in Figure 5.9. Of note, the calculated amount of Hg^{2+} reduced during one linear sweep ($8.47 \cdot 10^{12}$ ions in higher density sample/$1.93 \cdot 10^{12}$ ions in lower density sample) is small compared to the initial Hg^{2+} concentration in solution ($2.44 \cdot 10^{14}$ ions), showing that no depletion of the solution is taking place.

Consequently, the electrochemical sensitivity per nanorod of ITO/nanorod electrodes would be higher at lower nanorod density than that at higher nanorod density, i.e., more reduced Hg^{2+} ions per nanorod resulting in a higher mercury:gold atom ratio for the low nanorod density substrate. It has to be noted, that this possible explanation may only be valid under the condition that the reference electrode is stable. As will be discussed later, it is likely that platinum pseudo-reference electrode may be causing inconsistent results. Nonetheless, only a slight variation in the reduction potential (-0.3 V vs -0.26 V) was observed in the data discussed here, and the results are most probably comparable. Consequently, differences observed between the low and high density nanorod samples may effectively be associated with differences in the diffusional mass transport behaviour.

On a related matter, the influence of local nanorod density variations on one substrate on the optical response of nanorods to electrochemical reduction of $HgCl_2$ has been studied. Figure 5.11 shows optical dark field images of two different regions of interest

(ROIs) on the same sample before and after LSV in 0.1 M KCl containing 5 μM $HgCl_2$. Both ROIs, despite their different location on the sample and different nanorod density show the same optical response to the reduced mercury. This clarifies that results from different ROIs on one sample are comparable, independent of their location on the sample and the local nanorod density. Only the overall amount of nanorods on the active area of a sample and their separation is of importance to the spectroscopic and electrochemical response.

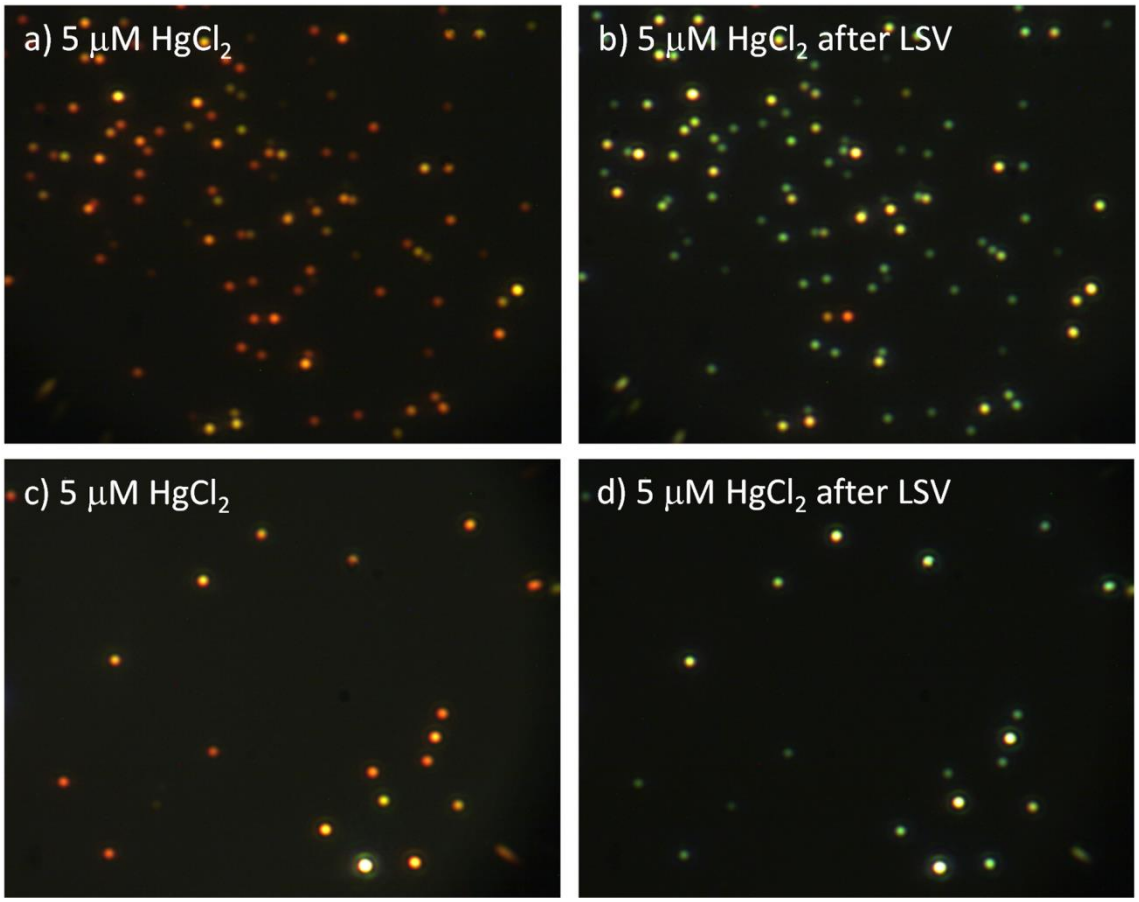


Figure 5.11: Darkfield images of an area of high nanorod density a) before and b) after LSV in 5 μM $HgCl_2$ and darkfield images of an area of low nanorod density c) before and d) after LSV in 5 μM $HgCl_2$ On the same sample (overall NR density on sample: ~1 NR/100 μm^2).

To summarise, a high nanorod density leads to a strong over-all electrochemical response but a lesser electrochemical response per nanorod, which in turn accounts for a smaller spectral shifts in the nanorods scattering spectra. In contrast, a lower nanorods density leads to a small over-all electrochemical response but a strong electrochemical response per nanorod due to increased diffusional mass transport leading to stronger spectral shifts in the nanorods scattering. This shows the

importance of knowing the nanorod density of a sample for quantitative experiments and indicates the route for future experiments to optimise the nanorod density for optimised electrochemical and optical read-out.

Response to Linear Sweeps in Mercury Solutions with Increasing Concentration

To study the response of gold nanorods to electrochemical reduction of mercury from solutions with various concentrations, consecutive LSV experiments with increasing concentration of the mercury solution from 1 to 4 μM have been carried out on the same ITO/ gold nanorod electrode. Figure 5.12a and b show darkfield images and scattering spectra of one selected nanorod before and after linear sweeps in 0.1M KCl solution containing 1, 2, 3 and 4 μM $HgCl_2$, and Figure 5.12c shows the corresponding linear sweep voltammograms.

For a 1 μM $HgCl_2$ solution, a similar linear sweep voltammogram as was previously observed was recorded; a distinct shoulder related to Hg^{2+} reduction. Despite the obvious reduction of Hg^{2+} as indicated by the voltammogram, only a minimal spectral shift was observed after LSV for the monitored single nanorod's λ_{max} from 661 nm to 658 nm and no chance of the FWHM of 60 nm. After the electrolyte was exchanged for a 2 μM $HgCl_2$ solution, the λ_{max} was shifted back to 661 nm. The linear sweep voltammograms for the 2 μM and higher concentrations were inconclusive; they differed from the KCl voltammogram but didn't show any distinct Hg^{2+} reduction features. Yet, after LSV in 2 μM $HgCl_2$ solution λ_{max} was shifted noticeably from 661 nm to 638 nm and the FWHM increased from 60 nm to 87 nm. After the electrolyte exchange for a 3 μM $HgCl_2$ solution, the λ_{max} was again shifted back slightly to 647 nm and was then blue shifted to 624 nm after LSV. The FWHM increased from 75 nm to 108 nm. Finally, after electrolyte exchange to 4 μM $HgCl_2$ solution, the λ_{max} was shifted back to 637 nm and was then dramatically blue shifted to ~479 nm after LSV. A FWHM could not be determined from the post-LSV spectrum.

As described above, the voltammogram for the 1 μM $HgCl_2$ solution showed a distinct shoulder related to Hg^{2+} reduction. However, the potential at which the reduction started was more positive (-0.1 V) than what was observed previously (-0.25 V). An explanation might be that the pseudo-reference electrode used (platinum wire) was

not stable enough or might have been contaminated. This shows that comparison between samples will be difficult. A possible solution to overcome the issue would be to carry out LSV over a larger potential window, to ensure the potential allowing complete reduction of mercury is included. Another solution would be to include a standard redox couple (e.g., Ferrocene/Ferrocenium or derivatives such as Decamethylferrocene/Decamethylferrocenium) into the solutions to act as internal reference. The potential of the platinum pseudo-reference electrode could then be calibrated against that of the redox couple prior to each experiment to ensure its stability.[299-301] The voltammograms for the higher concentrated $HgCl_2$ solutions were inconclusive, possibly due to a combined effect of an altered working electrode surface after the first deposition of mercury and instability of the platinum pseudo-reference electrode.

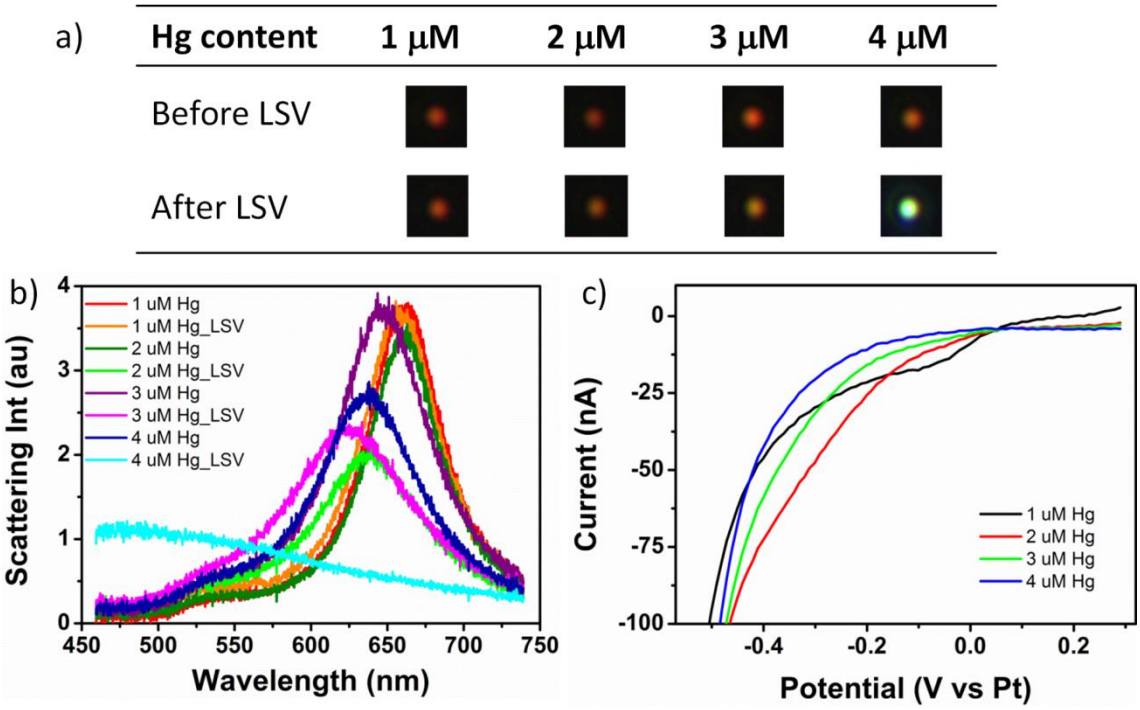


Figure 5.12: Darkfield images (a) and scattering spectra (b) of a single gold nanorod before and after LSV in KCl and in 0.1 M KCl, 1-4 µM $HgCl_2$ for two consecutive LSV. c) Background subtracted voltammograms of four consecutive LSVs in 0.1 M KCl, 1-4 µM $HgCl_2$. Overall NR density on sample: ~3 NR/100 µm^2.

A question that remains to be answered is what processes have possibly occurred after the LSVs had finished and caused the nanorod's λ_{max} to red shift towards its original position after each LSV. That further processes were taking place becomes also

obvious, when looking at the in-situ spectroscopic data for the linear sweeps in 2 and 4 μM $HgCl_2$ solutions presented in Figure 5.13 and Figure 5.14.

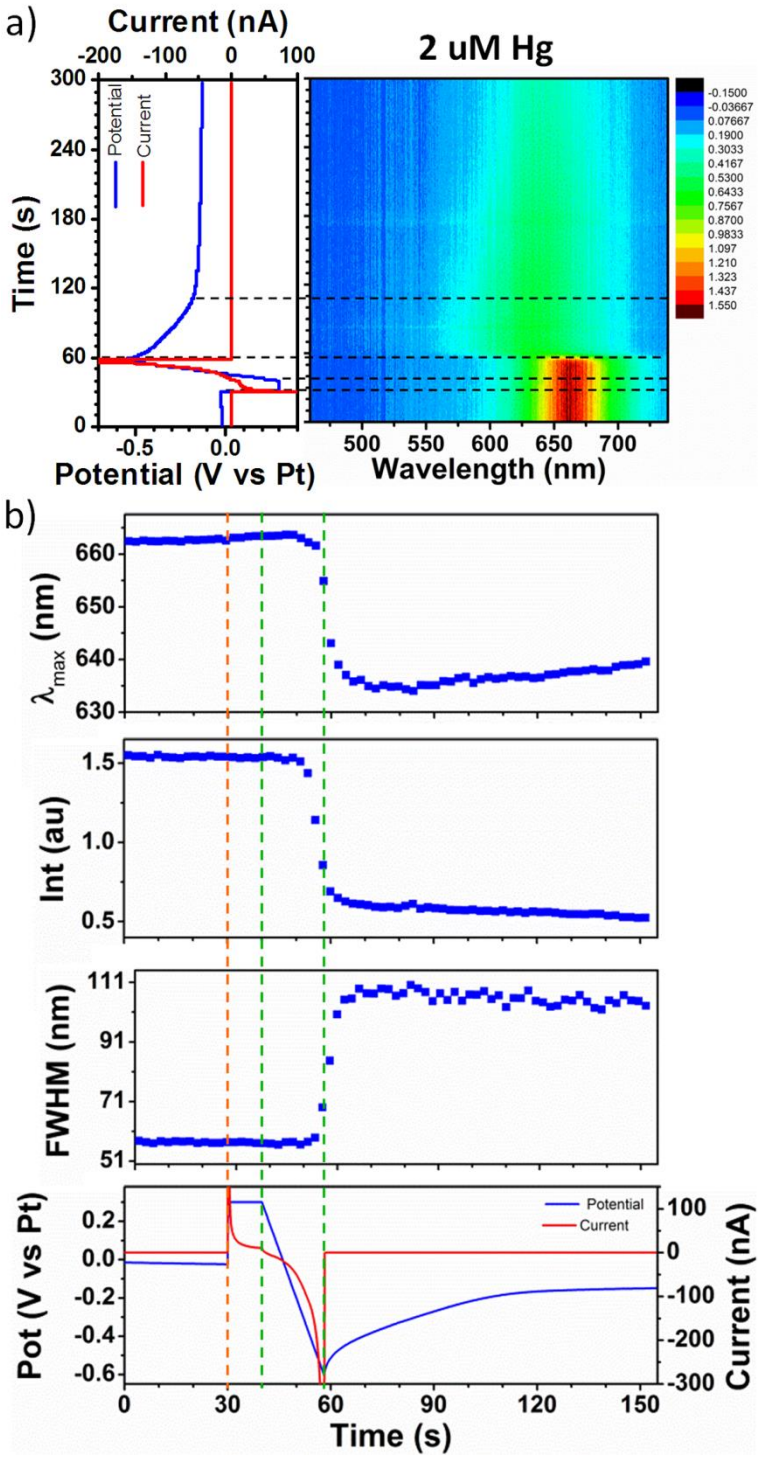


Figure 5.13: a) Potential and current curves of a LSV between 0.3 V and -0.6 V in 0.1 M KCl 2 μM $HgCl_2$ correlated with a 2D plot of 300 single nanorod scattering spectra recorded in-situ during the LSV. b) λ_{max}, peak intensity and FWHM values extracted from Lorentzian fits to spectral data correlated with potential and current curves recorded during LSV.

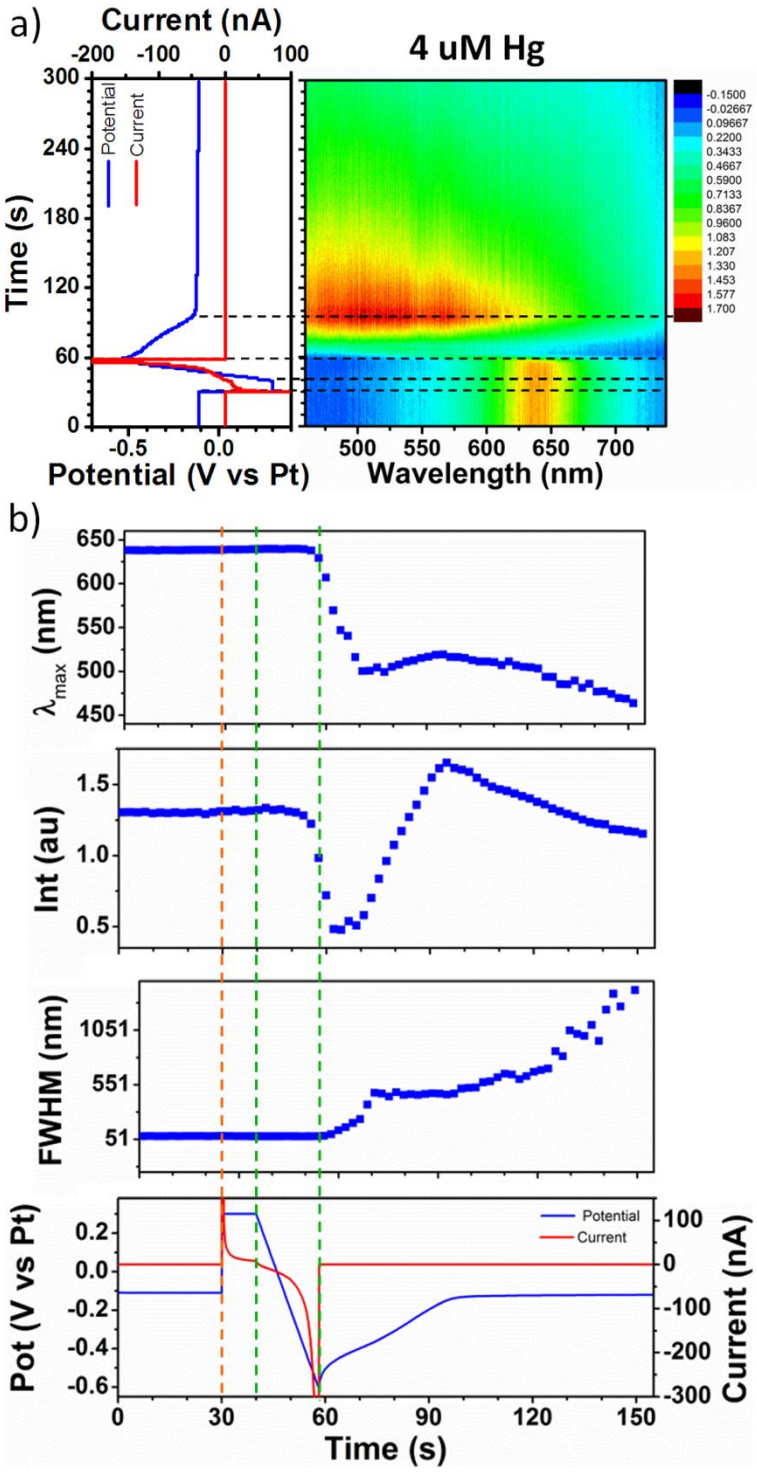


Figure 5.14: a) Potential and current curves of a LSV between 0.3 V and -0.6 V in 0.1 M KCl 4 µM $HgCl_2$ correlated with a 2D plot of 300 single nanorod scattering spectra recorded in-situ during the LSV. b) λ_{max}, peak intensity and FWHM values extracted from Lorentzian fits to spectral data correlated with potential and current curves recorded during LSV.

As previously mentioned, following LSV in 2 μM $HgCl_2$, 0.1 M KCl solution, the λ_{max} blue shifted from 661 nm until 634 nm, the peak intensity dropped and the FWHM increased from 60 nm to 87 nm. However, within a few seconds after the linear sweep was carried out, the λ_{max} began to red shift and also the FWHM decreased again. This behaviour was observed as well in several other samples, unless the spectrum was completely blue shifted. For this particular nanorod, the peak intensity further decreased after the LSV, which might, however, have been related to defocussing of the sample over the course of the experiment. In the 4 μM $HgCl_2$ linear sweep even more dramatic changes were observed. After the initial λ_{max} blue shift, peak intensity decrease and FWHM increase from 75 to 108 nm, the λ_{max} slowly started to red shift and in addition, the peak intensity increased superseding its original value until, at 96 s after the start of the experiment, the process seemed to be reversed. Moreover, at exactly the same time, the ocp seems to reach its equilibrium value. The increase in peak intensity until 96 s suggests reduction of Hg^{2+} and deposition on the nanorod until that point in time. Taking a closer look at the bottom panel in Figure 5.14b the measured ocp after the LSV until 96 s shows an unusual behaviour, suggesting further processes might be taking place apart from mercury reduction. In fact, the potential curves for all carried out linear sweeps of the sample, show that the ocp recovery curves after the linear sweeps look differently for each concentration (see Figure 5.15). Similar potential curves were recorded in 0.1 M KCl and 1 μM $HgCl_2$, 0.1 M KCl, which seem to follow an exponential relaxation behaviour towards the system's equilibrium ocp value that was measured before the LSV. For the higher concentrated $HgCl_2$ solutions clear deviations from that behaviour are observed. This further indicates additional processes occurred after the LSV.

Several processes could lead to the λ_{max} red shift after the LSV observed in the 2 μM $HgCl_2$ linear sweep and the decrease of the peak intensity after initial increase in the 4 μM $HgCl_2$ linear sweep: oxidation of mercury from the nanorods as the potential increases, dissolution of elemental mercury into the solution and diffusion of mercury into the nanorods or away from the rods. Dissolution of mercury into the solution is probable as the solubility of mercury in water is 300 nM at 298.15K.[274]

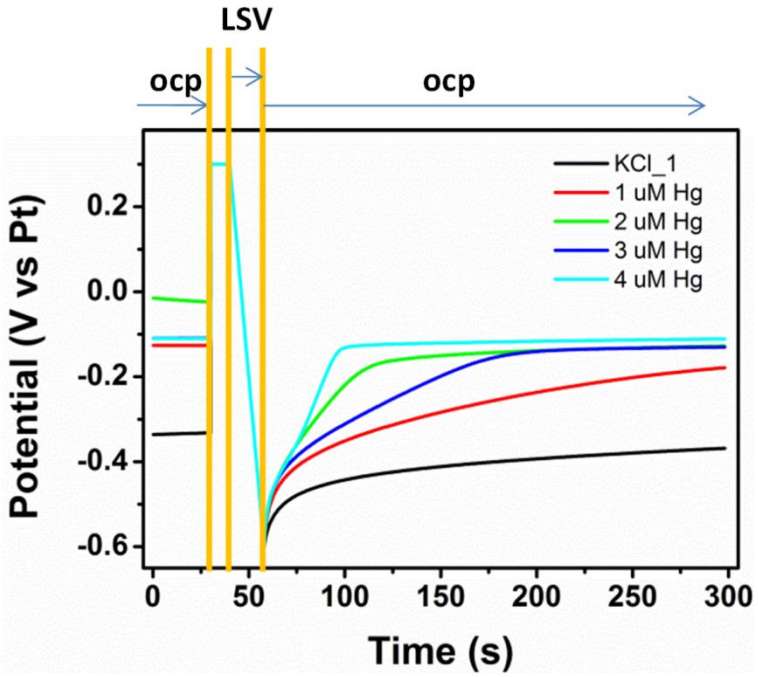


Figure 5.15: Potential curves for LSVs with preceding and subsequent ocp measurement in 0.1 M KCl, 1-4 µM $HgCl_2$.

Diffusion of mercury into the gold nanorod is expected and has been shown in Chapter 4 for nanorods and previously in literature for gold nanoparticles [208] to cause a red shift of a gold nanostructure's optical signature. Previously it was observed on a longer time scale, however, immersion in an electrolyte and Hg^{2+} ions in the nanorod's immediate environment might alter processes. The diffusion of mercury away from the nanorods is considered less probable due to the high affinity between gold and mercury.

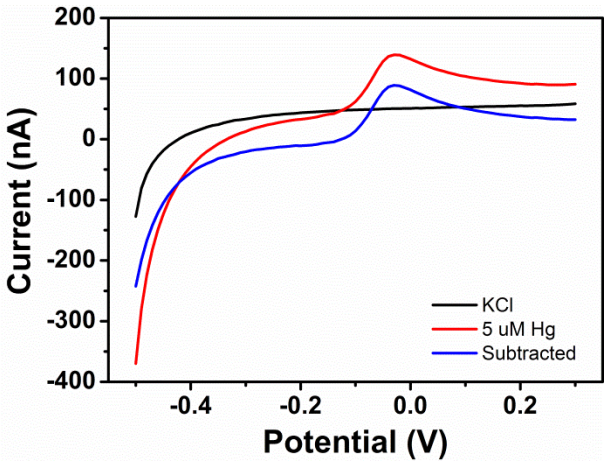


Figure 5.16: Voltammograms of LSVs from -0.5 V to 0.3 V in 0.1 M KCl, and 0.1 M KCl, 5 µM $HgCl_2$ and the subtracted curve.

Finally, oxidation of mercury is considered unlikely, as it would be expected only at higher potentials. LSV scans in 5 μM $HgCl_2$ solution from -0.5 V to 0.3 V at 50 mV/s showed an oxidation peak at -0.02 V (see Figure 5.16).

Response to Multiple Linear Sweeps in 5 μM $HgCl_2$ Solution

Following on from what was observed for the voltammograms in the previous set of experiments, the effect of multiple linear sweeps in the same solution has been studied. Figure 5.17 shows single particle scattering images and spectra of one selected nanorod and the corresponding voltammograms for the sample for three consecutive linear sweeps in 0.1 M KCl containing 5 μM $HgCl_2$. As can be seen in Figure 5.17c, the three recorded LSVs display completely different signals. The first one shows a large distinct reduction peak at -0.3 V, which is very consistent with previous results (see Figure 5.8e). The second one shows a broad peak at -0.28 V and the third has a small wave at -0.25V. As calculations showed in the previous section, the analyte solution is not depleted of Hg^{2+} ions after one linear sweep.

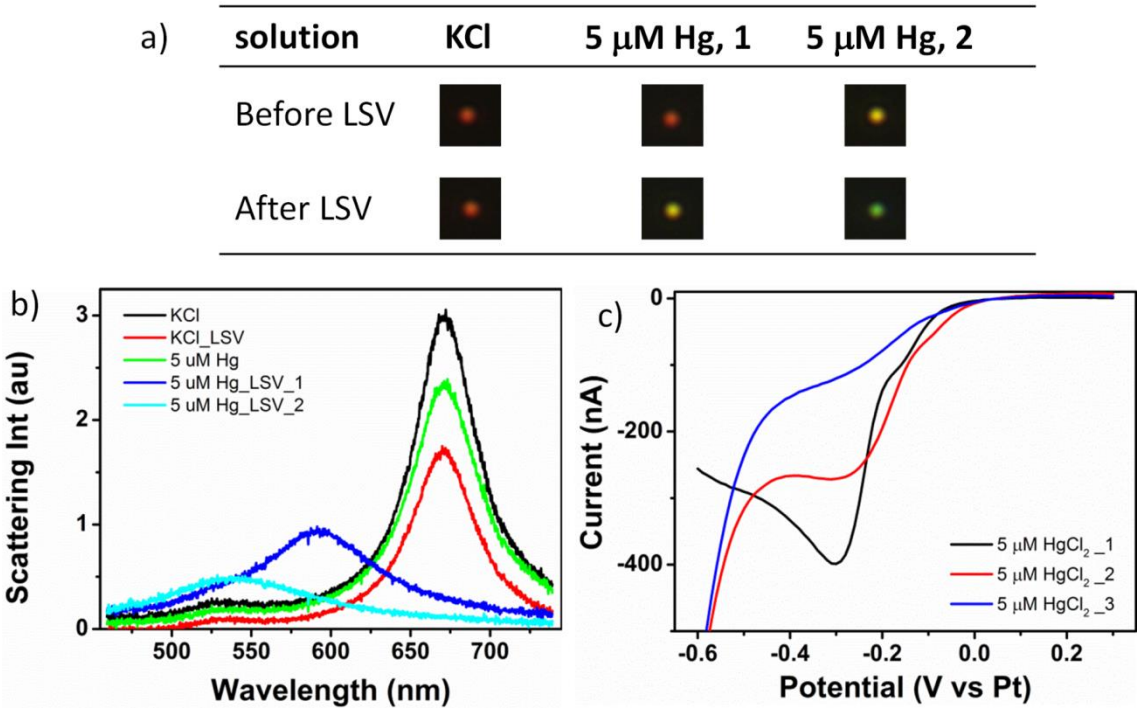


Figure 5.17: Darkfield images (a) and scattering spectra (b) of a single gold nanorod before and after LSV in KCl and in 0.1 M KCl, 5 μM $HgCl_2$ for two consecutive LSV. c) Voltammograms of three consecutive LSVs in 0.1 M KCl, 5 μM $HgCl_2$. Overall NR density on sample: ~8 NR/100 μm^2.

Therefore the non-reproducible voltammogram curves may be attributed to an altered working electrode surface after the deposition of mercury sweep after sweep. Regarding the optical response, the scattering images and spectra in Figure 5.17a and b show a further blue shift of the nanorods' optical signature after the second sweep. In conclusion, a stronger optical response for the same mercury concentration can be achieved with multiple sweeps, however, changes in the working electrode material make the electrochemical data less conclusive.

The deposition of mercury on the gold nanorods is an irreversible process for several reasons. The high affinity of mercury for gold makes it challenging to electrochemically remove mercury again completetly from amalgamated gold nanorods. This has been the topic of various publications on the electrochemical detection of mercury.[302-305] Additionally, in the specific present case, where mercury is deposited on gold nanorods, the amalgamation of mercury with the gold nanorods is very likely associated with an irreversible shape change of the nanorods towards a spherical shape as it was observed for chemical mercury reduction in Chapter 4. The rod shape can not be recovered even if all mercury were to be removed from the amalgam structure, e.g. by heating. Thus, for further investigation of mercury solutions with varying concentrations, ideally a fresh ITO/gold nanorod working electrode should be used for each reduction. To make these results comparable, however, identical working electrodes would be required, which is highly challenging using chemically synthesised nanorods deposited on ITO substrates. This topic of reproducible substrates for reproducible results was discussed previously in Chapter 4 Section 4.3.3.

Chronoamperometry

Chronoamperometry was investigated as an alternative technique for electrochemical Hg^{2+} reduction. After a period of ocp measurement, the potential was set directly to -0.3 V, the potential at which the Hg^{2+} reduction peak was observed earlier. The single nanorod response to a 2 μM $HgCl_2$, 0.1 M KCl solution is shown in Figure 5.18. Compared to the LSV measurement in a 2 μM $HgCl_2$, 0.1 M KCl solution discussed in the previous section the spectroscopic response of the single nanorod was slower but much stronger. The λ_{max} blue shifted from 676 nm to 513 nm as long as the potential

of -0.3 V was applied, then stayed stable without red shifting. The peak intensity dropped in the first 10 s when the potential was applied then stayed constant.

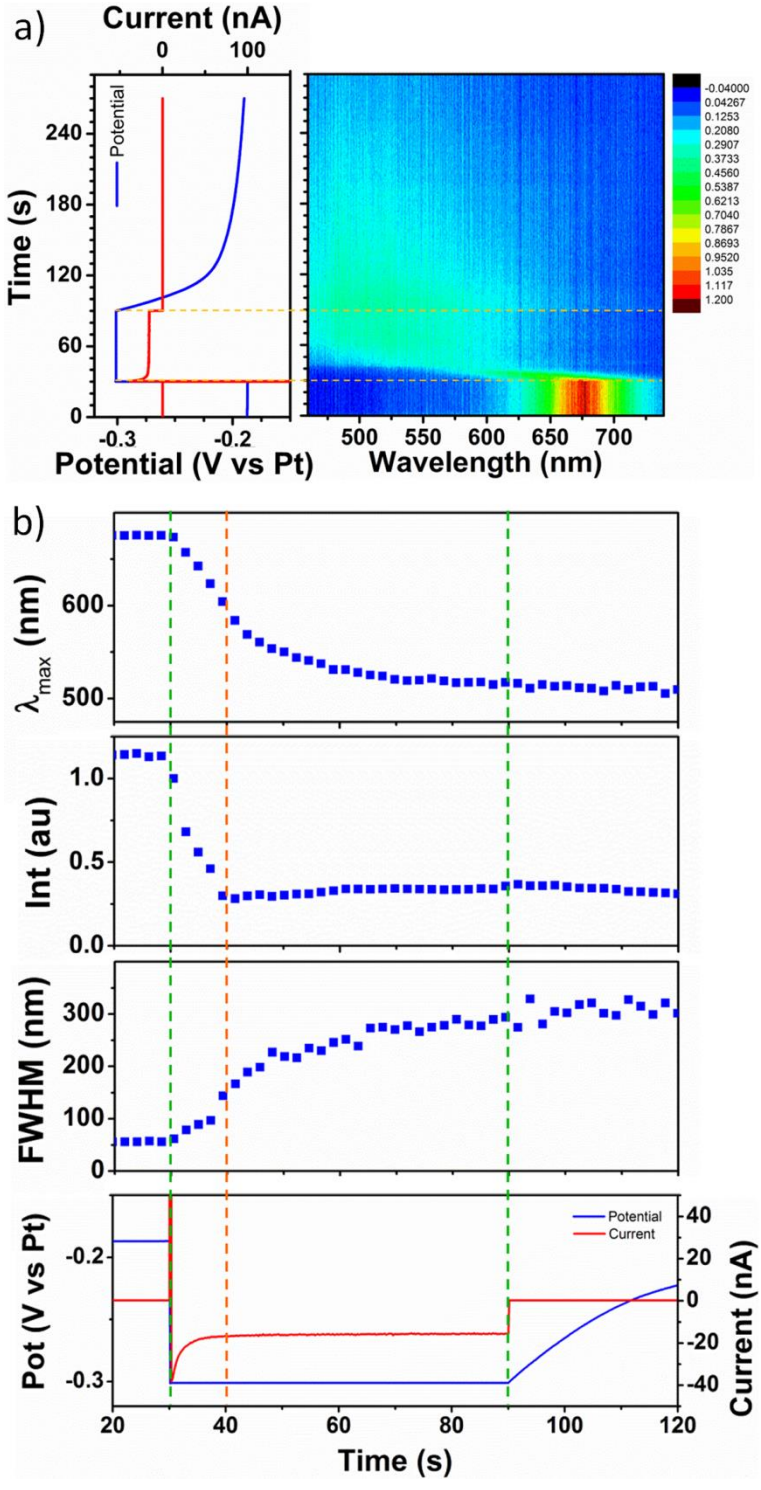


Figure 5.18: a) Potential and current curves during CA at -0.3 V and ocp measurements before and after CA in 0.1 M KCl 2 μM $HgCl_2$ correlated with a 2D plot of 300 single nanorod scattering spectra recorded in-situ during the CA. b) λ_{max}, peak intensity and FWHM values extracted from Lorentzian fits to spectral data correlated with potential and current curves recorded during CA.

The decrease of the peak intensity later on in the experiment can be attributed to defocussing of the microscope over time. The FWHM increased from 26 nm to 315 nm while the potential was applied, then remained constant. Compared to the LSV measurement benefits of the CA measurement are the strong and the, for the timescale of the measurement, permanent optical response, which would potentially allow the detection of lower mercury concentrations than with LSV. A downside of CA is that the electrochemical read out is less straightforward to interpret compared to LSV. Furthermore, the accuracy of CA relies on the application of the exact mercury reduction potential. Therefore, a more significant challenge applying the CA technique is a possible potential variability caused by the fact that a platinum pseudo-reference electrode is used, which was estimated to up to 0.15 V in a previous section. To address this issue multipotential steps could be chosen as a more suitable technique which allows for several successive CA steps set for x amount of time such that a wider potential range can be covered but uncertainty in the potential remains. Another possibility would be again to use a standard redox couple as an internal standard so as to identify precisely the mercury reduction potential.

5.4. Conclusion

In conclusion, this chapter describes (to the best of my knowledge) the first investigation of electrochemical reduction of Hg^{2+} ions on gold nanorods and the resulting amalgamation of the nanorods by a single particle dark field spectroelectrochemical method.

A spectroelectrochemical cell with three electrode configuration was designed for the use in a single particle dark field spectroscopy setup. Initially, the ITO/gold nanorod working electrode was analysed by capacitive charging experiments in KCl where the capacitive charging of gold nanorods led to a reversible modification of the nanorod's optical signature. Linear sweep voltammetry of bare ITO and ITO/gold nanorod working electrodes in 0.1 M KCl and 5 μM $HgCl_2$, 0.1 M KCl solutions confirmed that Hg^{2+} reduction is confined to the surface of the gold nanorods without surface passivation of the ITO leading to a pronounced blue shift of the nanorod scattering spectra of up to 197 nm. The reduction peak was observed at -0.3 V. Experiments with substrates of varying nanorod densities indicated that dependent on the nanorod density a trade-off exists between the magnitude of the optical and electrochemical signal caused by the overlapping of diffusion volumes. Mercury concentrations from 1-4 μM were analysed by in-situ real-time spectroscopy during LSV on one substrate. An increase in mercury concentration resulted in an increased optical response. The electrochemical data, however, becomes inconclusive after the first sweep probably due to an altered electrode surface after deposition of initial amounts of mercury. From these results, ideally a fresh working electrode should be used for each reduction. However, to make these results comparable, identical working electrodes are required; a challenge that needs to be addressed separately. Additionally, LSV and CA were compared as techniques for the reduction of Hg^{2+} on gold nanorods. LSV delivers more information output which is useful especially when studying a new system. On the other hand, CA has the potential to be more sensitive for lower mercury concentrations.

While this work is far from being complete, first steps have been made to a potential very powerful detection method for Hg^{2+} ions in water using single nanoparticle

spectroelectrochemistry. Suggestions for future work directed towards the optimisation of the here presented method are the optimisation of the nanorod density on the working electrodes to ensure maximum signal read-out from single nanorods and the optimisation of electrochemical parameters for the usage of a platinum pseudo reference electrode or alternative miniaturised reference electrodes (e.g. Ag/AgCl) could be investigated.

Chapter 6 - Conclusions and Future Work

6.1. Summary and Conclusions

For this thesis, the goal was to investigate the properties of various plasmonic gold nanostructures and explore their application in mercury detection.

Chapter 1 outlined concerns about the presence of mercury in the environment, gave an introduction to plasmonic nanoparticles, their properties, characterisation and application in general and mercury detection methods as well as an introduction to the relevance of nanoalloys.

In chapter 2 the optical properties of potential plasmonic building blocks or platforms were studied and assessed by correlated spectroscopic and structural analysis. Silver nanoparticles were found to be more efficient scatterers than gold nanoparticles of the same size but with less monodisperse size and shape distribution and inferior stability in ambient conditions. Gold nanorods showed widely tuneable and polarised plasmon resonance corresponding to longitudinal and transversal plasmon modes. Polarisation dependent plasmon coupling was observed for nanoparticle clusters and nanorod arrays. The creation of electromagnetic field hot spots in these structures make them suitable for sensing techniques like surface enhanced fluorescence and Raman spectroscopy. Additionally, the application of highly ordered nanorod arrays as anti-clonal tags was demonstrated.

In chapter 3 a plasmon resonance energy transfer (PRET) based detection strategy was explored using immobilised 60 nm gold nanoparticles functionalised with organic molecules that can complex Hg^{2+} ions and exhibit an absorption band close to the plasmon resonance band of the nanoparticles. The initially designed hybrid sensing structure could be fabricated successfully but showed no response to Hg^{2+} ions. Improved hybrid structures with enhanced spectral overlap between nanoparticle and molecule based on pseudo-silver core – gold shell nanoparticles were fabricated. Additionally, the Hg^{2+} detection was performed in organic medium where the molecule-Hg^{2+} complex had shown improved stability compared to water. Following these changes a scattering intensity quenching was observed for 100 μM Hg^{2+} concentration. However, the incompatibility of ethanol with the microfluidic setup made the method experimentally extremely challenging. Additionally, the affinity of

Hg^{2+} to the thiol group of the organic ligand and silver and gold present as plasmonic nanostructures led to difficult to control competing processes. Eventually, the decision had to be made not to investigate further this route of Hg^{2+} ion detection via PRET but to instead explore and develop alternative routes for mercury detection.

In chapter 4 a new approach to mercury detection was pursued taking advantage of the affinity of mercury towards gold directly. Immobilised gold nanorods were exposed to Hg^{2+} ion solutions in the presence of reducing agent $NaBH_4$. Single particle dark field spectroscopy showed a remarkable optical response of the gold nanorods, whose plasmon resonance decreased in intensity and blue-shifted strongly. Blue shifts of 5 nm could be recorded for Hg^{2+} concentrations as low as 10 nM. The selectivity of the method was demonstrated versus common interfering metal ions and in local river and tap water. However, the carried out experiments showed also that a gap still exists between laboratory use demonstration and applicability as real sensors. In particular, for the presented system issues related to nanostructure shape and density distributions have to be addressed towards a more reproducible signal read-out. Additionally, minimising interferences in complex real water matrices will have to be addressed before highly sensitive real-world analysis can be performed. Nevertheless, the reported linear correlation and high selectivity make this approach potentially suitable for on-site mercury analysis using a miniaturized portable spectrometer. Further time-dependent studies were carried out to gain insights into the mercury deposition and alloying mechanism leading to the observed changes in the nanorods plasmonic signatures. Based on these experiments a 5 step model was proposed. The understanding of the mechanism regulating the incorporation of mercury into metal nanorods and the consequent reshaping process are technologically important for a number of applications ranging from sensing to catalysis. The present work also shows that nanoparticle alloys with specific optical features can be synthesised by controlling the mercury deposition conditions.

In chapter 5 a variation of the mercury detection method investigated in chapter 4 was explored, replacing the chemical reduction of Hg^{2+} ions to elemental mercury with an electrochemical reduction. This has been studied for the first time in a darkfield spectroelectrochemical setup that allows in-situ optical analysis of the electrochemical

reaction. For this purpose a suitable spectroelectrochemical cell for the intended experiments was designed. The ITO/gold nanorod working electrode was analysed by capacitive charging experiments in KCl before Hg^{2+} was reduced by linear sweep voltammetry (LSV). Without further electrode modification, reduction of Hg^{2+} ions was shown to be confined to the nanorod surfaces with negligible contribution from the ITO surface. In-situ LSV with dark field spectroscopy in 1-4 μM mercury solutions was performed and additionally, LSV and CA as Hg^{2+} reduction techniques were compared. The method has shown strong optical and electrochemical responses for 5 μM Hg^{2+} concentrations, a lower LOD is yet to be determined. I believe in an optimised setup simultaneous electrochemical and optical signal acquisition have great potential to lead to a highly sensitive mercury detection method. Furthermore, simultaneous optical spectroscopy during mercury reduction offered the opportunity to gain deeper insight into the interaction of elemental mercury with gold nanorods. The nanorods showed a strong blue shift within seconds of mercury reduction and the development of the nanorod scattering suggests further processes are continuing after the linear potential sweep is completed, possibly related to mercury diffusion.

6.2. Future Work

Though the mercury sensing strategy using PRET that was described in chapter 3 was not further pursued at this stage, there is potential in this approach as it has been shown to be highly sensitive for example in the detection of Cu^{2+} or TNT.[145, 147] If the work were to be continued several fundamental changes would have to be made. For the detection of Hg^{2+} ions a new organic ligand molecule should be considered/designed. Ideally the molecule should form a stable complex with Hg^{2+} ions in water but shouldn't have any other groups (like thiols) that have an affinity for Hg^{2+} ions. On the other side, the plasmonic nanostructure should not include silver if Hg^{2+} binding to the molecule is desired as the standard reduction potentials for the redox couples Hg^{2+}/Hg (0.851 V) and Ag^{+}/Ag (0.7996 V)[277] favour the reduction of mercury and the oxidation of silver.

The mercury detection approach using direct amalgamation of gold nanorods covered in chapter 4 showed great potential. Single gold nanorods showed a highly sensitive optical response to Hg^{2+} solutions down to 5 nM and a linear response in the range from 5 to 100 nM. Future work could be directed towards increasing the method's reproducibility which to date was limited by the inevitable size and shape distribution that chemically synthesised nanostructures possess and the variability in the number of nanorods deposited on a substrate. More reproducible samples would lead to more reproducible mercury detection results. This could either be addressed by improving the control over nanoparticle size and shape distribution in chemical synthesis or optimising nanostructure separation techniques, as well as improving control over the amount and density of deposited nanostructures. An example could be deposition of nanostructures in prefabricated positions.[306] Alternatively, highly uniform but more expensive electron-beam lithography or nanoimprint lithography fabricated nanostructures could be utilised. Furthermore, it would be interesting to investigate if different shapes of gold nanostructures could achieve an even higher sensitivity towards mercury. A possibility would be nanotriangles or nanourchins. Especially nanourchins should be promising candidates as they possess a peak surface plasmon resonance wavelength between 600 and 700 nm and a large surface-volume ratio where amalgamation induced morphological changes should provoke a large optical

response. For exact mercury detection in real water samples pre-treatment procedures might have to be developed. Initially, interfering factors would have to be identified and strategies developed to suppress or eliminate those.

Furthermore, future work should be dedicated to exploring the possibilities of a spectroelectrochemical setup for mercury detection via nanorod amalgamation. The work presented in this thesis serves as a proof of concept, indicating that, in an optimised setup, simultaneous electrochemical and optical signal acquisition has the potential to lead to a more sensitive mercury detection method. Initially, the optimisation of the working electrode would be beneficial. The nanorod density on a substrate could be optimised to avoid overlapping of diffusion volumes of neighbouring nanorods and to achieve the largest possible response from a single nanorod. Theoretical simulations could be useful in finding this optimum. Additionally, the substrate optimisation routes for increased substrate reproducibility suggested for the chemical mercury reduction could be implemented. A critical point would be the optimisation of electrochemical parameters to allow reliable read-out with the usage of a platinum pseudo reference electrode or alternatively the investigation of miniaturised reference electrodes (e.g. Ag/AgCl). The various electrochemical reduction methods for mercury (linear sweep, square wave voltammetry, chronoamperometry) could then be compared regarding their suitability. A benefit of electrochemical mercury reduction could be improved selectivity compared to a chemical reduction by precise adjustment of the electrochemical parameters. Moreover, detailed simultaneous optical observation of the processes during precisely controlled electrochemical reduction of mercury could give insights into the diffusion processes involved in the nanorod amalgamation.

Appendices

Appendix A

List of Symbols and Abbreviations

A	absorption
α	polarisability
AFM	atomic force microscopy
AFS	atomic fluorescence spectroscopy
APTES	(3-Aminopropyl)triethoxysilane
AR	aspect ratio
au	arbitrary units
B	area underneath lorentzian curve
BSA	bovine serum albumin
C_{ext}	extinction cross section
C_{sca}	scattering cross section
C_{abs}	absorption cross section
CA	chronoamperometry
CE	counter electrode
CTAB	hexadecyltrimethyl ammonium bromide
CV	cyclic voltammetry
CV-AAS	cold vapour atomic absorption spectroscopy
CV-ICP-MS	cold vapour inductively coupled plasma mass spectroscopy
CV-ICP-OES	cold vapour inductively coupled optical emission spectroscopy
d	diameter
DDA	discrete dipole approximation
DFOM	dark field optical microscopy
DFT	density functional theory
DI	deionised
DLS	dynamic light scattering
DNA	deoxyribonucleic acid
e	electron charge
E	eccentricity
ε	dielectric function

ε_1	real part dielectric function
ε_2	imaginary part dielectric function
ε_0	permittivity of vacuum
ECL	electrochmiluminescence
EDX	energy dispersive X-ray spectroscopy
FDTD	finite difference time domain
EtOH	ethanol
FIB	fucussed ion beam
FWHM	full width at half maxmium
γ	electron collision frequency
gsc	glass cover slip
HDMS	Hexamethyldisilazane
HPLC	high-performance liquid chromatography
I	intensity
IPA	isopropyl alcohol
IR	infra-red
ICP-AES	inductively coupled atomic emission spectroscopy
ICP-MS	inductively coupled mass spectroscopy
ITO	indium tin oxide
k	wavenumber
l	length
L_j	depolarisation factors
λ	wavelength
λ_{max}	peak surface plasmon resonance wavelength
LOD	limit of detection
LSPR	localised surface plasmon resonance
LSV	linear sweep voltammetry
m	electron effective mass
MeOH	methanol
n	refractive index
N	conduction electron concentration

NA	numerical aperture
NIR	near infra-red
NP	nanoparticle
NR	nanorod
ω	plasma frequency
ω_p	bulk plasma frequency
ocp	open circuit potential
OD	optical density
PRET	plasmon resonance energy transfer
QD	quantum dot
R^2	coefficient of determination
RE	reference electrode
ROI	region of interest
SEM	scanning electron microscope/microscopy
SERS	surface enhanced Raman spectroscopy
stdev	standard deviation
TEM	transmission electron microscope/microscopy
TNT	trinitrotoluene
UNEP	United Nations Environmental Programme
UV-Vis	ultra violet – visible spectrum
V	volume
w	full width at half maximum of lorentzian curve
WE	working electrode
WHO	World Health Organisation
x_c	centre wavelength of lorentzian curve peak
y	intensity of lorentzian curve
y_0	intensity offset of lorentzian curve

Appendix B

MATLAB Code for decoding of anti-counterfeit tags

```
clear all;
disp('load file');
[image_id, image_pathname, filterindex] = uigetfile;
image_path_full = strcat(image_pathname, image_id);

fid = fopen(image_path_full);
QRCODENUMBER = fgets(fid);
fclose(fid)

MatrixQR = zeros(100, 2);

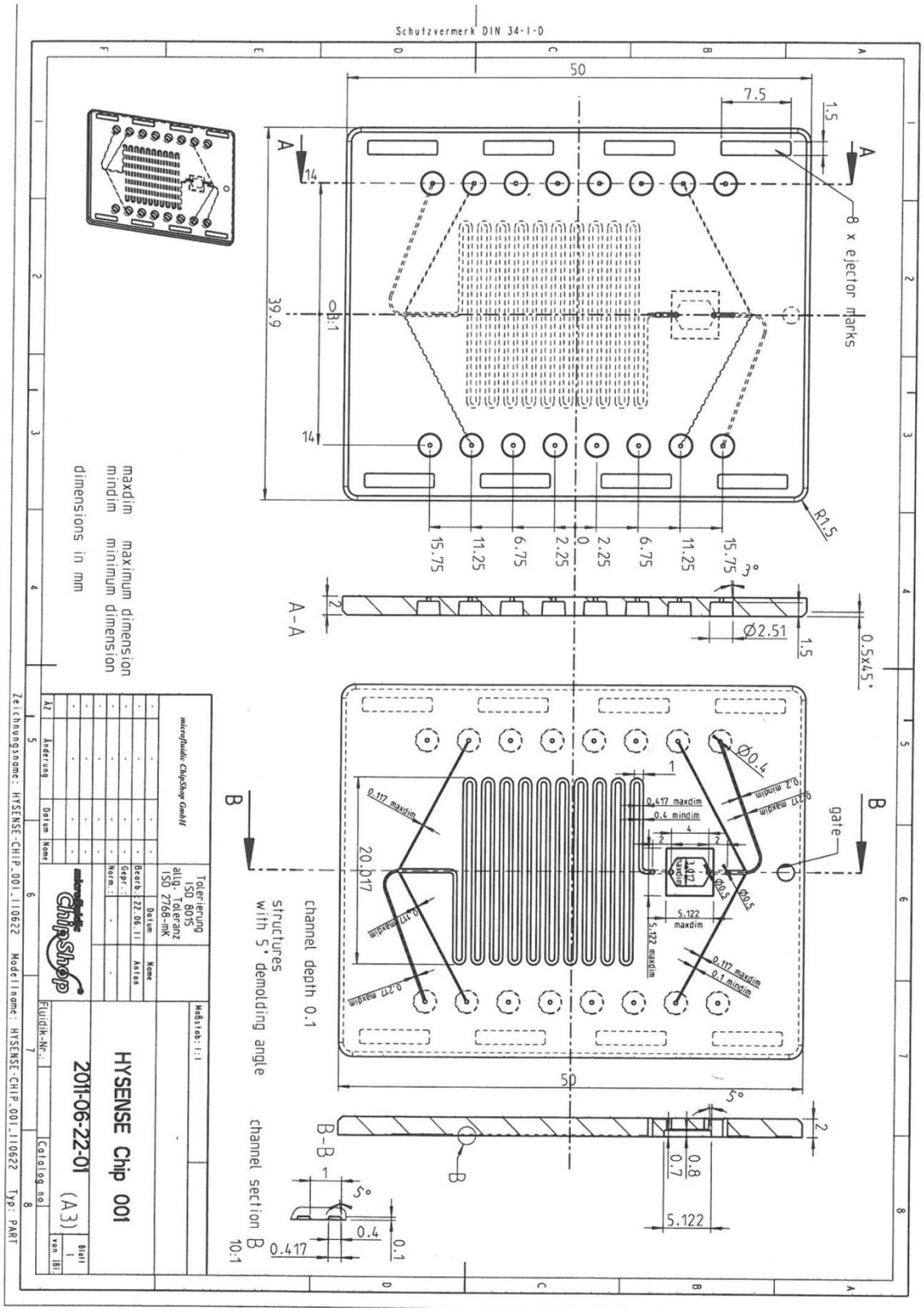
row = 1;
yFirstDigit = 1;
yNumberDigits = 2;
for x = 60:159
Packet = QRCODENUMBER(yFirstDigit:yNumberDigits);
Temp1 = str2double(Packet);

MatrixQR(row,1) = x;
MatrixQR(row,2) = (Temp1);
yFirstDigit = yFirstDigit + 2;
yNumberDigits = yNumberDigits + 2;
row = row + 1;
end

plot(MatrixQR(:,1),MatrixQR(:,2));
title('Green value histogram');
xlabel('Green Value');
ylabel('Pixel Count /100');
```

Appendix C

Technical drawing of HYSENS microfluidic cell



Appendix D

Peer reviewed Publications

Publications

- **Investigation of Au-Hg Amalgam Formation on Substrate-Immobilized Individual Au Nanorods** *Carola Schopf, Alfonso Martín, Michael Schmidt, Daniela Iacopino,* Journal of Materials Chemistry C,**2015**.3(34): p. 8865-8872

- **Au nanorod plasmonic superstructures obtained by a combined droplet evaporation and stamping method** *Carola Schopf, Alfonso Martín, Mícheál Burke, Daniel Jones, Andrea Pescaglini, Alan O'Riordan, Aidan J. Quinn, Daniela Iacopino*, Journal of Materials Chemistry C, **2014**. 2(18): p. 3536-3541

- **Surface-Enhanced Raman Scattering of 4-Aminobenzenethiol on Au Nanorod Ordered Arrays** *Alfonso Martín, Andrea Pescaglini, Carola Schopf, Vittorio Scardaci, Richard Coull, Lorraine Byrne, and Daniela Iacopino*, Journal of Physical Chemistry C, **2014.** 118(24): p. 13260-13267

- **Facile Formation of Ordered Vertical Arrays by Droplet Evaporation of Au Nanorod Organic Solutions**, *Alfonso Martín, Carola Schopf, Andrea Pescaglini, Jing Jing Wang, Daniela Iacopino*, Langmuir, **2014**. 30(34): p.10206-10212

- **Synthesis, Optical Properties and Self-Assembly of Gold Nanrods** *Alfonso Martin, Carola Schopf, Andrea Pescaglini, Alan O'Riordan, Daniela Iacopino,* Journal of Experimental Nanoscience, **2012**. 7(6): p. 688-702

Oral presentation

- **Single Au nanorods and for optical Hg detection**, *Carola Schopf, Alfonso Martín, Daniela Iacopino*, UCC Chemistry Research Day, Cork, July 2014

- **Single Au nanorods and for optical Hg detection**, *Carola Schopf, Alfonso Martín, Daniela Iacopino*, E-MRS Spring Meeting 2014, Lille, May 2014

Poster presentations

- **Single Gold Nanorods for Optical Mercury Detection**, *Carola Schopf, Alfonso Martín, Daniela Iacopino*, NanoMA 2015, Tsukuba, July 2015,

- **Single Gold Nanorods for Optical Mercury Detection**, *Carola Schopf, Alfonso Martín, Daniela Iacopino*, 9th NANOSMAT, Dublin, September 2014, **Poster Prize**

- **Optical properties of Au nanorods and 2D nanorod assemblies,** *Carola Schopf, Alfonso Martín, Daniela Iacopino*, RSC 11th International Conference on Materials Chemistry, Warwick, July 2013

- **Highly ordered Au nanorod arrays: assembly, optical properties and applications,** *Carola Schopf, Alfonso Martín, Daniela Iacopino*, Tyndall postgraduate poster competition, Cork, April 2013, **complimentary place**

- **Correlated Electron Microscopy/Optical Imaging and Spectroscopy of single Au nanorods and 2D nanorod assemblies,** *Carola Schopf, Alfonso Martín, Daniela Iacopino*, Tyndall postgraduate poster competition, Cork, July 2012, **complimentary place**

- **Correlated Optical/Electron Microscopy Imaging and Spectroscopy of Metal Nanostructures,** *Carola Schopf, Ethel Noonan, Gaëtan Lévêque, Aidan J. Quinn, Daniela Iacopino*, Postgraduate Symposium on Nanotechnology, Birmingham, December 2011, **Poster prize**

- **Dark field optical microscopy of single nanoparticles and ordered nanoparticle arrays,** *Carola Schopf, Andrea Pescaglini, Alan O'Riordan, Daniela Iacopino*, Sensors & their Application XVI, Cork, September 2011, **Poster prize**

- **Dark field optical microscopy of single nanoparticles and ordered nanoparticle arrays,** *Andrea Pescaglini, Carola Schopf Alan O'Riordan Daniela Iacopino*, ICONO-ICOPE 2011, Dublin, September 2011

- **Single nanoparticle dark field optical microscopy,** *Carola Schopf, Daniela Iacopino*, Tyndall postgraduate poster competition, Cork, July 2011

References

1. Selin, N.E., *Global Biogeochemical Cycling of Mercury: A Review.* Annual Review of Environment and Resources, 2009. **34**(1): p. 43-63.

2. Driscoll, C.T., et al., *Mercury as a global pollutant: sources, pathways, and effects.* Environmental Science & Technology, 2013. **47**(10): p. 4967-4983.

3. Branch, U.C., *The global atmospheric mercury assessment 2013: Sources, emissions, releases and environmental transport.* UNEP-Chemicals, Geneva, 2013.

4. Clarkson, T.W., L. Magos, and G.J. Myers, *The toxicology of mercury—current exposures and clinical manifestations.* New England Journal of Medicine, 2003. **349**(18): p. 1731-1737.

5. Grandjean, P., et al., *Adverse effects of methylmercury: environmental health research implications.* Environmental Health Perspectives, 2010: p. 1137-1145.

6. *Guidelines for drinking-water quality - 4th ed.* World Health Organization, 2011.

7. Yamini, Y., N. Alizadeh, and M. Shamsipur, *Solid phase extraction and determination of ultra trace amounts of mercury (II) using octadecyl silica membrane disks modified by hexathia-18-crown-6-tetraone and cold vapour atomic absorption spectrometry.* Analytica Chimica Acta, 1997. **355**(1): p. 69-74.

8. Welz, B., D.L. Tsalev, and M. Sperling, *On-line microwave sample pretreatment for the determination of mercury in water and urine by flow-injection cold-vapour atomic absorption spectrometry.* Analytica Chimica Acta, 1992. **261**(1): p. 91-103.

9. Ghaedi, M., et al., *Highly Selective and Sensitive Preconcentration of Mercury Ion and Determination by Cold Vapor Atomic Absorption Spectroscopy.* Analytical Letters, 2006. **39**(6): p. 1171-1185.

10. Karunasagar, D., J. Arunachalam, and S. Gangadharan, *Development of a 'collect and punch' cold vapour inductively coupled plasma mass spectrometric method for the direct determination of mercury at nanograms per litre levels.* Journal of Analytical Atomic Spectrometry, 1998. **13**(7): p. 679-682.

11. Bloom, N. and W.F. Fitzgerald, *Determination of volatile mercury species at the picogram level by low-temperature gas chromatography with cold-vapour atomic fluorescence detection.* Analytica Chimica Acta, 1988. **208**(0): p. 151-161.

12. Yu, L.P. and X.P. Yan, *Flow injection online sorption preconcentration coupled with cold vapor atomic fluorescence spectrometry with online oxidative elution for determination of trace mercury in water samples.* Atomic Spectroscopy, 2004. **25**(3): p. 145-153.

13. Wu, L., et al., *Microwave-enhanced cold vapor generation for speciation analysis of mercury by atomic fluorescence spectrometry.* Talanta, 2012. **94**: p. 146-151.

14. de Wuilloud, J.C.A., et al., *Sensitive determination of mercury in tap water by cloud point extraction pre-concentration and flow injection-cold vapor-inductively coupled*

plasma optical emission spectrometry. Spectrochimica Acta Part B: Atomic Spectroscopy, 2002. **57**(2): p. 365-374.

15. Zhu, X. and S.D. Alexandratos, *Determination of trace levels of mercury in aqueous solutions by inductively coupled plasma atomic emission spectrometry: Elimination of the 'memory effect'.* Microchemical Journal, 2007. **86**(1): p. 37-41.

16. de Torres, A.G., J.M.C. Pavón, and E.R. Castellon, *Automated on-line separation–preconcentration system for inductively coupled plasma atomic emission spectrometry and its application to mercury determination.* Journal of Analytical Atomic Spectrometry, 1998. **13**(4): p. 243-248.

17. Anthemidis, A.N., et al., *Time-based on-line preconcentration cold vapour generation procedure for ultra-trace mercury determination with inductively coupled plasma atomic emission spectrometry.* Analytical and Bioanalytical Chemistry, 2004. **379**(5-6): p. 764-769.

18. El-Safty, S.A. and M.A. Shenashen, *Mercury-ion optical sensors.* TrAC Trends in Analytical Chemistry, 2012. **38**(0): p. 98-115.

19. Aragay, G. and A. Merkoçi, *Nanomaterials application in electrochemical detection of heavy metals.* Electrochimica Acta, 2012. **84**(0): p. 49-61.

20. Zhang, L. and M. Fang, *Nanomaterials in pollution trace detection and environmental improvement.* Nano Today, 2010. **5**(2): p. 128-142.

21. Aragay, G., J. Pons, and A. Merkoçi, *Recent Trends in Macro-, Micro-, and Nanomaterial-Based Tools and Strategies for Heavy-Metal Detection.* Chemical Reviews, 2011. **111**(5): p. 3433-3458.

22. Botasini, S., G. Heijo, and E. Méndez, *Toward decentralized analysis of mercury (II) in real samples. A critical review on nanotechnology-based methodologies.* Analytica Chimica Acta, 2013. **800**(0): p. 1-11.

23. Wang, L., et al., *Nanoparticle-based environmental sensors.* Materials Science and Engineering: R: Reports, 2010. **70**(3): p. 265-274.

24. Wang, C. and C. Yu, *Detection of chemical pollutants in water using gold nanoparticles as sensors: a review.* Reviews in Analytical Chemistry, 2013. **32**(1): p. 1-14.

25. Selid, P.D., et al., *Sensing mercury for biomedical and environmental monitoring.* Sensors, 2009. **9**(7): p. 5446-5459.

26. Faraday, M., *The Bakerian Lecture: Experimatal Relations of Gold (and Other Metals) to Light.* Philosophical Transactions o the Royal Society of London, 1857. **147**: p. 145-181.

27. Tyndall, J., *On the blue colour of the sky, the polarization of skylight, and on the polarization of light by cloudy matter generally.* Proceedings of the Royal Society of London, 1868. **17**: p. 223-233.

28. Mie, G., *Beiträge zur Optik trüber Medien, speziell kolloidaler Metallösungen.* Annalen der Physik, 1908. **330**(3): p. 377-445.

29. Edwards, P.P. and J.M. Thomas, *Gold in a Metallic Divided State—From Faraday to Present-Day Nanoscience.* Angewandte Chemie International Edition, 2007. **46**(29): p. 5480-5486.

30. Turkevich, J., P.C. Stevenson, and J. Hillier, *A Study of the Nucleation and Growth Processes in the Synthesis of Colloidal Gold.* Discussions of the Faraday Society, 1951(11): p. 55-&.

31. Brust, M., et al., *Synthesis of thiol-derivatised gold nanoparticles in a two-phase liquid–liquid system.* J. Chem. Soc., Chem. Commun., 1994(7): p. 801-802.

32. Nikoobakht, B. and M.A. El-Sayed, *Preparation and growth mechanism of gold nanorods (NRs) using seed-mediated growth method.* Chemistry of Materials, 2003. **15**(10): p. 1957-1962.

33. Tao, A.R., S. Habas, and P. Yang, *Shape Control of Colloidal Metal Nanocrystals.* Small, 2008. **4**(3): p. 310-325.

34. Zhang, Q., et al., *Faceted Gold Nanorods: Nanocuboids, Convex Nanocuboids, and Concave Nanocuboids.* Nano Letters, 2015. **15**(6): p. 4161-4169.

35. Walsh, M.J., et al., *Symmetry Breaking and Silver in Gold Nanorod Growth.* Acs Nano, 2015. **9**(1): p. 715-724.

36. Lattuada, M. and T.A. Hatton, *Synthesis, properties and applications of Janus nanoparticles.* Nano Today, 2011. **6**(3): p. 286-308.

37. Sun, Y., et al., *Synthesis and Optical Properties of Nanorattles and Multiple-Walled Nanoshells/Nanotubes Made of Metal Alloys.* Journal of the American Chemical Society, 2004. **126**(30): p. 9399-9406.

38. Van Dijk, M.A., M. Lippitz, and M. Orrit, *Far-field optical microscopy of single metal nanoparticles.* Accounts of Chemical Research, 2005. **38**(7): p. 594-601.

39. Carbó-Argibay, E., et al., *The Crystalline Structure of Gold Nanorods Revisited: Evidence for Higher-Index Lateral Facets.* Angewandte Chemie, 2010. **122**(49): p. 9587-9590.

40. Arbouet, A., et al., *Direct Measurement of the Single-Metal-Cluster Optical Absorption.* Physical Review Letters, 2004. **93**(12): p. 127401.

41. Nie, S. and S.R. Emory, *Probing Single Molecules and Single Nanoparticles by Surface-Enhanced Raman Scattering.* Science, 1997. **275**(5303): p. 1102-1106.

42. Nelayah, J., et al., *Mapping surface plasmons on a single metallic nanoparticle.* Nat Phys, 2007. **3**(5): p. 348-353.

43. Ozbay, E., *Plasmonics: Merging Photonics and Electronics at Nanoscale Dimensions.* Science, 2006. **311**(5758): p. 189-193.

44. Ditlbacher, H., et al., *Two-dimensional optics with surface plasmon polaritons.* Applied Physics Letters, 2002. **81**(10): p. 1762-1764.

45. Quinten, M., et al., *Electromagnetic energy transport via linear chains of silver nanoparticles.* Optics Letters, 1998. **23**(17): p. 1331-1333.

46. Krenn, J., et al., *Non–diffraction-limited light transport by gold nanowires.* EPL (Europhysics Letters), 2002. **60**(5): p. 663.

47. Maier, S.A., et al., *Local detection of electromagnetic energy transport below the diffraction limit in metal nanoparticle plasmon waveguides.* Nat Mater, 2003. **2**(4): p. 229-232.

48. Anker, J.N., et al., *Biosensing with plasmonic nanosensors.* Nature Materials, 2008. **7**(6): p. 442-453.

49. Lee, K.S. and M.A. El-Sayed, *Gold and silver nanoparticles in sensing and imaging: Sensitivity of plasmon response to size, shape, and metal composition.* Journal of Physical Chemistry B, 2006. **110**(39): p. 19220-19225.

50. McFarland, A.D. and R.P. Van Duyne, *Single Silver Nanoparticles as Real-Time Optical Sensors with Zeptomole Sensitivity.* Nano Letters, 2003. **3**(8): p. 1057-1062.

51. Mayer, K.M. and J.H. Hafner, *Localized Surface Plasmon Resonance Sensors.* Chemical Reviews, 2011. **111**(6): p. 3828-3857.

52. Wieckowski, A., E.R. Savinova, and C.G. Vayenas, *Catalysis and electrocatalysis at nanoparticle surfaces*2003: CRC Press.

53. Astruc, D., F. Lu, and J.R. Aranzaes, *Nanoparticles as recyclable catalysts: the frontier between homogeneous and heterogeneous catalysis.* Angewandte Chemie International Edition, 2005. **44**(48): p. 7852-7872.

54. Narayanan, R. and M.A. El-Sayed, *Changing Catalytic Activity during Colloidal Platinum Nanocatalysis Due to Shape Changes: Electron-Transfer Reaction.* Journal of the American Chemical Society, 2004. **126**(23): p. 7194-7195.

55. Roucoux, A., J. Schulz, and H. Patin, *Reduced Transition Metal Colloids: A Novel Family of Reusable Catalysts?* Chemical Reviews, 2002. **102**(10): p. 3757-3778.

56. Olson, J., et al., *Optical characterization of single plasmonic nanoparticles.* Chemical Society Reviews, 2014.

57. Jain, P.K., et al., *Calculated Absorption and Scattering Properties of Gold Nanoparticles of Different Size, Shape, and Composition: Applications in Biological Imaging and Biomedicine.* The Journal of Physical Chemistry B, 2006. **110**(14): p. 7238-7248.

58. Maier, S.A., *Plasmonics: fundamentals and applications*2007: Springer Science & Business Media.

59. Mulvaney, P., et al., *Drastic Surface Plasmon Mode Shifts in Gold Nanorods Due to Electron Charging.* Plasmonics, 2006. **1**(1): p. 61-66.

60. Gans, R., *Über die Form ultramikroskopischer Goldteilchen.* Annalen der Physik, 1912. **342**(5): p. 881-900.

61. Sharma, V., K. Park, and M. Srinivasarao, *Colloidal dispersion of gold nanorods: Historical background, optical properties, seed-mediated synthesis, shape separation and self-assembly.* Materials Science & Engineering R-Reports, 2009. **65**(1-3): p. 1-38.

62. Zhao, J., et al., *Methods for Describing the Electromagnetic Properties of Silver and Gold Nanoparticles.* Accounts of Chemical Research, 2008. **41**(12): p. 1710-1720.

63. Mock, J.J., et al., *Shape effects in plasmon resonance of individual colloidal silver nanoparticles.* Journal of Chemical Physics, 2002. **116**(15): p. 6755-6759.

64. Song, Y., et al., *Correlation and Characterization of Three-Dimensional Morphologically Dependent Localized Surface Plasmon Resonance Spectra of Single Silver Nanoparticles Using Dark-Field Optical Microscopy and Spectroscopy and Atomic Force Microscopy.* The Journal of Physical Chemistry C, 2009. **114**(1): p. 74-81.

65. Huang, T. and X.H.N. Xu, *Synthesis and characterization of tunable rainbow colored colloidal silver nanoparticles using single-nanoparticle plasmonic microscopy and spectroscopy.* Journal of Materials Chemistry, 2010. **20**(44): p. 9867-9876.

66. Heckel, J.C. and G. Chumanov, *Depolarized Light Scattering From Single Silver Nanoparticles.* The Journal of Physical Chemistry C, 2011. **115**(15): p. 7261-7269.

67. Kelly, K.L., et al., *The Optical Properties of Metal Nanoparticles: The Influence of Size, Shape, and Dielectric Environment.* The Journal of Physical Chemistry B, 2003. **107**(3): p. 668-677.

68. Zhong Zhang, J., *Optical Properties and Spectroscopy of Nanomaterials*2009, Singapore: World Scientific Publishing.

69. Mock, J.J., D.R. Smith, and S. Schultz, *Local refractive index dependence of plasmon resonance spectra from individual nanoparticles.* Nano Letters, 2003. **3**: p. 485-491.

70. Miller, M.M. and A.A. Lazarides, *Sensitivity of Metal Nanoparticle Surface Plasmon Resonance to the Dielectric Environment.* The Journal of Physical Chemistry B, 2005. **109**(46): p. 21556-21565.

71. Chen, H., et al., *Shape- and Size-Dependent Refractive Index Sensitivity of Gold Nanoparticles.* Langmuir, 2008. **24**(10): p. 5233-5237.

72. Romero, I., et al., *Plasmons in nearly touching metallic nanoparticles: singular response in the limit of touching dimers.* Opt. Express, 2006. **14**(21): p. 9988-9999.

73. Zuloaga, J., E. Prodan, and P. Nordlander, *Quantum Description of the Plasmon Resonances of a Nanoparticle Dimer.* Nano Letters, 2009. **9**(2): p. 887-891.

74. Nordlander, P., et al., *Plasmon Hybridization in Nanoparticle Dimers.* Nano Letters, 2004. **4**(5): p. 899-903.

75. Rivera, T.P., et al., *Spectroscopic studies of plasmonic interactions in colloidal dimers fabricated by convective-capillary force assembly.* Microelectronic Engineering, 2008. **86**(4-6): p. 1089-1092.

76. Jain, P.K., W. Huang, and M.A. El-Sayed, *On the Universal Scaling Behavior of the Distance Decay of Plasmon Coupling in Metal Nanoparticle Pairs: A Plasmon Ruler Equation.* Nano Letters, 2007. **7**(7): p. 2080-2088.

77. Rechberger, W., et al., *Optical properties of two interacting gold nanoparticles.* Optics Communications, 2003. **220**(1–3): p. 137-141.

78. Barrow, S.J., et al., *Surface Plasmon Resonances in Strongly Coupled Gold Nanosphere Chains from Monomer to Hexamer.* Nano Letters, 2011. **11**(10): p. 4180-4187.

79. Maier, S.A., P.G. Kik, and H.A. Atwater, *Observation of coupled plasmon-polariton modes in Au nanoparticle chain waveguides of different lengths: Estimation of waveguide loss.* Applied Physics Letters, 2002. **81**(9): p. 1714-1716.

80. Brandl, D.W., N.A. Mirin, and P. Nordlander, *Plasmon Modes of Nanosphere Trimers and Quadrumers.* The Journal of Physical Chemistry B, 2006. **110**(25): p. 12302-12310.

81. Chuntonov, L. and G. Haran, *Trimeric Plasmonic Molecules: The Role of Symmetry.* Nano Letters, 2011. **11**(6): p. 2440-2445.

82. Tian, X., et al., *Plasmonic Coupling in Single Silver Nanosphere Assemblies by Polarization-Dependent Dark-Field Scattering Spectroscopy.* The Journal of Physical Chemistry C, 2014.

83. Fan, J.A., et al., *Self-Assembled Plasmonic Nanoparticle Clusters.* Science, 2010. **328**(5982): p. 1135-1138.

84. Prodan, E., et al., *A hybridization model for the plasmon response of complex nanostructures.* Science, 2003. **302**(5644): p. 419-422.

85. Biswas, S., et al., *Plasmonic Resonances in Self-Assembled Reduced Symmetry Gold Nanorod Structures.* Nano Letters, 2013. **13**(5): p. 2220-2225.

86. Slaughter, L.S., et al., *Effects of Symmetry Breaking and Conductive Contact on the Plasmon Coupling in Gold Nanorod Dimers.* Acs Nano, 2010. **4**(8): p. 4657-4666.

87. Yan, B., et al., *Engineered SERS Substrates With Multiscale Signal Enhancement: Nanoplarticle Cluster Arrays.* Acs Nano, 2009. **3**(5): p. 1190-1202.

88. Fan, M. and A.G. Brolo, *Silver nanoparticles self assembly as SERS substrates with near single molecule detection limit.* Physical Chemistry Chemical Physics, 2009. **11**(34): p. 7381-7389.

89. Zhang, D.F., et al., *Self-assembly of gold nanoparticles into chain-like structures and their optical properties.* Journal of Nanoparticle Research, 2011. **13**(9): p. 3923-3928.

90. Alvarez-Puebla, R.A., et al., *Gold nanorods 3D-supercrystals as surface enhanced Raman scattering spectroscopy substrates for the rapid detection of scrambled prions.* Proceedings of the National Academy of Sciences of the United States of America, 2011. **108**(20): p. 8157-8161.

91. Anger, P., P. Bharadwaj, and L. Novotny, *Enhancement and Quenching of Single-Molecule Fluorescence.* Physical Review Letters, 2006. **96**(11): p. 113002.

92. Ming, T., et al., *Plasmon-Controlled Fluorescence: Beyond the Intensity Enhancement.* The Journal of Physical Chemistry Letters, 2011. **3**(2): p. 191-202.

93. Liaw, J.-W., H.-Y. Tsai, and C.-H. Huang, *Size-Dependent Surface Enhanced Fluorescence of Gold Nanorod: Enhancement or Quenching.* Plasmonics, 2012. **7**(3): p. 543-553.

94. Haynes, C.L., et al., *Nanoparticle Optics: The Importance of Radiative Dipole Coupling in Two-Dimensional Nanoparticle Arrays†.* The Journal of Physical Chemistry B, 2003. **107**(30): p. 7337-7342.

95. Yun, S., et al., *Close-Packed Two-Dimensional Silver Nanoparticle Arrays: Quadrupolar and Dipolar Surface Plasmon Resonance Coupling.* Chemistry – A European Journal, 2015: p. n/a-n/a.

96. Kim, B., S.L. Tripp, and A. Wei, *Self-Organization of Large Gold Nanoparticle Arrays.* Journal of the American Chemical Society, 2001. **123**(32): p. 7955-7956.

97. Auguié, B. and W.L. Barnes, *Collective Resonances in Gold Nanoparticle Arrays.* Physical Review Letters, 2008. **101**(14): p. 143902.

98. Nie, Z.H., et al., *Plasmon spectra in two-dimensional nanorod arrays.* Nanotechnology, 2009. **20**(29).

99. Smythe, E.J., E. Cubukcu, and F. Capasso, *Optical properties of surface plasmon resonances of coupled metallic nanorods.* Optics Express, 2007. **15**(12): p. 7439-7447.

100. Evans, P.R., et al., *Optical Transmission Properties and Electric Field Distribution of Interacting 2D Silver Nanorod Arrays.* Advanced Functional Materials, 2008. **18**(7): p. 1075-1079.

101. Wurtz, G.A., et al., *Guided plasmonic modes in nanorod assemblies: strong electromagnetic coupling regime.* Opt. Express, 2008. **16**(10): p. 7460-7470.

102. Haiss, W., et al., *Determination of Size and Concentration of Gold Nanoparticles from UV−Vis Spectra.* Analytical Chemistry, 2007. **79**(11): p. 4215-4221.

103. Storhoff, J.J., et al., *One-pot colorimetric differentiation of polynucleotides with single base imperfections using gold nanoparticle probes.* Journal of the American Chemical Society, 1998. **120**(9): p. 1959-1964.

104. Badawy, A.M.E., et al., *Impact of environmental conditions (pH, ionic strength, and electrolyte type) on the surface charge and aggregation of silver nanoparticles suspensions.* Environmental Science & Technology, 2010. **44**(4): p. 1260-1266.

105. Sau, T.K. and C.J. Murphy, *Seeded high yield synthesis of short Au nanorods in aqueous solution.* Langmuir, 2004. **20**(15): p. 6414-6420.

106. Kalluri, J.R., et al., *Use of gold nanoparticles in a simple colorimetric and ultrasensitive dynamic light scattering assay: selective detection of arsenic in groundwater.* Angewandte Chemie, 2009. **121**(51): p. 9848-9851.

107. Jans, H., et al., *Dynamic light scattering as a powerful tool for gold nanoparticle bioconjugation and biomolecular binding studies.* Analytical Chemistry, 2009. **81**(22): p. 9425-9432.

108. Schultz, S., et al., *Single-target molecule detection with nonbleaching multicolor optical immunolabels.* Proceedings of the National Academy of Sciences, 2000. **97**(3): p. 996-1001.

109. Sönnichsen, C., et al., *Plasmon resonances in large noble-metal clusters.* New Journal of Physics, 2002. **4**(1): p. 93.

110. Sonnichsen, C., et al., *Drastic reduction of plasmon damping in gold nanorods.* Physical Review Letters, 2002. **88**(7): p. 077402-077402.

111. Nehl, C.L., et al., *Scattering spectra of single gold nanoshells.* Nano Letters, 2004. **4**(12): p. 2355-2359.

112. Berciaud, S., et al., *Photothermal Heterodyne Imaging of Individual Nonfluorescent Nanoclusters and Nanocrystals.* Physical Review Letters, 2004. **93**(25): p. 257402.

113. Chang, W.S., et al., *Plasmonic nanorod absorbers as orientation sensors.* Proceedings of the National Academy of Sciences of the United States of America, 2010. **107**(7): p. 2781-2786.

114. Selmke, M., M. Braun, and F. Cichos, *Photothermal single-particle microscopy: detection of a nanolens.* Acs Nano, 2012. **6**(3): p. 2741-2749.

115. Baida, H., et al., *Quantitative determination of the size dependence of surface plasmon resonance damping in single Ag@ SiO2 nanoparticles.* Nano Letters, 2009. **9**(10): p. 3463-3469.

116. Lindfors, K., et al., *Detection and spectroscopy of gold nanoparticles using supercontinuum white light confocal microscopy.* Physical Review Letters, 2004. **93**(3): p. 037401.

117. Billaud, P., et al., *Correlation between the Extinction Spectrum of a Single Metal Nanoparticle and Its Electron Microscopy Image.* The Journal of Physical Chemistry C, 2008. **112**(4): p. 978-982.

118. Wang, G., et al., *Resolving rotational motions of nano-objects in engineered environments and live cells with gold nanorods and differential interference contrast microscopy.* Journal of the American Chemical Society, 2010. **132**(46): p. 16417-16422.

119. Chen, H.J., et al., *Plasmon Coupling in Clusters Composed of Two-Dimensionally Ordered Gold Nanocubes.* Small, 2009. **5**(18): p. 2111-2119.

120. Funston, A.M., et al., *Plasmon coupling of gold nanorods at short distances and in different geometries.* Nano Letters, 2009. **9**(4): p. 1651-1658.

121. Hu, M., et al., *Correlated rayleigh scattering spectroscopy and scanning electron microscopy studies of Au-Ag bimetallic nanoboxes and nanocages.* Journal of Physical Chemistry C, 2007. **111**(34): p. 12558-12565.

122. Garg, N., et al., *The Role of Bromide Ions in Seeding Growth of Au Nanorods.* Langmuir, 2010. **26**(12): p. 10271-10276.

123. Johnson, C.J., et al., *Growth and form of gold nanorods prepared by seed-mediated, surfactant-directed synthesis.* Journal of Materials Chemistry, 2002. **12**(6): p. 1765-1770.

124. Liu, M. and P. Guyot-Sionnest, *Synthesis and Optical Characterization of Au/Ag Core/Shell Nanorods.* The Journal of Physical Chemistry B, 2004. **108**(19): p. 5882-5888.

125. Cao, W., et al., *Localized surface plasmon resonance of single silver nanoparticles studied by dark-field optical microscopy and spectroscopy.* Journal of Applied Physics, 2011. **109**(3).

126. Saha, K., et al., *Gold Nanoparticles in Chemical and Biological Sensing.* Chemical Reviews, 2012. **112**(5): p. 2739-2779.

127. Rosi, N.L. and C.A. Mirkin, *Nanostructures in Biodiagnostics.* Chemical Reviews, 2005. **105**(4): p. 1547-1562.

128. Wang, Z. and L. Ma, *Gold nanoparticle probes.* Coordination Chemistry Reviews, 2009. **253**(11–12): p. 1607-1618.

129. Willets, K.A. and R.P. Van Duyne, *Localized Surface Plasmon Resonance Spectroscopy and Sensing.* Annual Review of Physical Chemistry, 2007. **58**(1): p. 267-297.

130. Anker, J.N., et al., *Biosensing with plasmonic nanosensors.* Nat Mater, 2008. **7**(6): p. 442-453.

131. Pena-Rodriguez, O., et al., *Configuring Au and Ag nanorods for sensing applications.* Journal of the Optical Society of America B-Optical Physics, 2011. **28**(4): p. 714-720.

132. Malinsky, M.D., et al., *Chain length dependence and sensing capabilities of the localized surface plasmon resonance of silver nanoparticles chemically modified with alkanethiol self-assembled monolayers.* Journal of the American Chemical Society, 2001. **123**(7): p. 1471-1482.

133. Haes, A.J., et al., *Detection of a Biomarker for Alzheimer's Disease from Synthetic and Clinical Samples Using a Nanoscale Optical Biosensor.* Journal of the American Chemical Society, 2005. **127**(7): p. 2264-2271.

134. Raschke, G., et al., *Biomolecular Recognition Based on Single Gold Nanoparticle Light Scattering.* Nano Letters, 2003. **3**(7): p. 935-938.

135. Chen, C.-D., et al., *Sensing capability of the localized surface plasmon resonance of gold nanorods.* Biosensors and Bioelectronics, 2007. **22**(6): p. 926-932.

136. Kreuzer, M.P., et al., *Quantitative detection of doping substances by a localised surface plasmon sensor.* Biosensors and Bioelectronics, 2006. **21**(7): p. 1345-1349.

137. Mirkin, C.A., et al., *A DNA-based method for rationally assembling nanoparticles into macroscopic materials.* Nature, 1996. **382**(6592): p. 607-609.

138. Lin, S.-Y., et al., *A Cooperative Effect of Bifunctionalized Nanoparticles on Recognition: Sensing Alkali Ions by Crown and Carboxylate Moieties in Aqueous Media.* Analytical Chemistry, 2005. **77**(15): p. 4821-4828.

139. Huang, C.-C. and H.-T. Chang, *Parameters for selective colorimetric sensing of mercury(ii) in aqueous solutions using mercaptopropionic acid-modified gold nanoparticles.* Chemical Communications, 2007(12): p. 1215-1217.

140. Aslan, K., J.R. Lakowicz, and C.D. Geddes, *Nanogold-plasmon-resonance-based glucose sensing.* Analytical Biochemistry, 2004. **330**(1): p. 145-155.

141. Thaxton, C.S., D.G. Georganopoulou, and C.A. Mirkin, *Gold nanoparticle probes for the detection of nucleic acid targets.* Clinica Chimica Acta, 2006. **363**(1–2): p. 120-126.

142. Liu, J. and Y. Lu, *Fast colorimetric sensing of adenosine and cocaine based on a general sensor design involving aptamers and nanoparticles.* Angewandte Chemie, 2006. **118**(1): p. 96-100.

143. Liu, J. and Y. Lu, *A colorimetric lead biosensor using DNAzyme-directed assembly of gold nanoparticles.* Journal of the American Chemical Society, 2003. **125**(22): p. 6642-6643.

144. Yoosaf, K., et al., *In situ synthesis of metal nanoparticles and selective naked-eye detection of lead ions from aqueous media.* The Journal of Physical Chemistry C, 2007. **111**(34): p. 12839-12847.

145. Choi, Y., et al., *Selective and sensitive detection of metal ions by plasmonic resonance energy transfer-based nanospectroscopy.* Nature Nanotechnology, 2009. **4**(11): p. 742-746.

146. Choi, Y.H., T. Kang, and L.P. Lee, *Plasmon Resonance Energy Transfer (PRET)-based Molecular Imaging of Cytochrome c in Living Cells.* Nano Letters, 2009. **9**(1): p. 85-90.

147. Qu, W.-G., et al., *Plasmonic resonance energy transfer-based nanospectroscopy for sensitive and selective detection of 2,4,6-trinitrotoluene (TNT).* Chemical Communications, 2011. **47**(4): p. 1237-1239.

148. Wurtz, G.A., et al., *Molecular plasmonics with tunable exciton-plasmon coupling strength in J-aggregate hybridized Au nanorod assemblies.* Nano Letters, 2007. **7**(5): p. 1297-1303.

149. Fofang, N.T., et al., *Plexcitonic Nanoparticles: Plasmon−Exciton Coupling in Nanoshell−J-Aggregate Complexes.* Nano Letters, 2008. **8**(10): p. 3481-3487.

150. Novo, C., A.M. Funston, and P. Mulvaney, *Direct observation of chemical reactions on single gold nanocrystals using surface plasmon spectroscopy.* Nature Nanotechnology, 2008. **3**(10): p. 598-602.

151. Zhou, H., et al., *Optical monitoring of faradaic reaction using single plasmon-resonant nanorods functionalized with graphene.* Chemical Communications, 2015.

152. Seo, D., G. Park, and H. Song, *Plasmonic Monitoring of Catalytic Hydrogen Generation by a Single Nanoparticle Probe.* Journal of the American Chemical Society, 2011. **134**(2): p. 1221-1227.

153. Huang, C.C. and H.T. Chang, *Selective gold-nanoparticle-based "turn-on" fluorescent sensors for detection of mercury(II) in aqueous solution.* Analytical Chemistry, 2006. **78**(24): p. 8332-8338.

154. Dasary, S.S.R., et al., *Gold nanoparticle based surface enhanced fluorescence for detection of organophosphorus agents.* Chemical Physics Letters, 2008. **460**(1–3): p. 187-190.

155. Oh, E., et al., *Inhibition Assay of Biomolecules based on Fluorescence Resonance Energy Transfer (FRET) between Quantum Dots and Gold Nanoparticles.* Journal of the American Chemical Society, 2005. **127**(10): p. 3270-3271.

156. You, C.-C., et al., *Detection and identification of proteins using nanoparticle–fluorescent polymer 'chemical nose'sensors.* Nature Nanotechnology, 2007. **2**(5): p. 318-323.

157. He, X., et al., *Gold Nanoparticle-Based Fluorometric and Colorimetric Sensing of Copper(II) Ions.* Advanced Materials, 2005. **17**(23): p. 2811-2815.

158. Chen, S.-J. and H.-T. Chang, *Nile red-adsorbed gold nanoparticles for selective determination of thiols based on energy transfer and aggregation.* Analytical Chemistry, 2004. **76**(13): p. 3727-3734.

159. Li, M., et al., *Detection of Mercury(II) by Quantum Dot/DNA/Gold Nanoparticle Ensemble Based Nanosensor Via Nanometal Surface Energy Transfer.* Analytical Chemistry, 2011. **83**(18): p. 7061-7065.

160. Li, X., et al., *Fluorescence quenching of quantum dots by gold nanorods and its application to DNA detection.* Applied Physics Letters, 2009. **94**(6): p. 063111-3.

161. Ipe, B.I., K. Yoosaf, and K.G. Thomas, *Functionalized gold nanoparticles as phosphorescent nanomaterials and sensors.* Journal of the American Chemical Society, 2006. **128**(6): p. 1907-1913.

162. Kneipp, K., et al., *Ultrasensitive chemical analysis by Raman spectroscopy.* Chemical Reviews, 1999. **99**(10): p. 2957-2976.

163. Banholzer, M.J., et al., *Rationally designed nanostructures for surface-enhanced Raman spectroscopy.* Chemical Society Reviews, 2008. **37**(5): p. 885-897.

164. Yu, W.W. and I.M. White, *A simple filter-based approach to surface enhanced Raman spectroscopy for trace chemical detection.* Analyst, 2012. **137**(5): p. 1168-1173.

165. Zhu, Z., et al., *Superstructures and SERS Properties of Gold Nanocrystals with Different Shapes.* Angewandte Chemie International Edition, 2011. **50**(7): p. 1593-1596.

166. Crane, L.G., et al., *SERS surfaces modified with a 4-(2-pyridylazo) resorcinol disulfide derivative: Detection of copper, lead, and cadmium.* Analytical Chemistry, 1995. **67**(2): p. 360-364.

167. Alvarez-Puebla, R.A. and L.M. Liz-Marzán, *SERS detection of small inorganic molecules and ions.* Angewandte Chemie International Edition, 2012. **51**(45): p. 11214-11223.

168. Nikoobakht, B. and M.A. El-Sayed, *Surface-enhanced Raman scattering studies on aggregated gold nanorods.* Journal of Physical Chemistry A, 2003. **107**(18): p. 3372-3378.

169. Senapati, T., et al., *Highly selective SERS probe for Hg(ii) detection using tryptophan-protected popcorn shaped gold nanoparticles.* Chemical Communications, 2011. **47**(37): p. 10326-10328.

170. Chen, Y., et al., *Determination of mercury(II) by surface-enhanced Raman scattering spectroscopy based on thiol-functionalized silver nanoparticles.* Microchimica Acta, 2012. **177**(3-4): p. 341-348.

171. Yu, C.J. and W.L. Tseng, *Colorimetric Detection of Mercury(II) in a High-Salinity Solution Using Gold Nanoparticles Capped with 3-Mercaptopropionate Acid and Adenosine Monophosphate.* Langmuir, 2008. **24**(21): p. 12717-12722.

172. Kim, Y., R.C. Johnson, and J.T. Hupp, *Gold Nanoparticle-Based Sensing of "Spectroscopically Silent" Heavy Metal Ions.* Nano Letters, 2001. **1**(4): p. 165-167.

173. Walekar, L.S., et al., *A novel colorimetric probe for highly selective recognition of Hg2+ ions in aqueous media based on inducing the aggregation of CPB-capped AgNPs: accelerating direct detection for environmental analysis.* Analytical Methods, 2013. **5**(20): p. 5501-5507.

174. Lin, C.-Y., et al., *Colorimetric Sensing of Silver(I) and Mercury(II) Ions Based on an Assembly of Tween 20-Stabilized Gold Nanoparticles.* Analytical Chemistry, 2010. **82**(16): p. 6830-6837.

175. Placido, T., et al., *Ion-Directed Assembly of Gold Nanorods: A Strategy for Mercury Detection.* ACS Applied Materials & Interfaces, 2013. **5**(3): p. 1084-1092.

176. Lee, J.-S., M.S. Han, and C.A. Mirkin, *Colorimetric Detection of Mercuric Ion (Hg2+) in Aqueous Media using DNA-Functionalized Gold Nanoparticles.* Angewandte Chemie International Edition, 2007. **46**(22): p. 4093-4096.

177. Wei, Q., et al., *Detection and Spatial Mapping of Mercury Contamination in Water Samples using a Smart-Phone.* Acs Nano, 2014.

178. Wang, Y., F. Yang, and X.R. Yang, *Colorimetric Detection of Mercury(II) Ion Using Unmodified Silver Nanoparticles and Mercury-Specific Oligonucleotides.* ACS Applied Materials & Interfaces, 2010. **2**(2): p. 339-342.

179. Jinlong, C., et al., *A functionalized gold nanoparticles and Rhodamine 6G based fluorescent sensor for high sensitive and selective detection of mercury(II) in environmental water samples.* Analytica Chimica Acta, 2007. **599**(1): p. 134-142.

180. Darbha, G.K., A. Ray, and P.C. Ray, *Gold Nanoparticle-Based Miniaturized Nanomaterial Surface Energy Transfer Probe for Rapid and Ultrasensitive Detection of Mercury in Soil, Water, and Fish.* Acs Nano, 2007. **1**(3): p. 208-214.

181. Ganbold, E.-O., et al., *Gold Nanoparticle-Based Detection of Hg(II) in an Aqueous Solution: Fluorescence Quenching and Surface-Enhanced Raman Scattering Study.* Bulletin of the Korean Chemical Society, 2011. **32**(2): p. 519-523.

182. Li, F., et al., *Ultrasensitive and selective detection of copper (II) and mercury (II) ions by dye-coded silver nanoparticle-based SERS probes.* Biosensors and Bioelectronics, 2013. **39**(1): p. 82-87.

183. Guo, Z., et al., *A test strip platform based on DNA-functionalized gold nanoparticles for on-site detection of mercury (II) ions.* Talanta, 2012. **93**(0): p. 49-54.

184. Xing, C., et al., *Colorimetric detection of mercury based on a strip sensor.* Analytical Methods, 2014.

185. Duan, J. and Z.Y. Guo, *Development of a test strip based on DNA-functionalized gold nanoparticles for rapid detection of mercury (II) ions.* Chinese Chemical Letters, 2012. **23**(2): p. 225-228.

186. Chen, G.-H., et al., *Detection of mercury (II) ions using colorimetric gold nanoparticles on paper-based analytical devices.* Analytical Chemistry, 2014.

187. Apilux, A., et al., *Simple and rapid colorimetric detection of Hg(II) by a paper-based device using silver nanoplates.* Talanta, 2012. **97**(0): p. 388-394.

188. Norrby, L.J., *Why is mercury liquid? Or, why do relativistic effects not get into chemistry textbooks?* Journal of Chemical Education, 1991. **68**(2): p. 110.

189. Calvo, F., et al., *Evidence for Low-Temperature Melting of Mercury owing to Relativity.* Angewandte Chemie International Edition, 2013. **52**(29): p. 7583-7585.

190. Malm, O., *Gold Mining as a Source of Mercury Exposure in the Brazilian Amazon.* Environmental Research, 1998. **77**(2): p. 73-78.

191. Paruchuri, Y., et al., *Occupational and environmental mercury exposure among small-scale gold miners in the Talensi–Nabdam District of Ghana's Upper East region.* Science of The Total Environment, 2010. **408**(24): p. 6079-6085.

192. Ojea-Jiménez, I., et al., *Citrate-Coated Gold Nanoparticles As Smart Scavengers for Mercury(II) Removal from Polluted Waters.* Acs Nano, 2012. **6**(3): p. 2253-2260.

193. Battistoni, C., et al., *Interaction of mercury vapour with thin films of gold.* Applied Surface Science, 1996. **103**(2): p. 107-111.

194. Sabri, Y.M., et al., *Mercury diffusion in gold and silver thin film electrodes on quartz crystal microbalance sensors.* Sensors and Actuators B: Chemical, 2009. **137**(1): p. 246-252.

195. Thundat, T., et al., *Detection of mercury vapor using resonating microcantilevers.* Applied Physics Letters, 1995. **66**(13): p. 1695-1697.

196. George, M.A. and W.S. Glaunsinger, *The electrical and structural properties of gold films and mercury-covered gold films.* Thin Solid Films, 1994. **245**(1–2): p. 215-224.

197. Morris, T. and G. Szulczewski, *Evaluating the Role of Coinage Metal Films in the Detection of Mercury Vapor by Surface Plasmon Resonance Spectroscopy.* Langmuir, 2002. **18**(15): p. 5823-5829.

198. Chah, S., J. Yi, and R.N. Zare, *Surface plasmon resonance analysis of aqueous mercuric ions.* Sensors and Actuators B: Chemical, 2004. **99**(2–3): p. 216-222.

199. Muscat, V., T. Vickers, and A. Andren, *Simple and versatile atomic fluorescence system for determination of nanogram quantities of mercury.* Analytical Chemistry, 1972. **44**(2): p. 218-221.

200. Mercer, T., *Adsorption of mercury vapor by gold and silver.* Analytical Chemistry, 1979. **51**(7): p. 1026-1030.

201. Fitzgerald, W.F. and G.A. Gill, *Subnanogram determination of mercury by two-stage gold amalgamation and gas phase detection applied to atmospheric analysis.* Analytical Chemistry, 1979. **51**(11): p. 1714-1720.

202. Chan, C.C. and R.S. Sadana, *Automated determination of mercury at ultra trace level in waters by gold amalgam preconcentration and cold vapour atomic fluorescence spectrometry.* Analytica Chimica Acta, 1993. **282**(1): p. 109-115.

203. Debrah, E., E.R. Denoyer, and J.F. Tyson, *Flow injection determination of mercury with preconcentration by amalgamation on a gold–platinum gauze by inductively coupled plasma mass spectrometry.* Journal of Analytical Atomic Spectrometry, 1996. **11**(2): p. 127-132.

204. Gill, G.A. and W.F. Fitzgerald, *Picomolar mercury measurements in seawater and other materials using stannous chloride reduction and two-stage gold amalgamation with gas phase detection.* Marine Chemistry, 1987. **20**(3): p. 227-243.

205. Manganiello, L., A. Ríos, and M. Valcárcel, *A method for screening total mercury in water using a flow injection system with piezoelectric detection.* Analytical Chemistry, 2002. **74**(4): p. 921-925.

206. Rex, M., F.E. Hernandez, and A.D. Campiglia, *Pushing the Limits of Mercury Sensors with Gold Nanorods.* Analytical Chemistry, 2005. **78**(2): p. 445-451.

207. Hagen, D.F., et al., *Contacting with gold enmeshed in web on porous substrate to provide gold mercury amalgam*, 1996, Google Patents.

208. Mertens, S.F.L., et al., *Au@Hg Nanoalloy Formation Through Direct Amalgamation: Structural, Spectroscopic, and Computational Evidence for Slow Nanoscale Diffusion.* Advanced Functional Materials, 2011. **21**(17): p. 3259-3267.

209. Morris, T., et al., *The Effects of Mercury Adsorption on the Optical Response of Size-Selected Gold and Silver Nanoparticles.* Langmuir, 2002. **18**(20): p. 7261-7264.

210. Henglein, A. and M. Giersig, *Optical and Chemical Observations on Gold−Mercury Nanoparticles in Aqueous Solution.* The Journal of Physical Chemistry B, 2000. **104**(21): p. 5056-5060.

211. Bootharaju, M.S., K. Chaudhari, and T. Pradeep, *Real time plasmonic spectroscopy of the interaction of Hg2+ with single noble metal nanoparticles.* RSC Advances, 2012. **2**(26): p. 10048-10056.

212. Chemnasiri, W. and F.E. Hernandez, *Gold nanorod-based mercury sensor using functionalized glass substrates.* Sensors and Actuators B: Chemical, 2012. **173**(0): p. 322-328.

213. Liu, Y. and C.Z. Huang, *Real-Time Dark-Field Scattering Microscopic Monitoring of the in Situ Growth of Single Ag@Hg Nanoalloys.* Acs Nano, 2013. **7**(12): p. 11026-11034.

214. Ferrando, R., J. Jellinek, and R.L. Johnston, *Nanoalloys: from theory to applications of alloy clusters and nanoparticles.* Chemical Reviews, 2008. **108**(3): p. 845-910.

215. Cortie, M.B. and A.M. McDonagh, *Synthesis and Optical Properties of Hybrid and Alloy Plasmonic Nanoparticles.* Chemical Reviews, 2011. **111**(6): p. 3713-3735.

216. Moskovits, M., I. Srnova-Sloufova, and B. Vlckova, *Bimetallic Ag--Au nanoparticles: Extracting meaningful optical constants from the surface-plasmon extinction spectrum.* The Journal of Chemical Physics, 2002. **116**(23): p. 10435-10446.

217. Csapó, E., et al., *Synthesis and characterization of Ag/Au alloy and core(Ag)–shell(Au) nanoparticles.* Colloids and Surfaces A: Physicochemical and Engineering Aspects, 2012. **415**(0): p. 281-287.

218. Kim, Y., et al., *Synthesis, linear extinction, and preliminary resonant hyper-Rayleigh scattering studies of gold-core/silver-shell nanoparticles: comparisons of theory and experiment.* Chemical Physics Letters, 2002. **352**(5–6): p. 421-428.

219. Chirea, M., et al., *Spectroelectrochemistry of Silver Deposition on Single Gold Nanocrystals.* The Journal of Physical Chemistry Letters, 2014. **5**(24): p. 4331-4335.

220. Lu, D.L., K. Domen, and K.I. Tanaka, *Electrodeposited Au-Fe, Au-Ni, and Au-Co alloy nanoparticles from aqueous electrolytes.* Langmuir, 2002. **18**(8): p. 3226-3232.

221. Remita, S., M. Mostafavi, and M. Delcourt, *Bimetallic Ag@Pt and Au@Pt aggregates synthesized by radiolysis.* Radiation Physics and Chemistry, 1996. **47**(2): p. 275-279.

222. Doudna, C.M., et al., *Radiolytic synthesis of bimetallic Ag-Pt nanoparticles with a high aspect ratio.* The Journal of Physical Chemistry B, 2003. **107**(13): p. 2966-2970.

223. Henglein, A. and C. Brancewicz, *Absorption spectra and reactions of colloidal bimetallic nanoparticles containing mercury.* Chemistry of Materials, 1997. **9**(10): p. 2164-2167.

224. Link, S., Z.L. Wang, and M. El-Sayed, *Alloy formation of gold-silver nanoparticles and the dependence of the plasmon absorption on their composition.* The Journal of Physical Chemistry B, 1999. **103**(18): p. 3529-3533.

225. Nabika, H., et al., *Preparation and characterization of Au/Co nano-alloys.* Journal of Electroanalytical Chemistry, 2003. **559**: p. 99-102.

226. Hubenthal, F., N. Borg, and F. Träger, *Optical properties and ultrafast electron dynamics in gold–silver alloy and core–shell nanoparticles.* Applied Physics B, 2008. **93**(1): p. 39-45.

227. Hodak, J.H., et al., *Laser-induced inter-diffusion in AuAg core-shell nanoparticles.* The Journal of Physical Chemistry B, 2000. **104**(49): p. 11708-11718.

228. Shore, M.S., et al., *Synthesis of Au(Core)/Ag(Shell) Nanoparticles and their Conversion to AuAg Alloy Nanoparticles.* Small, 2011. **7**(2): p. 230-234.

229. Delogu, F., *Demixing phenomena in NiAl nanometre-sized particles.* Nanotechnology, 2007. **18**(6): p. 065708.

230. Delogu, F., *The mechanism of chemical disordering in Cu3Au nanometre-sized systems.* Nanotechnology, 2007. **18**(23): p. 235706.

231. Yang, Z., et al., *Impacts that pH and metal ion concentration have on the synthesis of bimetallic and trimetallic nanorods from gold seeds.* Journal of Materials Chemistry, 2005. **15**(25): p. 2450-2454.

232. Bönnemann, H. and R.M. Richards, *Nanoscopic metal particles− synthetic methods and potential applications.* European Journal of Inorganic Chemistry, 2001. **2001**(10): p. 2455-2480.

233. Molenbroek, A., S. Haukka, and B. Clausen, *Alloying in Cu/Pd nanoparticle catalysts.* The Journal of Physical Chemistry B, 1998. **102**(52): p. 10680-10689.

234. Lyman, C., R. Lakis, and H. Stenger, *X-ray emission spectrometry of phase separation in Pt Rh nanoparticles for nitric oxide reduction.* Ultramicroscopy, 1995. **58**(1): p. 25-34.

235. Yang, Y., et al., *Preparation of Au–Ag, Ag–Au core–shell bimetallic nanoparticles for surface-enhanced Raman scattering.* Scripta Materialia, 2008. **58**(10): p. 862-865.

236. Pande, S., et al., *Synthesis of normal and inverted gold-silver core-shell architectures in β-Cyclodextrin and their applications in SERS.* The Journal of Physical Chemistry C, 2007. **111**(29): p. 10806-10813.

237. Lu, L., et al., *Fabrication of core-shell Au-Pt nanoparticle film and its potential application as catalysis and SERS substrate.* Journal of Materials Chemistry, 2004. **14**(6): p. 1005-1009.

238. Mandal, M., et al., *Synthesis of Aucore–Agshell type bimetallic nanoparticles for single molecule detection in solution by SERS method.* Journal of Nanoparticle Research, 2004. **6**(1): p. 53-61.

239. Shibata, T., et al., *Size-dependent spontaneous alloying of Au-Ag nanoparticles.* Journal of the American Chemical Society, 2002. **124**(40): p. 11989-11996.

240. Alloyeau, D., et al., *Ostwald ripening in nanoalloys: when thermodynamics drives a size-dependent particle composition.* Physical Review Letters, 2010. **105**(25): p. 255901.

241. Haruta, M., *Size- and support-dependency in the catalysis of gold.* Catalysis Today, 1997. **36**(1): p. 153-166.

242. Gotschy, W., et al., *Optical dichroism of lithographically designed silver nanoparticle films.* Optics Letters, 1996. **21**(15): p. 1099-1101.

243. Brown, K.R. and M.J. Natan, *Hydroxylamine Seeding of Colloidal Au Nanoparticles in Solution and on Surfaces.* Langmuir, 1998. **14**(4): p. 726-728.

244. Michaels, A.M., M. Nirmal, and L.E. Brus, *Surface Enhanced Raman Spectroscopy of Individual Rhodamine 6G Molecules on Large Ag Nanocrystals.* Journal of the American Chemical Society, 1999. **121**(43): p. 9932-9939.

245. Sönnichsen, C., et al., *Plasmon resonances in large noble-metal clusters.* New Journal of Physics, 2002. **4**(1): p. 93.

246. Chang, W.-S., et al., *One-Dimensional Coupling of Gold Nanoparticle Plasmons in Self-Assembled Ring Superstructures.* Nano Letters, 2009. **9**(3): p. 1152-1157.

247. Grésillon, S., et al., *Experimental Observation of Localized Optical Excitations in Random Metal-Dielectric Films.* Physical Review Letters, 1999. **82**(22): p. 4520-4523.

248. Wang, X., et al., *Near- and Far-Field Effects on the Plasmon Coupling in Gold Nanoparticle Arrays.* The Journal of Physical Chemistry C, 2012. **116**(46): p. 24741-24747.

249. Yang, J., et al., *Organic solvent dependence of plasma resonance of gold nanorods: A simple relationship.* Chemical Physics Letters, 2005. **416**(4–6): p. 215-219.

250. Hohenester, U. and A. Trügler, *MNPBEM – A Matlab toolbox for the simulation of plasmonic nanoparticles.* Computer Physics Communications, 2012. **183**(2): p. 370-381.

251. Johnson, P.B. and R.W. Christy, *Optical Constants of the Noble Metals.* Physical Review B, 1972. **6**(12): p. 4370.

252. Novo, C., et al., *Influence of the Medium Refractive Index on the Optical Properties of Single Gold Triangular Prisms on a Substrate.* The Journal of Physical Chemistry C, 2007. **112**(1): p. 3-7.

253. Boening, D.W., *Ecological effects, transport, and fate of mercury: a general review.* Chemosphere, 2000. **40**(12): p. 1335-1351.

254. Hoyle, I. and R.D. Handy, *Dose-dependent inorganic mercury absorption by isolated perfused intestine of rainbow trout, Oncorhynchus mykiss, involves both amiloride-sensitive and energy-dependent pathways.* Aquatic Toxicology, 2005. **72**(1–2): p. 147-159.

255. Baughman, T.A., *Elemental Mercury Spills.* Environmental Health Perspectives, 2006. **114**(2): p. 147-152.

256. de Vries, W., P.A.M. Römkens, and G. Schütze, *Critical Soil Concentrations of Cadmium, Lead, and Mercury in View of Health Effects on Humans and Animals*, in *Reviews of Environmental Contamination and Toxicology*2007, Springer New York. p. 91-130.

257. Percy, A.J., et al., *Reversed-phase high-performance liquid chromatographic separation of inorganic mercury and methylmercury driven by their different coordination chemistry towards thiols.* Journal of Chromatography A, 2007. **1156**(1–2): p. 331-339.

258. Lou, T., et al., *Blue-to-Red Colorimetric Sensing Strategy for Hg2+ and Ag+ via Redox-Regulated Surface Chemistry of Gold Nanoparticles.* ACS Applied Materials & Interfaces, 2011. **3**(5): p. 1568-1573.

259. Manning, M. and G. Redmond, *Formation and characterization of DNA microarrays at silicon nitride substrates.* Langmuir, 2005. **21**(1): p. 395-402.

260. Mu, H., et al., *A novel colorimetric and fluorescent chemosensor: synthesis and selective detection for Cu2+ and Hg2+.* Tetrahedron Letters, 2007. **48**(31): p. 5525-5529.

261. Ballarin, B., et al., *Self-assembled gold nanoparticles modified ITO electrodes: The monolayer binder molecule effect.* Electrochimica Acta, 2008. **53**(27): p. 8034-8044.

262. Westcott, S.L., et al., *Formation and Adsorption of Clusters of Gold Nanoparticles onto Functionalized Silica Nanoparticle Surfaces.* Langmuir, 1998. **14**(19): p. 5396-5401.

263. R. Griffith Freeman, et al., *Self-Assembled Metal Colloid Monolayers: An Approach to SERS Substrates* Science, 1995. **267**: p. 1629.

264. Chen, Y., et al., *The Study of Surface Plasmon in Au/Ag Core/Shell Compound Nanoparticles.* Plasmonics, 2012. **7**(3): p. 509-513.

265. Sun, Y. and Y. Xia, *Alloying and Dealloying Processes Involved in the Preparation of Metal Nanoshells through a Galvanic Replacement Reaction.* Nano Letters, 2003. **3**(11): p. 1569-1572.

266. Cui, Y., et al., *Synthesis of AgcoreAushell Bimetallic Nanoparticles for Immunoassay Based on Surface-Enhanced Raman Spectroscopy.* The Journal of Physical Chemistry B, 2006. **110**(9): p. 4002-4006.

267. Kumar, G.V.P., et al., *Hot Spots in Ag Core−Au Shell Nanoparticles Potent for Surface-Enhanced Raman Scattering Studies of Biomolecules.* The Journal of Physical Chemistry C, 2007. **111**(11): p. 4388-4392.

268. Huang, X., S. Neretina, and M.A. El-Sayed, *Gold Nanorods: From Synthesis and Properties to Biological and Biomedical Applications.* Advanced Materials, 2009. **21**(48): p. 4880-4910.

269. Heider, E.C., et al., *Portable mercury sensor for tap water using surface plasmon resonance of immobilized gold nanorods.* Talanta, 2012. **99**(0): p. 180-185.

270. Quinten, M., *Optical Properties of Nanoparticle Systems - Mie and Beyond*2011, Weinheim: Wiley-VCH.

271. James, J.Z., D. Lucas, and C.P. Koshland, *Elemental mercury vapor interaction with individual gold nanorods.* Analyst, 2013. **138**(8): p. 2323-2328.

272. Inagaki, T., E.T. Arakawa, and M.W. Williams, *Optical properties of liquid mercury.* Physical Review B, 1981. **23**(10): p. 5246-5262.

273. Mulvaney, P., *Surface Plasmon Spectroscopy of Nanosized Metal Particles.* Langmuir, 1996. **12**(3): p. 788-800.

274. Clever, H.L., S.A. Johnson, and M.E. Derrick, *The Solubility of Mercury and Some Sparingly Soluble Mercury Salts in Water and Aqueous Electrolyte Solutions.* Journal of Physical and Chemical Reference Data, 1985. **14**(3): p. 631-680.

275. James, J.Z., D. Lucas, and C.P. Koshland, *Gold Nanoparticle Films As Sensitive and Reusable Elemental Mercury Sensors.* Environmental Science & Technology, 2012. **46**(17): p. 9557-9562.

276. Byers, C.P., et al., *Single-Particle Spectroscopy Reveals Heterogeneity in Electrochemical Tuning of the Localized Surface Plasmon.* The Journal of Physical Chemistry B, 2014.

277. Vanysek, P., *Electrochemical Series*, in *CRC Handbook of Chemistry and Physics*, D.R. Lide, Editor 2005, CRC Press: Boca Raton, FL.

278. Kittel, C., *Introduction to Solid State Physics*. 8th ed2005, Hoboken, NJ: John Wiley & Sons, Inc.

279. Perez-Juste, J., et al., *Gold nanorods: Synthesis, characterization and applications.* Coordination Chemistry Reviews, 2005. **249**(17-18): p. 1870-1901.

280. Kaim, W. and J. Fiedler, *Spectroelectrochemistry: the best of two worlds.* Chemical Society Reviews, 2009. **38**(12): p. 3373-3382.

281. Jeanmaire, D.L. and R.P. Van Duyne, *Surface raman spectroelectrochemistry: Part I. Heterocyclic, aromatic, and aliphatic amines adsorbed on the anodized silver electrode.* Journal of Electroanalytical Chemistry and Interfacial Electrochemistry, 1977. **84**(1): p. 1-20.

282. Gale, R.J., *Spectroelectrochemistry: Theory and Practice*2012: Springer US.

283. Cortés, E., et al., *Monitoring the Electrochemistry of Single Molecules by Surface-Enhanced Raman Spectroscopy.* Journal of the American Chemical Society, 2010. **132**(51): p. 18034-18037.

284. Dick, L.A., et al., *Metal Film over Nanosphere (MFON) Electrodes for Surface-Enhanced Raman Spectroscopy (SERS): Improvements in Surface Nanostructure Stability and Suppression of Irreversible Loss.* The Journal of Physical Chemistry B, 2002. **106**(4): p. 853-860.

285. Wu, D.-Y., et al., *Electrochemical surface-enhanced Raman spectroscopy of nanostructures.* Chemical Society Reviews, 2008. **37**(5): p. 1025-1041.

286. Li, L., et al., *Electrochemiluminescence energy transfer-promoted ultrasensitive immunoassay using near-infrared-emitting CdSeTe/CdS/ZnS quantum dots and gold nanorods.* Sci. Rep., 2013. **3**.

287. Liu, B., et al., *Spectroelectrochemistry of hollow spherical CdSe quantum dot assemblies in water.* Electrochemistry Communications, 2007. **9**(4): p. 551-557.

288. Hill, C.M., D.A. Clayton, and S. Pan, *Combined optical and electrochemical methods for studying electrochemistry at the single molecule and single particle level: recent progress and perspectives.* Physical Chemistry Chemical Physics, 2013. **15**(48): p. 20797-20807.

289. Novo, C., et al., *Electrochemical Charging of Single Gold Nanorods.* Journal of the American Chemical Society, 2009. **131**(41): p. 14664-14666.

290. Dondapati, S.K., et al., *Voltage-Induced Adsorbate Damping of Single Gold Nanorod Plasmons in Aqueous Solution.* Nano Letters, 2012. **12**(3): p. 1247-1252.

291. Alvarez-Puebla, R.A., et al., *Gold nanorods 3D-supercrystals as surface enhanced Raman scattering spectroscopy substrates for the rapid detection of scrambled prions.* Proceedings of the National Academy of Sciences, 2011. **108**(20): p. 8157-8161.

292. Sannomiya, T., et al., *Electrochemistry on a Localized Surface Plasmon Resonance Sensor.* Langmuir, 2009. **26**(10): p. 7619-7626.

293. Nicollian, E.H. and J.R. Brews, *MOS (metal oxide semiconductor) physics and technology*1982: Wiley.

294. Nagpal, P. and V.I. Klimov, *Role of mid-gap states in charge transport and photoconductivity in semiconductor nanocrystal films.* Nat Commun, 2011. **2**: p. 486.

295. Jeon, S., et al., *Gated three-terminal device architecture to eliminate persistent photoconductivity in oxide semiconductor photosensor arrays.* Nat Mater, 2012. **11**(4): p. 301-305.

296. Rees, N.V. and R.G. Compton, *Voltammetry as a probe of displacement.* Chemical Communications, 2010. **46**(24): p. 4238-4248.

297. Davies, T.J. and R.G. Compton, *The cyclic and linear sweep voltammetry of regular and random arrays of microdisc electrodes: Theory.* Journal of Electroanalytical Chemistry, 2005. **585**(1): p. 63-82.

298. Wahl, A., et al., *Gold nanowire electrodes in array: simulation study and experiments.* Faraday Discussions, 2013. **164**(0): p. 377-390.

299. Noviandri, I., et al., *The decamethylferrocenium/decamethylferrocene redox couple: a superior redox standard to the ferrocenium/ferrocene redox couple for studying solvent effects on the thermodynamics of electron transfer.* The Journal of Physical Chemistry B, 1999. **103**(32): p. 6713-6722.

300. Yang, E.S., M.-S. Chan, and A.C. Wahl, *Electron exchange between ferrocene and ferrocenium ion. Effects of solvent and of ring substitution on the rate.* The Journal of Physical Chemistry, 1980. **84**(23): p. 3094-3099.

301. Bond, A.M. and P.A. Lay, *Cyclic voltammetry at microelectrodes in the absence of added electrolyte using a platinum quasi-reference electrode.* Journal of Electroanalytical Chemistry and Interfacial Electrochemistry, 1986. **199**(2): p. 285-295.

302. Dong, Z.-M., X.-M. Qing, and G.-C. Zhao, *Highly Sensitive EQCM Sensor for Mercury Determination by Coupled Stripping Voltammetry.* Int. J. Electrochem. Sci, 2015. **10**: p. 2602-2612.

303. Watson, C.M., et al., *Stripping Analyses of Mercury Using Gold Electrodes: Irreversible Adsorption of Mercury.* Analytical Chemistry, 1999. **71**(15): p. 3181-3186.

304. Bonfil, Y., M. Brand, and E. Kirowa-Eisner, *Trace determination of mercury by anodic stripping voltammetry at the rotating gold electrode.* Analytica Chimica Acta, 2000. **424**(1): p. 65-76.

305. Schadewald, L.A., et al., *Deposition and Stripping of Mercury at Gold Electrodes in Acidic Media: I . Voltammetric Studies.* Journal of The Electrochemical Society, 1984. **131**(7): p. 1583-1587.

306. Kuemin, C., et al., *Precise Placement of Gold Nanorods by Capillary Assembly.* Langmuir, 2011. **27**(10): p. 6305-6310.